Experimental Characterization of Influence of Gaseous Hydrogen on Fatigue Crack Propagation and Crack Tip Plasticity in Commercially Pure Iron

Tomoki Shinko

THESE

Pour l'obtention du Grade de

DOCTEUR DE L'ECOLE NATIONALE SUPERIEURE DE MECANIQUE ET D'AEROTECHNIQUE

(Diplôme National – Arrêté du 25 mai 2016)

Ecole Doctorale :
Sciences et Ingénierie des Matériaux, Mécanique, Energétique

Secteur de Recherche :
Mécanique des solides, des matériaux, des structures et des surfaces

Présentée par :

Tomoki SHINKO

****

Experimental characterization of influence of gaseous hydrogen on fatigue crack propagation and crack tip plasticity in commercially pure iron

****

Directeurs de thèse : Gilbert HENAFF et Damien HALM

Soutenue le 26 mars 2019
devant la Commission d'Examen

JURY

Président:
Xavier Feaugas, Professeur, Université de La Rochelle, LaSie
Rapporteurs:
Afrooz Barnoush, Professeur, NTNU, Norvège
Laurent Briottet, Chercheur HDR, CEA, LITEN, Grenoble
Membres du jury :
Isabelle Aubert, Maître de Conférences, Université de Bordeaux, I2M
Milos Djukic, Associate professor, Université de Belgrade, Serbie
Gilbert Hénaff, Professeur, ISAE-ENSMA, Institut P'
Damien Halm, Professeur, ISAE-ENSMA, Institut P'

Acknowledgement

This thesis was financed by Région Nouvelle Aquitaine (formerly Poitou-Charentes) for salary and the French Government program “Investissements d’Avenir” (LABEX INTERACTIFS, reference ANR-11-LABX-0017-01).

Firstly, I would like to sincerely thank to my supervisors Prof. Gilbert Hénaff and Prof. Damien Halm for the continuous support of my Ph.D. study for three and half years, for their patience, motivation, inspiration, and expert advice. I was very lucky that I could do my Ph.D. under their supervision.

I would also like to thank the rest members of jury committee: Prof. Afrooz Barnoush, Dr. Laurent Briottet, Prof. Xavier Feaugas, Dr. Isabelle Aubert and Prof. Milos Djukic for their insightful comments and discussion.

I am very grateful to Guillaume (B.) for helping all my experimental works from specimen preparation to FCG test. I could not make such many difficult experiments using HYCOMAT test bench without his help. Besides, I also thank Guillaume (A.) and Hadi at Université de Poitiers for the FIB and STEM observations. I am also deeply grateful to Mandana and Battista for their helps for my experimental works and good discussions.

I want to express my deep gratitude to all the members at Institut Pprime. In particular, a very special word of thanks goes to Ravi, Satoshi, and Mahak. They are not only my colleagues but also my best friends in France. I will never forget many fun memories with them.

I appreciate the members at my office (Multimat): Julius, Anani and Guy as my friends having a lunch together with a fun. As well as them, Vincent, Aurélien, Emeline, Amelie, Julien, Roman and Carolina, who have friendly supported me even though I was not good at speaking in French. Besides, I also really thank Layra (speaking in Japanese very fluently) for helping me for many language and cultural problems.

Finally, my sincere thanks go to my parents Tadashi and Kumiko, my wife Risa, and her family Mitsue, Keiko, Satsuki and Shuichi for believing in me and their spiritual support in everything of my life.

Table of contents

Introduction

In coming years, due to a shortage of fossil fuels and air pollution problem, a realization of "fossil-fuel-free" society is strongly required for sustainable development. One of the most promising solutions for "fossil-fuel-free" society is hydrogen-based society. The hydrogen-based society is a clean and sustainable energy infrastructure using hydrogen as an energy carrier without consumption of fossil fuels and emission of greenhouse gases. For example, a fuel cell vehicle and a hydrogen refueling station already have been developed in industry [1]. However, a key issue related with the development of such infrastructures is the hydrogen compatibility of the materials used. Indeed it is well known that metallic materials exposed to gaseous hydrogen may undergo a significant degradation of mechanical properties commonly known as "hydrogen embrittlement (HE)" [2–4]. This detrimental effect of hydrogen remarkably reduces fatigue strength, which is a serious problem in guaranteeing the long-term reliability of the hydrogen-related equipment. Hence the elucidation of its mechanism is highly demanded.

Since the HE of iron and steels was firstly found by Johnson [5] in 1874, many studies have been conducted for investigating an effect of hydrogen on the mechanical properties of metallic materials. At the same time, numerous theories have been proposed to explain the mechanism of hydrogen embrittlement. In particular, the following three theories are today considered as the most important ones: HEDE (Hydrogen-Enhanced DEcohesion) [6, 7], HELP (Hydrogen-Enhanced Localized Plasticity) [8], AIDE (Adsorption-Induced Dislocation Emission) [9] and HESIV (Hydrogen-Enhanced Strain-Induced Void) [10]. The HEDE mechanism supposes that the hydrogen atoms adsorbed at a crack tip or segregated at the grain boundaries weaken interatomic bonds and cause an atomic decohesion. This leads to a brittle fracture such as a cleavage fracture and an intergranular decohesion. In the HELP mechanism, the solute hydrogen atoms in front of the crack tip enhance and localize the dislocation activity. This promotes a nucleation and coalescence of microvoids as crack embryos, resulting in a crack propagation with less blunting and less macroscopic ductility of the material. The fracture surface often exhibits small, shallow dimples [11, 12]. The AIDE mechanism is based on the facilitation of dislocation nucleation due to adsorbed hydrogen. In this mechanism, the adsorbed hydrogen on the surface or the sub-surface weakens interatomic bonds and promotes the dislocation nucleation at the crack tip which enhances the crack advancement. The main difference between the HELP and the AIDE is that the AIDE involves the sub-surface effect of adsorbed hydrogen while the effect of HELP is caused by the solute hydrogen in the material. The HESIV describes that hydrogen in the material assists the creation and stabilization of defects during plastic deformation. The embrittlement of the metals is caused due to an overconcentration of vacancies in the material, and not directly due to the presence of hydrogen.

Over the last decades, most of the studies concerning hydrogen embrittlement have concentrated on a framework of fracture under monotonic loading. In addition to this, research on materials in hydrogen charged state has been common due to its easiness. However, from the viewpoint of practical application, in many cases of hydrogen-related equipment, the material is subjected to a hydrogen gas environment and repeated loading. Since hydrogen distribution in a material exposed to hydrogen atmosphere is different from the hydrogen-charged case, these cases cannot

be identified [11]. Therefore, it is practically important to consider a problem of fatigue in a state of exposure to a hydrogen gas environment.

From this fact, in recent years, the influence of hydrogen on fatigue life has been actively investigated. A significant enhancement of Fatigue Crack Growth Rate (FCGR) under hydrogen-charged state and gaseous hydrogen atmosphere have been revealed [3, 13]. Especially, martensitic [14] and ferrite-pearlite steels [3] exhibit high susceptibility to hydrogen effect because of their high diffusivity of hydrogen.

Several models of mechanism of Hydrogen-Affected Fatigue Crack Growth (HAFCG) have been proposed in literature. For example, a hydrogen-induced cyclic cleavage model was proposed by Marrow et al. [15] in 1992. They concluded that when the applied loading starts increasing, dislocations are emitted from the crack tip and the crack tip starts blunting. The high hydrostatic stress field with high dislocation density is formed in front of the crack tip. Subsequently, the diffused hydrogen atoms are intensely trapped within this field. The highly accumulated hydrogen atoms reduce the lattice cohesive energy, and consequences a cleavage fracture by the HEDE mechanism. Matsuoka et al. [16, 17] proposed a "Hydrogen Enhanced Successive Fatigue Crack Growth (HESFCG)" model. They noticed that the localization of plastic deformation near the crack tip is associated with the FCGR enhancement in hydrogen-charged austenitic stainless steel and low carbon steel, by observing the suppression of slip deformation around crack path and the presence of brittle striation on the fracture surface. Based on their experimental evidence, they proposed the HESFCG model based on the HELP mechanism. In addition, Nishikawa et al. [18] proposed the mechanism of HAFCG driven by a micro-void coalescence ahead of the crack tip, induced by the HESIV mechanism.

From the recent studies, the modification of plasticity at the crack tip by hydrogen is recognized as a key factor of HAFCG mechanism. The hydrogen effect on crack tip plasticity has been evidenced by various means of observation techniques such as Electron Back Scattering Diffraction (EBSD) [19] and Transmission Electron Microscopy (TEM) [19–21]. Especially, Robertson et al. [12, 22, 23] have been leading the advancement of fundamental understanding of the interaction between solute hydrogen and mobile dislocations in the material by directly observing the dislocation activity by TEM technique.

For improving a safety design of hydrogen-related equipment, the research project by Pprime Institute [24–27] has dedicated to the development of numerical tool predicting the FCG in steels under hydrogen atmosphere based on a cohesive zone model. The latest result of the developed numerical model is presented in Figure 1, comparing the experimental data of FCGR in a precipitation-hardened martensitic stainless steel 15-5PH in hydrogen and the ones predicted by the numerical model. As this diagram exhibits, the numerical model correctly predicts the FCGR at low hydrogen gas pressure (0.09 MPa), while it underestimated the highly enhanced FCGRs at high hydrogen gas pressure (9 MPa). Therefore, this result indicates that advancement of the understandings for the influence of hydrogen gas pressure and loading frequency on the FCG mechanism in hydrogen is strongly required to improve the capability of the numerical model.

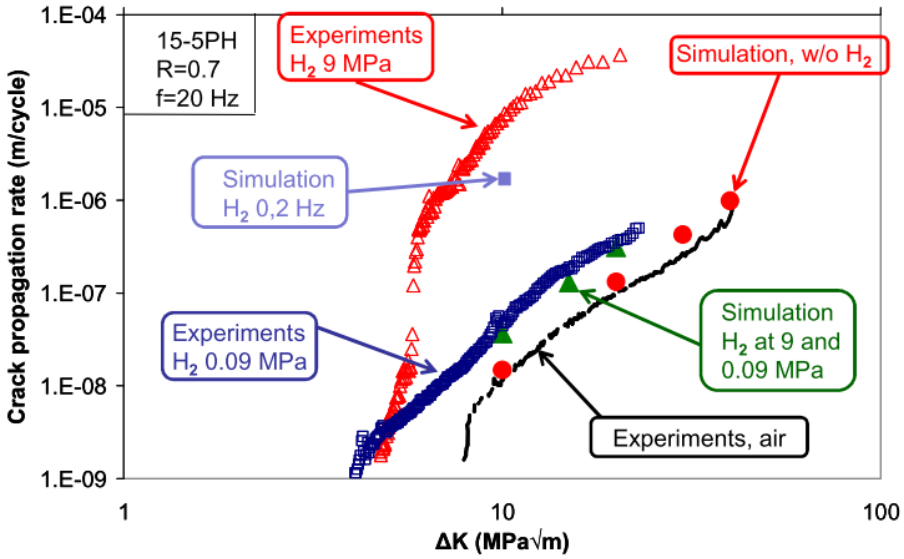

Figure 1 Numerical results obtained without hydrogen (●), at low and high pressure of hydrogen (0.09 and 9 MPa) at 20 Hz (▲) and at high pressure and 0.2 Hz (■) are compared to experimental ones [25]

From this point of view, the recent studies by Pprime Institute [28–30] have put the emphasis on FCG tests in a commercially pure iron, Armco iron, aiming to investigate the fracture mechanism under various hydrogen gas pressures and loading frequencies. Armco iron was selected as a sample material because it allows us to analyze the interaction between hydrogen and its simple ferrite microstructure. From the previous studies by Bilotta et al. [27, 28], it has been demonstrated that the FCGR at hydrogen gas pressure P_{H2} = 35 MPa is highly enhanced in this material. Besides, the clear dependence of HAFCG rate on the loading frequency has been observed. Nevertheless, the mechanism of FCG enhancement by hydrogen and its dependency on testing parameters are still unclear. This is because of a shortage of understandings for the interaction between hydrogen and plasticity of the material and the characteristics of FCG in hydrogen under wide range of testing parameters (hydrogen gas pressure, loading frequency etc.).

Therefore, the objective of this study is to advance in the understanding for the mechanism of FCG in the presence of hydrogen by clarifying the interaction between hydrogen and crack tip plasticity and the influence of testing parameters on hydrogen-affected FCG in Armco iron.

First of all, Chapter 1 reviews theoretical principles of a source, absorption, transportation, and trapping of hydrogen in metallic materials. After that, some models of HE mechanism and also hydrogen-affected FCG mechanism proposed in literature will be summarized.

For investigating the interaction between hydrogen and crack tip plasticity, since many complex factors (e.g. stress concentration, complex slip activity, variable loading etc.) are involved in the phenomenon of crack growth interacting with hydrogen, it is difficult to consider the hydrogen activity in the vicinity of the crack tip at first place. Thus, this study will start from considering the simplified situation (uniform stress field and monotonic loading), namely tensile deformation of the material with the presence of hydrogen will be considered for the beginning. For this purpose, in Chapter 2, the interaction between hydrogen and uniform plastic deformation is

investigated by conducting tensile tests under several atmospheres including gaseous hydrogen. In this test, strain rate and hydrogen exposure time before loading are variated in order to investigate the dependency of hydrogen embrittlement on these parameters.

In Chapter 3, the FCG test under gaseous hydrogen is conducted aiming to investigate the influence of hydrogen on FCG behavior as a function of crack tip stress intensity factor range ΔK, hydrogen gas pressure and loading frequency. Firstly, the FCG tests with increasing ΔK are performed at hydrogen gas pressure of 3.5 and 35 MPa and loading frequency from 0.2 to 20 Hz. After that, in order to analyze the dependency of FCG in hydrogen on a wider range of loading frequency, the FCG tests with a constant ΔK are conducted at loading frequency down to 0.02 Hz. Then, fracture surfaces of tested specimens are examined by means of Scanning Electron Microscopy (SEM) to identify the fracture mode of FCG in hydrogen.

In Chapter 4, aiming to address the crack tip plasticity in FCG with the presence of hydrogen, the near-tip plastic deformation produced during FCG is evaluated by several means of analysis techniques: optical observation, out-of-displacement measurement, and transmission electron microscopy. These analysis techniques examine the crack tip plasticity in a multiscale way from macroscopic scale to microscopic one corresponding to dislocation structure.

Finally, Chapter 5 presents an integration of obtained experimental insights and discussions on the mechanism of hydrogen-affected FCG and the mechanism of its dependency on various testing conditions.

Chapter 1

State of the art: hydrogen embrittlement

Résumé

Chapitre 1: Etat de l'art: fragilisation par l'hydrogène

R-1.1 Introduction

Le premier chapitre de cette thèse présente une étude bibliographique du phénomène de fragilisation par l'hydrogène (FPH), processus qui rend un métal "fragile" en raison de l'interaction entre l'hydrogène et le métal. Dans cette étude, l'influence de l'hydrogène sur la propagation d'une fissure de fatigue dans un matériau métallique est plus particulièrement examinée.

La revue de littérature se concentre sur les trois sujets suivants. Tout d'abord, un aperçu de la FPH et des effets néfastes de l'hydrogène sur la résistance des matériaux sous déformation monotone et cyclique sera présenté. Deuxièmement, le mécanisme d'influence de l'hydrogène sur la fissuration sera examiné en introduisant quatre modèles principaux proposés jusqu'à présent dans la littérature: HEDE, HELP, AIDE et HESIV. Nous passerons ensuite en revue trois modèles principaux de propagation des fissures de fatigue en présence d'hydrogène. Enfin, la motivation de cette étude sera exposée.

R-1.2 Mécanisme de FPH

Depuis que la FPH du fer et des aciers a été découverte par Johnson [5] en 1874, de nombreuses études ont été menées pour étudier l'effet de l'hydrogène sur les propriétés mécaniques des matériaux métalliques. Dans le même temps, de nombreuses théories ont été proposées pour expliquer le mécanisme de la FPH. Les trois théories suivantes sont aujourd'hui considérées comme les plus importantes: HEDE (Hydrogen-Enhanced DEcohesion) [6, 7], HELP (Hydrogen-Enhanced Localized Plasticity) [8], AIDE (Adsorption-Induced Dislocation Emission) [9] et HESIV (Hydrogen-Enhanced Strain-Induced Void) [10]. Le mécanisme HEDE suppose que les atomes d'hydrogène adsorbés au niveau du fond d'une fissure ou aux joints de grain affaiblissent les liaisons interatomiques et provoquent une décohésion atomique. Cela conduit à une rupture fragile de type clivage et une décohésion intergranulaire. Dans le mécanisme HELP, les atomes d'hydrogène dissous en pointe de fissure renforcent et localisent l'activité des dislocations. Ceci favorise la nucléation et la coalescence des microvides en tant qu'embryons de fissure, ce qui entraîne une propagation de la fissure avec une ductilité moins macroscopique du matériau. La surface de rupture présente souvent de petites cupules peu profondes [11, 12]. Le mécanisme AIDE est basé sur la facilitation de la nucléation des dislocations due à l'hydrogène adsorbé. Dans ce mécanisme, l'hydrogène adsorbé en surface ou sous-surface affaiblit les liaisons interatomiques et favorise la nucléation des dislocations au niveau du fond de fissure, ce qui augmente la déformation plastique locale près du fond de fissure. Le principe de l'amélioration de la propagation de fissure par l'AIDE est similaire au mécanisme HELP. Cependant, la principale différence est que l'AIDE implique l'effet sous-surfacique de l'hydrogène adsorbé, tandis que l'effet de HELP est provoqué par l'hydrogène dissous présent dans le matériau. Le HESIV

suppose que l'hydrogène dans le matériau aide à la création et à la stabilisation des défauts lors de la déformation plastique. La fragilisation des métaux est due à une surconcentration des lacunes dans le matériau et pas directement à la présence d'hydrogène.

R-1.3 Mécanisme d'accélération de la propagation des fissures de fatigue par l'hydrogène

Sur la base des mécanismes susmentionnés de la FPH, plusieurs modèles ont été proposés dans la littérature pour expliquer l'influence de l'hydrogène sur la propagation des fissures de fatigue. Cette section présente les trois modèles représentatifs de la propagation des fissures de fatigue affectée par l'hydrogène: modèle Hydrogen Enhanced Successive Fatigue Crack Growth (HESFCG) [16, 17], modèle de clivage cyclique induit par l'hydrogène [15] et modèle de coalescence des vides induit par l'hydrogène [18].

Le modèle HESFCG a été proposé par Matsuoka et al. [16, 17]. Ils ont constaté que la localisation de la déformation plastique près du fond de la fissure est associée à l'augmentation de la vitesse de propagation des fissures de fatigue dans les aciers inoxydables austénitiques et les aciers à faible teneur en carbone chargés en hydrogène, en observant la suppression de la déformation par glissement près du trajet de la fissure et la présence de stries sur la surface de rupture. Sur la base de leurs résultats expérimentaux, ils ont proposé un scénario de propagation des fissures de fatigue en présence d'hydrogène comme suit: pendant l'étape de chargement cyclique, l'hydrogène diffusé à partir du front de fissure est concentré dans le champ de fortes contraintes hydrostatiques situé en avant du front de fissure. L'hydrogène dissous fortement accumulé se localise et augmente la déformation plastique dans la zone situé en amont du front de fissure, grâce au mécanisme HELP. La taille de la zone plastique est beaucoup plus faible que dans l'air. Il en résulte une réduction de l'émoussement du front de fissure.

Deuxièmement, le modèle de clivage cyclique induit par l'hydrogène a été proposé par Marrow et al. [15] en 1992. Ils ont conclu que lorsque le chargement appliqué commence à augmenter, des dislocations sont émises à partir du front de fissure qui commence à s'émousser. Un champ de contraintes hydrostatiques et une forte densité de dislocations se forment devant le front de fissure. Par la suite, les atomes d'hydrogène diffusés sont piégés dans ce champ. Les atomes d'hydrogène fortement accumulés réduisent l'énergie de cohésion du réseau et entraînent une rupture par clivage selon le mécanisme HEDE. Ce modèle indique qu'un champ de déformation plastique intense se forme devant le front de fissure, même si le mécanisme de fissuration est une décohésion atomique qui ne nécessite pas de déformation plastique.

Troisièmement, le modèle de coalescence des vides induit par l'hydrogène a été proposé par Nishikawa et al. [18]. Ce modèle suppose que, lors du chargement, l'interaction entre l'hydrogène et la zone déformée plastiquement en amont du front de fissure génère une haute densité de microvides par le mécanisme HESIV. En conséquence, une déchirure ductile se produit entre les microvides sous la forme d'une coalescence qui entraîne la croissance de la fissure.

R-1.4 Motivation de cette étude

Afin de prédire la durée de vie en fatigue des équipements en contact avec l'hydrogène, le projet de recherche de l'Institut Pprime [24–27] a porté sur la compréhension de l'influence de la pression de l'hydrogène gazeux et de la fréquence de chargement sur le mécanisme de propagation des fissures de fatigue dans l'hydrogène. Ainsi, les récentes études [28–30] ont mis l'accent sur les essais de fissuration dans un fer commercialement pur, le fer Armco, visant à étudier le mécanisme de rupture sous diverses pressions et fréquences. Le fer Armco a été sélectionné comme matériau de référence car il nous permet d'analyser l'interaction entre l'hydrogène et sa microstructure en ferrite simple. D'après les études précédentes de Bilotta et al. [27, 28], il a été démontré que la vitesse de propagation des fissures de fatigue sous pression d'hydrogène gazeux P_{H2} = 35 MPa est fortement augmentée dans ce matériau. En outre, la dépendance évidente de la vitesse de propagation des fissures de fatigue affectées par l'hydrogène à la fréquence de chargement a été observée. Néanmoins, le mécanisme d'accélération de la propagation des fissures de fatigue par l'hydrogène et sa dépendance aux paramètres d'essai ne sont toujours pas clairs. Cela est dû à un manque de compréhension de l'interaction entre l'hydrogène et la plasticité du matériau et les caractéristiques de la propagation des fissures de fatigue dans l'hydrogène dans une large gamme de paramètres de test (pression d'hydrogène, fréquence de chargement, etc.).

Par conséquent, l'objectif de cette étude est de faire progresser la compréhension du mécanisme de propagation des fissures de fatigue en présence d'hydrogène en clarifiant principalement les deux points suivants:

- interaction entre l'hydrogène et la plasticité en pointe de fissures,

l'influence des paramètres d'essai sur la propagation des fissures de fatigue affectée par l'hydrogène dans le fer Armco.

----------(Fin du résumé)----------

1.1 Introduction

The first chapter of this thesis presents a bibliographic study of the phenomenon of Hydrogen Embrittlement (HE). In this study, the influence of hydrogen on a fatigue crack propagation in metallic material is more particularly addressed.

The literature review focuses on the following three topics. First, principles on absorption, diffusion and transportation of hydrogen in a material will be presented. Secondly, an overview of HE in terms of a detrimental effect of hydrogen on material strength under monotonic and cyclic deformation will be reviewed. Thirdly, a mechanism of influence of hydrogen on cracking will be reviewed by introducing four main models proposed so far in literature: HEDE, HELP, AIDE and HESIV. Subsequently, three main models of fatigue crack propagation in the presence of hydrogen will be reviewed. Finally, the motivation of this study will be stated.

1.2 Source of hydrogen

Hydrogen atoms can be introduced inside the material by the following four processes:

- during production or during transformation and implementation operations (heat treatment, welding);
- use of steels in the presence of hydrogen (storage of hydrogen gas) or hydrogenated gas mixtures;
- hydrogen generated by electrolytic reactions (surface treatments, cathodic protection);
- hydrogen generated by corrosion reactions (aqueous environments).

Due to the difference in these hydrogen supply methods, the distribution of hydrogen concentration in the material is different. In particular, it is known that the characteristics of HE effect is different depending on whether hydrogen is stored in the interior (internal hydrogen) or externally supplied (external hydrogen) during applying mechanical loading [11].

HE by internal hydrogen is investigated by a test in which hydrogen is pre-charged inside the material before performing a test and then a load is applied in air. Charging of hydrogen is generally performed electrochemically (e.g. electrolytic loading in aqueous medium or molten salt bath). On the other hand, HE by external hydrogen is investigated by conducting a test under a hydrogen gas environment or an in-situ hydrogen charging during the test.

San-Marchi and Somerday [12] give technical references for the use of metallic materials under hydrogen. They recommend selecting the hydrogen charging technique according to the hydrogen diffusivity of the material. The hydrogen pre-charging should be used only when the diffusivity of hydrogen is less than 10^{-15} m^2/s (typically on austenitic steels), to prevent a large amount of hydrogen desorbing before or during the test. In contrast, a test under gaseous hydrogen is recommended when the hydrogen diffusivity of the material is high. An in-situ hydrogen charging is not guaranteed to have a sufficient amount of hydrogen absorption if the test duration is relatively short.

From the viewpoint of practical application of hydrogen-related equipment, the material is often subjected to a hydrogen gas environment accompanied by a repeated loading. Therefore, it is practically important to consider the problem of cyclic deformation (i.e. fatigue) in a state of exposure to a hydrogen gas environment (i.e. external hydrogen).

In order to understand the role of hydrogen in HE, it is essential to know a process letting hydrogen enter the material. Sections 1.3 and 1.4 present the mechanisms of hydrogen entry into metals in a gaseous hydrogen atmosphere which is the case in the present study, and a "transportation" of hydrogen by interstitial diffusion and dislocation-dragging.

1.3 Hydrogen absorption

In this study, gaseous hydrogen will be used for hydrogen charging. The hydrogen charging will be conducted simultaneously with mechanical tests. It is therefore important to analyze the mechanisms of hydrogen entry into the material from the hydrogen atmosphere. The hydrogen entry into metals takes place in two distinct steps: adsorption and absorption.

1.3.1 Dissociation and adsorption

The adsorption of hydrogen in a gaseous environment is generally described by three steps:

1) Physisorption of the dihydrogen molecule on the surface of the metal. This step involves low energy levels (less than 0.5 eV) and is governed by the Van Der Waals bond between the H_2 molecule and the surface atoms.
2) Dissociation of the dihydrogen molecule.
3) Chemisorption of surface hydrogen atoms which involves the creation of atomic bonds.

Since a discontinuity in the periodic arrangement of atoms generally exists at the surface of the material, the surface atoms thus are subjected to force field, and they try to minimize it by creating new bonds with the atmospheric atoms. Their reaction results in the adsorption of molecules and/or atoms in the atmosphere.

This reaction of dissociation of the molecules of hydrogen and adsorption on the surface is reversible. Therefore, once the state reaches equilibrium, there will be molecules dissociating as many as atoms desorbing and re-associating to form a molecule of hydrogen gas, at a given temperature. A schematic diagram of this dynamic is presented by Figure 1 - 1, drawn by Hassan [31].

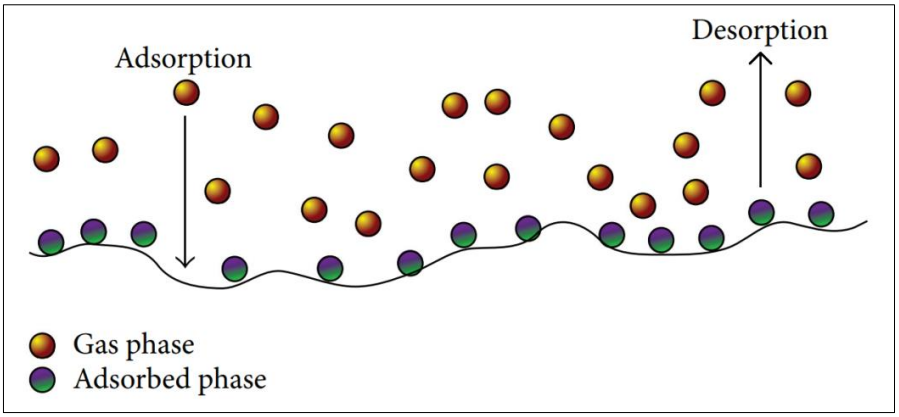

Figure 1 - 1 Schematic illustration of adsorption and desorption dynamics, by Hassan [31]

The ratio of the surface area coated with adsorbed atoms to the total available surface area is represented by a coverage ratio θ, between 0 and 1. $\theta = 1$ means that all available adsorption sites are occupied by adsorbed hydrogen atoms. The value of θ depends on several factors (the temperature and the pressure of gaseous hydrogen).

Diagram of θ as a function of gas pressure at constant temperature is called as a gas isotherm. Langmuir isotherm is an equilibrium between the hydrogen adsorption and desorption rates as expressed by Equation 1 - 1 which describes the dependency of the coverage rate on the hydrogen concentration C:

$$\theta = \frac{b(T)C}{1 + b(T)C} \qquad 1 - 1$$

In this equation, the adsorption coefficient b (T) is defined as:

$$b(T) = \frac{k_{ads}}{k_{des}} \qquad 1 - 2$$

where k_{ads} and k_{des} are the kinetic constants of the adsorption and desorption reactions. The coefficient b (T) can also be expressed as:

$$b(T) = \exp\left(\frac{\Delta g_b^0}{RT}\right) \qquad 1 - 3$$

where Δg_b^0 represents the difference in free energy between the surface and the core of the material, R is the constant of perfect gas and T is the temperature. Several values for Δg_b^0 have been proposed in the literature. Serebrinsky et al. [32] gave the value of 30 kJ/mol, as well as Gerberich et al. [33], while Hirth [34] used a slightly lower value, 28.6 kJ/mol. Moriconi et al. [24–26] used the value of Δg_b^0 = 36 kJ/mol in their cohesive zone model for simulating the propagation of fatigue cracks under hydrogen gas. The difference in these values between each literature indicates the difficulty of precisely identifying this energy.

The Langmuir isotherm is based on the following hypotheses:

- The surface on which there is adsorption is uniform;

- The adsorption energy is independent of the recovery rate;
- The adsorption is done in monolayer;
- There is a local equilibrium between adsorbed gas molecules and adsorption sites.

Under these conditions, the adsorption rate v_{ads} is proportional to the hydrogen concentration in solution C and to the fraction of unoccupied adsorption sites, while the desorption rate v_{des} is proportional to the fraction of occupied sites. Then, the following relations are given:

$$v_{ads} = k_{ads}(1-\theta)C \quad 1-4$$

$$v_{des} = k_{des}\theta \quad 1-5$$

Figure 1 - 2 represents the Langmuir isotherms for different values of the adsorption coefficient b (T) [27]. Concentration is normalized to an arbitrary maximum concentration. As shown in this diagram, the higher the value of $b(T)$, the higher the saturation plateau is reached for a low concentration.

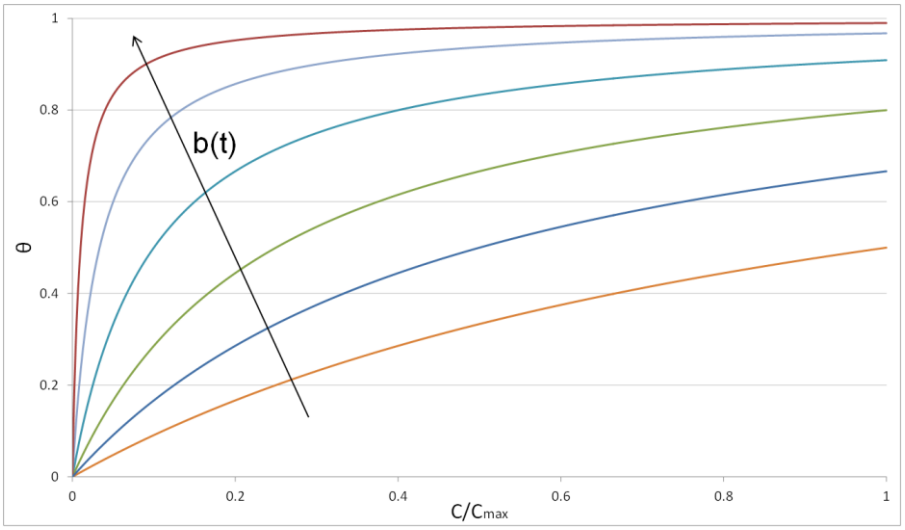

Figure 1 - 2 Evolution of the Langmuir isotherm according to the value of the adsorption coefficient b (T) [27]

This gives us an idea of the evolution of θ with the hydrogen pressure, at a given temperature in the assumption of uniform surface, without formation of the oxide layer, of constant adsorption energy for a value of θ data, etc.

1.3.2 Absorption

Hydrogen atoms adsorbed on the surface then move to the interstitial sites of the first layers of atoms of the metal. Since the target material in this study is commercially pure iron that consists of Body-Centered Cubic (BCC) structure, the BCC material will be considered in the following reviews. Jiang and Carter [35] conducted diffusion calculations in an ab initio approach. They deduced that hydrogen dissolved in BCC iron occupies tetrahedral sites in a wide range of concentrations. This validates the hypothesis that the hydrogen atoms diffuse and position

themselves in the interstitial sites of the metallic matrix. The hydrogen can then be trapped by the microstructural defects of the material.

The solubility of hydrogen in metals C_s can be evaluated by the Sieverts law [36]:

$$C_s = S_0\sqrt{p}\, e^{-\Delta H/RT} \qquad 1 - 6$$

where S_0 is a solubility constant, p the partial pressure, ΔH is the dissolution enthalpy [J/mol], R is the perfect gas constant (= 8.314 J/mol/K) and T the temperature [K]. Sievert's law is an empirical relation indicating that the penetration of a gas into a metal is preceded by a dissolution process of the molecules. This depends on the temperature and is proportional to the square root the pressure of the gas. Numerous works have been conducted for the identification of dissolution enthalpy. In particular, the hydrogen concentrations in alpha iron were identified as the order from 10^{-3} to 10^{-4} mass ppm at ambient temperature and less than 1 atm of hydrogen pressure [34]. On the other hand, Broudeur et al. [37] obtained the solubility for austenitic steels of 0.35 ppm mass under the same conditions of pressure and temperature. According to Sievert's law, therefore, the solubility of hydrogen is very low in alpha iron compared to austenitic steels.

The solubility of hydrogen depends on the gas pressure and temperature. Figure 1 - 3 shows this dependence, in the case of a dissolution enthalpy of 28600 J/mol (value identified by Hirth [34] on alpha iron).

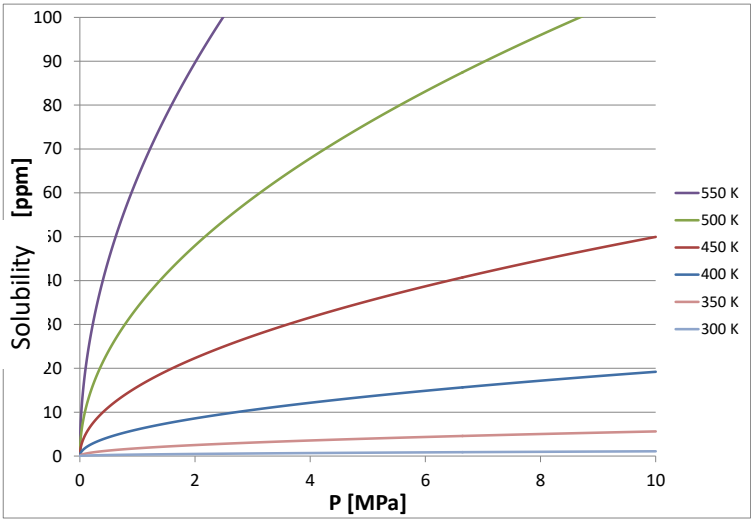

Figure 1 - 3 Evolution of the solubility of hydrogen in alpha iron as a function of pressure and temperature, in the case of a dissolution enthalpy of 28600 J/mol [34]

Figure 1 - 3 shows how solubility can vary greatly with temperature and pressure. These parameters should therefore be well controlled during mechanical testing, as a small variation in temperature and pressure may result in a change in the amount of hydrogen entering the material, and thus lead to a change in mechanisms of embrittlement. In particular, it is noted that the solubility of hydrogen in iron is quite low at room temperature.

1.4 Hydrogen transportation

Once the hydrogen atoms are absorbed into the material, they will be stored in the interstitial sites of the metal or trapped reversibly or irreversibly depending on the types of hydrogen traps (dislocations, precipitates, etc.). The total hydrogen concentration C is described by $C = C_L + C_T$ where C_L the interstitial hydrogen concentration, and C_T the trapped hydrogen concentration. Firstly, the mechanisms of hydrogen diffusion will be presented, after that the trapping of the hydrogen will be described. At last, the equilibrium between these two populations of hydrogen will be presented.

1.4.1 Interstitial diffusion

A cause of the interstitial diffusion of hydrogen in a metal is the hydrogen concentration gradient between the surface and the heart of the metal, created by the absorption of the hydrogen. Interstitial diffusion consists of a series of "jumps" from one interstitial site to the next one. The jumps require an activation energy to pass an energy barrier between two sites. The first and second Fick's laws classically describe the interstitial diffusion in the absence of any other driving force. Stress gradient, temperature or existence of an electric field can also trigger the diffusion of the hydrogen. Indeed, due to its large partial molar volume, hydrogen is sensitive to stress fields [38]. In the isothermal case and in the absence of an electric field, the flow of hydrogen $\vec{J}$ [atoms/m^2/s] is expressed by the following relation [39]:

$$\vec{J} = -D_L \nabla C_L + \frac{D_L C_L \bar{V}_H}{RT} \nabla \sigma_h \qquad 1 - 7$$

where D_L is the lattice diffusion coefficient [m^2/s] and C_L is the concentration of interstitial hydrogen which depends on axis and time, $\bar{V}_H$ the partial molar volume, R the perfect gas constant, T is the temperature, and σ_h the hydrostatic stress. According to this equation, the hydrogen diffusion is controlled by the hydrogen concentration gradient and the hydrostatic stress gradient. This relationship indicates that the hydrogen diffuses to areas where the concentration of interstitial hydrogen is lower, and where the hydrostatic stress is higher.

The diffusion coefficient D_L depends on the temperature. Crank [40] expresses this dependency in an exponential form:

$$D_L = D_0 * e^{-Q/RT} \qquad 1 - 8$$

For alpha iron, D_0 is 1.6×10^{-7} m^2/s and the activation energy Q = 7075 J/mol. If the temperature is T = 300 K, the diffusion coefficient is provided as approximately $D_L = 10^{-8}$ m^2/s. The value of the diffusion coefficient for pure iron is very high compared to steels. For example, for martensitic steels, the literature gives values of the order of $D_L = 10^{-12}$ m^2/s [41, 42]. An even lower value is given for austenitic steels, of the order of $D_L = 10^{-16}$ m^2/s [43].

1.4.2 Trapping

The presence of hydrogen traps in a steel greatly influences its behavior in the presence of hydrogen. The phenomenon of trapping increases the apparent solubility of hydrogen and reduces the apparent diffusivity. Besides, trapping favors phenomena of local over-concentration of hydrogen, enhancing the HE [43]. Trapping originates from the existence of a pulling force that modifies the jump probability in a given direction or a local perturbation of the crystal lattice that modifies the jump frequency. Thus, a trapping site is a preferred microstructural site [44] for hydrogen where the potential is lower than in an interstitial site.

The different types of possible hydrogen trapping sites in a metal can be categorized as follows:

- internal or superficial trapping location;
- electron (electrical field), chemical (chemical potential gradient) or elastic (stress field) interaction depending on its physical origin;

point (interstitial, substitutive, gap, etc.), linear (dislocation), plane (interface between phases or grain boundaries) or volume (micro-porosity, crack) to qualify the trap according to its size and its geometry. Figure 1 - 4 illustrates these different types of traps;

- "reversible" or "irreversible" trapping according to the value of the hydrogen-trap interaction energy.

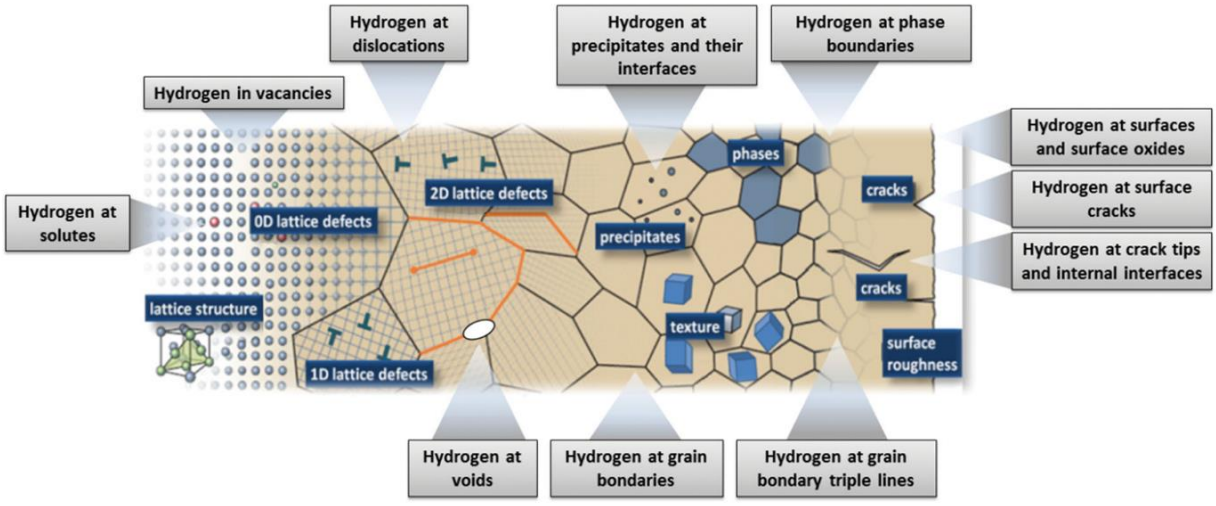

Figure 1 - 4 Schematic illustration of types of hydrogen trapping site [45].

The concepts of reversible and irreversible traps allow us to evaluate the de-trapping at a given temperature. The probability of deposition of hydrogen atoms depends on the potential well. A trap would be irreversible at a given temperature if it has a near-zero probability of allowing hydrogen to get out. The classification between reversible and irreversible traps strongly depends on the temperature, as well as the time which the hydrogen atoms take to desorb. The higher the temperature, the more traps become reversible. Similarly, for a sufficiently long time, the desorption probability becomes close to 1, and all types of traps can be considered as reversible.

Vucko [46] has studied the hydrogen trapping in fatigued high-strength steel by a combination of mechanical testing, electrochemical permeation and Thermal Desorption Spectrometry (TDS). He has identified that the dislocation cell walls developed due to cyclic deformation likely act as the main trapping site during fatigue.

Sofronis and McMeeking [39] have proposed a relationship between the density of hydrogen traps per unit volume N_T and the equivalent plastic strain ε_p, obtained from the experimental data in iron by Kumnick and Johnson [47], as expressed by:

$$\log_{10} N_T = 23.26 - 2.33 * \exp(-5.5\varepsilon_p) \quad 1 - 9$$

This equation is associated with the hydrogen trapping in iron with the nucleation of dislocations during plastic deformation. According to this relationship, the increase in equivalent plastic strain ε_p results in an increase in the number of hydrogen traps due to the presence of dislocations. This equation makes it possible to locally calculate the density of traps N_T at the equivalent plastic strain.

Metsue et al. [48, 49] have determined the hydrogen trapping / detrapping kinetics in a vacancy in Ni by means of ab initio calculations. Their calculations have clarified that the hydrogen trapping at the vacancy core is significant at low temperature. The change in the migration energies by the temperature is mainly contributed by the thermal expansion and the vibration of the lattice. The effect of electronic excitations on the migration energies is minor.

1.4.3 Equilibrium

The local equilibrium between the amount of the diffusible hydrogen and the reversibly trapped hydrogen has been studied by Oriani [50] in 1970. According to his work, the equilibrium is governed by an equilibrium constant K_T which depends on trapping energy E_a and the temperature T:

$$K_T = \exp\left(\frac{-E_a}{RT}\right) \quad 1 - 10$$

The trapping energy E_a depends on the type of trap. This relationship is able to express the gradient of concentration of the reversibly trapped hydrogen C_T as a function of a concentration of lattice hydrogen C_L:

$$\partial C_T = \frac{N_T}{N_L}(1 - \theta_T)^2 K_T \partial C_L \quad 1 - 11$$

where N_T is the density of trapped hydrogen atoms [m^{-3}], N_L the density of lattice hydrogen atoms [m^{-3}] and θ_T is the coverage rate of the traps. These equations indicate that a change in the interstitial hydrogen concentration modifies the reversibly trapped hydrogen concentration. Conversely, the diffusion of hydrogen into the atomic matrix of the metal is directly affected by the presence of traps in the material. It should be noted that this theory considers that hydrogen

trapping is reversible. The occupancy rate of a trap increases with the trapping energy and decreases as the temperature increases.

1.5 Overview of hydrogen embrittlement

The influence of hydrogen on the mechanical properties of metals has been known for more than 140 years. The detrimental effect of hydrogen on metals, and particularly on iron and steel, has been firstly demonstrated by Johnson [5] in 1874. He found out a drop in the ductility of pure iron after cathodic loading. Since then, many types of research have been dedicated to elucidating the effect of hydrogen on the mechanical properties of materials, particularly metals.

For example, Moro [51] conducted tensile tests in Armco iron, X80 steel and a pearlite steel under high pressure gaseous hydrogen atmosphere at 300 bar. Her result shown in Figure 1 - 5 indicates that ductility is clearly reduced by the tests under hydrogen compared to the ones under 300 bar of nitrogen.

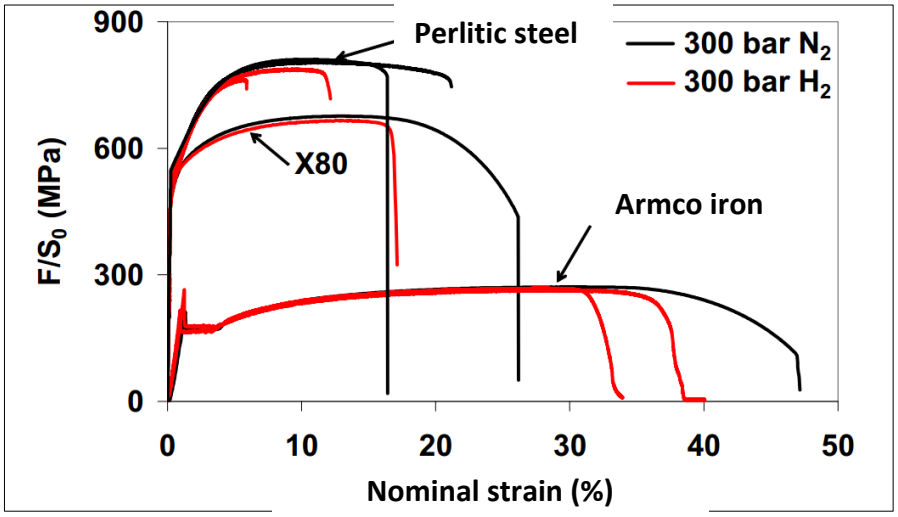

Figure 1 - 5 Reduction of ductility in a tensile test carried out at 300 bar of hydrogen compared to the test carried out under nitrogen, for three different metals [51].

The ductility reduction of steels has also been demonstrated by the works of Hardie et al. [52], Trasatti et al. [53] and Cialone et al. [54] in ferritic steels used for a pipeline. Their experimental works revealed that the extent of HE depends on the following three factors:

- The grade of steel, namely its yield strength. For higher yield strength, the HE is more intense. This result is highlighted by Hardie et al. [52].
- Hydrogen charging mode. Cathodic hydrogen charging induces a greater embrittlement than the case of hydrogen atmosphere. This result can be explained by the amount of hydrogen in the material and its concentration profile are closely related to the loading mode.
- The chemical composition of the steel. In the study of eight cathodic-charged Cr-Ni austenitic steels (H_2SO_4 + $NaAsO_2$, 48 h, 20 °C, 25 mA/cm²), Gavriljuk and al. [55] show that the observed ductility drop differs among these eight materials.

The series of study in hydrogen-charged pure iron by Matsui et al. [56–58] revealed that hydrogen-induced softening or hardening is controlled by the purity of the material and the conditions of loading and testing. Their works highlight the importance of the purity of material, the temperature, the strain rate, and the hydrogen content. Matsui et al. thus evidenced that when the dislocations no longer trap hydrogen atoms in the form of Cottrell atmosphere (due to high strain rate, low temperature, etc.), the material tends to be hardened. The explanation is that the hydrogen atoms may pin the dislocations. As their mobility is reduced, the material is hardened. However, for many authors [52, 59], hydrogen does not induce any modification of the yield strength in ferritic steels.

The study by Trasatti et al. [53] showed that hydrogen has little effect on the tensile strength of ferritic steels, except when the material is subjected to a high triaxial stress which locally increases the interstitial hydrogen content. The influence of hydrogen on the tensile strength of austenitic steels is more complex. Ulmer et al. [60] demonstrated that 304 and 310S steels cathodically-charged exhibit difference in their embrittlement. At first, tensile strength increases with the hydrogen content. Then, while the tensile strength becomes steady for 304 steel, it drops sharply for 310S steel when the hydrogen content exceeds a threshold value. Therefore, the influence of hydrogen on the tensile strength depends on the microstructure of the steel, its chemical composition, and its hydrogen content. In most of the steels, hydrogen decreases the tensile strength. However, for austenitic steels with a low hydrogen content, the effect is opposite.

1.6 Influence of hydrogen on crack propagation

In the presence of a hydrogenating environment (gaseous or liquid), the interaction between hydrogen and material can lead to a drastic degradation of fatigue lifetime [61]. This phenomenon is generally interpreted as a result of HE, and more specifically, a crack growth enhancement due to hydrogen.

In this section, the bibliographic review on the influence of hydrogen on the fatigue crack propagation will be presented aiming to give elements to see a current situation of study about the Fatigue Crack Growth (FCG) influenced by hydrogen. Particularly, experimental evidence of an influence of hydrogen on Fatigue Crack Growth Rate (FCGR) and fractography will be reviewed.

1.6.1 Influence of hydrogen on fatigue crack growth rate

An influence of hydrogen on the fatigue crack growth of metals have been investigated by many studies [3, 13, 14, 25, 30, 62–66]. For example, Bilotta et al. [14, 25, 62, 63] have conducted a fatigue crack growth test in a precipitation-hardened martensitic stainless steel 15-5PH under gaseous hydrogen atmosphere aiming to understand the characteristics of fatigue cracking in the presence of hydrogen. They examined the dependency of FCG in hydrogen on hydrogen gas pressure and loading frequency by changing these parameters. Their results are presented in Figure 1 - 6 showing the influences of hydrogen gas pressure (a) and loading frequency (b). These

diagrams present the relationship between FCGR d*a*/d*N* [m/cycle] and crack tip stress intensity factor range Δ*K* [MPa×m$^{1/2}$] As shown in Figure 1 - 6a, the FCGRs of the tests under gaseous hydrogen are higher than the ones in air and nitrogen. This result clearly evidences that hydrogen atmosphere increases the FCGR, in other words, degrades the fatigue life of the material. Also, in the comparison of the FCGRs by hydrogen gas pressure, the FCGR in hydrogen is higher by the order of 40, 9, and 0.09 MPa. Thus, the FCGR enhancement by hydrogen is higher at a higher hydrogen gas pressure (i.e. hydrogen amount ahead of the crack tip). Besides, the FCGR is not enhanced by hydrogen in low Δ*K* range (< 5 MPa×m$^{1/2}$), and it starts highly increasing in higher Δ*K* range. For the dependency on loading frequency, by comparing the FCGRs in hydrogen (9 MPa) between the loading frequencies of 0.2 and 20 Hz in Figure 1 - 6b, the FCGR at 0.2 Hz is higher than that at 20 Hz. This result indicates that a lower loading frequency has an effect increasing the FCGR in hydrogen.

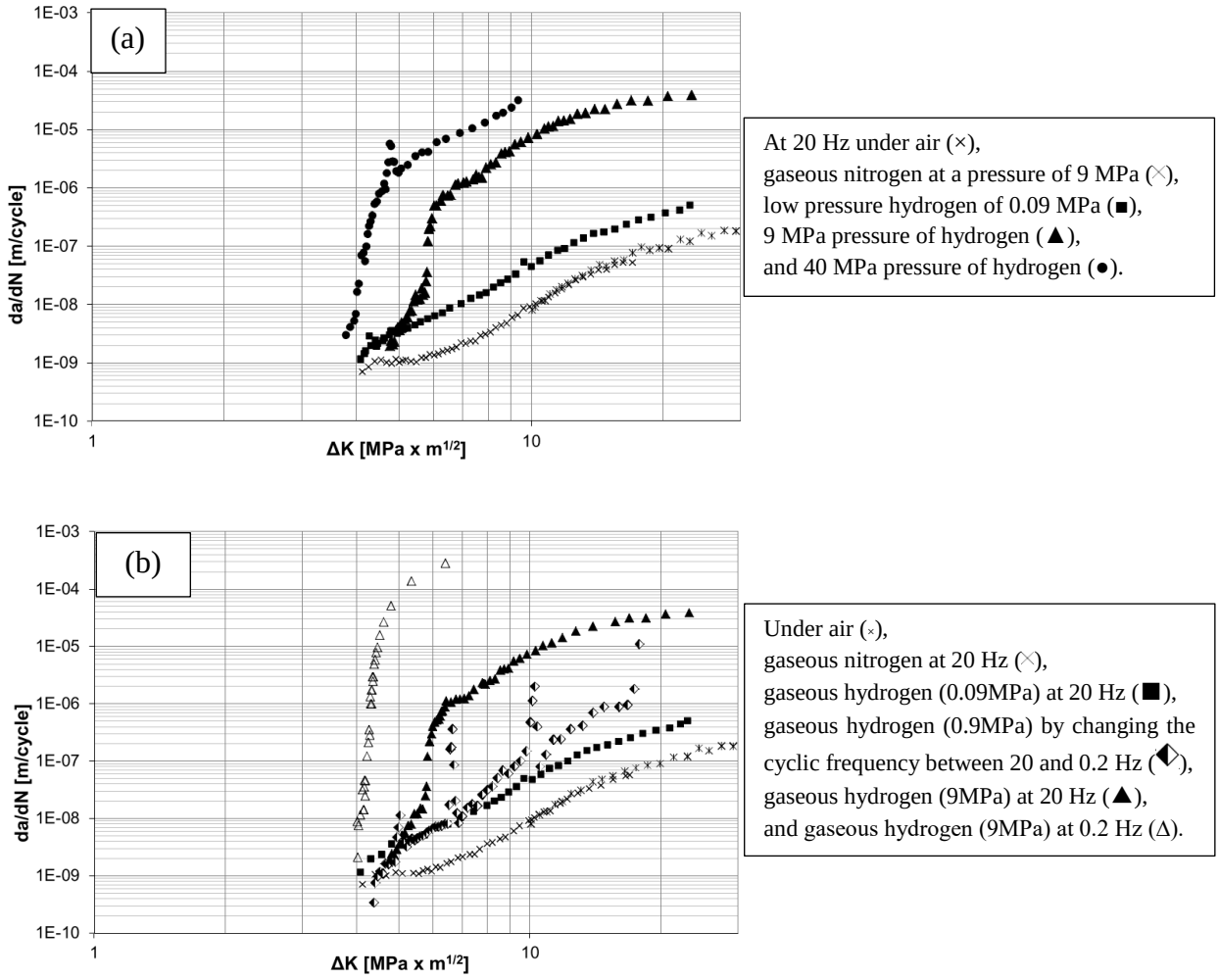

*Figure 1 - 6 FCGR curves in 15-5PH steel at various hydrogen gas pressures of 0.09, 9 and 40 MPa (a) and at various loading frequencies of 0.2 and 20 Hz (b) obtained by Bilotta et al. [*14, 25, 62, 63*]*.

HYDROGENIUS laboratory at Kyushu University has dedicated a large amount of effort on a study of FCG in the presence of hydrogen in many kinds of steels, such as austenitic stainless steels [17, 66–69], ferritic stainless steels [61], martensitic stainless steel [70], Cr-Mo steel [3, 71],

Ni-Cr-Mo steel [72], low and medium carbon steels [18, 19, 73] and so on. From their investigation, it has been revealed that the characteristics and the mechanisms of FCG enhancement in hydrogen are different depending on microstructure and composition of a material.

1.6.2 Influence of hydrogen on fracture mode

Since the FCGR can be greatly enhanced by hydrogen as described in the previous sub-section, in order to investigate the mechanism of hydrogen-induced FCG enhancement, the fracture surface and the microstructure produced by the FCG in hydrogen have been investigated by many studies using SEM. The literature reports that the fracture mode changes in the presence of hydrogen. Particularly, a brittle intergranular fracture surface [74–80] and a Quasi-Cleavage (QC) fracture surface [33, 70, 81–83] are recognized as the characteristic fracture surfaces of fatigue and tensile fractures in the presence of hydrogen.

For example, Bilotta et al. [14, 25, 62, 63] observed the fracture surface of the specimen in 15-5 PH steel tested under gaseous nitrogen and hydrogen (whose result of FCGR is shown in Figure 1 - 6). Figure 1 - 7 shows the SEM images of the corresponding fracture surfaces. The fracture surface in nitrogen is a typical ductile transgranular fracture surface as shown in Figure 1 - 7a. On the other hand, in hydrogen (9 MPa, 0.2 Hz), a brittle intergranular fracture surface was observed at low ΔK (= 6 MPa×m$^{1/2}$, Figure 1 - 7b) which corresponds to the not-enhanced FCGR in Figure 1 - 6. At high ΔK (= 10 MPa×m$^{1/2}$) corresponding to the highly enhanced FCGR in Figure 1 - 6, the fracture surface was a brittle transgranular fracture surface with cleavage-like facets and secondary cracks as shown in Figure 1 - 7c. These observations clearly indicate that the presence of hydrogen apparently changes the fracture mode depending on the level of ΔK. Moreover, the change in the fracture mode is associated with the FCGR enhancement.

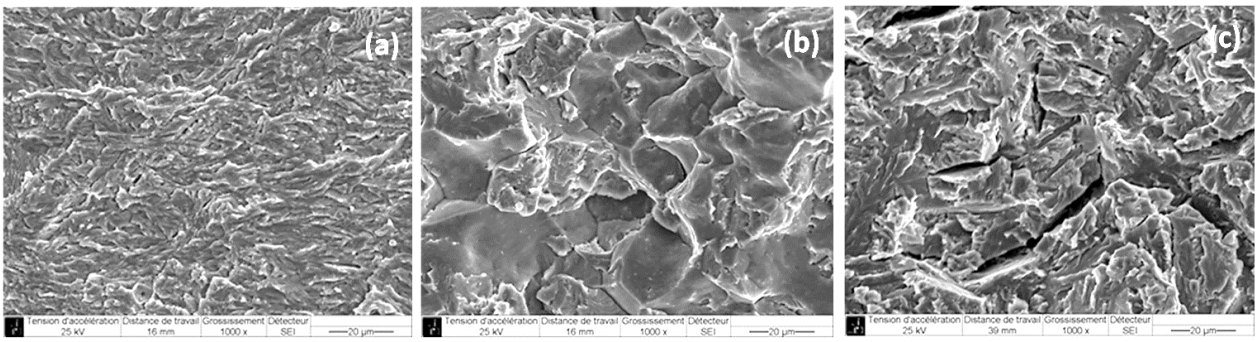

Figure 1 - 7 SEM images of fracture surfaces of the FCG tests in 15-5PH: ductile transgranular fracture surface at ΔK = 10 MPa×m$^{1/2}$under nitrogen(a), brittle intergranular fracture surface at low ΔK (= 6 MPa×m$^{1/2}$) under hydrogen (9 MPa, 0.2 Hz) (b), brittle transgranular fracture surface with cleavage-like facets and secondary cracks at high ΔK (= 10 MPa×m$^{1/2}$) under hydrogen (9 MPa, 0.2 Hz) (c) [62].

Murakami et al. [3, 17, 66, 84] have investigated crack tip plasticity during the FCG in hydrogen in austenitic stainless steels by observing the surface near the crack path, as shown in Figure 1 - 8 for example. In hydrogen-uncharged specimen (Figure 1 - 8a), many slip markings indicating plastic deformation were observed on the surface around the fatigue crack path. On the other hand,

much fewer slip markings are visible near the crack path of the hydrogen-charged specimen (Figure 1 - 8b) compared to the hydrogen-uncharged one. They have revealed that hydrogen influences the crack tip plasticity during the FCG. Besides, a correlation between the FCGR and the reduction of plastic deformation in the vicinity of the crack tip by hydrogen has been confirmed. They argued that this hydrogen effect reducing the crack tip plasticity is the main cause of hydrogen-induced FCG enhancement.

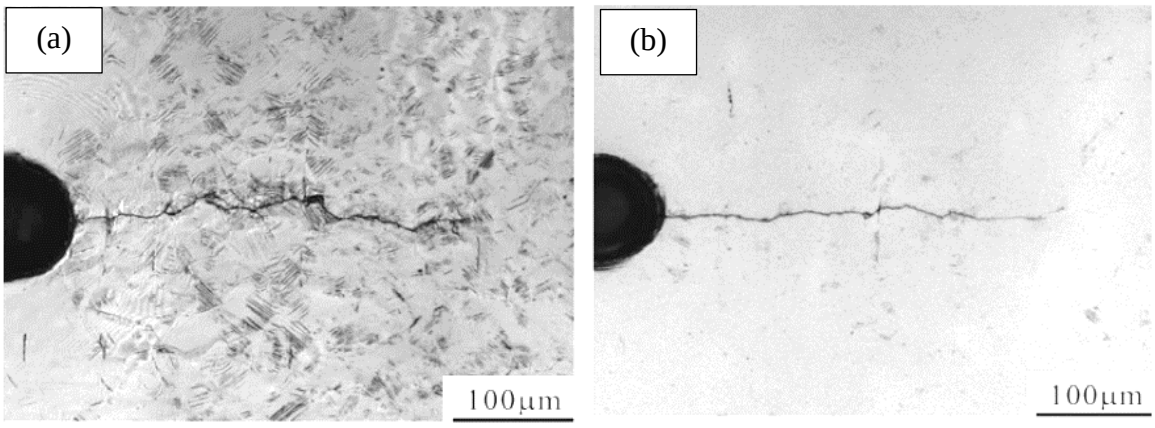

*Figure 1 - 8 Optical images showing difference in crack growth behavior between hydrogen-charged specimens and uncharged specimens of type 304: (a) uncharged (f = 1.2 Hz, crack length 2a = 782 μm, 2.2 wppm) and (b) H-charged (f = 1.2 Hz, crack length 2a = 801 μm, 3.7 wppm) [*17*].*

It is known that the flux of hydrogen atoms entering the material is increased at the crack tip due to the stress concentration ahead of the crack tip [85, 86]. Besides, cyclic loading applied to fatigue crack promotes the transportation of hydrogen dragged by mobile dislocations in the vicinity of the crack tip [87–89]. Saintier et al. [90] performed Secondary Ion Mass Spectrometry (SIMS) analyses to investigate the hydrogen-plasticity interaction at the crack tip for 304 type austenitic stainless steel subjected to cyclic loading. They showed that the apparent crack tip diffusion is four orders of magnitude higher than the undeformed material. They claim that this high diffusion results from plastic activity at the crack tip, because of the dislocation mobility during the cyclic loading. Their SIMS analyses also evidenced that the distance at which hydrogen concentration becomes the highest from the crack tip is 180 times greater than that calculated by interstitial diffusion. Therefore, the hydrogen diffuses rapidly in the vicinity of the crack tip. This may be related to a cause of the FCG enhancement by hydrogen.

1.7 Mechanism of hydrogen embrittlement

Since the phenomenon of HE has been observed, many authors have proposed mechanisms for explaining the influence of hydrogen on the mechanical properties of the metallic materials. Although many theories have been proposed in the literature, the following four theories are today considered as the most widely accepted ones: Hydrogen-Enhanced DEcohesion (HEDE) [50, 91], Hydrogen-Enhanced Localized Plasticity (HELP) [8], Adsorption-Induced Dislocation Emission

(AIDE) [9] and Hydrogen-Enhanced Strain-Induced Void (HESIV) [10]. These theories are presented in the following sub-sections.

1.7.1 Hydrogen-Enhanced DEcohesion (HEDE)

The HEDE mechanism was proposed by Troiano [91] in 1960 and developed by Oriani [50]. This model assumes that the presence of interstitial or segregated hydrogen atoms at grain boundary leads to an expansion of the atomic network, thereby reducing the cohesion energy of the atoms and the energy barrier of surface creation. This mechanism is very close to the concept of surface energy reduction [92], which states that the presence of impurities (such as hydrogen) lowers the surface energy. This effect increases the driving force of surface creation, resulting in crack creation. Therefore, the hydrogen atoms accumulated in trapping sites (such as interfaces or grain boundaries) reduce the cohesive energy.

The diffusion of the hydrogen is not only guided by the hydrogen concentration gradient, but also by the hydrostatic stress gradient. On the other hand, high strength steels are generally associated with a limited plastic zone at the crack tip, inducing a high hydrostatic stress gradient. Thus, it is easy to reach the critical hydrogen concentration in the vicinity of the crack tip, causing the crack propagation by atomic decohesion.

This model requires very high local concentrations of hydrogen. This may be achieved at, for example, the crack tip, defects and interfaces. Figure 1 - 9 [93] illustrates the possible zones where the HEDE may occur: (a) at the crack tip (Figure 1 - 9a) where high hydrostatic stress and plastic deformation cause a high hydrogen concentration; (b) few tens of nanometers away from the crack tip (Figure 1 - 9b) where the barrier effect of the dislocations leads to a maximum hydrostatic stress; (c) at interfaces between grains or with precipitates up to several micrometers away from the crack tip (Figure 1 - 9c).

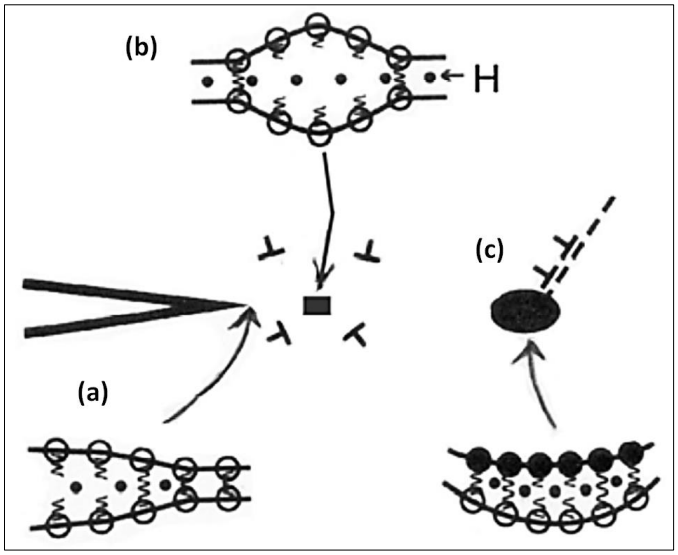

Figure 1 - 9 Schematic illustration of possible zones where the HEDE may occur [93]: (a) at the crack tip; (b) few tens nanometers away from the crack tip; (c) at interfaces between grains or with precipitates.

The HEDE mechanism may explain the brittle transgranular cleavage-like fracture in hydrogen. In this case, the cleavage fracture driven by the HEDE likely occurs along a crystallographic weak plane (e.g. {100} plane in bcc).

In addition, the HEDE mechanism may also explain the intergranular fracture in hydrogen. As hydrogen tends to highly concentrate at grain boundaries as a trapping site, the atomic decohesion may occur along the grain boundary in the framework of the HEDE. However, the observation of the intergranular facets is not sufficient to validate this mechanism. Robertson et al. [75, 77] observed the presence of plastic markings on intergranular facets, implying that a certain degree of plastic activity might happen inside the grains even though it seems macroscopically to undergo brittle fracture. Because of this, Lynch [93] stated that the SEM observation of the fracture surfaces is not sufficient to evidence what happens inside the grains and at the boundary. It is difficult to obtain experimental evidence that supports the HEDE mechanism, given the scales involved.

1.7.2 Hydrogen-Enhanced Localized Plasticity (HELP)

The HELP mechanism was firstly proposed by Beachem [94] in 1972 on the basis of fracture surface observations. This mechanism assumes that hydrogen in the material causes a strong localization of plasticity, which induces a degradation of the cracking resistance of the material. This mechanism is supported by in-situ TEM during a tensile test in a hydrogen environment. For example, Robertson [95] applied TEM on a thin tensile specimen in 310S austenitic steel. He revealed that the distance between two dislocations decreases and the mobility of dislocations is increased with the presence of hydrogen.

Ferreira et al. [96] showed that, in a highly pure aluminum, the cross slip is inhibited by the presence of hydrogen via the stabilization of the wedge components of dislocations and the reduction of the stacking fault energy. They concluded that hydrogen promotes planar slips inducing dislocation stacks.

Birnbaum and Sofronis [8, 97] claimed that, because of a high hydrogen concentration at the crack tip, the dislocation mobility is increased in a very localized area ahead of the crack tip which is smaller than the plastic zone in the absence of hydrogen. This causes a brittle fracture. They assumed that crack propagation occurs through a process of coalescence of microcavities in the zone of high hydrostatic stress and hydrogen concentration, much more localized than in an inert environment as shown in Figure 1 - 10 [93].

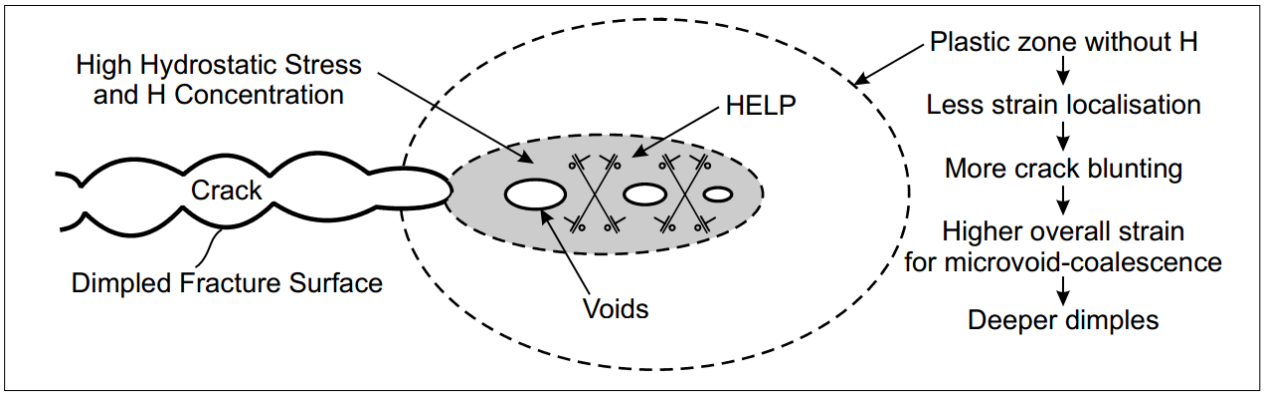

Figure 1 - 10 Schematic illustration of the HELP mechanism [93]: the presence of hydrogen promotes the dislocation mobility and a localization of the plastic deformation at the crack tip; the crack propagation occurs by a process of coalescence of the microcavities in this zone of hydrostatic stress and high hydrogen concentration.

The fracture is macroscopically brittle but also microscopically ductile at the level of micro-cavities at the crack tip. The crack path may be transgranular or intergranular, depending on the location of the dislocation activity and the nucleation and coalescence of the cavities. This may depend on a higher local concentration of hydrogen (inside grains or on grain boundaries).

1.7.3 Adsorption-Induced Dislocation Emission (AIDE)

AIDE mechanism was proposed by Lynch [4, 93, 98–101] following the observation of strong similarities between the fracture surfaces of materials in hydrogen and liquid metals. The AIDE mechanism is based on the effect of hydrogen adsorbed at the surface or located in the interstitial sites of the first few atomic layers from the surface. It assumes that these two groups of hydrogen locally reduce the cohesion energy of the matrix and promote the dislocation emission from the surface.

In the classical ductile fracture of steel, dislocations are essentially emitted from the volume of the material by Franck-Read sources. Only a small proportion of them interact with the crack front to cause a fracture or the void nucleation. The crack propagation therefore requires a strong plastic

deformation. The adsorption of hydrogen at the surface and subsurface of the material disrupts the organization of the first atomic layers of the surface and decreases its cohesion energy. Hydrogen then promotes the dislocation emission from the surface. Besides, the nucleation of microvoids ahead of the crack is facilitated and it assists the crack propagation as illustrated in Figure 1 - 11. The microvoid coalescence produces small dimples on the fracture surface.

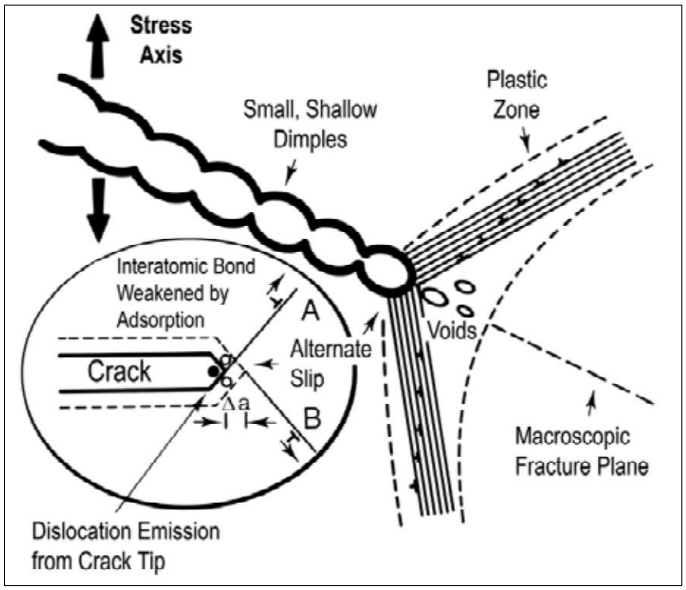

*Figure 1 - 11 Schematic illustration of the AIDE Mechanism [*93*]: embrittlement is composed of two stages: local reduction of the cohesion energy of the material, which promotes the nucleation and the emission of dislocations from the crack tip; and nucleation and growth of microcavities ahead of the tip of the crack.*

The AIDE mechanism therefore involves the fundamental principles of the HEDE and the HELP models, but also assumes that the atomic decohesion and plasticity localization occur at the surface or the sub-surface, not in the volume of the material. In the framework of the AIDE mechanism, the crack path can be transgranular or intergranular, depending on the areas where dislocation nucleates and microcavities are formed.

This model is supported by atomic calculations of crack propagation in nickel [102] which indicated that hydrogen adsorbed at the crack tip promotes the dislocation emission and that the slip planes are favorably oriented to the cracking plane. Besides, the experimental studies by Barnoush et al. [103–105] using a nano-indentation technique on hydrogen-charged materials have also evidenced the hydrogen effect enhancing the dislocation emission.

1.7.4 Hydrogen-Enhanced Strain-Induced Void (HESIV)

HESIV mechanism was proposed by Nagumo [10] and has been developed by Takai et al. [106, 107] using Thermal Desorption Analysis (TDA) and hydrogen tensile tests with thermal aging.

This model is based on the assumption that hydrogen in the material assists the creation and stabilization of defects during plastic deformation. The embrittlement of the metals is caused by

an overconcentration of vacancies in the material, and not directly due to the presence of hydrogen. Except for the process of nucleation and growth of vacancies, the interpretation of the crack growth process driven by void coalescence is the same as the HELP and AIDE mechanisms.

This model is based on experimental evidences. Takai et al. [106, 107] conducted tensile testing in Inconel 625 and pure iron interposing unloading and reloading with/without hydrogen charging. Aging at 30 °C or annealing at 200 °C was also conducted during the unloaded stage in order to diffuse out hydrogen or to anneal out strain-induced defects. As a result, the fracture strain decreased in the initially hydrogen-charged specimens even though hydrogen was absent at the late stage of straining. Annealing at the unloaded stage greatly recovered the decrease in fracture strain. Enhancement of strain-induced defects by hydrogen and their involvement in degradation were revealed by TDA of hydrogen. The results provide direct evidence of the primary role of vacancies rather than hydrogen itself in hydrogen degradation.

1.7.5 Mechanism of FCG enhancement by hydrogen

Based on the above mechanisms of HE, several FCG models have been proposed in literature explaining the influence of hydrogen on FCG as described in Section 1.6. This sub-section presents three representative models of hydrogen-affected FCG as schematically summarized by Figure 1 - 12 [108]:

Hydrogen Enhanced Successive Fatigue Crack Growth (HESFCG) model [16, 17] based on the HELP mechanism (Figure 1 - 12b);

hydrogen-induced cyclic cleavage model [15] based on the HEDE mechanism (Figure 1 - 12c); and

hydrogen-induced void-coalescence model [18] based on the HESIV mechanism (Figure 1 - 12d).

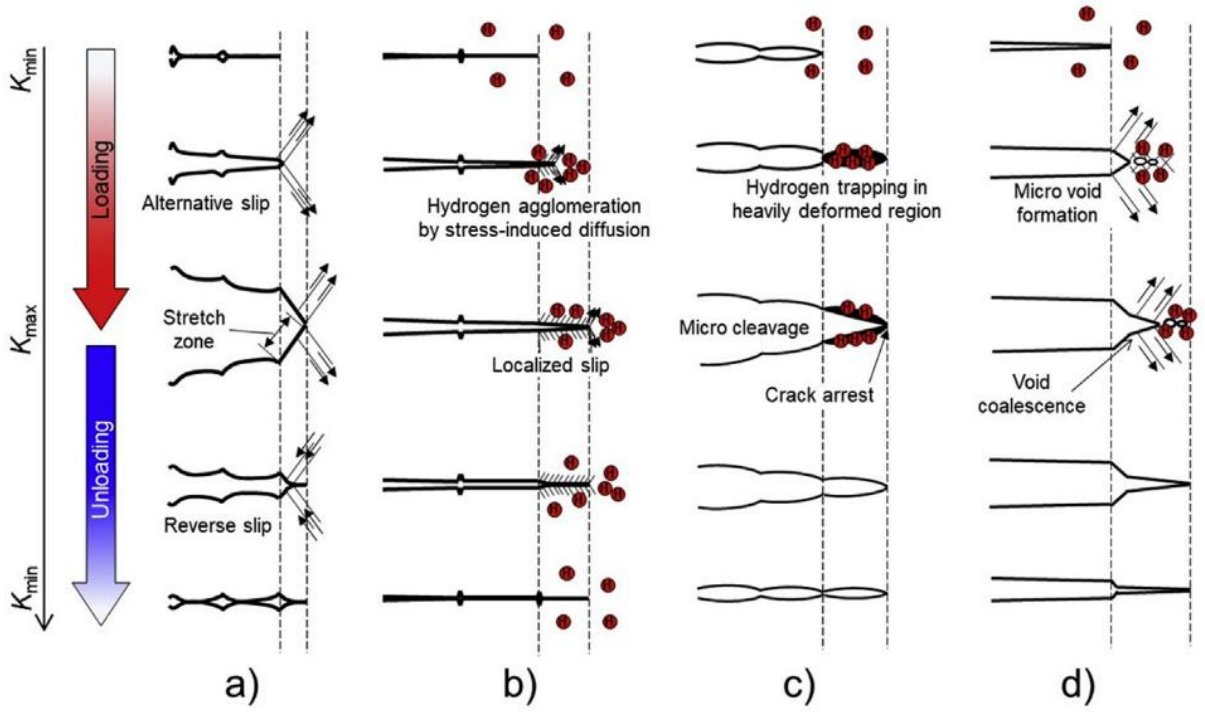

*Figure 1 - 12 Schematic illustration of mechanism models proposed in past literature, drawn by Birenis et al. [*108*]. (a) Ductile fatigue striation formation model in air. (b) HESFCG model proposed by Matsuoka et al. [*16, 17*]. (c) Hydrogen-induced cyclic cleavage model proposed by Marrow et al. [*15*]. (d) Hydrogen-induced void coalescence model proposed by Nishikawa et al. [*18*].*

The HESFCG model (Figure 1 - 12b) was proposed by Matsuoka et al. [16, 17]. They noticed that the localization of plastic deformation near the crack tip is associated with the FCGR enhancement in hydrogen-charged austenitic stainless steel and low carbon steel, by observing the suppression of slip deformation near the crack path and the presence of brittle-like striation on the fracture surface. Based on their experimental results, they proposed a scenario of FCG with the presence of hydrogen as: during loading stage of cyclic loading, hydrogen diffused from the crack tip is concentrated in the high hydrostatic stress field ahead of the crack tip. Highly accumulated solute hydrogen localizes and enhances slip deformation within the limited zone ahead of the crack tip due to the HELP mechanism which is much smaller than the case in air (Figure 1 - 12a). This results in the inhibition of crack tip blunting. Consequently, the sharp crack tip continuously advances by intense slip deformation during the loading part of cyclic loading.

Secondly, the hydrogen-induced cyclic cleavage model was proposed by Marrow et al. [15] in 1992. They concluded that when the applied loading starts increasing, dislocations are emitted from the crack tip and the crack tip starts blunting. The high hydrostatic stress field with high dislocation density is formed in front of the crack tip. Subsequently, the diffused hydrogen atoms are intensely trapped within this field. The highly accumulated hydrogen atoms reduce the lattice cohesive energy, and consequences a cleavage fracture by the HEDE mechanism. This model states that intense plastic strain field ahead of the crack tip is required to achieve the high hydrogen

concentration even though the cracking mechanism is atomic decohesion without accompanying the plastic deformation of the crack tip.

Thirdly, the hydrogen-induced void-coalescence model (Figure 1 - 12d) was proposed by Nishikawa et al. [18]. This model assumes that, during the loading is applied, the interaction between hydrogen and the plastically deformed zone ahead of the crack tip generates a high density of microvoids by the HESIV mechanism. Consequently, ductile tearing occurs between the microvoids, leading to microvoid coalescence and crack growth.

It is unlikely that only one of these models is correct and the others are wrong, because it is known that the dominant mechanism of hydrogen-affected FCG may change depending on the experimental conditions and the type of material, such as hydrogen content, hydrogen diffusion coefficient (for BCC or FCC), load frequency, localization of fatigue slip bands, strain-induced martensite and so on [3]. Therefore, it is important to identify the type of HE mechanism “case by case”.

1.8 Motivation of study

As presented in this chapter, several models have been proposed about the mechanism of the influence of hydrogen on fatigue crack propagation. However, multiple different models are argued and common consensus among the researchers has not been obtained yet. This reflects that the history of research on this theme is not long yet, and the experimental verification and analysis of the phenomenon are not sufficient.

From this fact, as mentioned in Introduction, for the purpose of investigating the interaction of hydrogen and FCG phenomena in more detail, Pprime Institute [28–30] has carried out the FCG tests under hydrogen environment using Armco iron composed of a basic ferrite structure which allows us to analyze a pure interaction between hydrogen and ferrite structure. However, the mechanism of FCG enhancement by hydrogen has not been clearly revealed yet due to the lack of verifications about the influence of hydrogen on the microscopic crack tip plasticity (i.e. dislocation activity) and the influence of test conditions (hydrogen gas pressure, loading frequency, etc.).

Although the analyses of the interaction between hydrogen and dislocation during cyclic deformation by Robertson et al. [12, 22, 23] have made many findings, they have not been sufficiently linked to the mechanism of FCG enhancement yet. In addition, although the influence of external factors (such as hydrogen gas pressure and test frequency) on hydrogen-affected FCG has been actively investigated by HYDROGENIUS laboratory [3, 17, 61, 66–72], an explicit mechanism of this influence has not been clarified yet.

Therefore, this study is aimed to intensively investigate these two issues and finally to clarify the mechanism of FCG in hydrogen. For this purpose, firstly, a tensile test in a hydrogen environment will be performed in Armco iron in order to investigate the influence of hydrogen on plastic deformation of the material. At this time, strain rate and hydrogen exposure time will be changed

in order to investigate the influence of strain rate and hydrogen concentration distribution in the material. Next, aiming to examine the influence of hydrogen on FCG, FCG tests in hydrogen environment will be carried out. In these tests, hydrogen gas pressure and loading frequency are changed over a wide range of 3.5, 35 MPa and from 0.02 Hz to 20 Hz, respectively. Subsequently, plastic deformation remaining around the crack path after the test will be analyzed, and the change in the crack tip plasticity due to hydrogen will be investigated. In this analysis, optical observation around the crack path, measurement of out-of-plane displacement, and direct observation of the dislocation structure immediately beneath the fracture surface by means of TEM will be performed. Based on the obtained findings, the mechanism of FCG in hydrogen will be discussed. In addition, the mechanisms of its dependency on hydrogen gas pressure and loading frequency will also be considered.

The next chapter presents the characteristics of the material and the results of the tensile test in hydrogen environment.

Chapter 2

Analysis of influence of hydrogen on plastic deformation and tensile fracture

Résumé

Chapitre 2: Analyse de l'influence de l'hydrogène sur la déformation plastique et la rupture en traction

R-2.1 Introduction

Le chapitre 2 vise à étudier l'interaction entre l'hydrogène et la plasticité, la déformation en traction et le comportement à la rupture sous hydrogène gazeux sous haute pression (35 MPa). Les essais de traction ont été réalisés sur le banc d'essai HYCOMAT à Poitiers. De plus, l'influence des paramètres d'essai, la vitesse de déformation et la durée d'exposition à l'hydrogène ont été étudiées.

R-2.2 Matériau

Le matériau utilisé dans cette étude est un fer commercialement pur, le fer Armco (AK Steel Corp.). Un traitement thermique de recuit à 1073 K (800 °C) pendant 60 minutes a été appliqué afin de relaxer les contraintes résiduelles et d'homogénéiser la microstructure de ferrite. La taille moyenne des grains après le traitement thermique est d'environ 90 µm. Les propriétés mécaniques déterminées après traitement thermique sont la limite d'élasticité σ_y = 170 MPa, l'allongement maximal A = 25% et la résistance à la traction σ_{TS} = 280 MPa.

R-2.3 Résultat de l'essai de traction sous hydrogène gazeux

À la suite des essais de traction, il a été révélé que la déformation élastique (et par conséquent le module de Young) et la déformation plastique uniforme avant la striction (c'est-à-dire la limite d'élasticité et la résistance à la traction) n'étaient pas influencées par l'hydrogène.

La Figure R - 1 montre le résultat de réduction de la section (« Reduction of Area (*RA*) ») pour chaque condition de test. Comme le montre cette figure, les valeurs de la *RA* (ainsi que de l'allongement à rupture bien qu'elle ne soit pas indiquée ici) sont réduites (jusqu'à 10%) en raison de la présence d'hydrogène.

En outre, l'hydrogène modifie clairement le mode de rupture, passant d'une rupture par coalescence de vides à une rupture de type quasi-clivage (QC) fragile avec de nombreuses fissures superficielles et secondaires. L'allongement à la rupture diminue lorsque la vitesse de déformation diminue de $d\varepsilon/dt = 5\times10^{-5}\ s^{-1}$ à $5\times10^{-6}\ s^{-1}$ sous hydrogène et sous azote. Cette dépendance à la vitesse de déformation est toutefois probablement liée à la nature du matériau, et non à l'influence de l'hydrogène.

L'allongement à la rupture suite à une courte durée d'exposition à l'hydrogène (4 minutes) et à de très longues durées (5340 minutes) est aussi grand que sous air et sous azote. La valeur de *RA* pour une longue durée d'exposition à l'hydrogène (5340 minutes) est supérieure à celle

correspondant à une durée intermédiaire d'exposition (30 minutes), comme le montre Figure R - 1, et une surface de rupture ductile est observée dans la partie centrale de la surface de rupture. Ce résultat suggère que la concentration en hydrogène saturé n'induit pas un effet intense de fragilisation par l'hydrogène malgré la quantité élevée d'hydrogène dans l'échantillon.

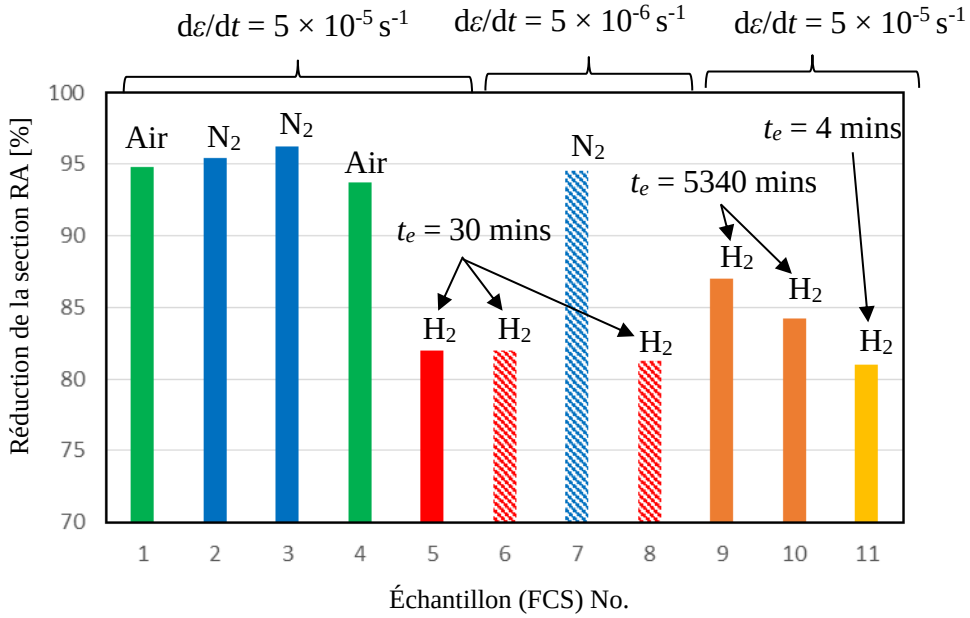

Figure R - 1 Comparaison des réductions de la section RA entre divers environnements, taux de contrainte et durées d'exposition.

Dans cette perspective expérimentale, les deux faits suivants sont particulièrement importants pour considérer l'influence de l'hydrogène sur la propagation des fissures de fatigue:

- l'hydrogène n'influence pas le comportement de déformation uniforme du matériau, alors qu'il influence le processus de fissuration lors de la déformation de striction.
- une concentration en hydrogène saturé n'entraîne pas nécessairement une fragilisation. En revanche, l'importance du gradient d'hydrogène sur la propagation de fissure a été démontrée. Ceci est lié au mécanisme d'apparition de l'effet de l'hydrogène sur la propagation des fissures de fatigue.

----------(Fin du résumé)----------

2.1 Introduction

This chapter firstly presents a selection of material used for this study and a reason of the selection. Also, characteristics of the material determined by several means of analyses are presented.

Since fatigue crack growth phenomenon involves many complex factors such as heterogeneous stress field ahead of crack tip, stress variation by time, complex fracture mechanism etc., it is difficult to consider an interaction between hydrogen and material deformation in a framework of fatigue crack growth phenomenon. Therefore, this study firstly focuses on a simplified subject: an influence of hydrogen on monotonic and uniform deformation of material, namely tensile deformation of material.

For this purpose, a tensile test under gaseous hydrogen environment is an effective method to investigate pure interaction between hydrogen and plasticity of material. Besides, as mentioned in Chapter 1, several experimental studies have dedicated to study the tensile deformation and fracture in the presence of hydrogen. Thus, it is possible to compare a result of this study to other ones in the literatures. Because of the above reasons, a tensile test has been conducted with changing gaseous environment, strain rate, and exposure time as parameters, aiming to investigate an influence of hydrogen on material plasticity and its dependency on the testing parameters.

2.2 Material

2.2.1 Selection of material and general characteristics

First of all, this sub-section presents the material of study, as well as the applied heat treatment and the microstructure analysis. As mentioned in Introduction, in order to investigate an interaction between hydrogen and ferrite microstructure, the selected material should consist of pure ferrite structure for this purpose. For this reason, Armco iron was chosen for the material of study. Armco iron is a commercially pure iron manufactured by AK Steel Corporation. Thanks to its simple bcc microstructure, it allows to analyze the hydrogen diffusivity, hydrogen trapping energy in the matrix and hydrogen effects on a microstructure such as dislocation structure. The chemical composition of the impurities of this material, measured by AK Steel Corp., is presented in *Table 2 - 1*.

Table 2 - 1: Chemical composition of Armco iron impurities, measured by AK Steel.

Chemical composition [mass %]											
C	Mn	P	S	Cu	N	Si	Al	Cr	Mo	Ni	Sn
0.001	0.050	0.003	0.003	0.009	0.0035	0.004	0.005	0.015	0.002	0.14	0.002

The mechanical properties of this material announced by the manufacturer are:

- Yield stress $R_{P0.2}$ = 182 MPa;
- Brinell hardness HB = 71;
- Fracture elongation ε_f = 52%.

2.2.2 Heat treatment

The material was received as a form of a hot-rolled sheet with the thickness of 20 mm and the dimensions of 1000 × 2000 mm. Since the received material plate was not annealed after rolling, the heat treatment has to be performed on the material before taking the samples from the plate. The heat treatment and the following verification of material properties mentioned below were done by Bilotta [27].

The annealing was applied for attenuation or relaxation of the residual stresses that may exist as a result of rolling, and for homogenizing the microstructure (grain size and structure). The procedure of heat treatment was a uniform heating of the structure to an appropriate temperature below the transformation range (A_{c1} = 723 °C for ferrite steels), held at this temperature for a predetermined period of time, followed by a uniform and slow cooling [109]. If the temperature exceeds A_{c1}, the material undergoes recrystallization, which may be controlled by the chosen temperature and the holding time. The condition of heat treatment was chosen as follows to obtain a uniform structure with slight recrystallization:

- 90 minutes at 830 °C (higher than A_{c1} = 723 °C);
- Cooling by 1 °C / min to room temperature.

The microstructures of material before and after the heat treatment were observed on the three planes corresponding to the three main directions, namely: thickness (C), transverse (T) and longitudinal (L), which corresponds to the rolling direction as indicated in Figure 2 - 1. These planes were mechanically polished up to grade 1 μm and then etched for 4 seconds in 4% Nital solution (ethanol solution with 4% volume nitric acid) at room temperature [110].

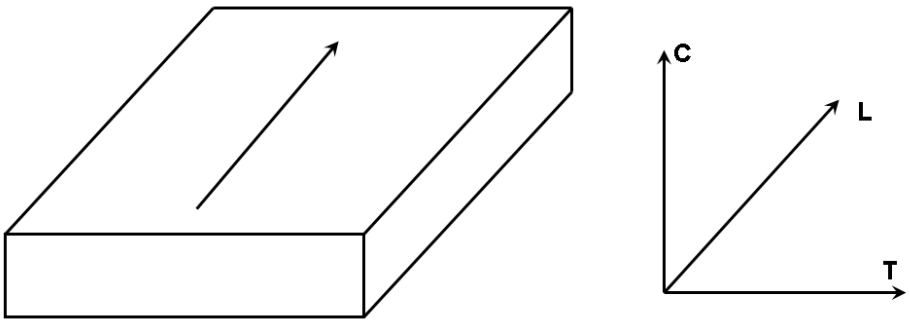

Figure 2 - 1 Schematic diagram of the material plate and indication of the three directions: thickness (C), transverse (T) and longitudinal (L).

Figure 2 - 2 shows microstructures on the different planes after the heat treatment. Optical microscopy observations revealed a more uniform microstructure with a slight increase in grain

size after heat treatment, a sign of the relaxation of initial microstructural anisotropy due to sheet rolling. The heat treatment also provided a homogeneous grain boundary thickness.

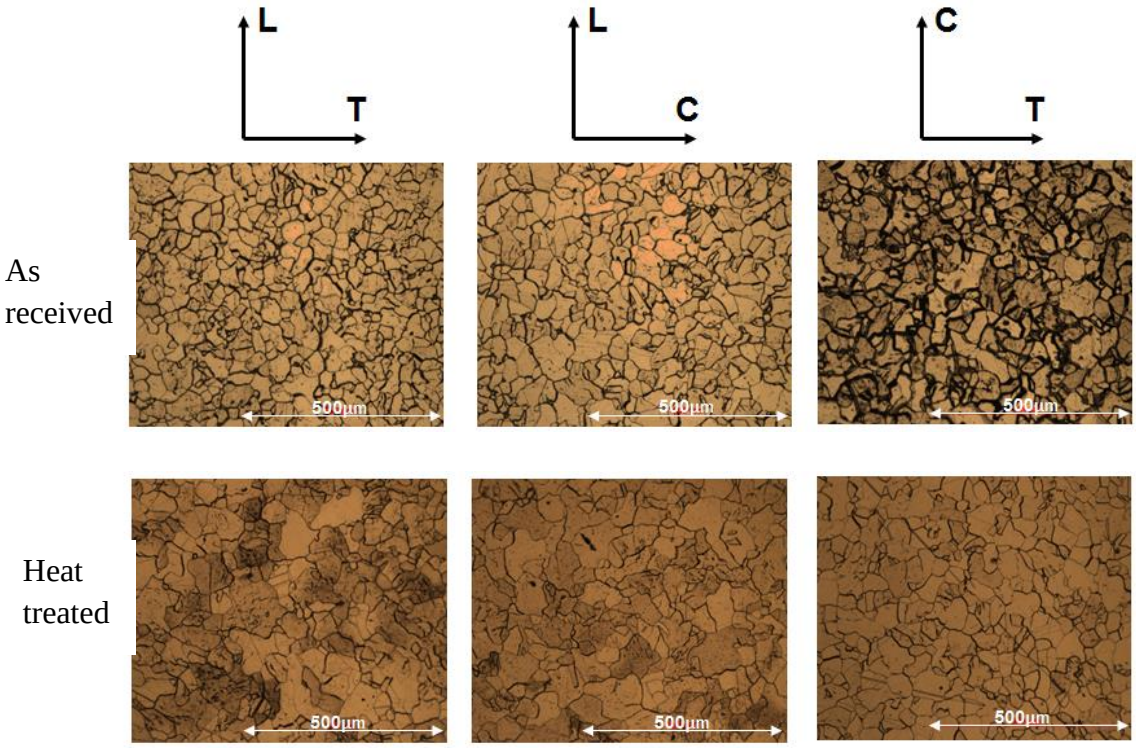

Figure 2 - 2 Micrographs of the microstructure on the three planes of the samples before and after the heat treatment.

Although a layer comprising coarse grains was still observed near the surface of the plate as shown in Figure 2 - 3, their average thickness was greatly reduced from more than 1 mm to about 0.4 mm by the heat treatment.

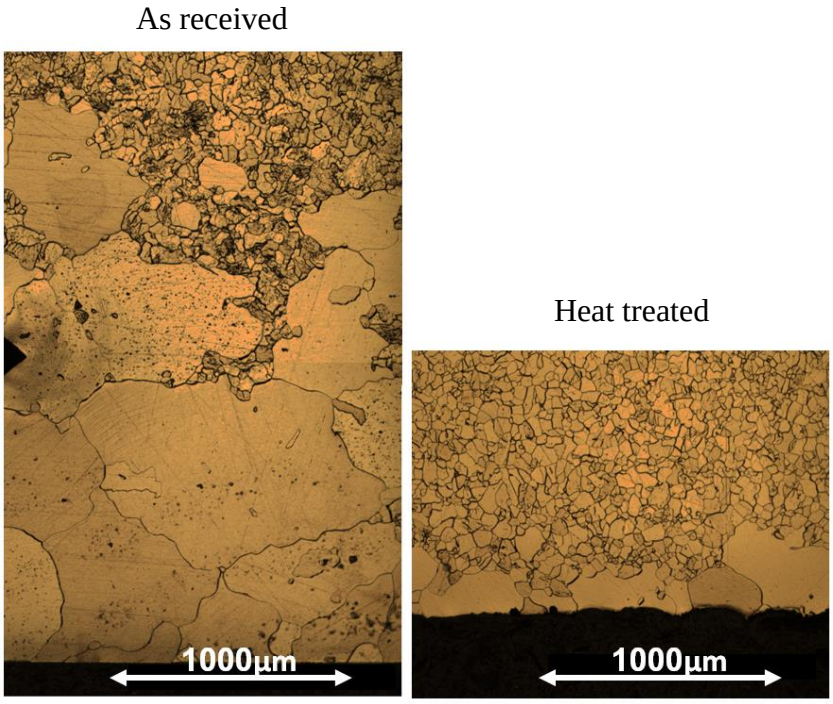

Figure 2 - 3 Reduction of coarse grains near the surface by the heat treatment.

In order to evaluate the homogeneity of the material before and after the heat treatments, the hardness of the material was measured. Three Vickers hardness measurements with a force of 200 N were performed in each plane of the plate. It provides a quantitative evaluation of the homogeneity of the microstructure and thus the quality of the heat treatment.

Table 2 - 2 shows the result of Vickers hardness (HV) measurement in all the three planes and the standard deviation. Larger standard deviations of the hardness in the reference sample (σ_{Ref}) were observed in all the planes compared to the ones with heat treatment (σ_{HT}). In addition, the reference sample shows a large variation of the hardness between the different planes. On the other hand, the hardness of the sample after the heat treatment shows more moderate deviations from the reference state. The obtained value of hardness is similar to the one reported in the literature for Armco iron after annealing [111].

Table 2 - 2 Hardness in the three planes and standard deviation.

Plane	HV_{Ref}	σ_{Ref}	HV_{HT}	σ_{HT}
LT	73.37	1.45	68.97	0.97
LC	70.57	0.75	68.53	0.65
CT	57.90	2.42	67.87	0.65
Average	67.28	7.29	68.46	0.82

The specimens were therefore taken from the plate after the heat treatment. In order to avoid the influence of microstructural heterogeneity near the surface of the plate, the specimens were taken from the center part of the plates. For the cylindrical specimen, the axis of symmetry was chosen in the longitudinal direction. For the Compact Tension (CT) type fracture specimen used in this study, the loading axis was chosen parallel to the longitudinal direction and the direction of crack propagation is hence transverse to the rolling direction.

2.2.3 Microstructure

After the heat treatment, it is necessary to conduct a more in-depth analysis of the microstructure, in particular, its uniformity. For this purpose, the size of grains, their shape and homogeneity were evaluated in the different directions.

The intercept method was used for measurement of the grain size. This method is defined by ASTM E112 [112] for determining grain size from an image of the microstructure. Figure 2 - 4 shows an example of optical images at 100 times magnification used for the measurement. The procedure of the measurement is the following: lines are drawn in two perpendicular directions, and the grain size is estimated from the total length of these lines and the total number of intersections with the grain boundaries. In order to have a good estimation, at least 50 intersections with the grain boundaries were taken over the total length of the lines drawn in each direction.

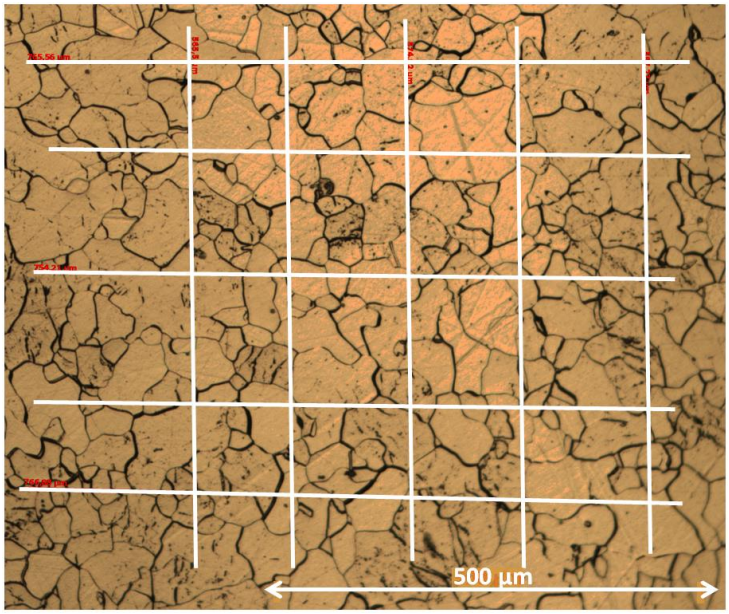

Figure 2 - 4 Intercept method used for the measurement of grain size.

The measured grain sizes by this method varied from 55 to 60 µm for the heat-treated sample, from 40 to 60 µm for the reference sample (without the heat treatment). In the latter case, the grain size variation was larger, and a larger difference in grain sizes between the different planes was confirmed.

In order to obtain more accurate values, SEM observation with EBSD analysis was carried out for the heat-treated sample. To carry out this analysis, the sample was prepared from the center of the plate and polished up to the grade of 1 µm associated with electrochemical polishing. The grain size distribution and the crystallographic texture were particularly examined. Figure 2 - 5 shows the EBSD mapping established from a sufficient number of grains. In the EBSD mapping, each color represents the crystal orientation determined by a standard triangle (Inverse Pole Figure (IPF)). It provided a more accurate value of the average grain size in the order of 90 µm. This measurement also provided the grain size distribution evidencing that the annealing heat treatment homogenized well the microstructure by a slight recrystallization.

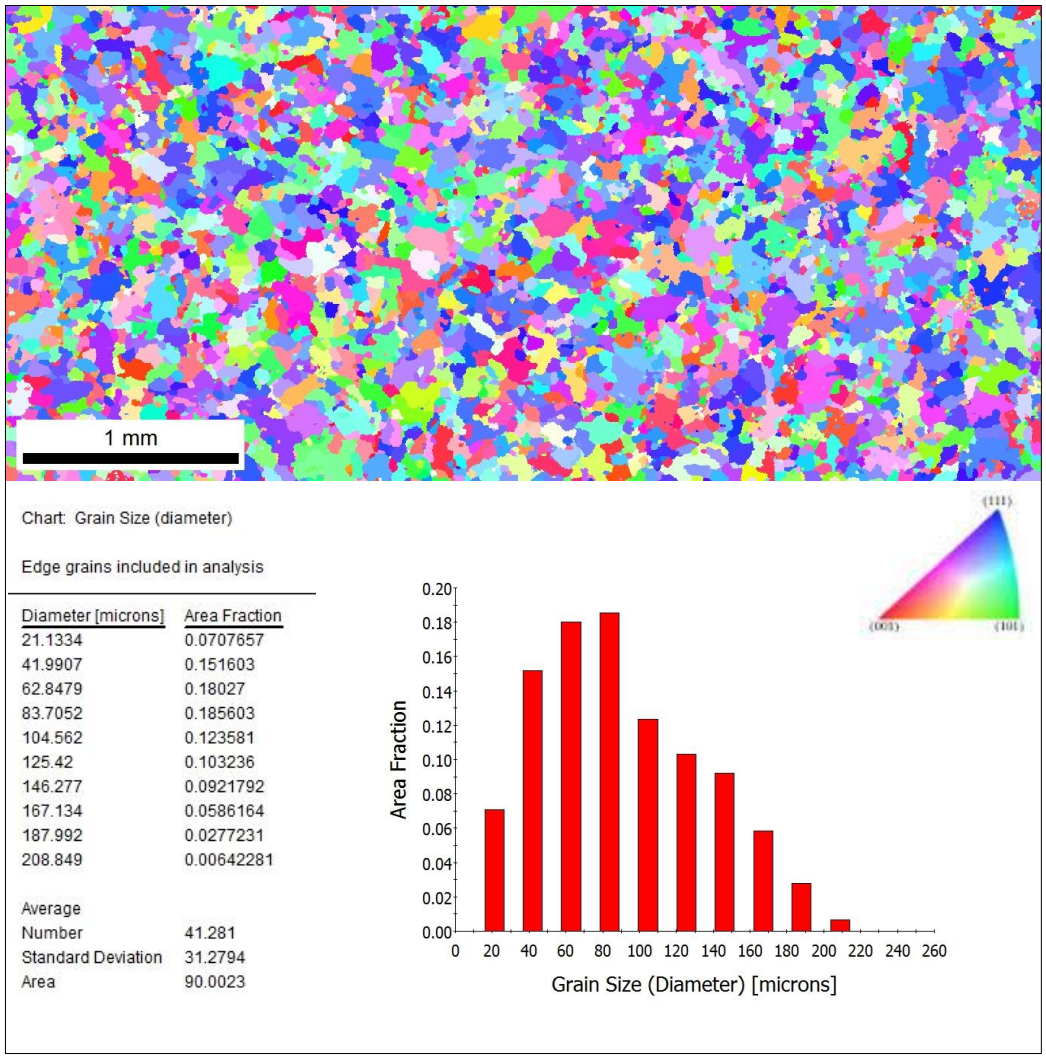

Figure 2 - 5 EBSD mapping of the microstructure and grain size distribution.

From the EBSD mapping, the characteristics of grain boundary was analyzed by using MTEX [113]. As a result, the misorientation angle of majority of grain boundaries is a more than 15° [27]. Besides, Figure 2 - 6 shows a mapping of the types of the grain boundaries. In this mapping, in addition to a general random grain boundary indicated by black, some special types of grain boundary ("Coincidence Site Lattice" (CSL) [114], indicated by "Σ") are indicated by several colors. The amount of a special type of grain boundary (Σ 3 – Σ 11) is very few. Therefore, the Armco iron used in this study mainly consists of a general random grain boundary. Oudriss et al.

[115] have shown that, for a polycrystalline nickel, a general random grain boundary represents the most favorable path of hydrogen diffusion. The knowledge of the type of grain boundaries is important because it is necessary to deepen the discussion on the hydrogen diffusion behavior and its influence on the fatigue crack propagation kinetics.

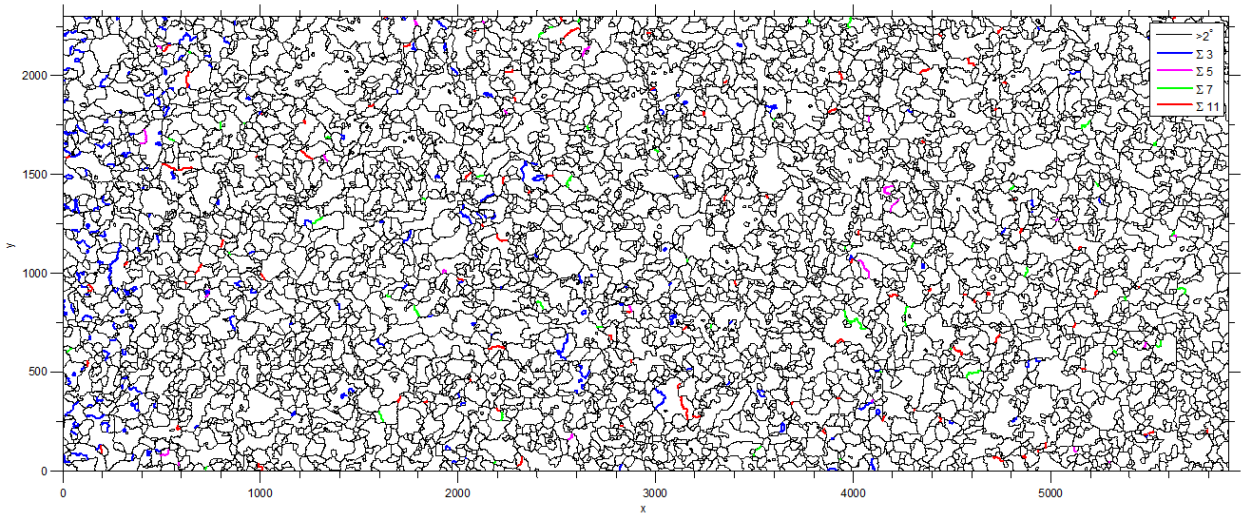

Figure 2 - 6 Mapping of the type of the grain boundary.

2.2.4 Mechanical properties

The mechanical properties of the Armco iron after the heat treatment was examined by Bilotta [27] by means of a tensile test, performed on an electric fatigue testing machine Instron 1362. This machine has a maximum capacity of 50 kN and the maximum loading frequency is 1 Hz. The extensometer with a working distance of 12.5 mm and a capacity of ± 5 mm (maximum deformation ± 40%) was used for the strain measurement.

The specimen type was a cylinder with a minimum diameter of 8 mm and a length of minimum diameter part of 20 mm as shown in Figure 2 - 7. The tensile tests were conducted at room temperature and in air. The strain was measured by the extensometer attached to the minimum diameter part of the specimen. These tests were conducted by following ASTM standard E8 / E8M-13a: "Standard Test Methods for Tension Testing of Metallic Materials" (2013) [116]. Three different initial strain rates were applied: 0.01, 0.1 and 1 %/s. The elongation of the specimen (using the extensometer) and the applied loading were recorded. True stress σ_t and true strain ε_t were calculated [117].

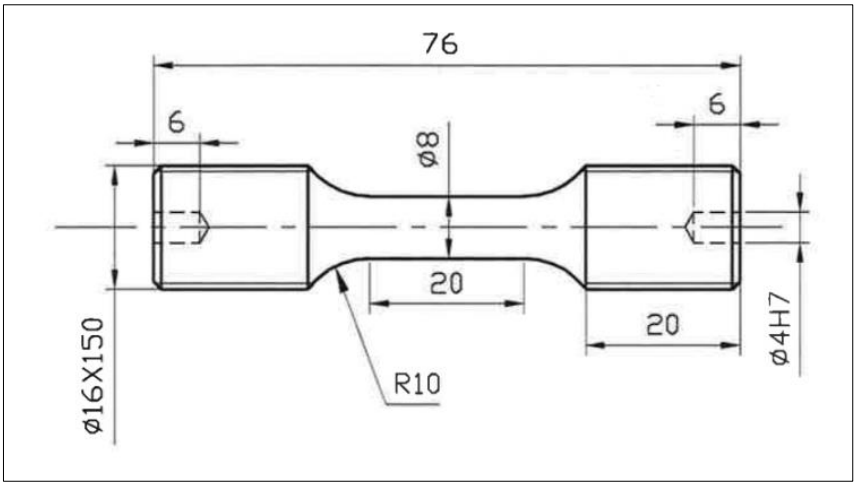

Figure 2 - 7 Geometry of cylindrical specimen of the tensile test by Bilotta [27].

From the stress-strain relationship obtained from the tensile tests, the values of Young's modulus E, upper and lower yield stresses σ_{YU} and σ_{YL}, tensile strength σ_m and the strain at the maximum stress at different strain rates were obtained as shown in Table 2 - 3. The average value of Young's modulus was E = 226 GPa, which is used for the following calculations in this study. This value is slightly higher than the value announced by AK steel Corp., 207 GPa [118]. The upper yield stress (the peak stress of elastic deformation) σ_{YU} increases from 210 to 290 MPa depending on the strain rate, while the lower yield stress σ_{YL} exhibited the same value 170 MPa at all the strain rates. The tensile strength σ_{TS}, around 280 MPa, slightly increased with the strain rate. These maximum stresses were established at almost the same strain around 25 %. A similar dependency of deformation behavior on strain rate has been also confirmed for metals with a BCC lattice by Armstrong and Walley [119].

Table 2 - 3 Measured values of Young's modulus, upper and lower yield stresses, tensile strength and elongation at the maximum stress at different strain rates.

Strain rate [%/s]	Young's modulus E [GPa]	Upper yield stress σ_{YU} [MPa]	Lower yield stress σ_{YL} [MPa]	Tensile strength σ_{TS} [MPa]	Elongation for maximum stress ε_{TS} [%]
0.01	233	210	170	270	25
0.1	222	245		280	
1	223	290		290	

2.3 Tensile test under gaseous hydrogen

In this section, for a purpose of investigation on a monotonic deformation behavior of Armco iron in the presence of hydrogen, tensile tests under gaseous hydrogen environment were conducted. In the tensile tests, gaseous environment, strain rate and exposure time were controlled as influential parameters to investigate a dependency of hydrogen embrittlement on these parameters.

2.3.1 Experimental method

2.3.1.1 Specimen

The specimen type was a cylindrical specimen with a minimum diameter of 6 mm and a length of minimum diameter part of 20 mm. The geometry of the specimen is shown in Figure 2 - 8.

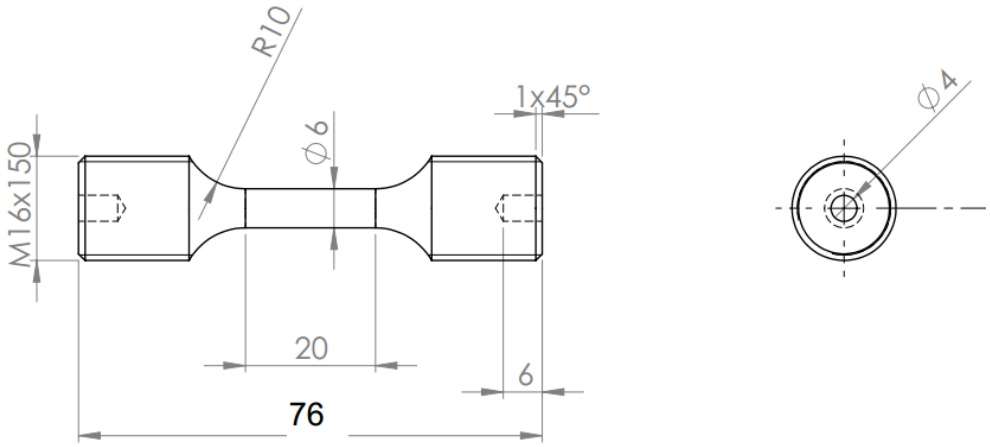

Figure 2 - 8 Geometry of cylindrical specimen for the tensile test.

The specimens were taken from a rolled plate of Armco iron after the annealing heat treatment in the longitudinal direction (rolling direction). The geometry of the plate is 20 x 80 x 250 mm. A total of 18 specimens were prepared from 2 plates as illustrated in Figure 2 - 9.

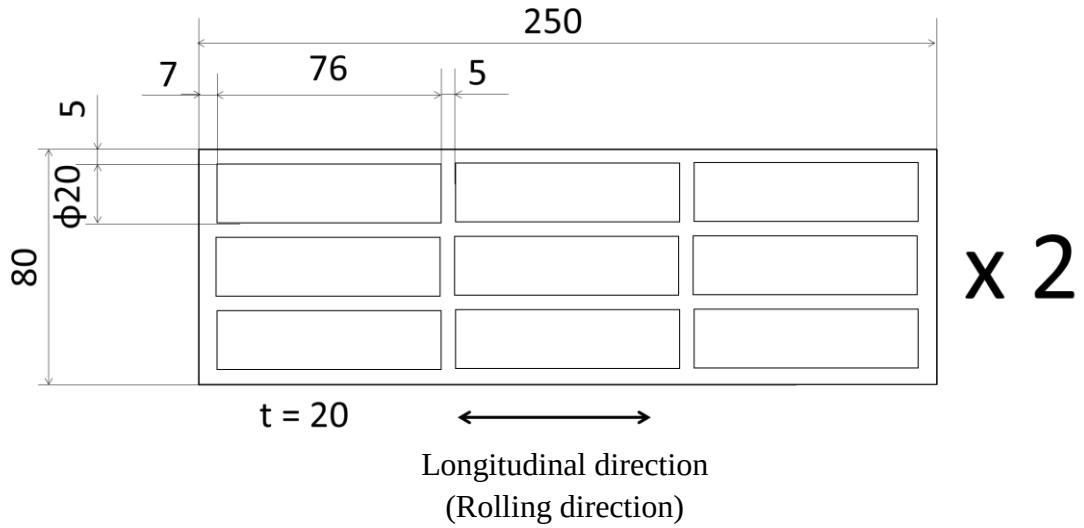

Figure 2 - 9 Layout drawing of cutting out the specimens from the plate.

The surface of minimum diameter part of the specimen was polished by using polishing papers up to grade 4000, and the final polishing was done in the longitudinal direction of the specimen to avoid affecting on crack initiation.

2.3.1.2 Presentation of Hycomat test bench

For performing the tensile test with a control of the surrounding gaseous environment, the Hycomat test bench [120, 121] was used. The Hycomat test bench was developed by Pprime Institute in Poitiers, on the CEAT (Centre d'Etudes Aérodynamiques et Thermiques) site. The Hycomat test bench is an experimental device dedicated to the study of the effects of environment (in particular gas at high pressure) on the mechanical behavior of materials. It consists of an INSTRON 8802 hydraulic tensile machine with a chamber that can be pressurized Figure 2 - 10a). The interior of the chamber is cylindrical, 150 mm in diameter and 100 mm in depth for a working volume of 1.77 liters. This volume allows the assembly of a CT type fracture specimen as well as a cylindrical specimen. Figure 2 - 10b shows the inside of the chamber with grips designed for crack propagation test on a CT specimen. The maximum stroke of the rod is limited to 20 mm, which restricts the dimensions of the specimens. A schematic 3D model of the chamber with the loading rod is shown in Figure 2 - 10c. The two loading cells, internal and external, are equipped. The internal loading cell is compensated with respect to the gas pressure inside the chamber, to cancel a shift of the measured value of loading due to the pressure applied to the loading rod.

Several safety devices are installed in and around the machine. The control system for pressurizing the chamber and for starting and stopping the test is in particular placed distant from the test machine, in a separated room. H_2 and CO_2 detectors and an air ventilation system are always working during the test. A water circulation system is equipped for cooling the machine, and a thermocouple allows to know the temperature inside the chamber.

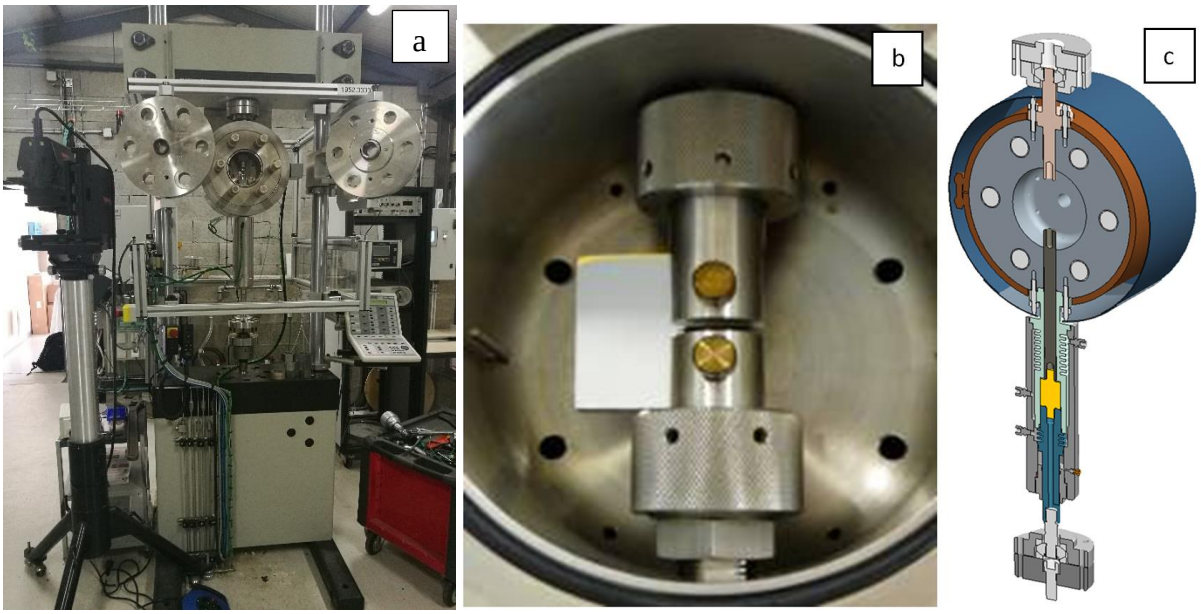

Figure 2 - 10 Hycomat test bench: the INSTRON 8802 hydraulic tensile machine with a chamber that can be pressurized (a). Inside the chamber with the grips for crack propagation test (b) and a schematic 3D model of the chamber equipped with the loading rods (c).

The maximum capacity of loading of Hycomat is 25 kN in tension. On the other hand, the machine cannot work in compression, because of its alignment system at the top and bottom of the chamber. The cyclic loading frequency is limited to a maximum of 40 Hz. In this configuration, the machine can perform conventional mechanical tests of uniaxial tension, creep and fatigue (positive loading ratio). In terms of gaseous atmosphere, in addition to a test under ambient air, it is possible to carry out tests under nitrogen (N_2), carbon dioxide (CO_2), or hydrogen gas (H_2) up to a gas pressure of 40 MPa (400 bar). The chamber is thermally regulated by means of a heating collar to enable to control temperature up to 150 °C.

The machine has two different pressure doors. The first door can be used up to a gas pressure of 4 MPa. It has a 40 mm diameter window at the center of the chamber. The second door is designed to carry out tests up to a pressure of 40 MPa as shown in Figure 2 - 11a. This door has a smaller window, 26mm in diameter, shifted from the center to observe a crack propagation in a CT specimen installed inside. In addition to these doors with window, the Hycomat bench has another window on the back side of the chamber as shown in Figure 2 - 11b. This window is located on the loading axis, hence this was used for the marker tracking method, which is explained in the next sub-section, to measure the elongation of the specimen during the tensile test.

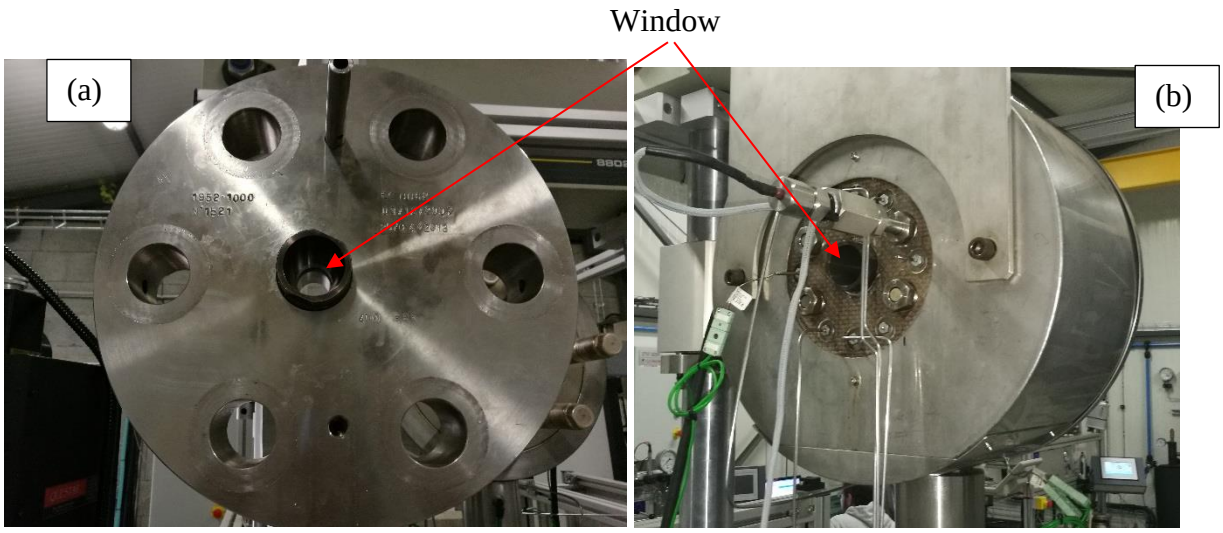

Figure 2 - 11 Door with a window of 26mm in diameter (a) and the back side with a window (b) of the pressure chamber of Hycomat test bench.

A mass spectrometer (a hygrometer, shown in Figure 2 - 12) equips the machine to measure the amounts of oxygen and water vapor contained in gaseous atmosphere in the chamber during the test. Table 2 - 4 shows the measured impurity levels of a hydrogen and nitrogen gases. The measurement was made at atmospheric pressure (around 1 bar). Since the proportion of impurities remains the same for any pressure, higher absolute amounts of oxygen and water vapor are probably contained in gaseous atmosphere at higher pressure (3.5 or 35 MPa as applied in this study).

Figure 2 - 12 Hygrometer equipped to Hycomat test bench.

Table 2 - 4 Amount of impurities contained in hydrogen and nitrogen gases, measured by the mass spectrometer.

	H_2O [ppm]	**O_2 [ppm]**
Nitrogen	25	15
Hydrogen	18	10

For removing the impurities of the gases in the chamber, nitrogen was injected up to a pressure of 30 bar and then removed. This operation has been repeated three times before pressuring hydrogen or nitrogen gas. The gas insertion process was controlled by linearly increasing a gas pressure up to a target value, taking 10 minutes in the case of 3.5 MPa and 20 minutes in the case of 35 MPa.

2.3.1.3 Procedure and test condition

A procedure of tensile tests followed the ASTM standard E8 / E8M-13a: "Standard Test Methods for Tension Testing of Metallic Materials" (2013) [116].

The elongation of the specimen during the test has been measured by cross-head displacement and by marker tracking method. The cross-head displacement method measures the displacement of the loading rod (equaling to the elongation of the specimen) to calculate a strain in the minimum diameter part of the specimen. This calculation of strain assumes that the deformation of the rest of the specimen is negligible. The marker tracking method records the image of the specimen surface by a camera through the window of the back side as shown in Figure 2 - 13, in order to measure the distance between two dots painted on the surface. For this method, the specimen surface was painted black by spray, and two white dots with an initial distance of 10 mm were painted as shown in Figure 2 - 14. The specimen surface was monitored by the camera attached to the machine through the window on the back side of the chamber. A software developed by Pprime Institute was used to calculate the distance between the two dots in real time from the video taken by the camera. An extensometer used in the tensile tests for determining the mechanical properties of the material (Section 2.2) was not used in these tests because the gaseous hydrogen may affect its accuracy due to a modification of properties of the material used in strain gages inside the extensometer. A strain gauge available in hydrogen atmosphere has been developed by Kyowa Electronic Instruments [122] by using a material with high resistance against hydrogen embrittlement. This is one possible option of strain measurement for tests under gaseous hydrogen in the future.

Figure 2 - 13 Camera set-up in the back side of Hycomat test bench for the marker tracking method.

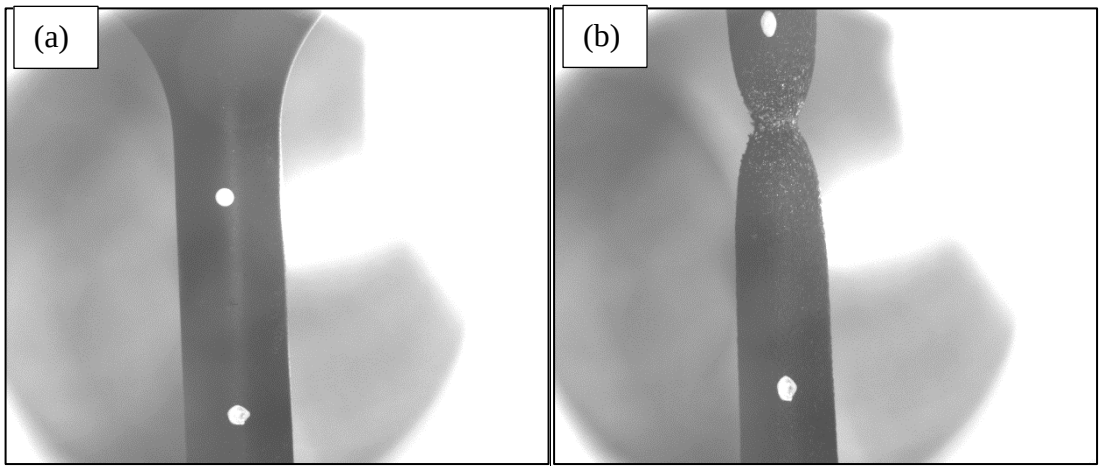

Figure 2 - 14 Photographs of specimen surface painted black with two white dots taken by the camera before the test (a) and after the test (b).

The testing condition is summarized in Table 2 - 5. The environment applied for the tests were gaseous hydrogen and nitrogen at a gas pressure of 35 MPa and ambient air. The gaseous nitrogen at 35 MPa was chosen as a reference for gas pressure influence. The gas temperature was room temperature. The exposure time t_e, defined as the time between the end of gas insertion process and the beginning of the test, took the values 4, 30 or 5340 minutes (89 hours). Applied initial strain rates $d\varepsilon/dt$ were 5×10^{-5} s^{-1} and $5 \times 10^{-6} s^{-1}$. These values of strain rates were chosen by referring to the testing condition used in the thesis of Moro [51]. The test was controlled by a constant rate of displacement of the rod, and the displacement rate was fixed to have a given strain rate. A total of 11 specimens were tested. Each specimen is named as "FCS (Number)". FCS stands for "Fe Cylindrical Specimen".

Table 2 - 5 Conditions of tensile tests under various gaseous environments.

No. (FCS)	Test condition		
	Environment [MPa]	Initial strain rate $d\varepsilon/dt$ [s^{-1}]	Exposure time t_e [mins]
1	Air: 0.1	5×10^{-5}	
2	N_2: 35	5×10^{-5}	
3	N_2: 35	5×10^{-5}	
4	Air: 0.1	5×10^{-5}	
5	H_2: 35	5×10^{-5}	30
6	H_2: 35	5×10^{-6}	30
7	N_2: 35	5×10^{-6}	
8	H_2: 35	5×10^{-6}	30
9	H_2: 35	5×10^{-5}	5340
10	H_2: 35	5×10^{-5}	5340
11	H_2: 35	5×10^{-5}	4

Nominal stress σ_n and nominal strain ε_n were calculated from the measured loading and the elongation of the specimen [117].

Before analyzing the test result, an issue which has to be considered is a drift of the loading value due to the high pressure of the gas. Although Hycomat is designed to cancel the influence of gas pressure in the vessel on the internal load cell, there was still a drift of the loading value due to gas pressure. For example, in the test under nitrogen pressure of 35 MPa, the loading value measured by the internal load cell which was reset to 0 before the insertion of the gas became -980 N at the end of the tensile test (after fracture of the specimen, before depressurizing). Because of this, the loading values of all following tests were calibrated so that the load at the end of the test is zero.

2.3.2 Tensile tests under air and gaseous nitrogen: as reference

The tensile tests under air and gaseous nitrogen of 35 MPa were performed as a reference for the comparison with the ones under hydrogen. The initial strain rate was $5 \times 10^{-5}\ s^{-1}$. The result of the tensile tests is shown in Figure 2 - 15. Figure 2 - 15a and b show the stress-strain curves of the

tests with cross-head displacement measurement, while Figure 2 - 15c and d show the ones of the tests with the marker tracking method. Figure 2 - 15b and d zoom in on the strain range [0,2%] and are compared with the theoretical elastic curve, whose Young's modulus E is 226 GPa.

First of all, for the tests with cross-head displacement measurement (Figure 2 - 15a), the curves in air and nitrogen exhibit almost the same values except one curve in nitrogen (FCS3). Fracture elongations (nominal strain at the fracture) of two tests in air and one test in nitrogen are approximately 59 % while another one (FCS3) in nitrogen is 65 %. The maximum stresses of all the four tests are almost the same level, approximately 270 MPa. In the elastic deformation part (Figure 2 - 15b), elastic curve is increasing linearly and is followed by a plateau. The slopes of the measured elastic curves are much smaller than the one of the theoretical elastic curves. A reason of this difference might be a gap between the grips and the specimen, and also the deformation in the other part from the minimum diameter part of the specimen. Hence, the strain in the elastic deformation range was not accurately measured by the cross-head displacement measurement.

On the other hand, in the case of the marker tracking method shown in Figure 2 - 15c, although all the stress-strain curves are almost identical until the stress reaches the maximum value, the strain values vary a lot in the decreasing part. The strain value of one curve in air (FCS4) drops at ε_n = 35 %, while the strain value of one in nitrogen (FCS3) reaches 91 %. The cause of the drop observed on FCS4 is that the necking of the specimen happens out of the range between the markers, as shown in Figure 2 - 16. Also, all the curves except the one in air (FCS4) exhibit larger variation in final strain values compared to the case of the cross-head displacement measurement. This is because the strain value measured by the marker tracking method depends on the position of necking. Even when the necking occurs between the markers, if the necking happens near the position of the marker, the shift of marker position can be influenced by the shrinkage due to the necking. Because of this problem, in the case of this study, the marker tracking method is not an appropriate way to measure the elongation of the specimen after the necking. The elastic deformation curves (Figure 2 - 15d) show that the experimental curves match well with the theoretical one except for one case in nitrogen (FCS2). The marker tracking method is, therefore, able to measure the accurate value of strain in the elastic deformation range because this method directly measures the deformation of the minimum diameter part without the influences of a gap and of the deformation of the other part.

Based on the above pros and cons of the two strain measurement methods, for the following tests, the strain value obtained by the marker tracking method is used for the analysis of elastic deformation, and the one obtained by cross-head displacement measurement is used for the analysis of plastic deformation.

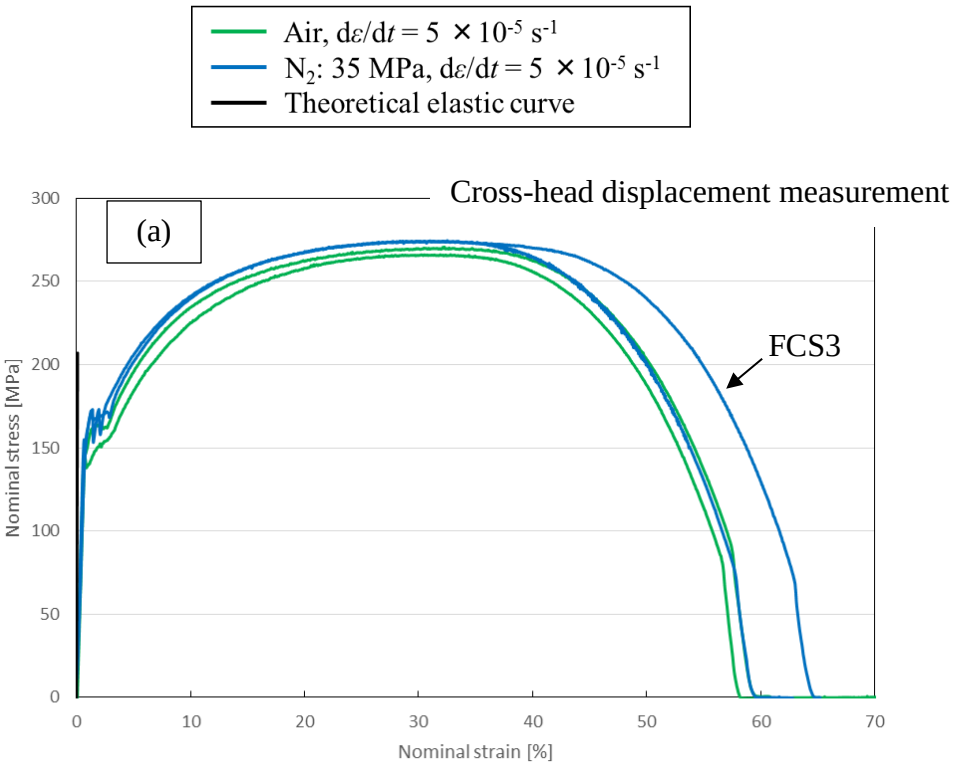
Air, dε/dt = 5 × 10-5 s-1
N2: 35 MPa, dε/dt = 5 × 10-5 s-1
Theoretical elastic curve
(a)
Cross-head displacement measurement
FCS3
Nominal stress [MPa]
Nominal strain [%]
0
50
100
150
200
250
300
0
10
20
30
40
50
60
70

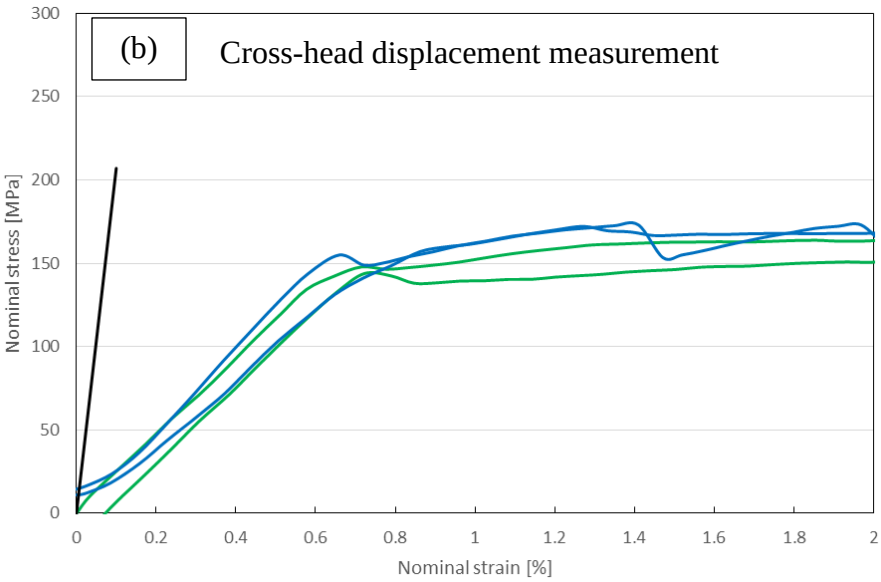
(b)
Cross-head displacement measurement
Nominal stress [MPa]
Nominal strain [%]
0
50
100
150
200
250
300
0
0.2
0.4
0.6
0.8
1
1.2
1.4
1.6
1.8
2

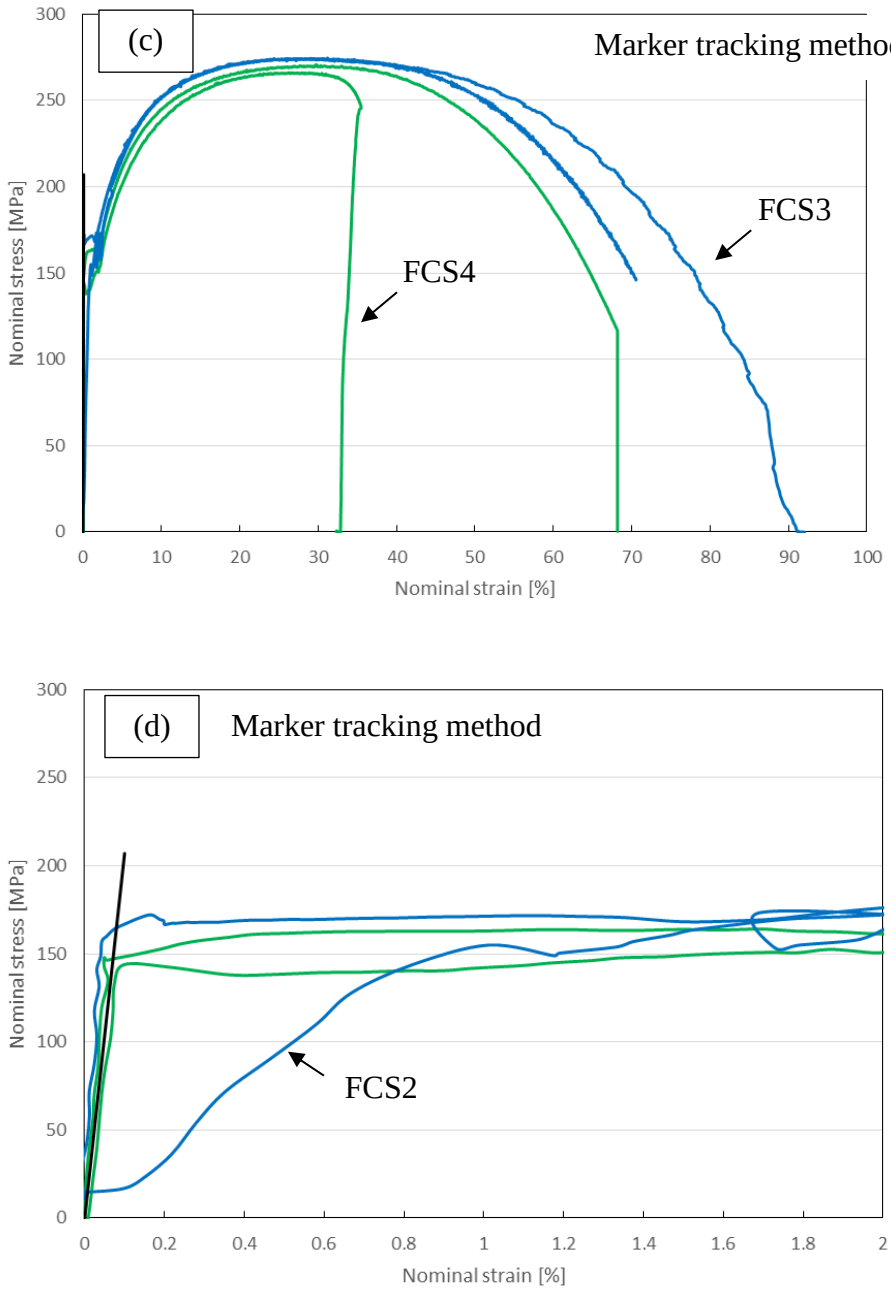

Figure 2 - 15 Stress-strain curves in air and nitrogen of 35 MPa. The strain was measured by cross-head displacement measurement (a)(b) and marker tracking method (c)(d). (b) and (d) are zoomed in curves on the strain range (< 2%), respectively.

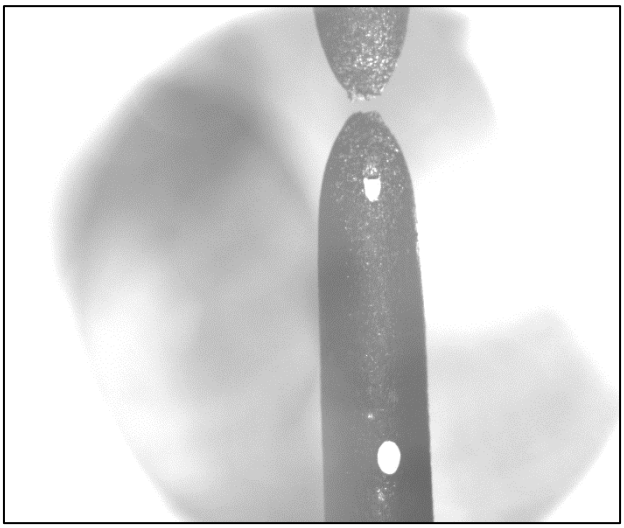

Figure 2 - 16 Fractured specimen tested in air (FCS4). The necking and fracture occurred out of the range between the markers.

The SEM images of the fracture surface and of the side-view of fracture part of the specimen tested under nitrogen are shown in Figure 2 - 17. The figure shows the top (a) and side (c) views of the specimen and the fracture surface (b). The fracture surface exhibits dimples typical from ductile materials [51, 123–125]. The mechanism of this type of ductile fracture starts from the nucleation of voids around inclusions and their coalescence in a core of specimen. When the development of voids reaches a certain level and shear stress on the edge of specimen exceeds the shear strength of material, a final shearing fracture occurs. The same type of fracture surface was observed on the other specimens tested in air and nitrogen. It can also be seen that the fractured part of the specimen is severely shrunken, and the side surface became rough. The reduction of area (*RA*) is an index of material ductility defined as:

$$\mathrm{RA} = \frac{A - A_0}{A_0} \times 100\ [\%] \qquad 2\text{ - }1$$

The cross-sectional area was calculated from the minimum diameter of the specimen measured by an optical scale measurement microscope. The values of *RA* in air and nitrogen reached 94 – 96 %. From the above results, no clear influence of nitrogen gas pressure at 35 MPa on the deformation behavior of Armco iron was observed.

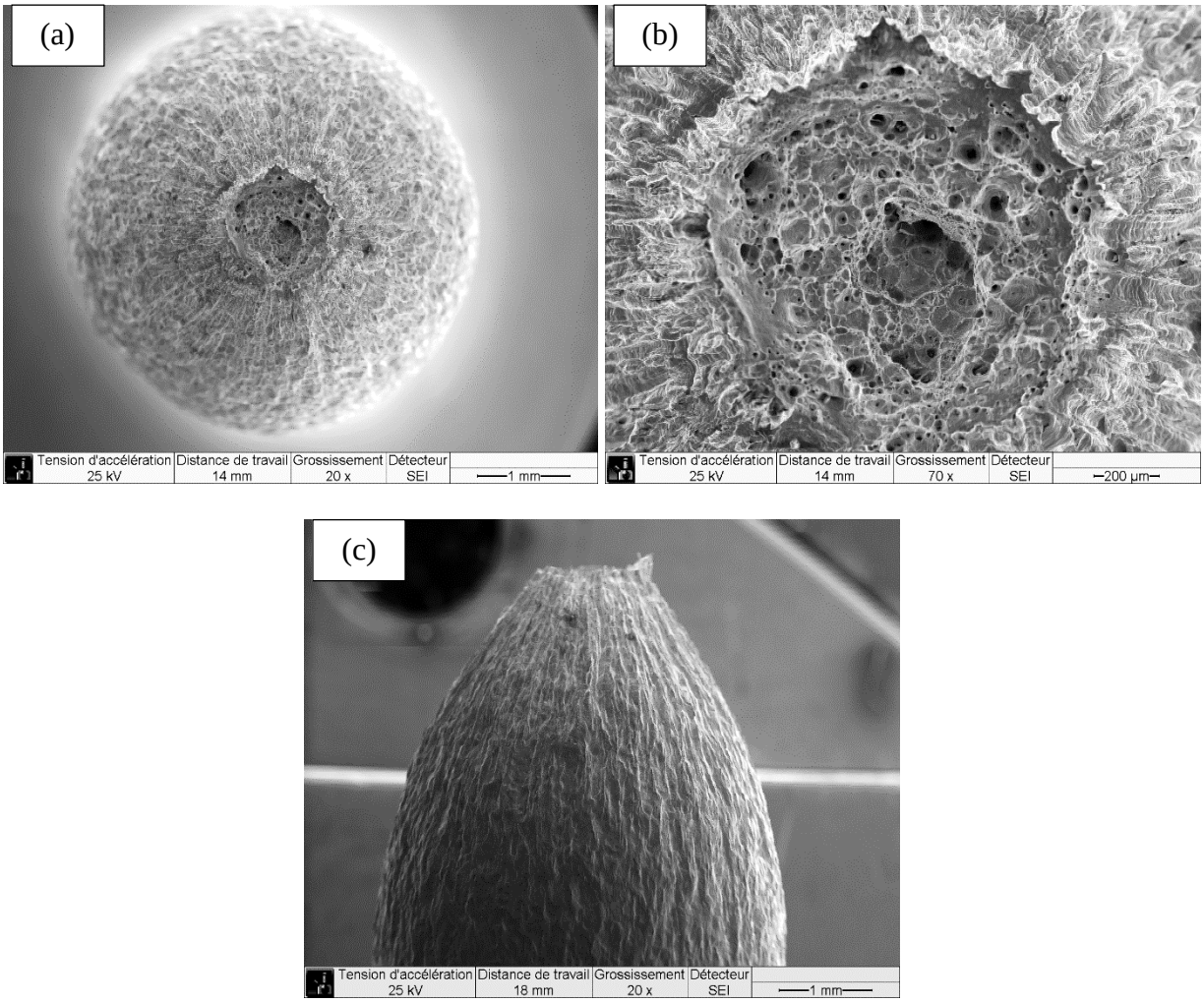

Figure 2 - 17 SEM images of the top (a) and side (c) views of fracture part and the fracture surface (b) of the specimen tested under nitrogen (FCS2).

2.3.3 Discussion on validity of test results

Before conducting the tensile test under gaseous hydrogen, it is necessary to examine the validity of the present tensile test by comparing it with the other tensile tests in literature.

First of all, the test result was compared with the one by Bilotta [27] as mentioned in Sub-section 2.2.4. The main difference is here the strain rate and the diameter of specimen (8 mm in case of Bilotta [27] as shown in Figure 2 - 7). Figure 2 - 18 shows the nominal stress – nominal strain curves of 8 mm specimen. The nominal strain in this diagram was calculated from the elongation measured by the cross-head displacement. If we compare the result of 8 mm specimen with the one of 6 mm specimen in the present study, the maximum stress measured on 8 mm specimen is almost the same level or slightly higher than the one of 6 mm specimen. In contrast, the fracture elongations of 8 mm specimens range from 70 to 80 % which are larger than the ones of 6 mm specimen (around 60 %). Besides, the fracture elongation of 8 mm specimens clearly depends on the strain rate. A lower strain rate results in a lower fracture elongation. Since the test of 6 mm

specimen was performed at lower strain rate (0.005 %/s) than the ones on 8 mm specimens (≥ 0.01 %/s), thus the lower value of fracture elongation of 6 mm specimen can be explained in terms of the dependence on strain rate. A similar dependence of strain at fracture on strain rate in pure iron has also been confirmed by Johnson et al. [126]. They have found out that the fracture elongation is proportional to a logarithm of strain rate.

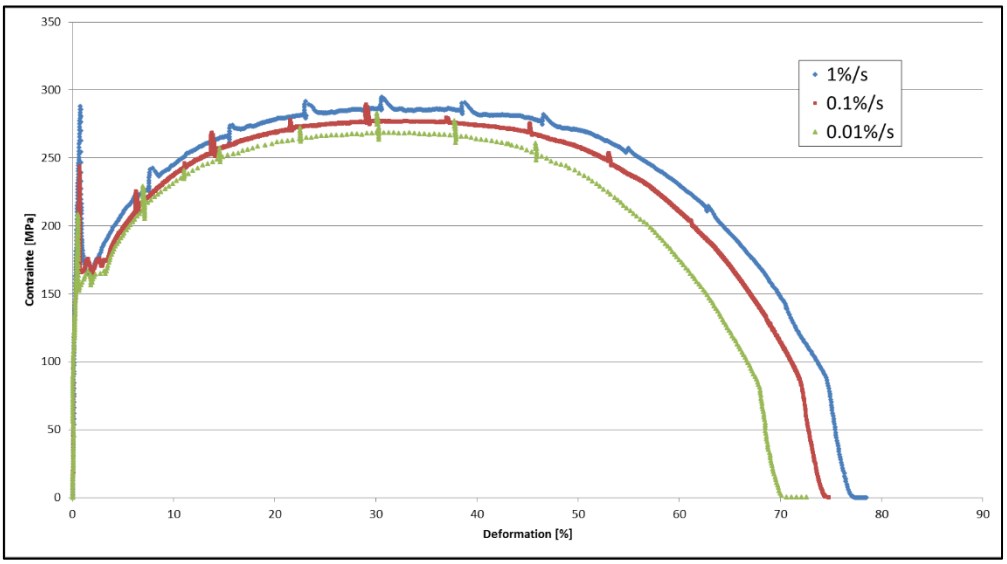

Figure 2 - 18 Stress-strain curve of tensile tests of the specimen with a diameter of 8 mm by Bilotta [27].

In a second step, the present result was compared with the work by Moro [51]. Figure 2 - 19 displays the geometry of the cylindrical specimen used by Moro. The specimen has a diameter of 6 mm and a length of the minimum diameter part of 30 mm which is longer than the one in this study. The strain rate was $d\varepsilon/dt = 5x10^{-5}\ s^{-1}$ which is the same as the one in this study. Figure 2 - 20 shows the nominal stress – nominal strain curve of her test. The curve exhibits a maximum stress of 270 MPa and an fracture elongation of 47 %. Even though the maximum stress is similar to the present ones, the fracture elongation is much smaller than the present ones.

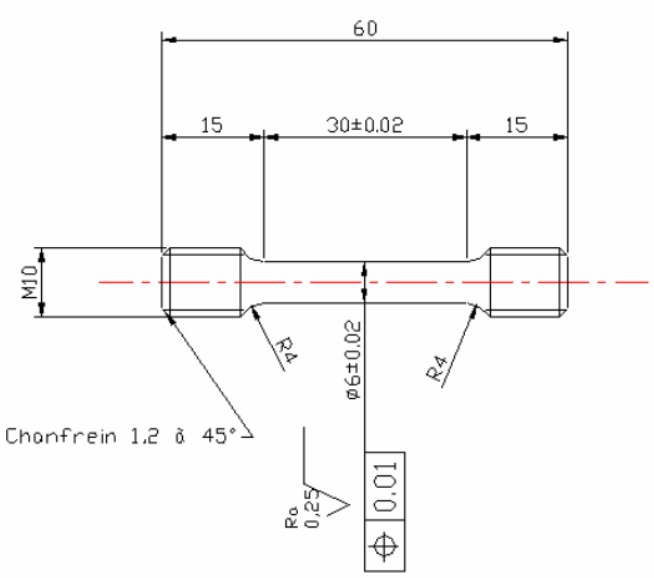

Figure 2 - 19 Geometry of cylindrical specimen used by Moro [51].

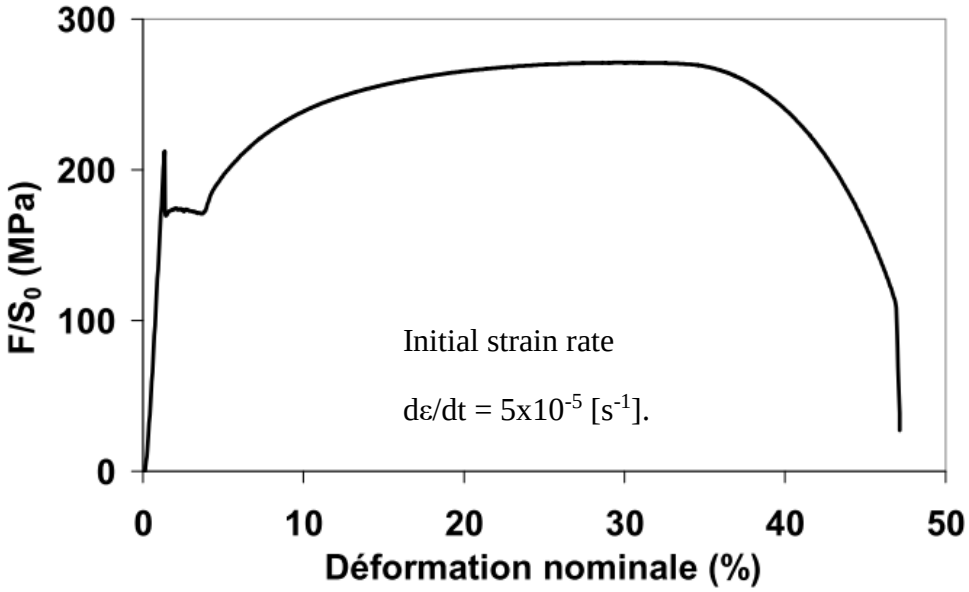

Figure 2 - 20 Stress-strain curve of Armco iron obtained by Moro [51].

Therefore, the large difference in fracture elongation between these tensile tests was confirmed. This difference can be explained by the influence of the specimen size. According to Oliver's formula prescribed by ISO 2566-1 [127], the fracture elongation ε_r depends on the specimen size (cross-sectional area A_0 and gauge length l_0) as expressed by the following equation:

$$\varepsilon_r = 2\varepsilon_r{}' \left(\frac{\sqrt{A_0}}{l_0} \right)^{0.4} \qquad 2 - 2$$

where ε_r' is a reference fracture elongation of specimen with a gauge length of $5.65\sqrt{A_0}$. Thus, this equation requires all specimens have the same cross-sectional area (i.e. diameter). Besides, a value of fracture elongation of specimen with a specific gauge length ($5.65\sqrt{A_0}$) is necessary as a reference value. Fortunately, the 6 mm specimen in the this study and Moro's one have the same diameter, and Moro's one satisfies the condition of geometry. Because of this, the fracture elongation of 6 mm specimen tested in air was estimated from the one of Moro's specimen (47 %) as a reference value, by using Oliver's formula. Table 2 - 6 shows the calcuration result. The estimated values of fracture elongation of 6 mm specimens is ε_r = 55.3 % which is close to the actual values, 59.1 and 58.1 %. This agreement indicates that the observed difference in fracture elongation between the tests with different specimen geometry was caused by the specimen size effect.

Table 2 - 6 Calculation result of estimation of fracture elongation by Oliver's formula.

Specimen	6 mm specimen		Moro's specimen
Gauge length l_0 [mm]	20		30
Diameter d [mm]	6		6
$5.65\sqrt{A_0}$	30.0		30.0
Measured fracture elongation in air $\varepsilon_{r\text{-}air}$ [%]	59.1	58.1	47 (= ε_r')
Estimated fracture elongation ε_r [%]	55.3		47.0

2.3.4 Tensile test under gaseous hydrogen

While the previous section dealt with tensile tests under air and nitrogen, considered as a reference, Figure 2 - 21 shows the stress-strain curve of the test (FCS5) under gaseous hydrogen at the gas pressure P_{H2} = 35 MPa, the initial strain rate $d\varepsilon/dt = 5\times10^{-5}$ s^{-1} and the exposure time t_e =30 mins, compared with the previous results of tests under air and nitrogen. Figure 2 - 21a and b plot the entire curves with the strain measured by the cross-head displacement and the elastic part with the strain measured by the marker tracking method. The maximum stress of the test in hydrogen was 269 MPa, which is the same level as the ones in air and nitrogen. On the other hand, the fracture elongation of the test in hydrogen was 53.5 %, which is lower than the ones in air and nitrogen. Therefore, in this result, the clear influence of gaseous hydrogen decreasing the fracture elongation was observed. In contrast, in elastic part (Figure 2 - 21b), although the curve in hydrogen shows large variation in the strain value, the slope of the curves and the elastic limit are roughly the same as in inert environments. Thus, hydrogen seems not to affect the elastic deformation.

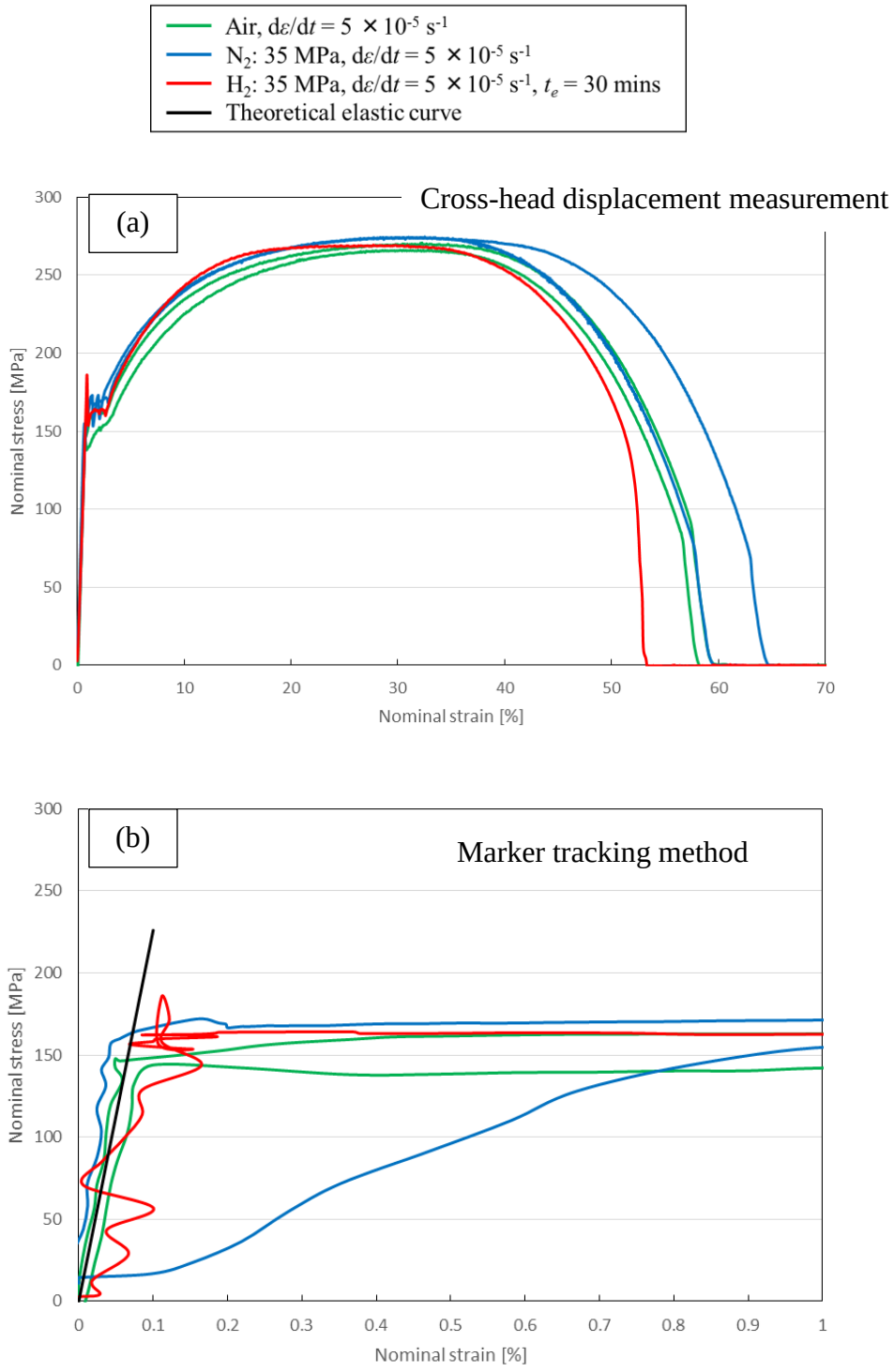

Figure 2 - 21 Stress-strain curves of tensile tests under air, nitrogen, and hydrogen at 35 MPa (FCS5). The entire curve measured by the cross-head displacement measurement (a) and the elastic part measured by the marker tracking method (b).

Figure 2 - 22 shows the SEM images of the fracture surface (a), the side view of fracture part (b) and the magnified image of the side surface (c) of the specimen tested under hydrogen (FCS5). The fracture surface (Figure 2 - 22a) exhibits a brittle QC fracture with numerous secondary cracks without dimples, unlike the case of fracture surface in nitrogen (Figure 2 - 17b). In addition, many

cracks were observed on the side surface of the specimen as shown in Figure 2 - 22c, while no crack was observed on the side surface of specimens in air or nitrogen.

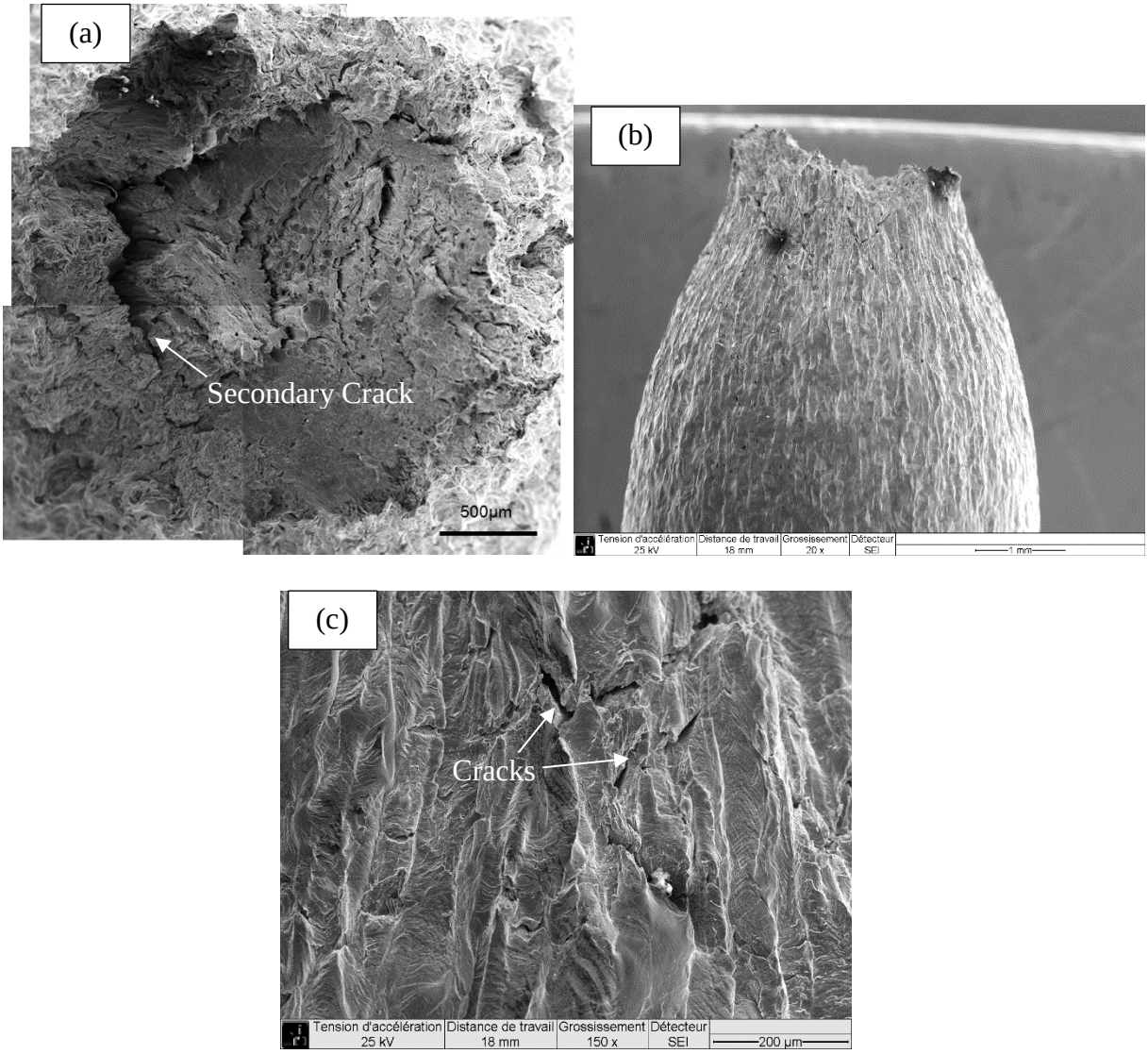

Figure 2 - 22 SEM images of the fracture surface (a) and the side view of the fracture part (b) of the specimen tested under hydrogen (FCS5).

In addition, Figure 2 - 23 shows the comparison of *RA* according to the different environments. The *RA* in hydrogen was 82 %, which is smaller than the one in air or nitrogen. This can be confirmed by comparing the SEM image of shrinkages of specimens tested in nitrogen (Figure 2 - 17b) with the one in hydrogen (Figure 2 - 22b). The change in the fracture surface to a more ductile feature and the reduction of fracture elongation and *RA* are consistent with the influences of hydrogen embrittlement reported by literature [11, 51, 128–131].

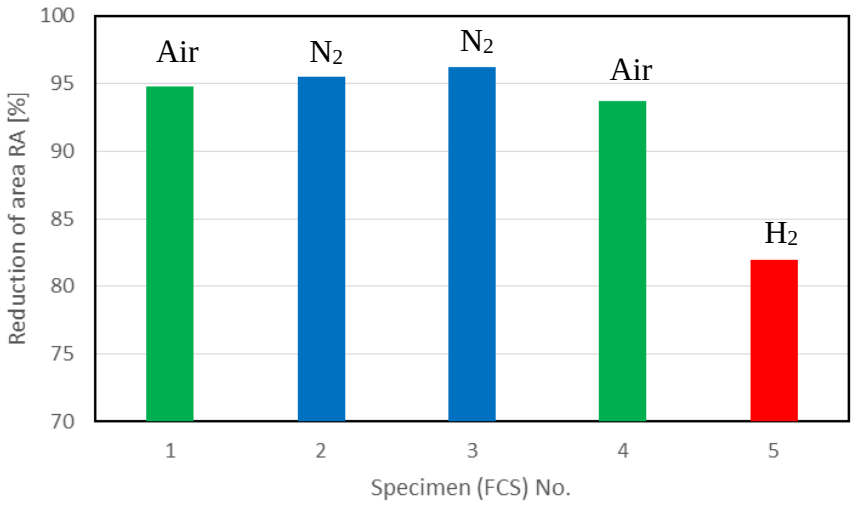

Figure 2 - 23 Comparison of reductions of area RA in various environments.

2.3.5 Influence of strain rate

In order to investigate the dependence of hydrogen-affected tensile fracture process on strain rate, the tensile tests under nitrogen and hydrogen at a strain rate of one order lower, $d\varepsilon/dt = 5 \times 10^{-6}\ s^{-1}$, have been conducted.

Figure 2 - 24 shows the stress-strain curves of the tests under nitrogen and hydrogen at $d\varepsilon/dt = 5 \times 10^{-6}\ s^{-1}$ indicated by dashed lines, in addition to the other tests. During the test in hydrogen (FCS6), the hydrogen gas pressure accidentally dropped from 35 MPa to 0 MPa at a strain of 43 % indicated by (*) in Figure 2 - 24, due to the mistake of operation. The stress value of the curve after the accident (*) was calibrated for canceling the value shifting due to the change in gas pressure. The shape of the curve after the accident (*) seems not to be affected by this gas pressure drop.

From this diagram, it has been clarified that the fracture elongations at $d\varepsilon/dt = 5 \times 10^{-6}\ s^{-1}$ in both nitrogen and hydrogen are lower (about 5 %) than the ones at $d\varepsilon/dt = 5 \times 10^{-5}\ s^{-1}$. This reduction of fracture elongation by strain rate is likely caused by the nature of strain rate sensitivity of the material, not by an effect of hydrogen because the same amount of reduction is found in nitrogen. As mentioned in Sub-section 2.3.3, it has been confirmed that Armco iron exhibits a strain rate dependency of fracture elongation. Therefore, no particular influence of hydrogen on the strain rate dependency was observed.

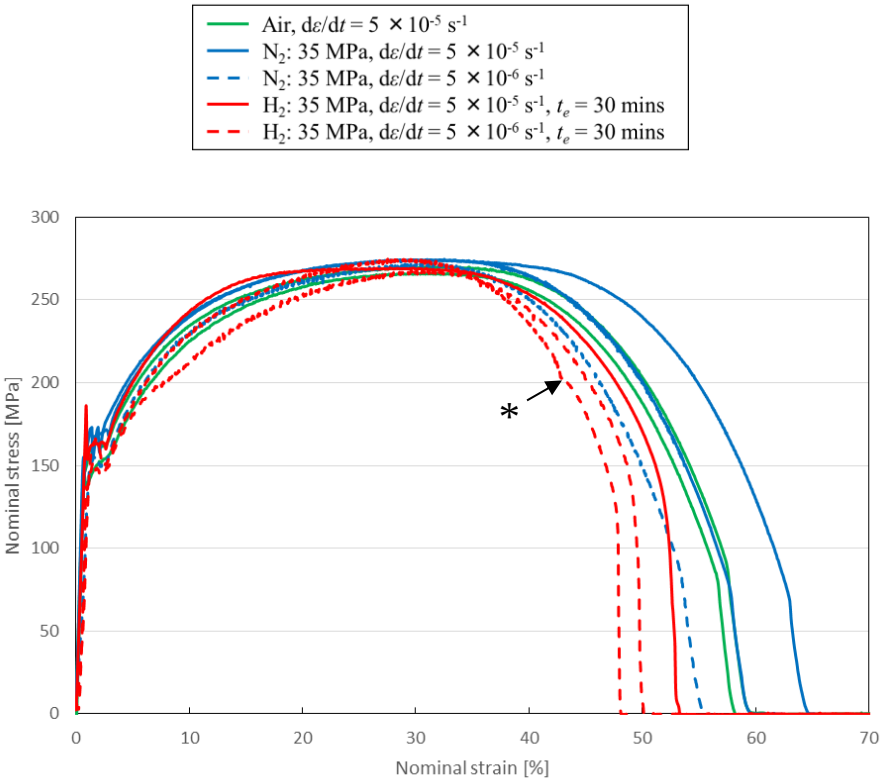

Figure 2 - 24 Stress-strain curves of tensile tests under air, nitrogen, and hydrogen at strain rates 5 × 10^{-5} and 5 × 10^{-6} s^{-1}.

Figure 2 - 25, Figure 2 - 26 and Figure 2 - 27 show the SEM images of the fracture surface (a) and the side view of fracture part (b) of the specimen tested at $d\varepsilon/dt = 5 \times 10^{-6}\ s^{-1}$ under nitrogen and hydrogen (FCS7, FCS8, and FCS6), respectively. The fracture surface at $d\varepsilon/dt = 5 \times 10^{-6}\ s^{-1}$ in nitrogen (FCS7) is a ductile fracture surface with a large number of dimples, like those at $d\varepsilon/dt = 5 \times 10^{-5}\ s^{-1}$. Besides, the fracture surface at $d\varepsilon/dt = 5 \times 10^{-6}\ s^{-1}$ in hydrogen (FCS8) is a QC fracture surface with secondary cracks like the one at $d\varepsilon/dt = 5 \times 10^{-5}\ s^{-1}$. On the other hand, as shown in Figure 2 - 27, the center part (indicated by the red dashed line) of the fracture surface of another test in hydrogen (FCS6) exhibits a ductile fracture with dimples while the fringe part exhibits a QC fracture. This change in fracture surface morphology is likely corresponding to the drop of hydrogen gas pressure during the test. The removal of hydrogen atmosphere immediately causes a dissipation of hydrogen embrittlement effect, resulting in the change in fracture mode to ductile fracture, even though this was obtained by an accident of gas pressure drop. Moreover, this change in the center part of fracture surface near the end of test evidences that the cleavage cracks are initiated from the specimen surface and they propagate towards the center of specimen. This is the opposite direction of fracture process against the ductile fracture in air or nitrogen.

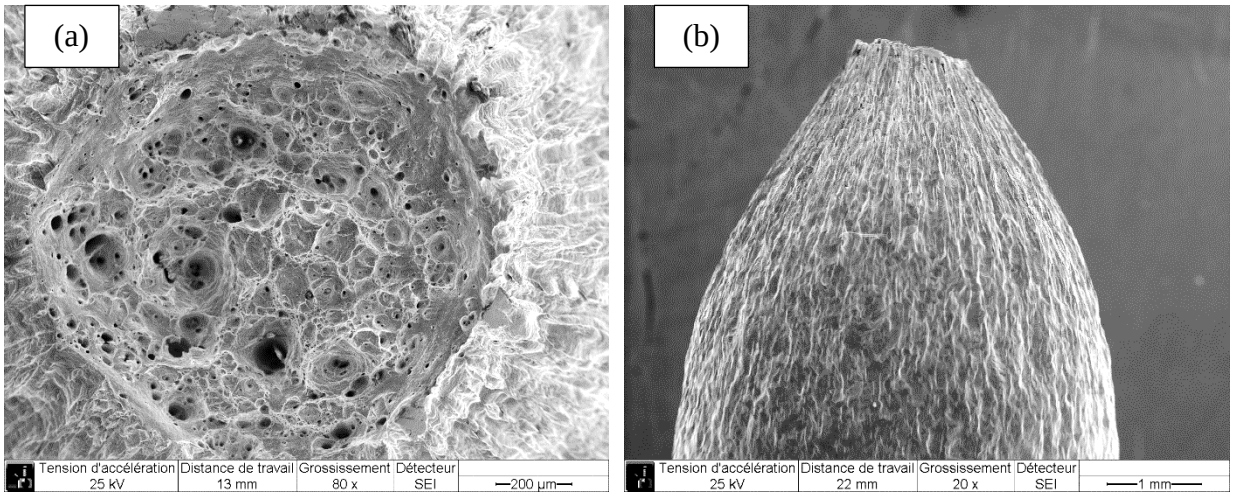

Figure 2 - 25 SEM images of the fracture surface (a) and the side view of fracture part (b) of the specimen tested under nitrogen at $d\varepsilon/dt = 5 \times 10^{-6}\ s^{-1}$ (FCS7).

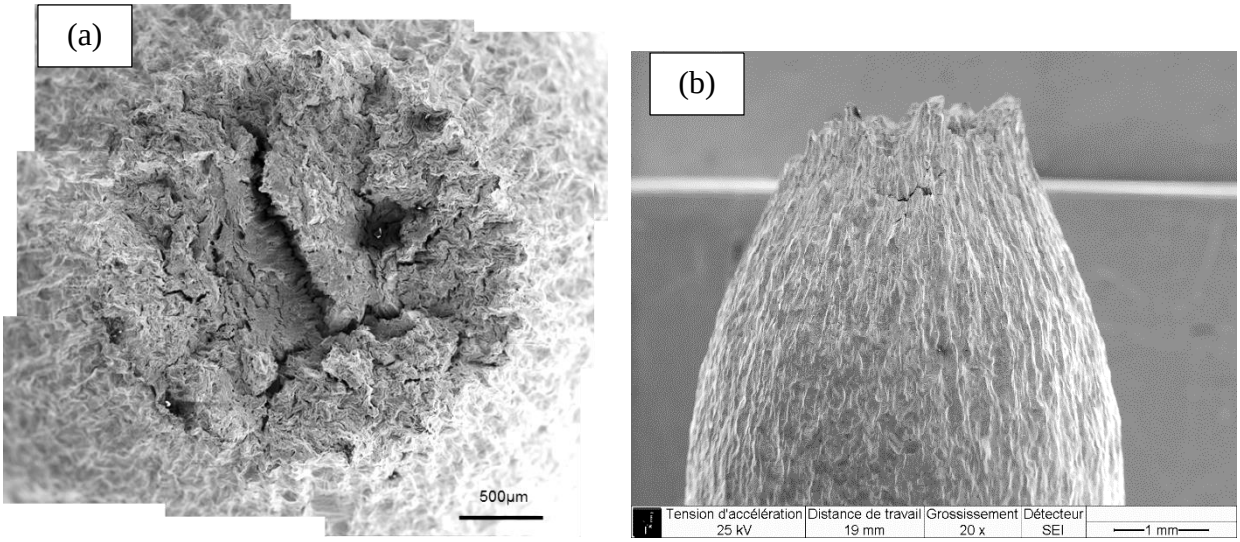

Figure 2 - 26 SEM images of the fracture surface (a) and the side view of fracture part (b) of the specimen tested under hydrogen at $d\varepsilon/dt = 5 \times 10^{-6}\ s^{-1}$ (FCS8).

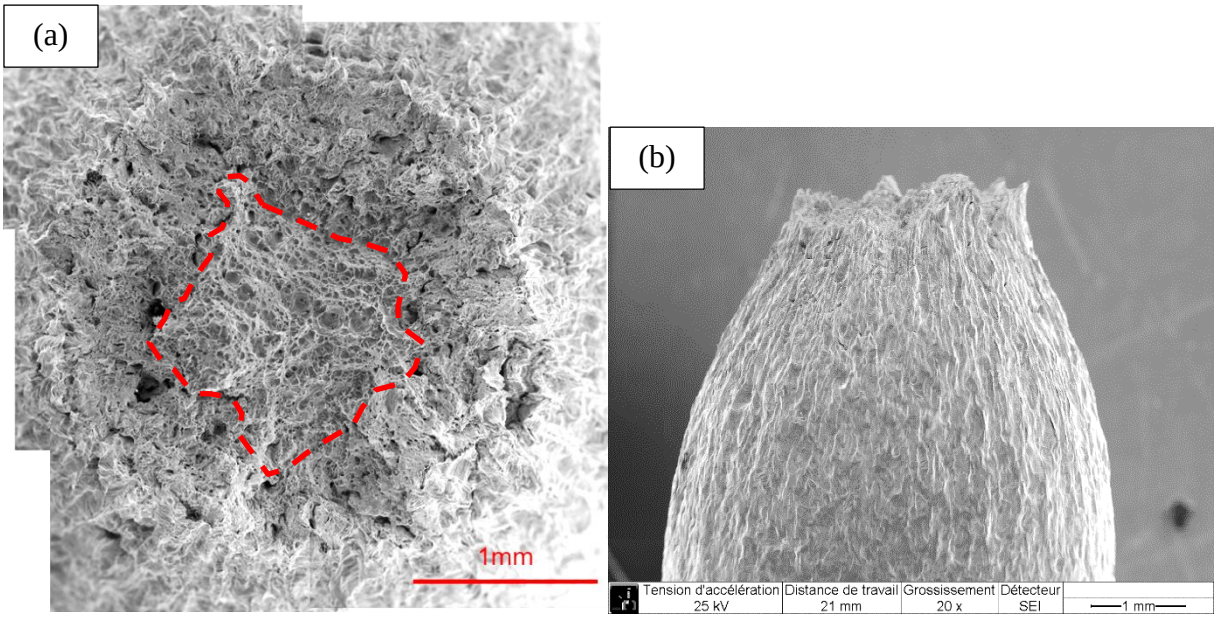

Figure 2 - 27 SEM images of the fracture surface (a) and the side view of fracture part (b) of the specimen tested under hydrogen at $d\varepsilon/dt = 5 \times 10^{-6}\ s^{-1}$ with the accidental drop of gas pressure during the test (FCS6). The area indicated by red dashed line shows the fracture surface with dimples.

A comparison of the values of *RA* in various environments and at various strain rates is shown in Figure 2 - 28. The value of *RA* in nitrogen at $d\varepsilon/dt = 5 \times 10^{-6}\ s^{-1}$ was 95 %, while the ones in hydrogen were 81 and 82 %, which are almost the same as the ones at $d\varepsilon/dt = 5 \times 10^{-5}\ s^{-1}$. Therefore, it has been revealed that the *RA* in both nitrogen and hydrogen do not change by decreasing the strain rate.

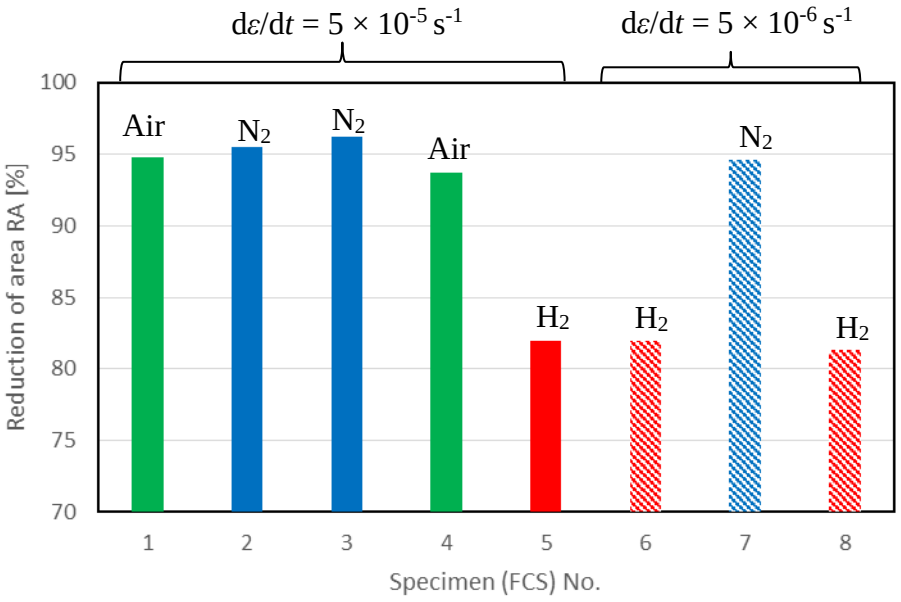

Figure 2 - 28 Comparison of reductions of area RA in various environments and at various strain rates.

2.3.6 Influence of exposure time

In this sub-section, the tensile tests under gaseous hydrogen with pre-exposure times to hydrogen atmosphere of 4, 30 and 5340 minutes (89 hours) were performed in order to investigate the influence of this parameter on hydrogen-affected tensile fracture process. The strain rate of these tests was $d\varepsilon/dt = 5 \times 10^{-5}\ s^{-1}$.

Figure 2 - 29 plots the stress-strain curves of the tensile tests under gaseous hydrogen at $d\varepsilon/dt = 5 \times 10^{-5}\ s^{-1}$ with exposure times of 4, 30 and 5340 minutes (89 hours), as well as the previous ones in air and nitrogen. This diagram has revealed that the tests with very short exposure time (4 minutes) and very long exposure time (5340 minutes) exhibit larger values of fracture elongation than the one with the medium time (30 minutes). Surprisingly, the values of fracture elongation at 4 and 5340 minutes are similar to the ones in air or nitrogen. On the other hand, no clear difference in the elastic deformation part and the tensile strength was confirmed.

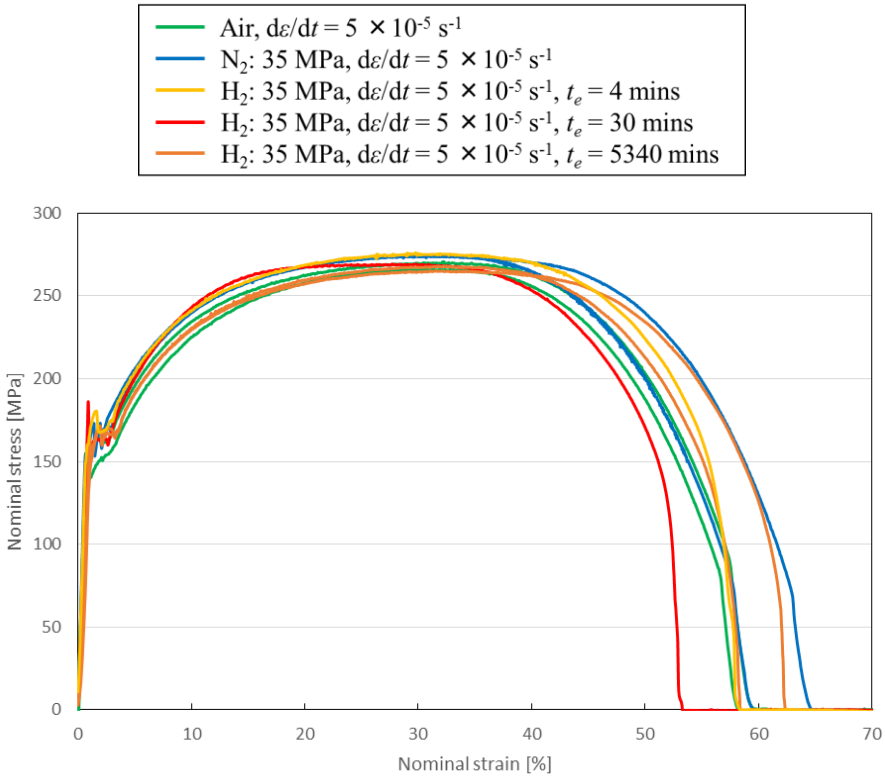

Figure 2 - 29 Stress-strain curves of tensile tests under air, nitrogen, and hydrogen at $d\varepsilon/dt = 5 \times 10^{-5}\ s^{-1}$ *with various exposure times of 4, 30 and 5340 minutes (89 hours).*

Figure 2 - 30 and Figure 2 - 31 show the SEM images of the fracture surface (a) and the side view of fracture part (b) of the specimens tested under hydrogen with t_e = 4 minutes (FCS11) and 5340 minutes (FCS9), respectively. The fracture surface of the test with t_e = 4 minutes (Figure 2 - 30a) represents a QC fracture with secondary cracks in the entire surface, even though the fracture elongation is the same level as the one in air or nitrogen. On the other hand, the fracture surface of the test with t_e = 5340 minutes (Figure 2 - 31a) represents a QC fracture in the fringe part while the center part indicated by red dashed line shows dimples, namely a ductile fracture surface.

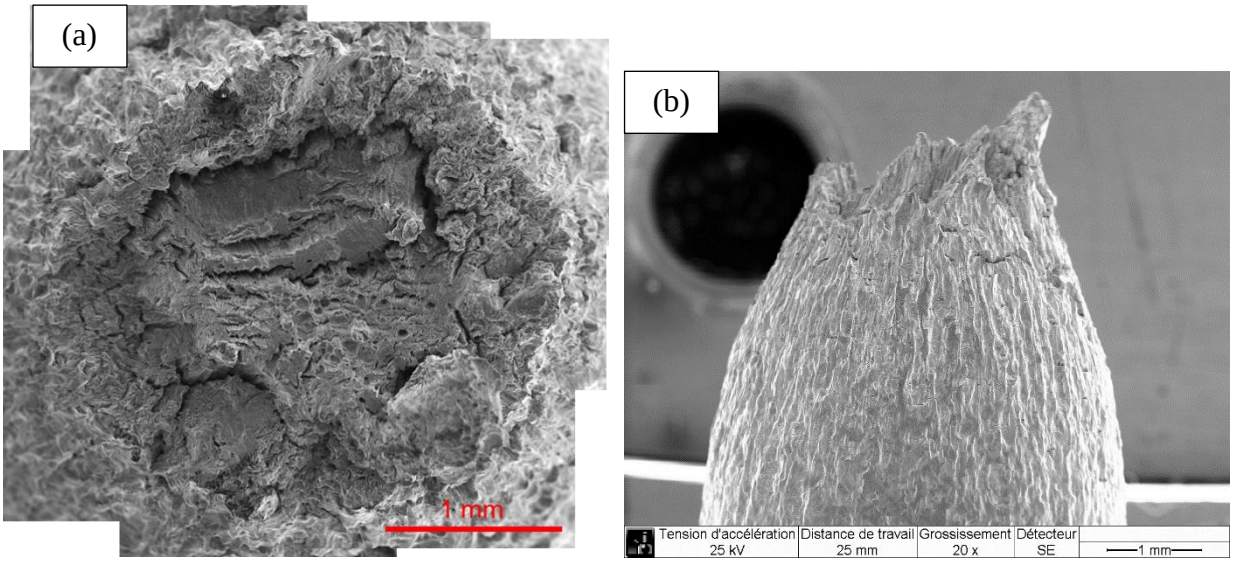

Figure 2 - 30 SEM images of the fracture surface (a) and the side view of fracture part (b) of the specimen tested under hydrogen with exposure time t_e = 4 minutes (FCS11).

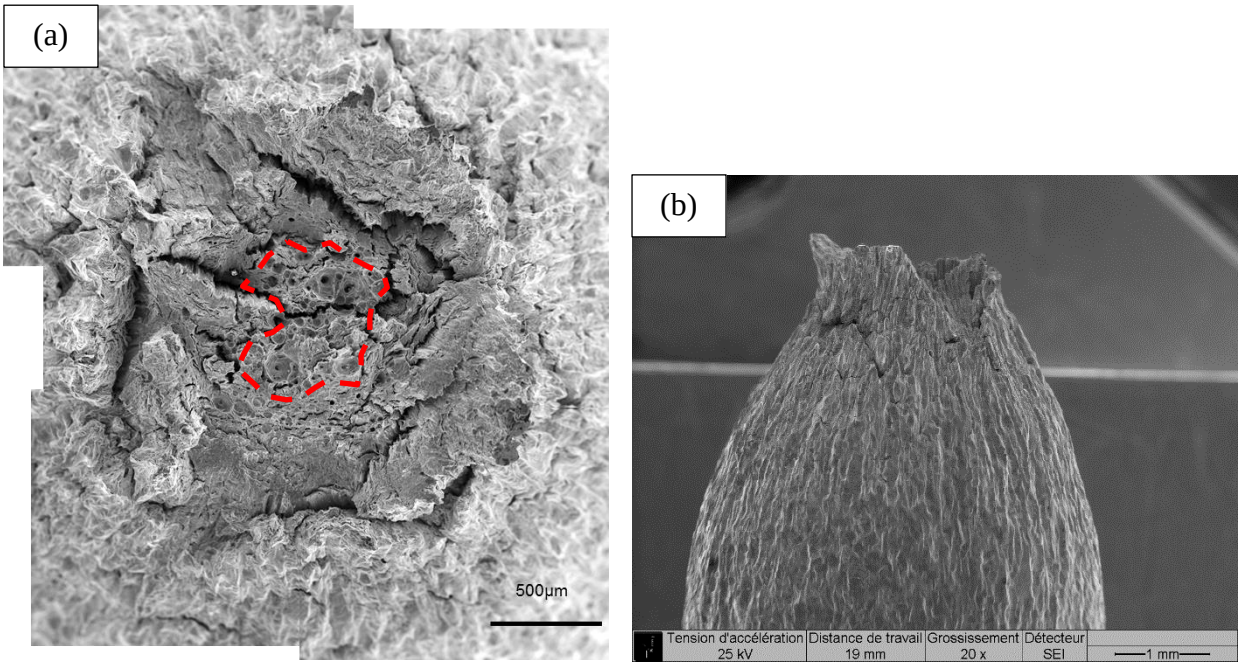

Figure 2 - 31 SEM images of the fracture surface (a) and the side view of fracture part (b) of the specimen tested under hydrogen with exposure time t_e = 5340 minutes (FCS9).

Figure 2 - 32 shows the comparison of the *RA* according to the environments, strain rates and exposure times. The value of *RA* in hydrogen at t_e = 4 minutes (FCS11) was 81 % which is the same level as the ones in hydrogen at t_e = 30 minutes. In contrast, the values of *RA* in hydrogen at t_e = 5340 minutes (FCS9 and FCS10) were 87 and 84 % which are slightly higher than the ones in hydrogen at the other exposure times. This result suggests that very long exposure time (5340 minutes) results in an increase in *RA*, i.e. a recovery of ductility. This is also confirmed by the increase in fracture elongation (Figure 2 - 29) and the presence of a ductile feature on the fracture

surface (Figure 2 - 31a) as mentioned above. However, since the difference in the RA between t_e = 4 and 5340 minutes are small (3 to 6 %), this might be an experimental dispersion. Enrichment of experimental data and further investigation on this point are required to obtain a reliable conclusion.

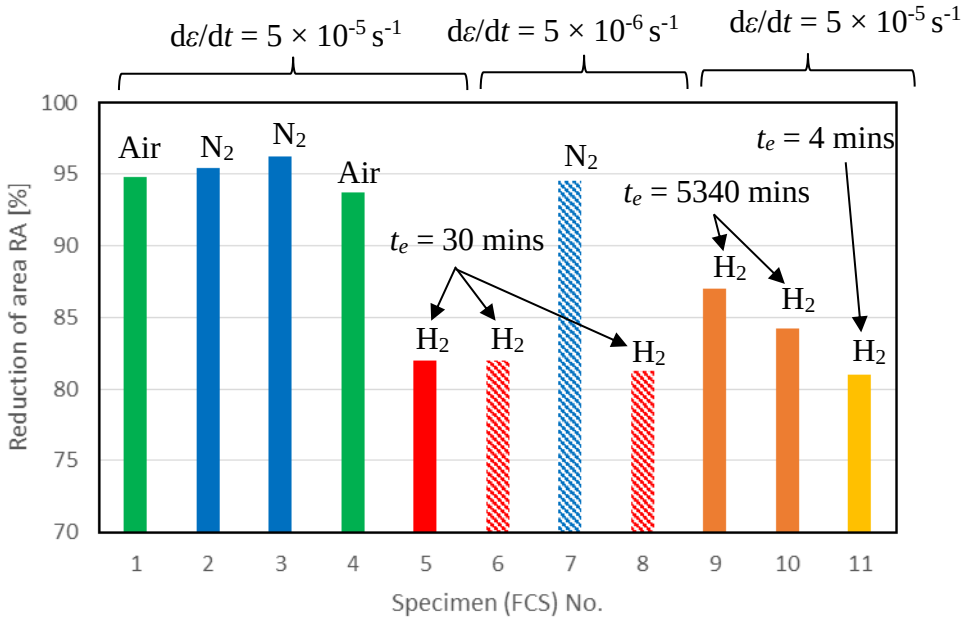

Figure 2 - 32 Comparison of reductions of area RA among various environments, strain rates and exposure times.

2.4 Discussion

In this section, based on the results of the tensile tests obtained in the previous section, the mechanism of the influence of hydrogen on the tensile fracture process in Armco iron and its dependence on strain rate and exposure time are discussed.

2.4.1 Mechanism of hydrogen-affected tensile fracture

The tensile tests under gaseous hydrogen environment exhibited lower fracture elongation and lower *RA*, compared with the ones under an inert atmosphere, i.e. air and gaseous nitrogen. Besides, gaseous hydrogen induced the change in fracture mode from a ductile void-coalescence fracture in air or nitrogen to a brittle QC fracture. This sub-section presents a discussion on the mechanism of the fracture process modification by the diffused hydrogen inside the material.

A first important result for elucidating the mechanism is that no influence of hydrogen on the uniform deformation before necking occurs (i.e. before the nominal stress reaches the maximum value) was observed. On the other hand, after necking occurs, hydrogen clearly reduces the material ductility and changes the fracture mode from ductile fracture to brittle one involving a crack propagation. This fact suggests that hydrogen may influence mainly the initiation and propagation of cracks, not a uniform deformation of the material.

Matsunaga et al. [128] argued similar assumption as above based on their results of tensile tests in a Cr-Mo steel under a hydrogen environment. To investigate this point in detail, they also conducted tensile tests with a switch of the gaseous environment from hydrogen to nitrogen, and from nitrogen to hydrogen, at the point of maximum stress during the tensile test. As a result, although no decrease in ductility was observed in the tensile test with the switch from hydrogen to nitrogen, a significant decrease in ductility was observed in the test with the switch from nitrogen to hydrogen. Therefore, they concluded that hydrogen influences the cracking process of the material after a necking occurs.

In addition, Matsunaga et al. [128] measured the number and length of the surface cracks generated on the side surface of the tensile specimen, and they compared the results between in nitrogen and in hydrogen [128]. As a result, a higher number and longer length of surface cracks were confirmed in the hydrogen compared to the ones in the nitrogen. This result is consistent with the present observations, confirming that many surface cracks initiated on the side surface of the specimen tested in hydrogen. These results suggest that hydrogen may promote both crack initiation and propagation.

Secondly, regarding the influence of hydrogen on crack initiation and propagation, Wang et al. [130] investigated the mechanism of the hydrogen effect promoting the crack initiation by the tensile tests in a pure iron under gaseous hydrogen, using specimens with a machined surface and an electropolished surface. As a result, the ductility of the machined specimen was lower than that of the electro-polished one, and many surface cracks were observed on the machined surface.

From these results, they concluded that crack initiation is promoted by hydrogen environment when a work-hardened layer exists on the specimen surface. They argued that, as hydrogen may be intensively trapped in the defects present in the work hardened layer, the difference in the hydrogen concentrations between the work-hardened layer and the bulk material underneath induces a local stress between them. The local stress in the sub-surface promotes the surface crack initiation. Since the surface of the specimen in the present study was finished by abrasive paper (# 4000) as well as the ones of Matsunaga et al [128] which were finished by buffing with a colloidal SiO_2 solution, a work-hardened layer may exist on the sub-surface in both cases. Thus, the above theory of Wang et al. [130] can also hold in both cases.

Finally, a mechanism of hydrogen effect promoting crack propagation is discussed. Matsuoka et al. [132] proposed that this mechanism follows the HESFCG model [16, 72]. Though this model was originally proposed as a model to explain the mechanism of fatigue crack propagation in a hydrogen environment, they argued that the mechanism for hydrogen-affected crack growth under tensile loading can be explained by a load-increase part of the HESFCG model. This model states that a cause of crack propagation acceleration by hydrogen is a sharpening of the crack tip which is resulted from the localization of the plastic strain near the crack tip by the HELP mechanism [132]. They also argued that the fracture mode is not a QC fracture but a shearing fracture due to localized plastic strain. As well as this theory, some researches [133–140] have evidenced that hydrogen may reduce the resistance against unstable cracking (i.e. fracture toughness, J_{IC} or K_{IC}) in metallic materials. For example, the fracture toughness tests (J_{IC} test) in a low carbon steel under gaseous hydrogen by Ogawa et al. [140] exhibited a decrease in the value of *J*-integral against crack propagation by hydrogen. In addition, Bertolino et al. [134] have revealed that the threshold of *J*-integral causing unstable fracture (J_{IC}) in zirconium alloy decreases as the amount of charged hydrogen in the material increases. Therefore, as the fracture toughness of the material is reduced by hydrogen, thus the crack propagation during the tensile fracture process may be also promoted, resulting in the reductions of the fracture elongation and *RA* values.

2.4.2 Influence of strain rate

As revealed in Section 2.3.5, the decrease in fracture elongation due to a low strain rate was observed in the tensile tests under the gaseous hydrogen. However, since the same amount of reduction of fracture elongation was also observed in gaseous nitrogen, the dependence of hydrogen effect on the strain rate was not particularly observed. Therefore, it is probable that the strain rate dependency is peculiar to the material.

On the other hand, Moro [51, 129] investigated the strain rate dependence of the high strength steel X80 by means of the tensile test under a gaseous hydrogen. Figure 2 - 33 shows the stress-strain curves of tensile tests in X80 under gaseous nitrogen and hydrogen at 300 bar (30 MPa) at various strain rates. As shown in this figure, the tests in hydrogen were carried out at various strain rates from $d\varepsilon/dt = 5.5 \times 10^{-7}$ to 0.55 s^{-1}. The lower strain rate, the lower the fracture elongation. From this result, Moro concluded that the tensile fracture process under gaseous hydrogen has a strain rate dependency.

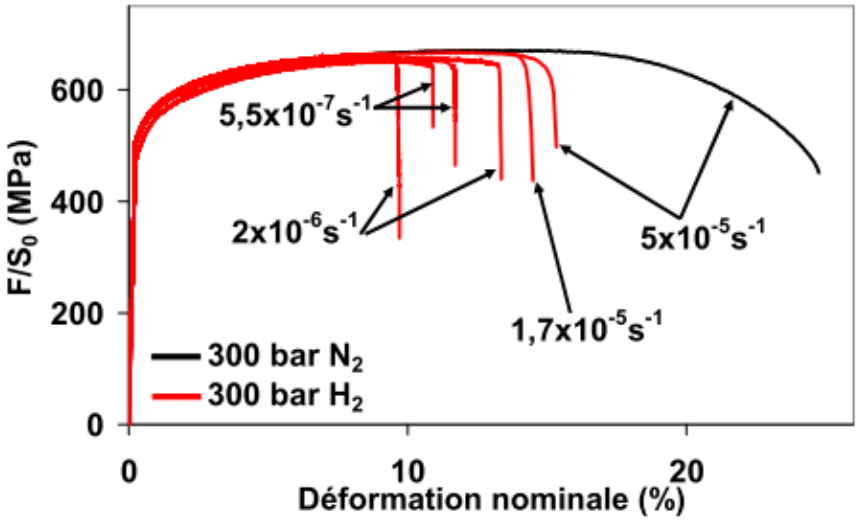

Figure 2 - 33 Stress-strain curves of tensile tests in X80 under gaseous nitrogen and hydrogen at 300 bar (30 MPa) at various strain rates by Moro [51].

In addition, Wu et al. [81] performed tensile tests in a hydrogen-charged pressure vessel steel AS508 at various strain rates to investigate the strain rate dependences of yield strength, tensile strength, and fracture elongation. The results are shown in Figure 2 - 34. As shown in this figure, the strain rate dependencies of fracture elongation and *RA* have been confirmed in the hydrogen-charged specimen, whereas these strain rate dependencies have not been observed in the hydrogen-uncharged specimen.

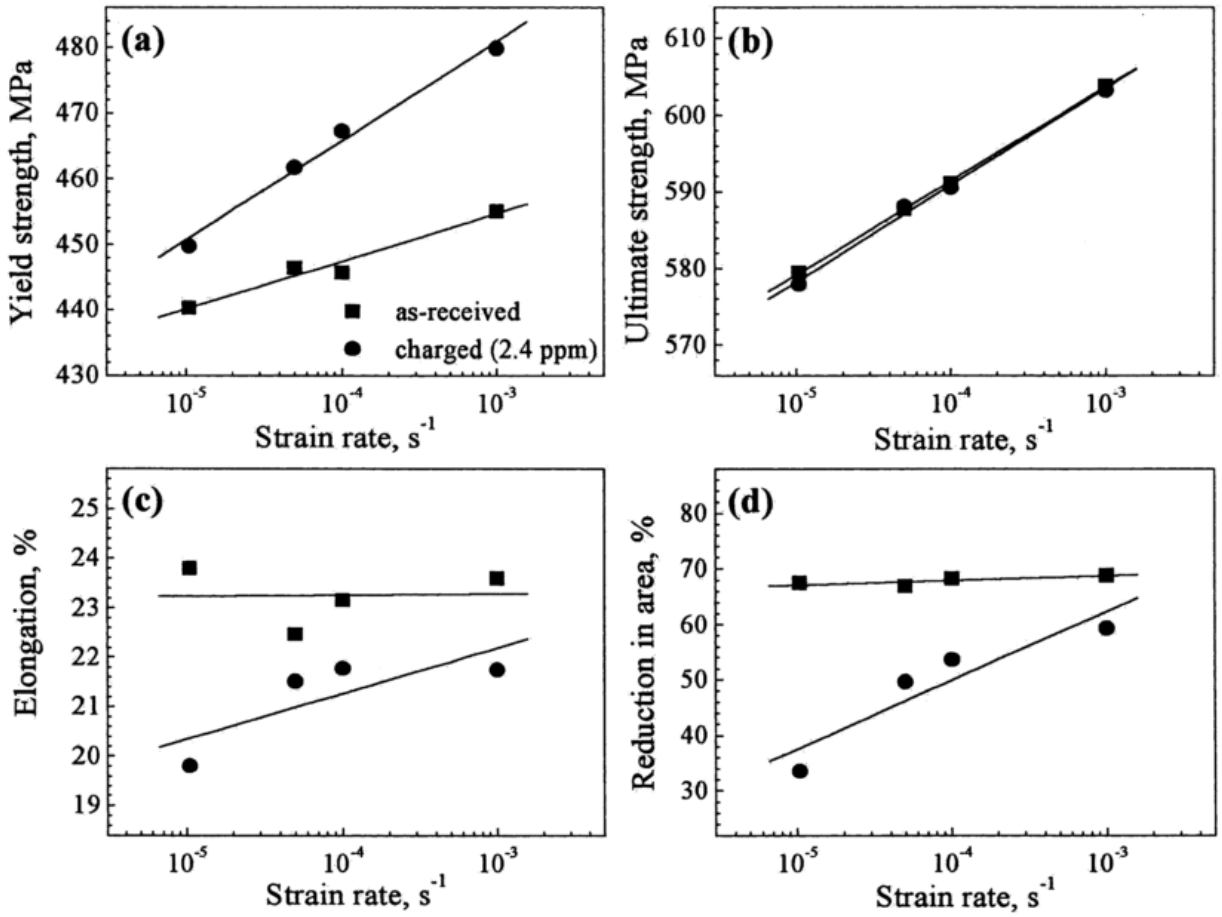

*Figure 2 - 34 Tensile properties in SA508: (a) yield strength; (b) ultimate strength; (c) elongation; (d) reduction in area as functions of strain rate by Wu et al. [*81*].*

The reason why the result of this study and the one of Wu et al. show inconsistency is possibly a difference in the composition of materials or the testing methods (in particular, the difference in the method for hydrogen introduction). This assumption has to be confirmed by further investigations.

2.4.3 Influence of exposure time

As revealed in Section 2.3.5, the fracture elongations in the tests at the short (4 minutes) and very long (5340 minutes) hydrogen exposure time were as large as in air and nitrogen. In addition, at the long hydrogen exposure time (5340 minutes), the *RA* was larger than the one at the intermediate exposure time (30 minutes), and a ductile fracture surface was observed in the central part of the fracture surface. In order to investigate the mechanism of the exposure time dependency, the hydrogen concentration inside the specimen was calculated by the following method.

Assuming the hydrogen diffusion is governed by the Fick's law, the hydrogen concentration is the solution of the following equation in cylindrical coordinates [40]:

$$\frac{\partial C_H(r,t)}{\partial t} = D\left\{\frac{\partial^2 C_H(r,t)}{\partial r^2} + \frac{1}{r}\cdot\frac{\partial C_H(r,t)}{\partial r}\right\} \qquad 2\text{ - }3$$

where C_H is the hydrogen concentration, r is the radius, t is the time and D is the diffusion coefficient of hydrogen in Armco iron. Euler method [141] was used to solve discretely this equation. By Euler method, the hydrogen concentration C_H is expressed as:

$$\begin{aligned} C_H(r,t) = C_H(r,t-\Delta t) + D\cdot\Delta t \\ \cdot\left\{\frac{C_H(r+2\Delta r) - 2C_H(r) + C_H(r+2\Delta r)}{\Delta r^2} + \frac{1}{r}\right. \\ \left.\cdot\frac{C_H(r+\Delta r) - C_H(r-\Delta r)}{\Delta r}\right\}_{t-\Delta t} \end{aligned} \qquad 2\text{ - }4$$

This discrete equation can be solved numerically. The calculation was performed using Microsoft Excel®. The radius step Δr was 0.05 mm and the time step Δt was 10 seconds. The value of D was 2.5×10^{-10} m^2/s, which was determined by a permeation test on the undeformed Armco iron performed by Bilotta [27]. The hydrogen concentration ratio C_H / C_s was calculated, where C_s is the saturated hydrogen concentration at the surface. The boundary condition for the calculation is C_H / C_s = 1 at r = 3 mm (at the surface). It has to be noted that this estimation ignores many factors affecting the hydrogen diffusion, in particular, the effect of plastic strain and of hydrostatic stress. Even though, this estimation provides an order of hydrogen concentration in the material to allow us to consider a relationship between exposure time and hydrogen effect.

Table 2 - 7 shows the test durations (when the test starts, when the nominal stress reaches the maximum value and when the test finishes) of each test under hydrogen with various conditions. Since the hydrogen likely affects the fracture process after the necking occurs as mentioned in Sub-section 2.3.1, it is important to estimate the hydrogen concentration when the stress reaches the maximum stress as well as the one before the test starts. Therefore, the hydrogen distribution in the specimen was calculated corresponding to the times t = 4, 30, 100, 120 and 333 minutes.

The calculation results of hydrogen distribution in the specimen are shown in Figure 2 - 35. The evolution of hydrogen concentration C_H / C_s by increasing the exposure time can be seen in this figure. At t = 4 minutes, the hydrogen diffuses less than 1 mm in the depth from the surface. At t = 30 minutes, the hydrogen diffusion reaches the depth of about 2.5 mm. At t = 100 or 120 minutes, the hydrogen concentration at the center of specimen (r = 0 mm) becomes about 40 - 50 % of the saturated concentration (C_s). At t = 333 minutes, the hydrogen concentration almost saturates in the entire part of the specimen. Therefore, it can be considered that the hydrogen concentration in the specimen after t = 333 minutes is saturated.

Table 2 - 7 Exposure durations of the tests under hydrogen when the test starts, when the nominal stress reaches to the maximum value and when the test finishes.

FCS	Test conditions	Before starting the test [mins]	At maximum stress point (necking starts) [mins]	End of test (total duration) [mins]
5	P_{H2} = 35MPa, t_e = 30 mins, $d\varepsilon/dt = 5x10^{-5}$ s^{-1}	30	120	210
6, 8	P_{H2} = 35MPa, t_e = 30 mins, $d\varepsilon/dt = 5x10^{-6}$ s^{-1}	30	750	1630
9, 10	P_{H2} = 35MPa, t_e = 5340 mins, $d\varepsilon/dt = 5x10^{-5}$ s^{-1}	5340	5430	5550
11	P_{H2} = 35MPa, t_e = 4 mins, $d\varepsilon/dt = 5x10^{-5}$ s^{-1}	4	100	200

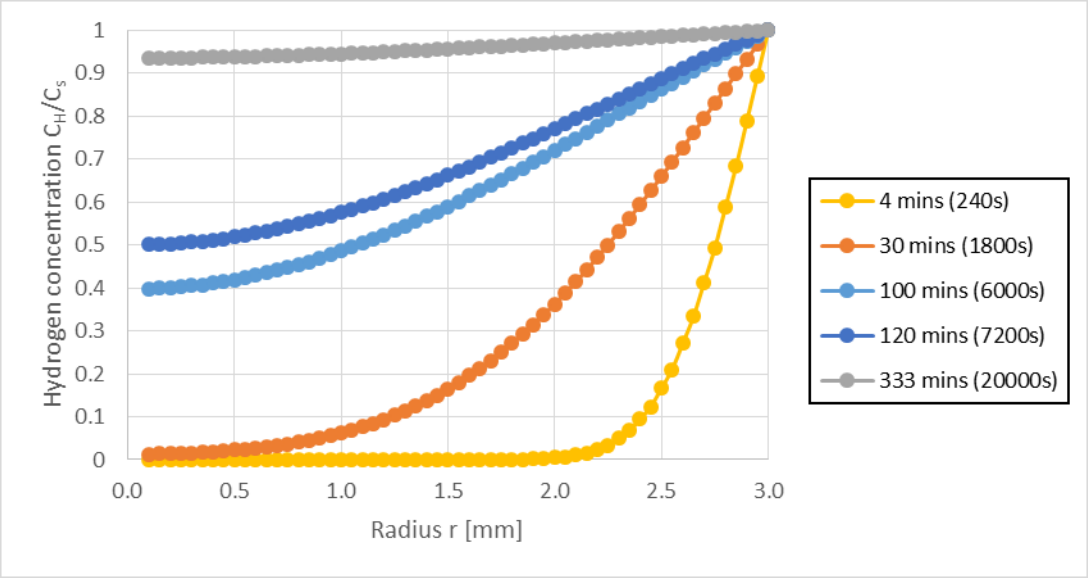

Figure 2 - 35 Hydrogen distribution in the cylindrical specimen in Armco iron after various durations of exposure to hydrogen gas environment.

In comparison between the tests with t_e = 4 and 30 minutes, even though the initial hydrogen concentrations when the tests start are very different, the hydrogen concentrations when necking starts (t = 100 and 120 minutes) are not so different. The result that both tests with t_e = 4 and 30 minutes exhibits the same level of reduction of *RA* can be understood in terms of the same level of hydrogen concentration after the necking starts (t = 100 and 120 minutes).

In the case of t_e = 5340 minutes, the hydrogen concentration is completely saturated when the tensile test starts. Though the specimen contains a high amount of hydrogen, this test exhibited a higher value of *RA*, i.e. less embrittlement by hydrogen, compared to the ones with t_e = 4 or 30 minutes. This result seems contradicting a conventional understanding that higher hydrogen

concentration (i.e. higher hydrogen gas pressure [137] or higher charging current [52]) always result in more significant hydrogen embrittlement. This reduction of hydrogen effect due to very long exposure time may be explained in terms of a gradient of hydrogen concentration in the material. Yoshikawa et al. [142, 143] found that, by means of a fatigue crack propagation test in a low carbon steel under hydrogen gas environment, the FCGR enhancement by hydrogen does not occur if a gradient of hydrogen concentration ahead of the crack tip is smaller than a certain value. This finding suggests that the gradient of hydrogen concentration is an important factor for the hydrogen embrittlement effect. Therefore, less effect of hydrogen embrittlement in the present case of t_e = 5340 minutes might be interpreted by its saturated hydrogen concentration exhibiting a very small gradient. This point is revisited in Chapter 5.

The hydrogen concentration inside the specimen is also affected by hydrogen gas pressure. An influence of hydrogen gas pressure has not been investigated in this study, but it has to be investigated in the future. Nanninga et al. [131] have reported that the hydrogen embrittlement effect is enhanced by increasing hydrogen gas pressure in pipeline steels.

2.5 Conclusion

In this chapter, the material properties of Armco iron have been identified. And then, the tensile deformation and fracture behaviors in Armco iron under high pressure gaseous hydrogen (35 MPa) have been investigated aiming to clarify the influence of hydrogen on plasticity of the material. In addition, the influence of the test parameters, the strain rate and the exposure time were characterized. The main conclusions are summarized below.

1. Elastic deformation (i.e. Young's modulus) and uniform plastic deformation before necking occurs (i.e. yield strength and tensile strength) are not influenced by hydrogen.
2. Fracture elongation and a reduction of area (*RA*) are decreased by about 10 % due to the presence of hydrogen.
3. Hydrogen clearly changes a fracture mechanism from ductile voids-coalescence fracture to brittle QC fracture with many surface cracks and secondary ones.
4. Fracture elongation (but not *RA*) decreases by decreasing strain rate from $d\varepsilon/dt = 5 \times 10^{-5}\ s^{-1}$ to $5 \times 10^{-6}\ s^{-1}$ in both hydrogen and nitrogen. This strain rate dependency is likely peculiar to the material, not the influence of hydrogen.
5. Fracture elongation at short (4 minutes) and very long (5340 minutes) hydrogen exposure time were as large as in air and nitrogen. And, the *RA* at long hydrogen exposure time (5340 minutes) was larger than the one at the intermediate exposure time (30 minutes), and a ductile fracture surface was observed in the central part of the fracture surface. This suggests that the saturated hydrogen concentration does not induce the intense hydrogen embrittlement effect despite of the high hydrogen amount inside the specimen.

There are two noteworthy insights obtained in this chapter which are important for considering an influence of hydrogen on FCG. First one is that the hydrogen does not influence uniform deformation behavior of the material, while it does influence the cracking process during the necking deformation. This interesting fact points out that the hydrogen effect on crack propagation

is a core issue of hydrogen embrittlement, and this emphasizes the importance of the investigation of hydrogen effect on crack propagation. Another one is that a saturated hydrogen concentration does not necessarily cause a severe hydrogen embrittlement effect. In contrast the importance of a hydrogen gradient for hydrogen effect on crack propagation has been evidenced. This will be related to the later discussion about the issue of the onset of hydrogen effect on FCG.

Chapter 3

Analysis of influence of gaseous hydrogen on fatigue crack propagation

Résumé

Chapitre 3: Analyse de l'influence de l'hydrogène gazeux sur la propagation des fissures de fatigue

R-3.1 Introduction

Au chapitre 3, les propriétés de propagation des fissures de fatigue sous l'influence de l'hydrogène ont été étudiées en effectuant des essais de fissuration sous hydrogène gazeux. L'influence de l'hydrogène sur la vitesse de propagation des fissures de fatigue et le mode de rupture ont été examinés. De plus, la propagation de fissures de fatigue affectées par l'hydrogène a été analysée en fonction du facteur d'intensité de contrainte ΔK, de la pression de l'hydrogène P_{H2} et de la fréquence de chargement f.

R-3.2 Résultat des essais de fissuration

La Figure R - 2 montre la vitesse de propagation des fissures de fatigue en fonction de ΔK. La vitesse de propagation de fissure de fatigue affectée par l'hydrogène présente trois régimes distincts: (a) un régime non accéléré à de faibles valeurs de ΔK, (b) un régime de transition et (c) un régime accéléré à des valeurs de ΔK élevées indiquant l'augmentation de la vitesse de propagation des fissures de fatigue jusqu'à 50 fois supérieure à celle dans l'air.

En régime non accéléré, la vitesse de propagation des fissures de fatigue dans l'hydrogène est presque la même que celle dans l'air. Le mode de rupture dans l'hydrogène est une rupture intergranulaire fragile, alors qu'elle est transgranulaire sous air à la même valeur ΔK De plus, des marquages plastiques en forme de bande ont été observés sur les facettes intergranulaires.

Dans le régime de transition, le mode de rupture passe progressivement d'une rupture intergranulaire à une rupture transgranulaire QC, alors que la vitesse de propagation de la fissure de fatigue affectée par l'hydrogène augmente fortement. Lorsque la vitesse de propagation des fissures de fatigue atteint une certaine amplitude, la pente de la courbe de vitesse de propagation des fissures de fatigue affectée par l'hydrogène revient au même niveau que dans l'air (régime accéléré). En régime accéléré, la surface de rupture est de type QC avec présence de stries « fragiles ».

La valeur de ΔK_{tr} (valeur minimale de ΔK déclenchant l'augmentation de la vitesse de propagation des fissures de fatigue (c'est-à-dire le régime de transition)) diminue lorsque la pression d'hydrogène augmente.

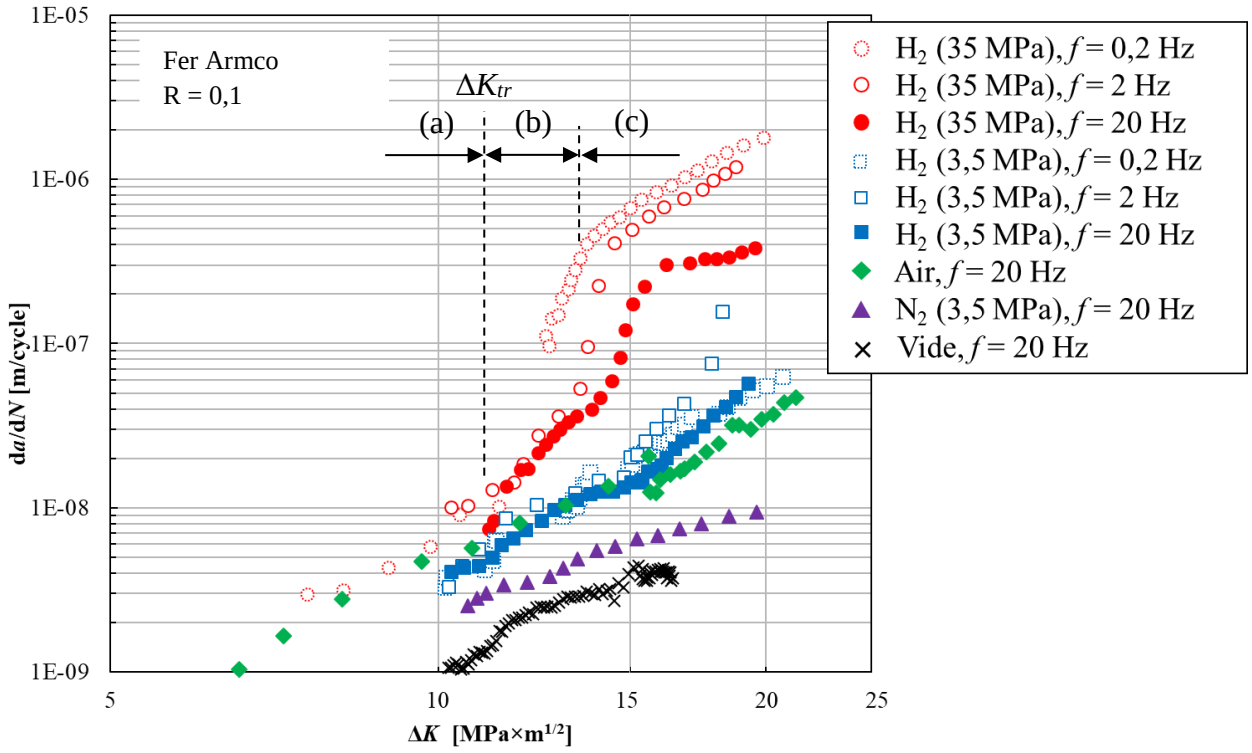

Figure R - 2 Vitesse de propagation des fissures de fatigue en fonction de ΔK à f = 0,2, 2 et 20 Hz sous hydrogène gazeux à P_{H2} = 3,5 et 35 MPa, et essais en milieu inerte.

De plus, la vitesse de propagation augmente lorsque la fréquence de chargement diminue jusqu'à une valeur critique fonction de la pression d'hydrogène gazeux (2 Hz pour P_{H2} = 3,5 MPa et 0,2 Hz pour P_{H2} = 35 MPa).

Une fois que la fréquence de chargement devient inférieure à la valeur critique, la vitesse de propagation diminue de manière significative jusqu'au même niveau que dans l'azote. Le mode de rupture change également avec une atténuation de la vitesse de propagation à faible *f*.

Même si le changement significatif du mode de rupture associé à l'augmentation de la vitesse de propagation des fissures de fatigue a été révélé, le mécanisme de cet effet de l'hydrogène nécessite davantage d'investigations. Etant donné que l'interaction entre l'hydrogène et la plasticité en pointe de fissure doit être un facteur clé pour comprendre le mécanisme de propagation, cette plasticité sera examinée au chapitre 4.

----------(Fin du résumé)----------

3.1 Introduction

In the previous chapter, the influences of gaseous hydrogen on the plasticity and the tensile fracture process in Armco iron have been revealed. The obtained insights include some interesting facts such as: the hydrogen does not influence uniform deformation behavior of Armco iron, but it does influence the unstable crack propagation; and a saturated hydrogen concentration does not cause a severe hydrogen embrittlement effect. These facts might have important implications for an interaction between gaseous hydrogen and fatigue crack propagation. This subject is thus treated in this chapter.

This chapter presents the results of Fatigue Crack Growth (FCG) tests in Armco iron under gaseous hydrogen, in order to analyze the influence of gaseous hydrogen on fatigue crack propagation properties (Fatigue Crack Growth Rate (FCGR) and fracture mode) of the material. Specifically, the stress intensity factor range ΔK, the hydrogen gas pressure P_{H2} and the loading frequency f are controlled as influential parameters. The FCG behavior is analyzed as a function of these three parameters.

3.2 Experimental method

3.2.1 Test procedure

The FCG test was conducted according to the standard ASTM E647 [144]. This standard provides an experimental procedure to determine a fatigue crack growth rate (FCGR).

The type of test specimen used for the present FCG tests was a Compact Tension (CT) specimen. According to ASTM E647, the dimension of the CT specimen is determined from width W and thickness B as shown in Figure 3 - 1.

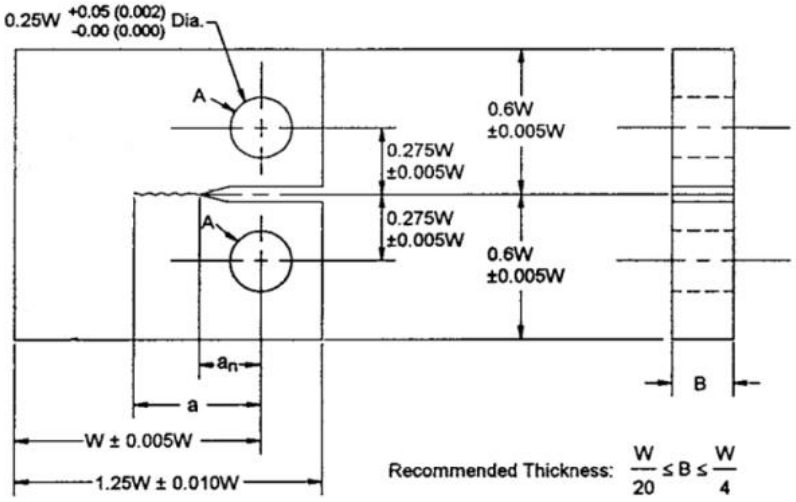

Figure 3 - 1 Dimension of CT specimen determined from width W and thickness B defined by ASTM E647[144].

In this study, the dimensions W = 40 mm and B = 8 mm were selected: they are compatible with the inner dimension of the Hycomat test bench (described in the previous chapter) used for testing at high hydrogen gas pressures and similar to the test pieces used by Bilotta [27].

The fatigue crack growth rate (FCGR) is expressed in length unit per cycle or length unit per second. The value of ΔK is calculated from the applied loading, the dimensions of the specimen, and the current crack length as [144]:

$$\Delta K = \frac{\Delta F}{B\sqrt{W}} * \alpha \qquad 3 - 1$$

where α is a function of a/W which is valid if $a/W \geq 0.2$. α is expressed as:

$$\alpha = \frac{(2 + a/W)}{(1 - a/W)^{\frac{3}{2}}}(0.886 + 4.64\,a/W - 13.32(a/w)^2 + 14.72(a/w)^3 - 5.6(a/w)^4) \qquad 3 - 2$$

where a is a distance between the crack tip and the loading axis. The standard thus enables us to obtain the FCGR, da/dN (where N is a number of cycle) as a function of ΔK which is independent of the geometry of specimen. However, in order to obtain a valid result according to this test method, it is required to meet the "small-scale yielding" condition of linear elasticity at all values of applied loading. Because of this reason, the length of the specimen's uncracked ligament (W - a) has to satisfy the following condition:

$$(W - a) \geq \left(\frac{4}{\pi}\right)\left(\frac{K_{max}}{\sigma_y}\right)^2 \qquad 3 - 3$$

where K_{max} is the maximum stress intensity factor.

All the CT specimens used for the test were taken from the L-T plane of the rolled plate after the heat treatment as mentioned in Sub-section 2.2.2. The crack propagation direction is perpendicular to the rolling direction (L direction). The surface of specimens was polished with emery papers from # 180 to # 4000. After this, the surface was finished by buffing with a diamond solution of the grade 1 μm in order to have a mirror finishing (very low surface roughness).

The FCG tests under various gaseous environments were conducted using the Hycomat test bench (as explained in Sub-section 2.3.1.2). The CT specimen was held by the special grip inside the gas chamber as shown in Figure 3 - 2. The strain gauge for a crack closure measurement was attached to the left side surface of the specimen. The four cables for the crack length measurement (explained below) were attached to the right side of the specimen. The FCG tests were performed by controlling the applied load. A computer system was used to pilot the test and acquire the data in an automated way with Instron's WaveMatrix® or ACG® (Advanced Crack Growth) software.

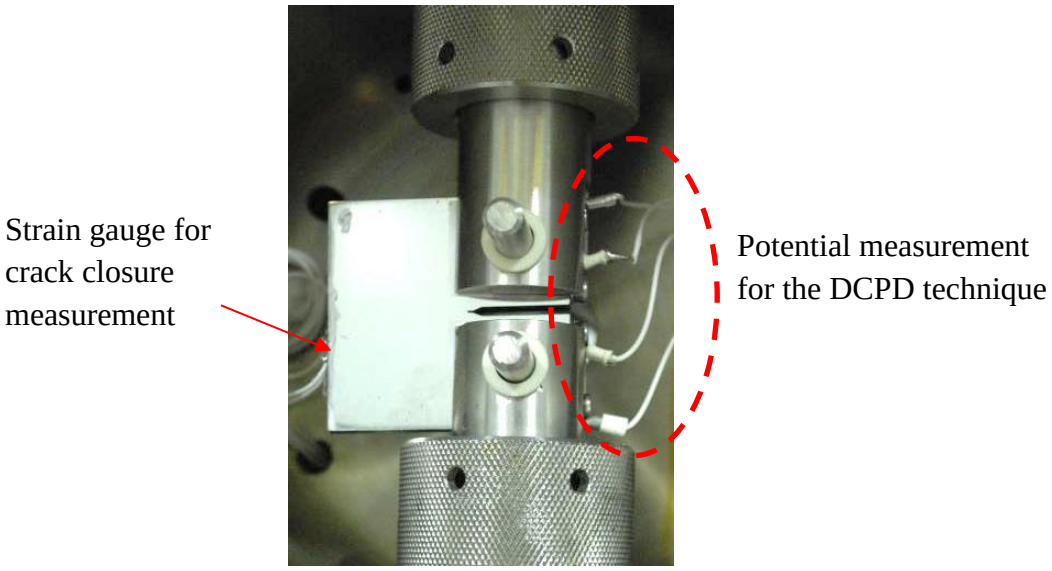

Figure 3 - 2 CT specimen placed in the gas chamber of the Hycomat test bench. Strain gauge for crack closure measurement is attached to the back surface (left side) of the specimen. Four cables for a Direct Current Potential Drop (DCPD) technique are attached to the front surface (right side) of the specimen.

Before starting the FCG test, the specimen has been pre-cracked in order to avoid influences of the dimension of the notch and of the work-hardened layer on the FCGR data. The pre-cracking was carried out in air at room temperature. The pre-crack length was ensured to be longer than 1 mm in order to avoid the above-mentioned influences and to have an initial a/W ratio of about 0.3 for satisfying the validity range $0.3 \leq a/W \leq 0.7$, defined by the standard [144].

3.2.2 Crack length measurement

The crack length during the FCG test was measured by the following two methods: a direct optical measurement and a Direct Current Potential Drop (DCPD) technique.

For the direct optical measurement, the surface of the CT specimen was directly observed by using a Questar-type long-range microscope through the window of the door as shown in Figure 3 - 3a. Figure 3 - 3b shows an example of an optical image of the crack tip taken by this method. The direct optical measurement of crack length can measure precisely the crack length. However, the test has to be stopped at each measurement which cannot be automatized.

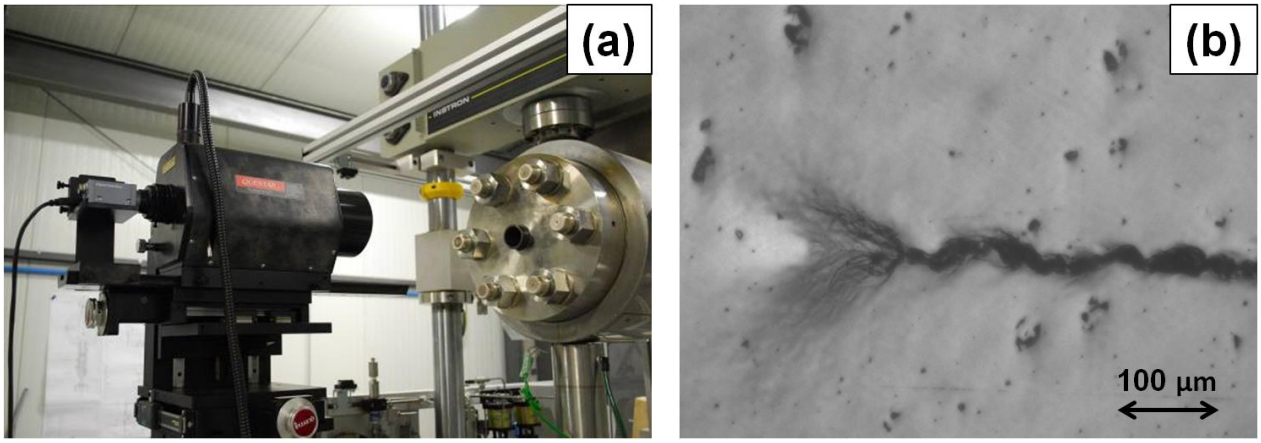

Figure 3 - 3 Questar-type long-range microscope installed in front of the window of the door (a) and optical tracking of the crack path (b).

On the other hand, the DCPD technique [144] is a method to measure the crack length by passing an electric current through the specimen and measuring a variation of potential difference due to the crack propagation. For the potential measurement, the four cables are fixed on the front surface, on both sides of the crack (Figure 3 - 2). The advantage of this method is that the measurement can be automatized, so that the test can be continued without stopping, allowing to optimize the testing time.

For using the DCPD technique, the relationship between the crack length *a/W* and the relative variation of potential difference V/V_0 (V: current potential, V_0: initial potential at the end of the pre-cracking) was determined. The polynomial function of this relationship in Armco iron was obtained experimentally by Bilotta [27] as:

$$\frac{a}{W} = -0.8782\left(\frac{V}{V_0}\right)^4 + 4.9753\left(\frac{V}{V_0}\right)^3 - 10.771\left(\frac{V}{V_0}\right)^2 + 11.091\left(\frac{V}{V_0}\right) - 4.1322 \qquad 3 - 4$$

This polynomial function was used for the determination of the crack length from the measured potential values during the test. Since all the FCG tests were conducted at a stress ratio of $R = \sigma_{min}/\sigma_{max} = 0.1$ (where σ_{min} is the minimum stress and σ_{min} is the maximum stress), a crack closure may occur when the loading is close to the minimum value. During the crack closure, both sides of fracture surface come into contact. Because of this, the potential value varies a lot while a loading cycle. In order to avoid this problem and obtain the proper potential when the crack mouth is opened at the maximum loading, the potential measurement was synchronized with the loading cycle.

The crack length calculated by the DCPD technique $(a/W)_{pot}$ was corrected by the final crack length optically measured $(a/W)_{opt,fin}$ as:

$$\left(\frac{a}{W}\right)_{mod} = \left(\frac{a}{W}\right)_{pot} + \left\{\left(\frac{a}{W}\right)_{opt,fin} - \left(\frac{a}{W}\right)_{pot,fin}\right\} \times \left\{\left(\frac{a}{W}\right)_{pot} - \left(\frac{a}{W}\right)_{ini}\right\} \Big/ \left\{\left(\frac{a}{W}\right)_{opt,fin} - \left(\frac{a}{W}\right)_{ini}\right\} \quad 3 - 5$$

where, $(a/W)_{mod}$ is the modified crack length, $(a/W)_{pot,fin}$ is the final crack length measured by the DCPD technique, $(a/W)_{ini}$ is the initial crack length (the pre-crack length). This correction aims at taking into account the influence of the plastic deformation at the crack tip on the drift of potential value.

3.2.3 Testing conditions

The waveform of applied cyclic loading was a sinusoidal tension-tension type with a stress ratio R of 0.1. Since Armco iron is a very ductile material with a relatively low yield strength, the plastic deformation generated at the crack tip is large. A low stress ratio is appropriate to avoid having too much extent of the monotonic plastic deformed zone in the uncracked ligament. However, a low stress ratio may cause a problem of crack closure.

The crack closure is the phenomenon by which the two fracture surfaces come into contact around the minimum loading of cyclic loading. Elber [145] has highlighted this phenomenon and proposed a hypothesis that the effective cyclic loading contributing the crack propagation is a part of loading only when both crack mouth and crack path are opened. Consequently, the effective stress intensity factor range ΔK_{eff} is less than the applied one ΔK. ΔK_{eff} can be calculated as the difference between the maximum value K_{max} and the value of K at crack mouth opening, i.e. K_{op}: $\Delta K_{eff} = K_{max} - K_{op}$. Elber has demonstrated that the influence of the loading ratio on the FCGR can be eliminated by using ΔK_{eff}.

Pippan [146, 147] has studied the fatigue crack propagation near the threshold value of ΔK in Armco iron under various atmospheres. As a result, the crack closure effect at R = 0.1 was different between in air and in high vacuum near the threshold value of ΔK, while it was almost the same at higher values of ΔK. This result suggests that, as long as in the range of ΔK higher than the threshold value, the difference in FCGRs between in air and in vacuum does not change by considering the nominal value ΔK or the actual value ΔK_{eff}. This fact was confirmed in Armco iron by Bilotta [27].

Since this study is aimed to study the FCG behavior in the medium and high ΔK ranges under only one condition of stress ratio (R = 0.1, thus no comparison between different stress ratios), the crack closure behavior was not considered in this study. All the FCGR data in this study is indicated by ΔK. Today the influence of hydrogen on the crack closure is not clear, and it must be investigated in the future.

The FCG tests were performed under ΔK-increasing and ΔK-constant conditions. A ΔK-increasing FCG test is a FCG test by keeping a load amplitude at a constant, thus the ΔK value gradually increases by an increase in crack length. In the ΔK-increasing FCG tests in this study, the applied loading was occasionally increased to optimize the testing time. The ΔK-increasing FCG test is a method to investigate the FCGR for a certain range of ΔK (7 – 20 MPa$\times$m$^{1/2}$ in this study) at a fixed testing condition (ex. P_{H2} and f).

On the other hand, the ΔK-constant FCG test is the FCG test by controlling (gradually decreasing) the applied loading to maintain ΔK at a constant value. In this study, the applied loading was manually controlled as follows. The tests were regularly stopped, and the crack length was optically measured during the test. And then, the loading amplitude was modified to maintain the ΔK within the range of 20 ± 0.5 MPa$\times$m$^{1/2}$. The ΔK-constant FCG test enables us to investigate the FCGR at fixed ΔK for several test conditions by using one specimen. This test method is especially useful to obtain the FCGR at very low loading frequency by a reasonable testing time because the crack at one condition needs to propagate for a short distance (ex. 1 mm).

For the ΔK-increasing FCG tests, the applied gaseous environments were air, vacuum (at the pressure of 5×10^{-5} mbar), and gaseous nitrogen at the gas pressure P_{N2} = 3.5 MPa as an inert environment for reference data, as well as gaseous hydrogen at P_{H2} = 3.5 and 35 MPa. The tests under air and vacuum were conducted by using a hydraulic fatigue testing machine, Instron8800. The tests under nitrogen and hydrogen were conducted by using the Hycomat test bench. The applied loading frequencies were f = 0.2, 2, and 20 Hz. The crack length was measured by the DCPD technique with the aforementioned correction. The results of most of the ΔK-increasing FCG tests (except the test at P_{H2} = 3.5 MPa, f = 0.2 Hz) were obtained by Bilotta in his doctoral thesis [27].

For the ΔK-constant FCG tests, the applied environments were gaseous nitrogen at P_{N2} = 3.5 MPa and gaseous hydrogen at P_{H2} = 3.5 and 35 MPa. The applied loading frequencies were f = 0.02 Hz as well as 0.2, 2, and 20 Hz. Each step with one loading frequency was performed in the order of 20, 2, 0.2, and 0.02 Hz as shown in Figure 3 - 4. For each step, the crack was propagated longer than 1 mm at least. All the ΔK-constant FCG tests were conducted by using the Hycomat test bench. The crack length was measured by the direct optical measurement.

After the FCG tests, in order to investigate the fracture mode, the fracture surface of tested specimens was observed by means of SEM.

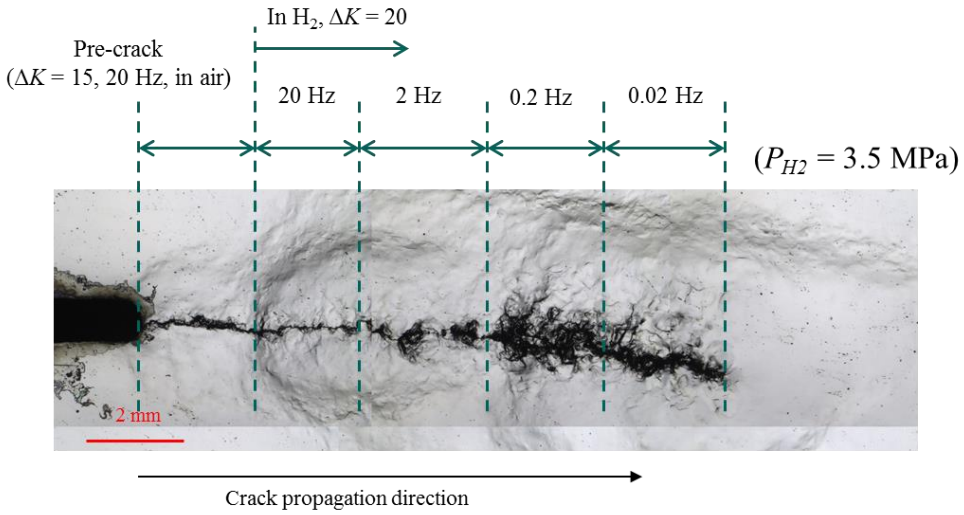

Figure 3 - 4 Example of the crack appearance for a ΔK-constant FCG test (P_{H2} = 3.5 MPa) with the indication of the test steps.

3.3 Δ*K*-increasing FCG test

3.3.1 Tests under air, nitrogen, and vacuum

The FCG tests in air, nitrogen (P_{N2} = 3.5 MPa), and vacuum were performed to obtain reference data of FCGR in Armco iron. The obtained FCGRs (= d*a*/d*N*) are shown in Figure 3 - 5. The indicated FCGR curve in air is composed of the results of two different specimens tested for a different range of Δ*K* (the boundary is indicated by (*)). As shown in this figure, most of FCGR curves in all the three environments exhibit a linear relationship (in a bi-logarithmic plot) of FCGR (da/dN [m/cycle]) vs. Δ*K* [MPa×m$^{1/2}$] thus being governed by Paris law [148]. The slopes of FCGRs in the three environments are almost the same, indicating that the presence of oxygen and water vapor does not clearly change the fracture mechanism. In a comparison of FCGRs among the environments, the values of FCGR is higher in air, then in nitrogen, and then in vacuum. The FCGR in air is about 5 times higher than that in vacuum. These values of FCGRs agrees well with the result in Armco iron under air and vacuum obtained by Pippan [147].

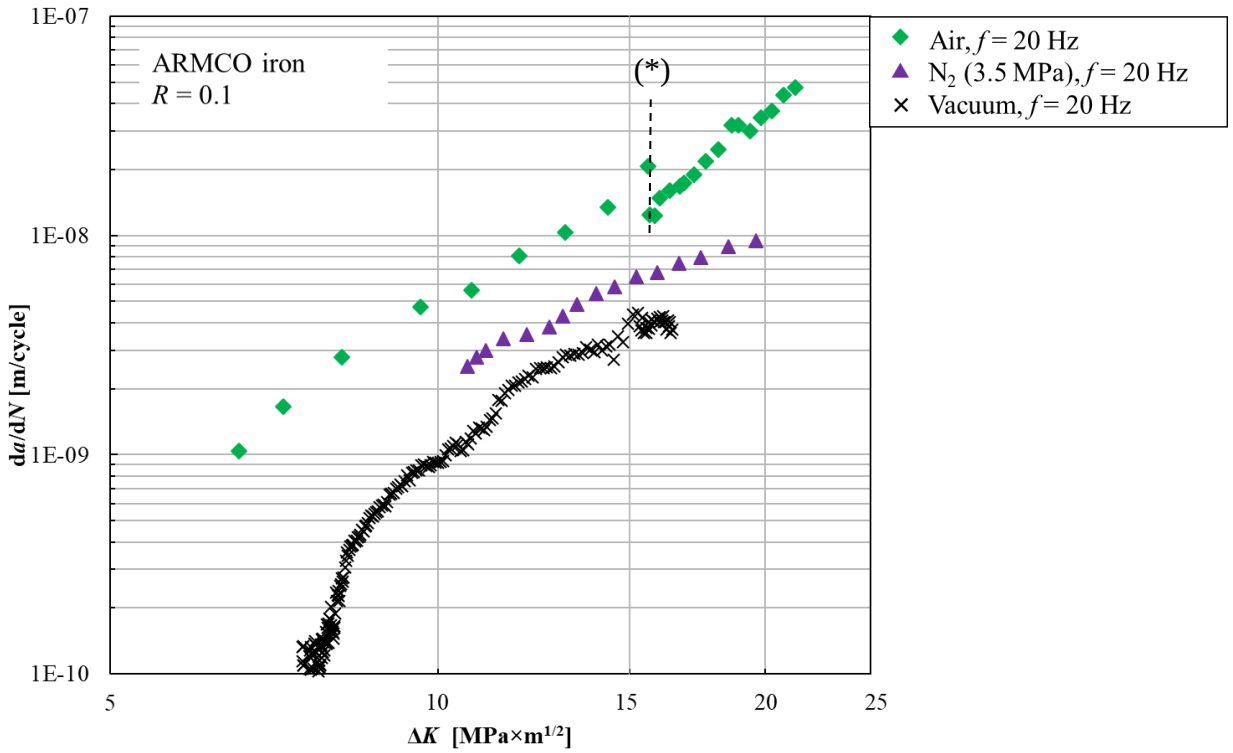

Figure 3 - 5 FCGR vs. ΔK curves of the tests under air, vacuum, and nitrogen.

Figure 3 - 6 shows the SEM images of fracture surfaces of specimens at Δ*K* = 10 MPa×m$^{1/2}$ in air (a)(b), nitrogen (c)(d), and vacuum (e)(f). The images in lower magnification (×1000, Figure 3 - 6a, c, and e) show that the fracture surfaces in all the environments present linear markings in the crack propagation direction, which are known as tear ridges (or river-pattern). The tear ridge is a result of a local shearing fracture. Besides, if we observe the fracture surfaces in higher magnification (×5000, Figure 3 - 6b, d, and f), we can notice that the fracture surfaces are covered by small dimples which are a consequence of a microvoid nucleation and coalescence process.

This type of fracture surface evidences that the fracture mechanism was a combination of microvoid coalescence and shearing fracture which is a typical fracture mechanism for ductile materials [125, 149]. This type of fracture surface was confirmed for the entire range of ΔK. The observed fracture surface feature is consistent with the one reported by Pippan [146, 147].

The comparison of the images at low magnification (Figure 3 - 6a, c, and e) indicates that the morphologies of fracture surfaces are slightly different. Indeed, the amount of tear ridges seems higher in the order of air, nitrogen, and vacuum. This difference in fracture surface is probably caused by the difference in the FCGRs by the environments. The reason for the difference in the FCGRs is probably an influence of oxygen and water vapor contained in air, according to the literature [150, 151]. Oxygen and water vapor may cause oxidation on the fresh surface at the crack tip. The oxidation layer formed on the surface at the crack tip restricts a slip reversibility, promoting an accumulation of slip displacement by one loading cycle. This consequences the increase of the crack tip advance per cycle, as suggested by Pelloux [150, 151]. In the case of nitrogen environment, nitrogen gas does not contain oxygen but a small amount of water vapor about 25 ppm. This water vapor likely caused a slight enhancement of FCGR with respect to the FCGR in vacuum. This above-mentioned mechanism may explain well the difference in the FCGRs among air, nitrogen, and vacuum.

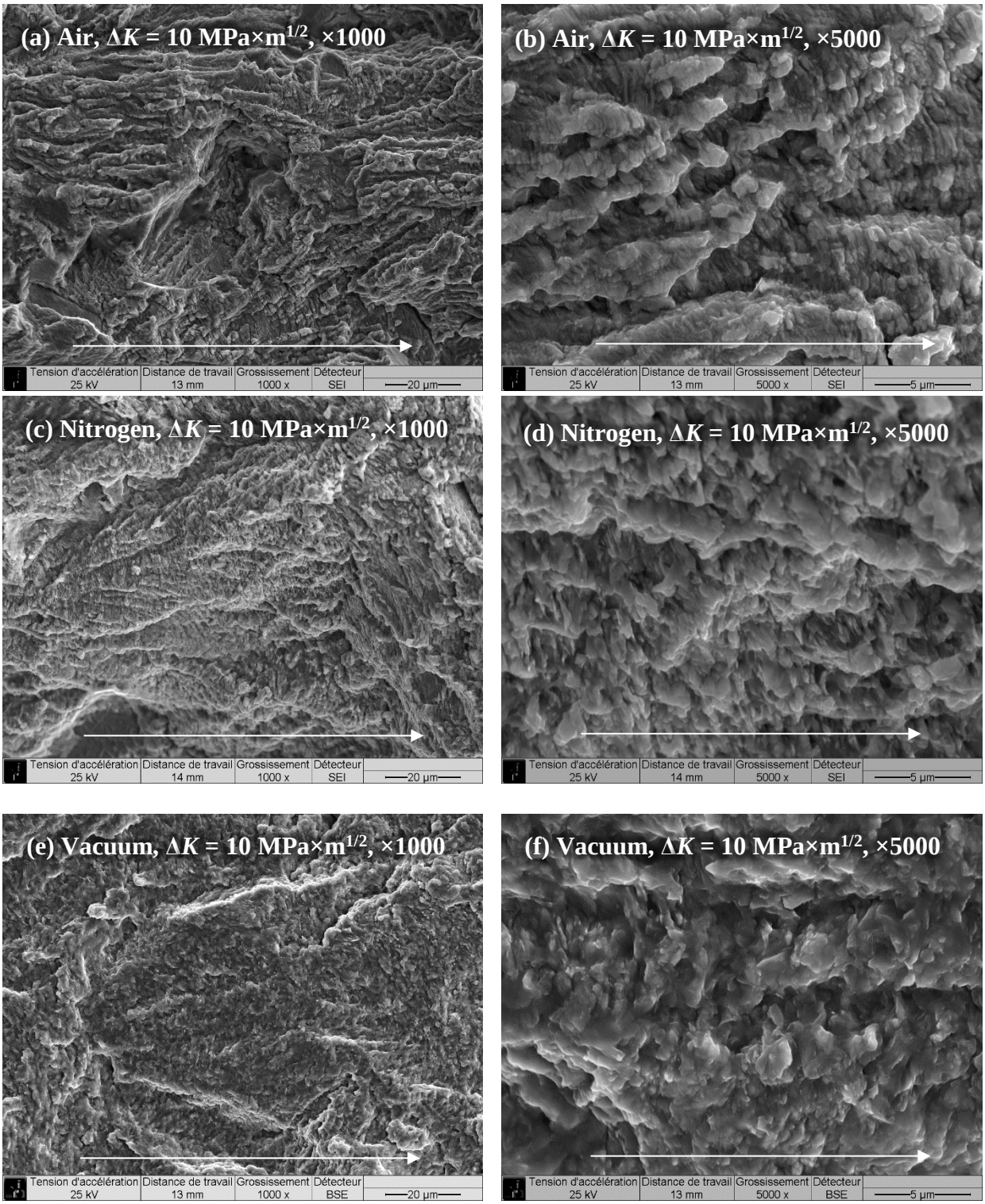

Figure 3 - 6 Fracture surfaces of the tests at $\Delta K = 10\ MPa \times m^{1/2}$ in air (a)(b), nitrogen (c)(d), and vacuum (e)(f) with two magnifications ×1000 and ×5000, respectively. The crack propagation direction is from left to right.

Figure 3 - 7 shows the fracture surfaces of the specimens at ΔK = 20 MPa×m$^{1/2}$ in air (a), nitrogen (b), and vacuum (c). The fracture surfaces in all the environments slightly change from the ones at lower ΔK (= 10 MPa×m$^{1/2}$). The tear ridges can be observed, but the dimples are not clearly observed on the fracture surfaces at ΔK = 20 MPa×m$^{1/2}$. This indicates that the fracture mechanism became mainly the shearing fracture, rather than the microvoid coalescence. Consequently, the difference in the fracture surface depending on the environment became unclear. Figure 3 - 7d shows the higher magnification image of the fracture surface in air at ΔK = 15 MPa×m$^{1/2}$. This image shows stripe marking (striations) in an orientation perpendicular to the crack propagation direction. The striations were not observed in nitrogen and vacuum likely because of two reasons: the FCGR is very low so that the spacing of striations is too small to be observed; and striation is not formed by high crack growth rate under vacuum [151].

From these FCG tests, the influences of oxygen on the FCGR has been confirmed, even though oxygen have a little effect on the fracture mechanism.

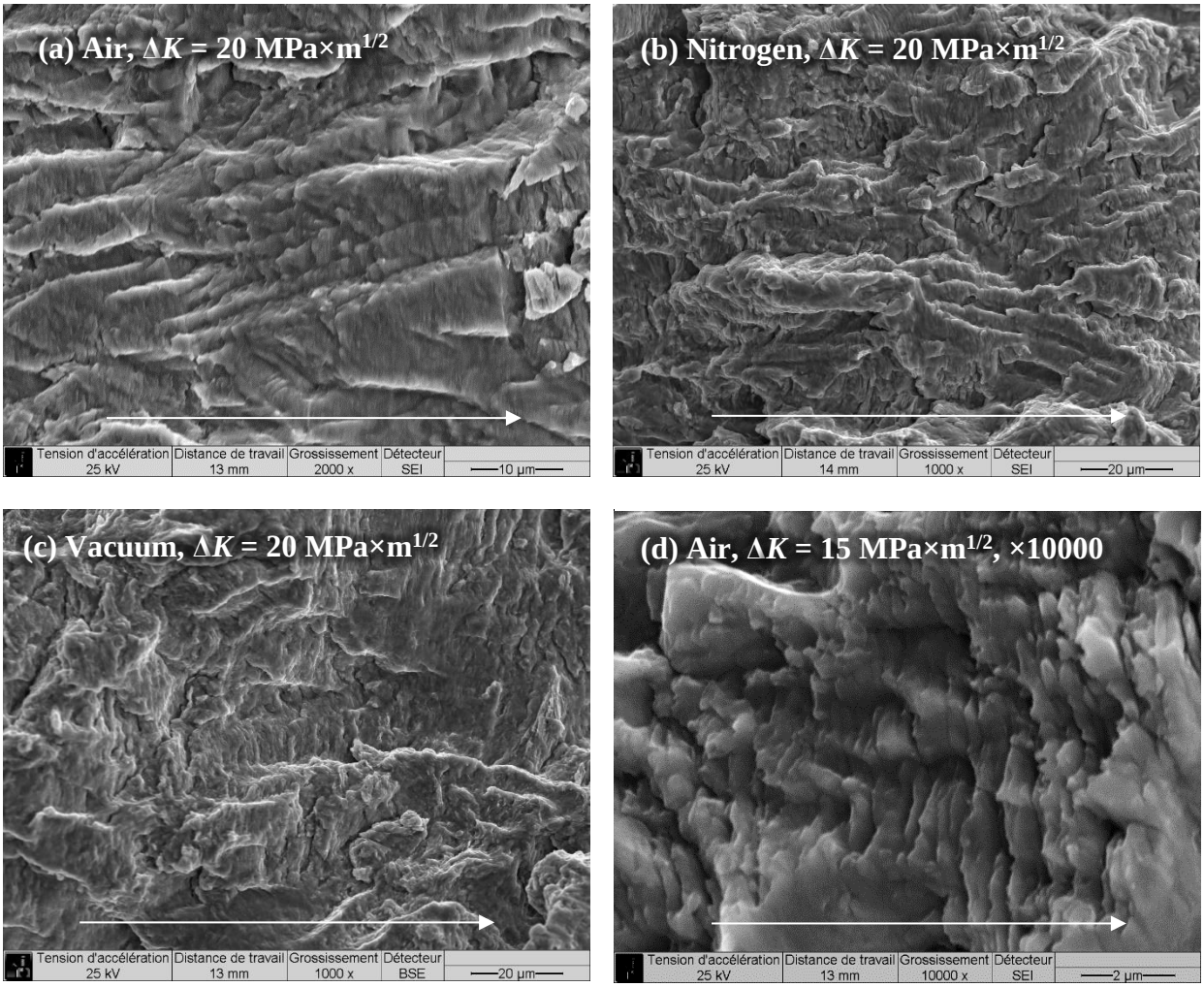

Figure 3 - 7 Fracture surfaces of the tests at ΔK = 20 MPa×m$^{1/2}$ in air (a), nitrogen (b), and vacuum (c). High magnification image of striations at ΔK = 20 MPa×m$^{1/2}$ in air (d). The crack propagation direction is from left to right.

3.3.2 FCGR of Δ*K*-increasing tests under hydrogen

After the FCG behavior of Armco iron under inert or mildly aggressive atmospheres was confirmed, in order to investigate the influence of gaseous hydrogen on FCG behavior as well as its dependencies on hydrogen gas pressure and loading frequency, the FCG tests under gaseous hydrogen at two hydrogen gas pressures, namely P_{H2} = 3.5 and 35 MPa, and three loading frequencies f = 0.2, 2, and 20 Hz were performed. The obtained FCGRs in hydrogen are shown in Figure 3 - 8 in addition to the results of the inert environments.

In this figure, one can see that the most of FCGR curves in hydrogen are above the ones in the inert environments: air, nitrogen, and vacuum. Besides, the FCGRs in hydrogen exhibit different trends depending on Δ*K* value, which can be defined by three distinct regimes. For example, in the case of the curve at P_{H2} = 35 MPa and f = 0.2 Hz:

a) A non-accelerated regime (ΔK < 12 MPa×m$^{1/2}$): in the low Δ*K* range, the FCGR in hydrogen is similar to the one in air.
b) A transition regime (12 < ΔK < 14 MPa×m$^{1/2}$): the FCGR in hydrogen sharply increases up to 50 times higher than that in air.
c) An accelerated regime (14 MPa×m$^{1/2}$ < ΔK): after the transition regime, the slope of the curve in hydrogen is nearly similar to the one in air but the FCGRs are significantly enhanced.

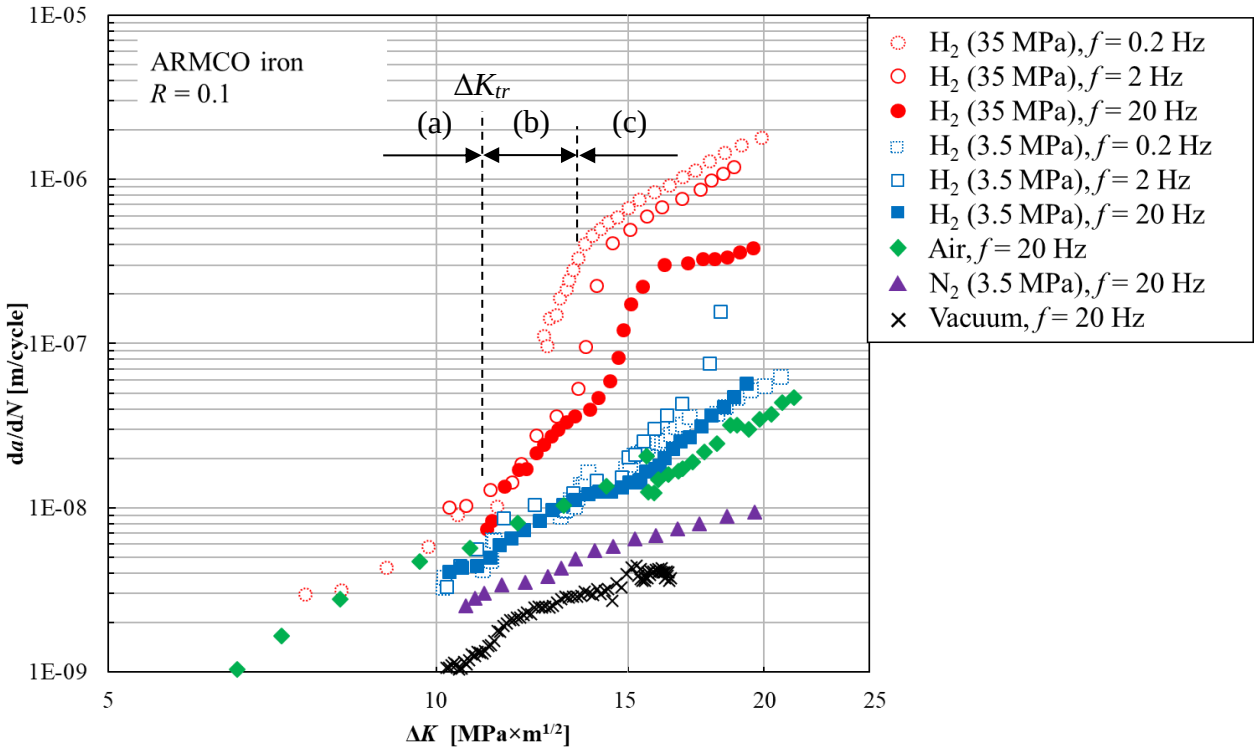

Figure 3 - 8 FCGR vs. ΔK curves of the tests at f = 0.2, 2, and 20 Hz under gaseous hydrogen at P_{H2} = 3.5 and 35 MPa, as well as the tests in inert environments.

This type of FCGR behavior with the presence of a characteristic "knee" has also been confirmed in many types of steel [28, 30, 62, 152–158].

In terms of influence of hydrogen gas pressure, when one compares the FCGR curves at f = 2 Hz, P_{H2} = 3.5 and 35 MPa, the ΔK value at the beginning of the transition regime, named as ΔK_{tr}, at P_{H2} = 35 MPa is lower ($\Delta K_{tr} \approx 11$ MPa×m$^{1/2}$) than that at P_{H2} = 3.5 MPa ($\Delta K_{tr} \approx 15$ MPa×m$^{1/2}$). This dependency of ΔK_{tr} on the hydrogen gas pressure has also been confirmed in a precipitation-hardened martensitic stainless steel [159] and in a low carbon steel [142, 160]. The FCGR curves at P_{H2} = 3.5 MPa ended in the transition regime, and the accelerated regime was not confirmed within the investigated range of ΔK. The FCGRs at P_{H2} = 3.5 MPa and f = 0.2 and 20 Hz do not show clear enhancement by hydrogen and are almost at the same level as in air even in the transition regime.

In terms of influence of loading frequency, at P_{H2} = 35 MPa, a higher magnitude of the FCGR enhancement is exhibited at a lower frequency. The difference in the FCGRs at P_{H2} = 35 MPa between f = 0.2 Hz and 2 Hz is smaller compared with that between f = 2 and 20 Hz. On the other hand, at P_{H2} = 3.5 MPa, even though the FCGR at f = 2 Hz is higher than that at f = 20 Hz, the FCGR at f = 0.2 Hz is much lower than that at f = 2 Hz. Thus, the effect of loading frequency on FCGR at P_{H2} = 3.5 MPa is reversed below f = 2 Hz. This result is surprising because it contradicts our conventional understanding that a lower loading frequency always induces a higher FCGR enhancement or saturation [14, 28–30, 62, 161]. In order to clarify the mechanism of this attenuation of FCG enhancement at very low loading frequency, it is necessary to further investigate the FCGR in hydrogen at lower loading frequency than 0.2 Hz. For this reason, the ΔK-constant FCG tests have been performed at a wider range of loading frequency including 0.02 Hz, as presented in the next section.

The FCGR in hydrogen is named "Hydrogen-Affected FCG (HAFCG)" in this study. Though some other works in the literature call it "Hydrogen-Enhanced (HE)" or "Hydrogen-Assisted (HA)", this study calls it as above because a part of FCGR (the non-accelerated regime) was not enhanced by hydrogen.

The HAFCG rate in a commercially pure iron has also been investigated by Ogawa et al. [157, 162, 163]. They used a JIS-C2504 grade as a material. The comparison between the FCGRs in the present study and their results in hydrogen (at P_{H2} = 0.2, 0.7, 20, 90 MPa and f = 1, 5 Hz) and in air (f = 1 Hz) is presented in Figure 3 - 9. Some of the FCGR curves of JIS-C2504 in hydrogen exhibit similar characteristic regimes (non-accelerated, transition and accelerated) to the present ones. The FCGR curves of JIS-C2504 clearly show the dependency on hydrogen gas pressure which is the shift of ΔK_{tr}, similar to the result of this study. Note also that there is no influence of hydrogen gas pressure on the magnitude of FCGR acceleration in the accelerated regime. This fact was not confirmed by the present results (Figure 3 - 8) because the accelerated regime in P_{H2} = 3.5 MPa was not observed within the investigated range of ΔK < 20 MPa×m$^{1/2}$.

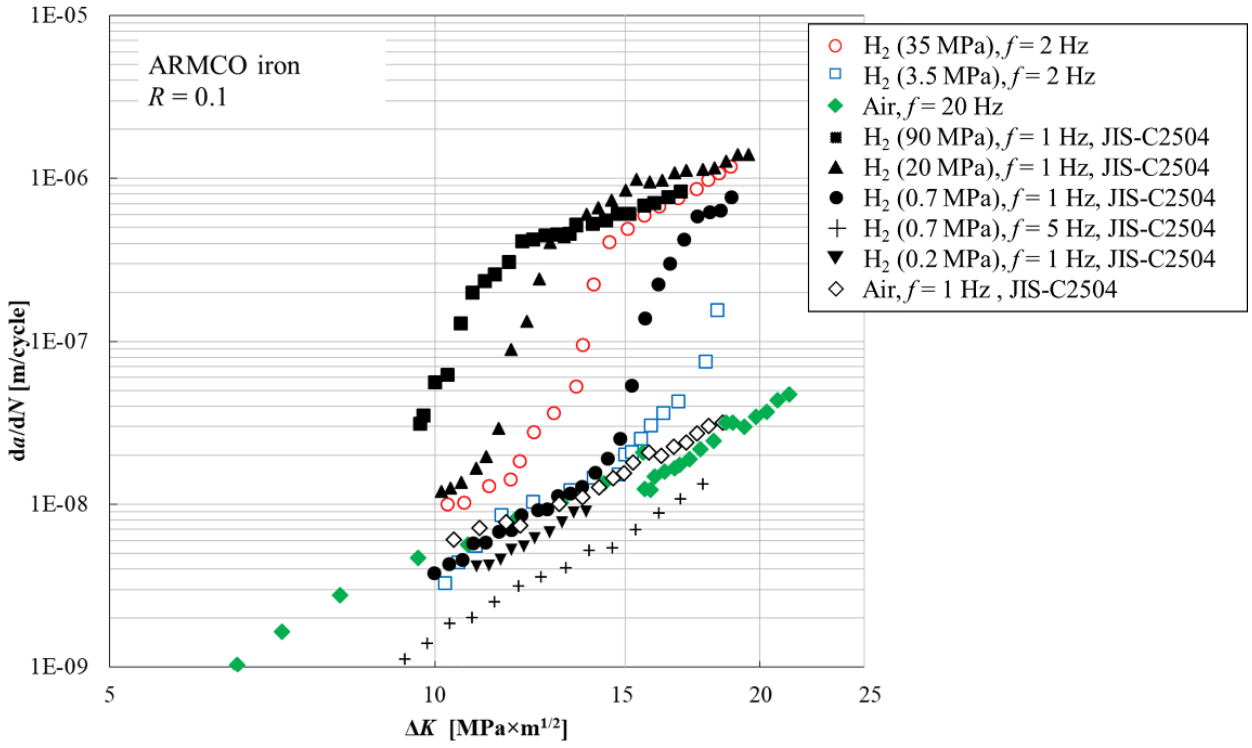

Figure 3 - 9 Comparison between the FCGRs in Armco iron and the ones in commercially pure iron, JIS-C2504, in hydrogen and in air obtained by Ogawa et al. [157, 162, 163].

3.3.3 Fracture surfaces of Δ*K*-increasing tests under hydrogen

To examine a fracture mode in hydrogen and associate it with the FCGR tendency, this sub-section presents the result of SEM observations of the fracture surfaces in the Δ*K*-increasing tests in hydrogen. Firstly, the fracture surfaces of the tests at P_{H2} = 35 MPa are presented. Figure 3 - 10 shows the fracture surfaces of the tests in hydrogen at P_{H2} = 35 MPa, f = 0.2 (a)(b), 2 (c)(d), and 20 Hz (e)(f) in the non-accelerated regime (ΔK = 8 – 12 MPa×m$^{1/2}$). Figure 3 - 10b, d, and f are the SEM images with higher magnification. As one can notice in these images, the fracture surfaces at all the loading frequencies are mostly covered by the intergranular facets. Although some small parts of fracture surface were ductile transgranular, the fracture mode is basically a brittle intergranular fracture. The appearance of the fracture surfaces is totally different from the case of inert environments as presented in the previous sub-section. Some intergranular secondary cracks were observed as shown in Figure 3 - 10e. This type of intergranular fracture surface is known as one of the typical hydrogen-induced fracture surfaces [12, 151, 164–166]. However, although the fracture surface seems to show a brittle feature at lower magnification, stripe-like plastic markings were observed on the surface of intergranular facets in higher magnification as shown in Figure 3 - 10b, d, and f. In literature, such stripe-like markings on intergranular facets have also been confirmed in hydrogen-assisted fracture of pure iron [77, 163, 167], pure copper [168], and pure nickel [75].

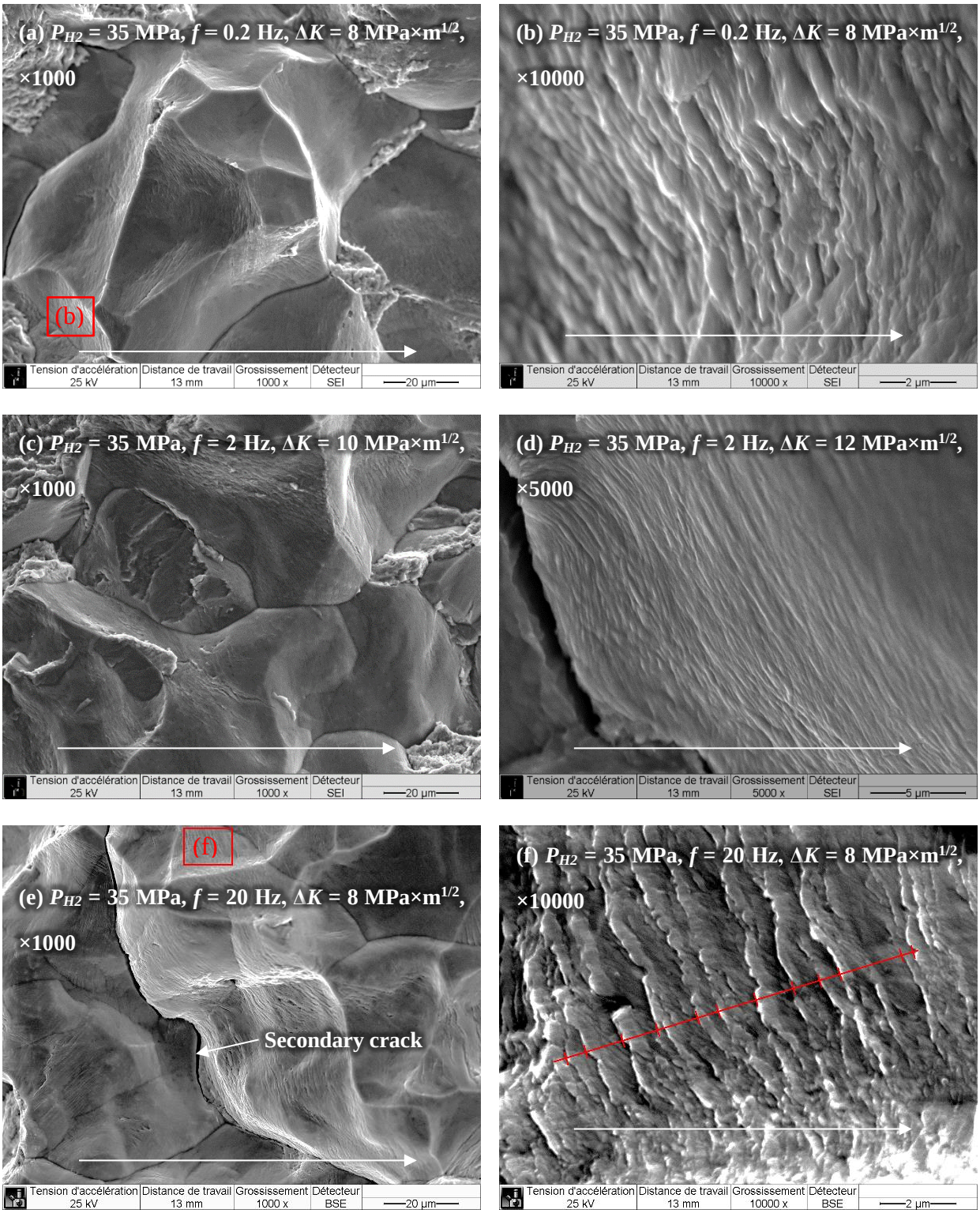

Figure 3 - 10 Fracture surfaces of the tests in hydrogen at P_{H2} = 35 MPa, f = 0.2 (a)(b), 2 (c)(d), and 20 Hz (e)(f) in the non-accelerated regime (ΔK = 8 – 12 MPa×m$^{1/2}$). The crack propagation direction is from left to right.

Next, once the FCG enters the transition regime, in other words, and the FCGR enhancement process is initiated, the fracture surface gradually changed from an intergranular fracture to a transgranular one (more precisely, a quasi-cleavage fracture as explained below). An example of the fracture surface in the transition regime (of the test in hydrogen at P_{H2} = 35 MPa, f = 2 Hz, and ΔK = 12 MPa×m$^{1/2}$) is shown in Figure 3 - 11. Figure 3 - 11 shows that the fracture surface in the transition regime is a mix of intergranular fracture and transgranular fracture.

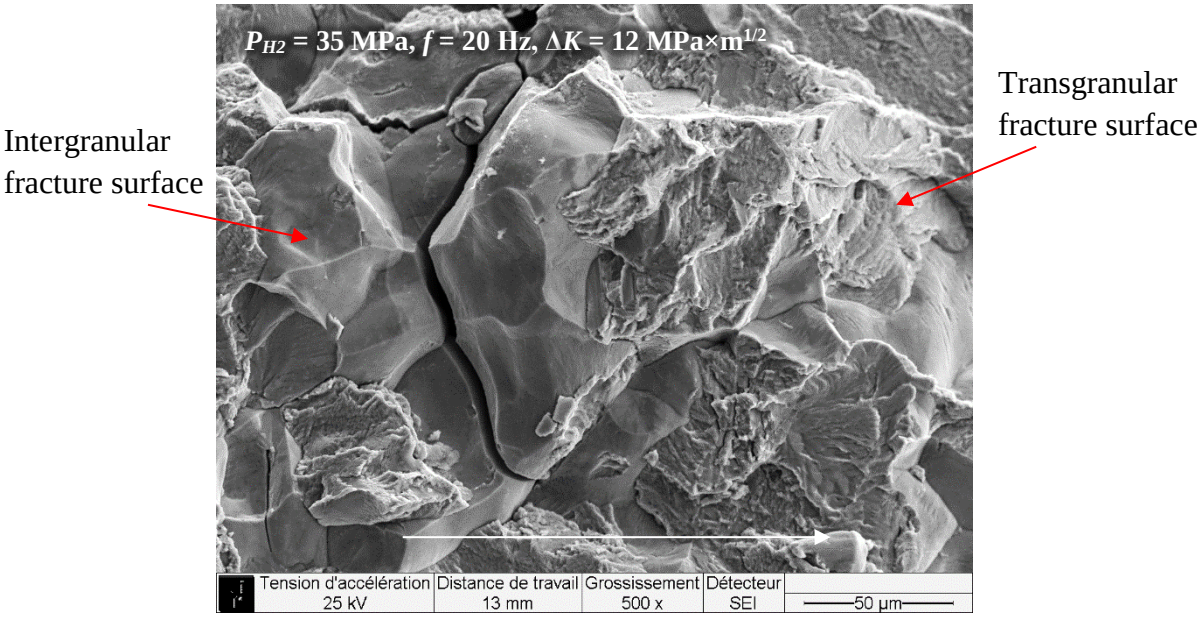

Figure 3 - 11 Example of fracture surface in the transition regime (the test in hydrogen at P_{H2} = 35 MPa, f = 20 Hz, and ΔK = 12 MPa×m$^{1/2}$). The crack propagation direction is from left to right.

Finally, in the accelerated regime, the fracture surface became fully transgranular. Figure 3 - 12a, b, and c show the fracture surfaces of the tests in hydrogen at P_{H2} = 35 MPa, f = 0.2 (a), 2 (b)(d), and 20 Hz (c) in the accelerated regime (ΔK = 15, 18 MPa×m$^{1/2}$), respectively. In these fracture surfaces, many tear ridges in the direction of crack propagation and some flat surface parts can be observed. Figure 3 - 12d shows a higher magnification image of the flat surface part at ΔK = 15 MPa×m$^{1/2}$, P_{H2} = 35 MPa, and f = 0.2 Hz. These flat surface parts look a cleavage-like facet. Besides, its surface pattern is a combination of striations and river patterns which is generally called as "herring-bone pattern". The spacing of the striations in this image is about 2 µm which is nearly one order of magnitude higher than the macroscopic FCGR (da/dN = 5×10^{-7} m/cycle). The spacing of striation in low strength steels is typically one order of magnitude higher than the macroscopic FCGR under relatively low stress intensity (ΔK = 10 – 20 MPa×m$^{1/2}$) [169, 170]. Because the undulations of the surface with these striations are much smaller compared to a normal ductile striation as observed in Figure 3 - 7d for example, these striations are likely a brittle striation. To determine whether the flat surface part is a cleavage-like facet or not, it is necessary to verify the crystal orientation of these flat surface is along a {100}-type cleavage plane. Birenis et al. [108, 157] have observed that the transgranular crack propagation in hydrogen exhibiting the flat fracture surface is along a {100}-type cleavage plane of the grains by means of EBSD

analysis in pure iron. They concluded that the fracture mode in the accelerated regime is a Quasi-Cleavage (QC) fracture with a formation of brittle-like striations. The QC fracture was also observed in the tensile tests under hydrogen as presented in Chapter 2.

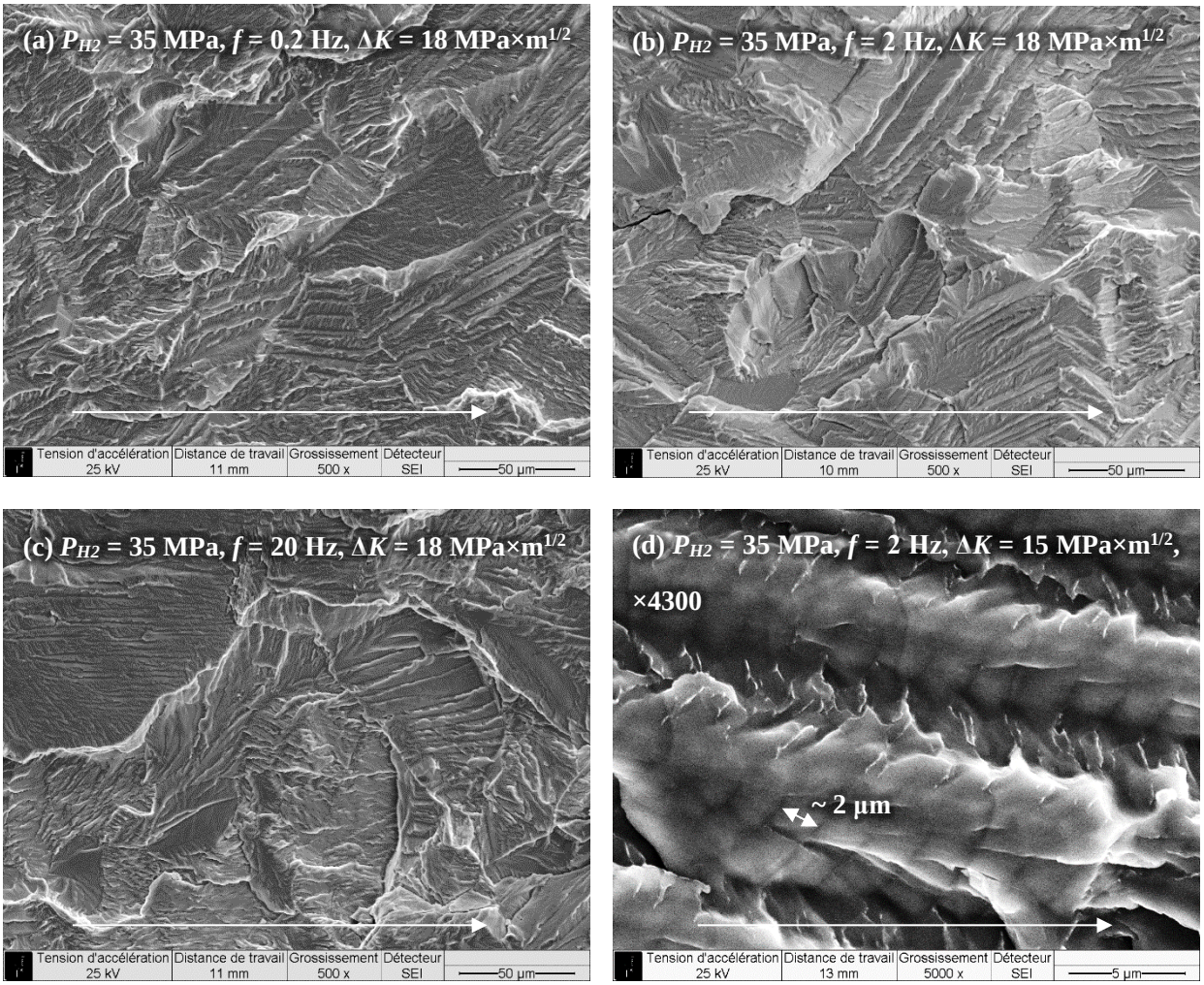

Figure 3 - 12 Fracture surfaces of the tests in hydrogen at P_{H2} = 35 MPa, f = 0.2 (a), 2 (b), and 20 Hz (c) in the accelerated regime (ΔK = 18 MPa×m$^{1/2}$). High magnification image of brittle striations at ΔK = 15 MPa×m$^{1/2}$, P_{H2} = 35 MPa, and f = 0.2 Hz (d). The crack propagation direction is from left to right.

Figure 3 - 13 shows the low magnification image of the fracture surface of the test at P_{H2} = 35 MPa, f = 0.2 Hz. This figure demonstrates the clear difference in the contrast of image corresponding to the transitions of the regimes from the pre-cracking in air, the intergranular fracture surface in the low range of ΔK in hydrogen, to the transgranular QC fracture surface in the high range of ΔK in hydrogen. The change in the contrast of image indicates the changes in morphology of fracture surface.

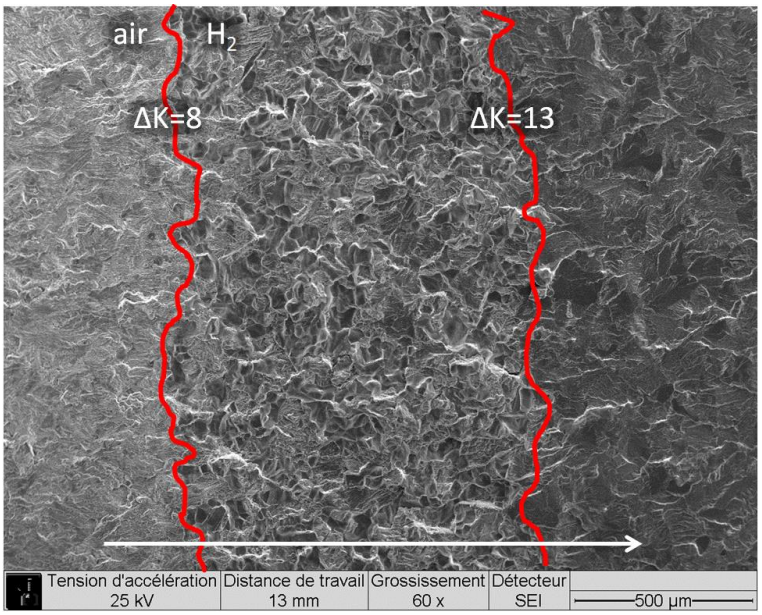

Figure 3 - 13 Low magnification image of the fracture surface of the test at P_{H2} = 35 MPa, f = 0.2 Hz showing clear transitions of the regimes (including a pre-cracking in air). The crack propagation direction is from left to right.

The fracture surfaces of the tests at P_{H2} = 3.5 MPa are presented below to see the difference in the fracture surface by decreasing the hydrogen gas pressure. Figure 3 - 14 shows the fracture surfaces of the tests in hydrogen at P_{H2} = 3.5 MPa, f = 0.2 (a), 2 (b-e), and 20 Hz (f) in the non-accelerated regime (ΔK = 10 – 14 MPa×m$^{1/2}$). The fracture surface at f = 2 Hz (Figure 3 - 14b) exhibits a mix of intergranular and transgranular fracture surfaces. Figure 3 - 14c presents a high magnification image of the intergranular fracture surface part, while Figure 3 - 14d shows the high magnification image of the mix part of the intergranular and transgranular fracture surface. By observing the transgranular fracture surface part, one can notice that it is a rather ductile transgranular fracture, and not a QC fracture. This is thus different from the fracture surface in the transition regime of the tests at 35 MPa of hydrogen which is a mix of intergranular and transgranular QC fracture surfaces. The mix of intergranular and ductile transgranular fracture continued until the end of the non-accelerated regime (ΔK ~ 15 MPa×m$^{1/2}$) as shown by Figure 3 - 14e (at ΔK = 14 MPa×m$^{1/2}$). The same type of fracture surface was observed for the test at f = 2 Hz (Figure 3 - 14f). On the other hand, in the case of f = 0.2 Hz, the fracture surface fully exhibits a ductile transgranular fracture surface without any intergranular facet as shown in Figure 3 - 14a.

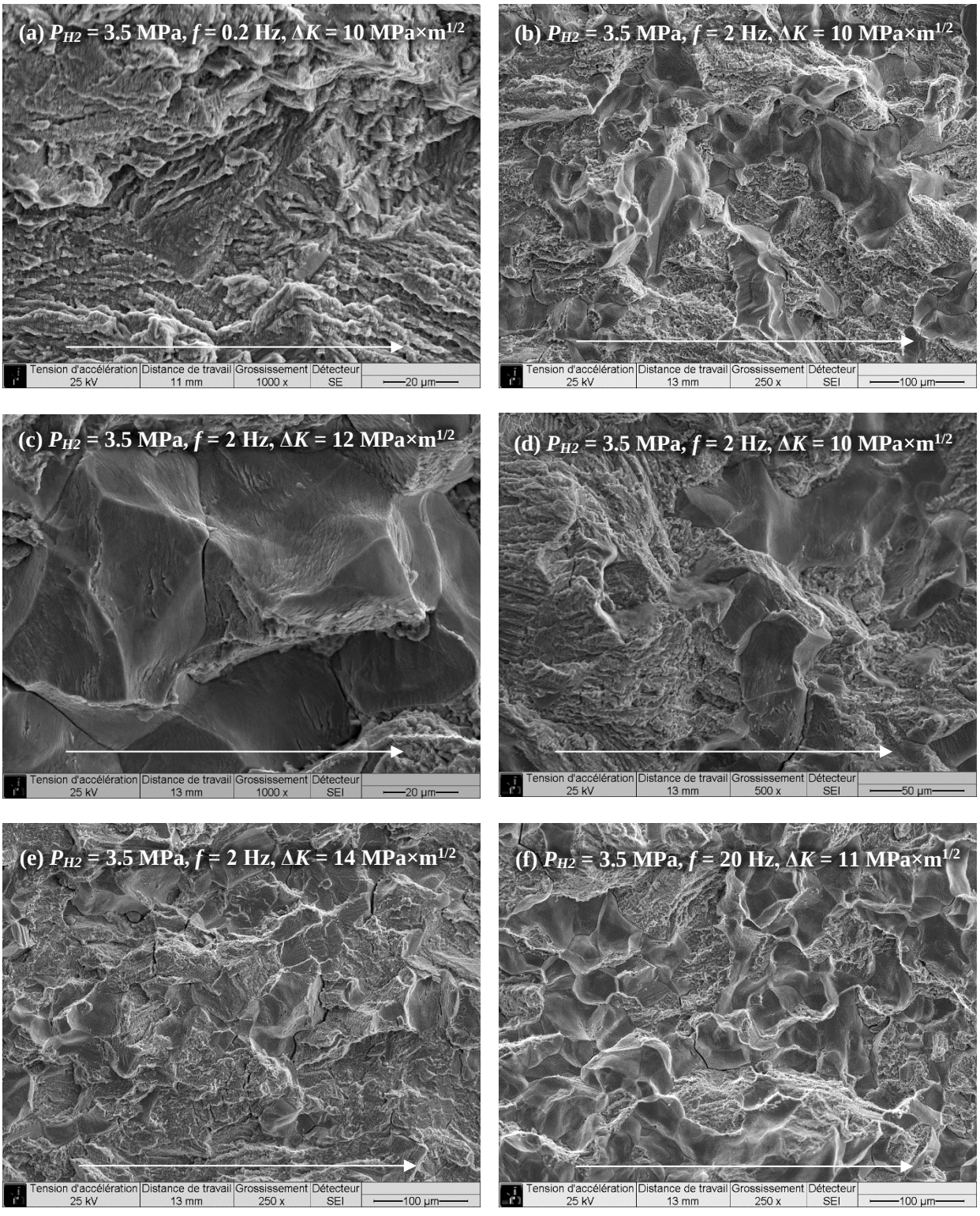

Figure 3 - 14 Fracture surfaces of the tests in hydrogen at P_{H2} = 3.5 MPa, f = 0.2 (a), 2 (b-e), and 20 Hz (f) in the non-accelerated regime (ΔK = 10 – 14 MPa×m$^{1/2}$). The crack propagation direction is from left to right.

Figure 3 - 15 shows the fracture surfaces of the tests in hydrogen at P_{H2} = 3.5 MPa, f = 0.2 (a), 2 (b)(c), and 20 Hz (d) in the transition regime (ΔK = 18 MPa×m$^{1/2}$). The fracture surfaces at f = 2 and 20 Hz (Figure 3 - 15b and d) exhibit a QC fracture surface with brittle striations (Figure 3 - 15c) but without any intergranular facet. These fracture surfaces are not consistent with the ones at P_{H2} = 35 MPa showing a mix of intergranular and QC fracture surfaces (Figure 3 - 11). On the other hand, the fracture surface at f = 0.2 Hz (Figure 3 - 15a) exhibits a ductile transgranular fracture. Therefore, the test at P_{H2} = 3.5 MPa, f = 0.2 Hz demonstrated a different fracture mode from the one of the tests at f = 2 and 20 Hz, even though the FCGRs at f = 0.2 and 20 Hz are almost the same level. This difference in fracture modes between low and high loading frequencies was also further examined by the ΔK-constant FCG tests presented in the next section.

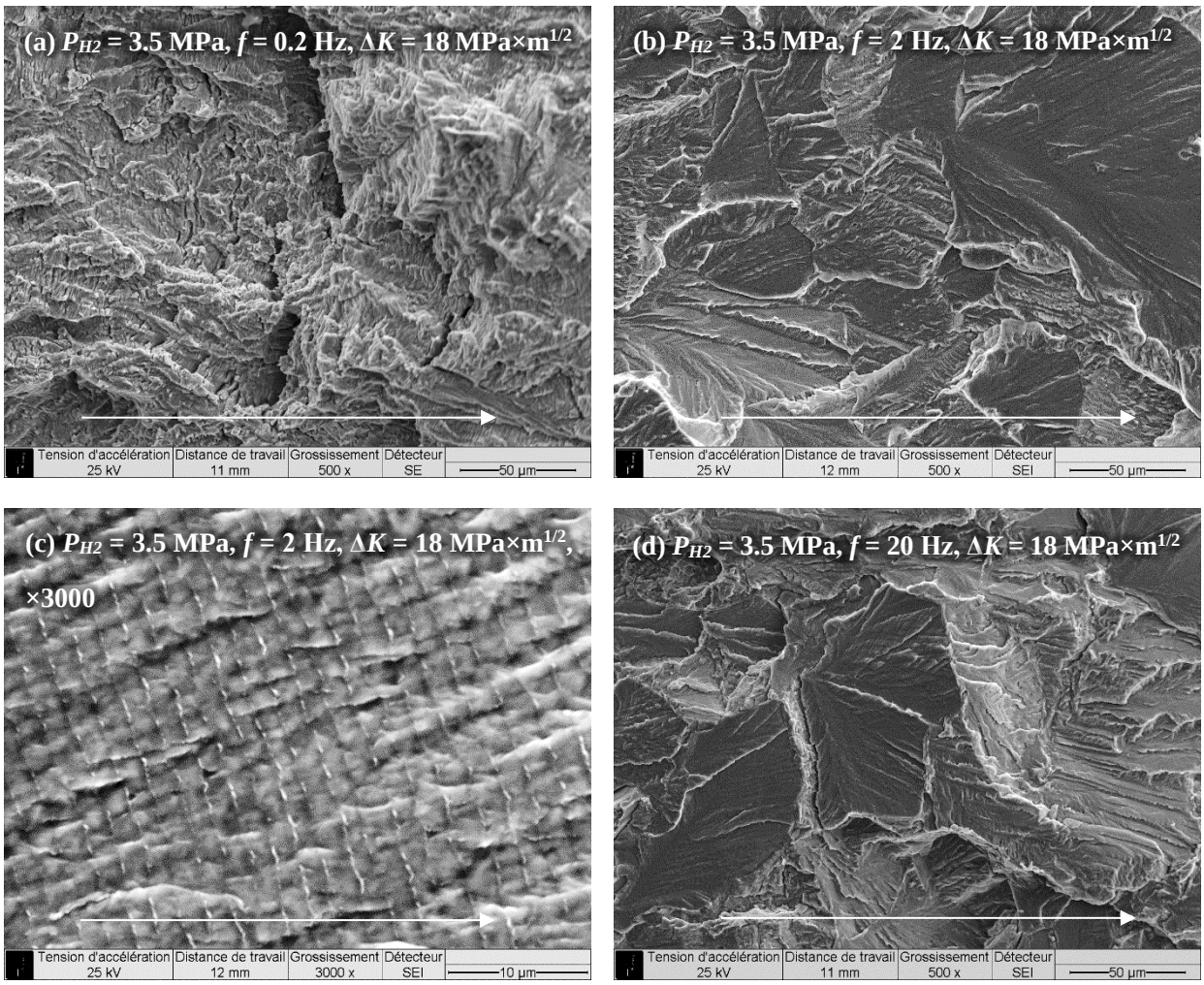

Figure 3 - 15 Fracture surfaces of the tests in hydrogen at P_{H2} = 3.5 MPa, f = 0.2 (a), 2 (b)(d), and 20 Hz (d) in the transition regime (ΔK = 18 MPa×m$^{1/2}$). The crack propagation direction is from left to right.

3.4 Δ*K*-constant FCG test

From the results of Δ*K*-increasing FCG tests presented in the previous section, the dependencies of the FCGR and the fracture mode on Δ*K*, hydrogen gas pressure and loading frequency have been revealed. Interestingly, some peculiar effects of loading frequency, especially at low loading frequency, on the FCGR in the accelerated regime were found out. Therefore, the Δ*K*-constant FCG tests were conducted aiming to investigate the influence of loading frequency lower than f = 0.2 Hz. This section presents the results of FCGR and fracture surface observation of the Δ*K*-constant FCG tests.

Firstly, the FCGRs of the Δ*K*-constant FCG tests at ΔK = 20 MPa×m$^{1/2}$ under hydrogen and nitrogen are presented by the relationship between the FCGR and the loading frequency as shown in Figure 3 - 16. This diagram also shows the results of the Δ*K*-increasing FCG tests. As shown in this diagram, the FCGRs in air and nitrogen are lower than the ones in hydrogen at any loading frequency. Also, the FCGRs in nitrogen increases a little bit by decreasing the loading frequency from 20 to 0.02 Hz, but it is a very small increment in terms of the order of magnitude.

On the other hand, in hydrogen at P_{H2} = 35 MPa, the FCGRs increased by decreasing the loading frequency from 20 to 0.2 Hz. However, in contrast, the FCGR decreased by decreasing the loading frequency from 0.2 to 0.02 Hz. In case of P_{H2} = 3.5 MPa, although there is a quite big difference in the values of FCGRs between the Δ*K*-increasing and the Δ*K*-constant FCG tests, the FCGRs in both tests increased by decreasing the loading frequency until 2 Hz. Once the loading frequency decreases to 0.2 or 0.02 Hz, the FCGRs drastically decreased by one order of magnitude and became almost the same level as in nitrogen. Therefore, the attenuation of FCGR enhancement has been confirmed even at P_{H2} = 35 MPa by very low loading frequency 0.02 Hz, as well as at P_{H2} = 3.5 MPa.

The FCGR of the Δ*K*-constant test is slightly higher than the one of the Δ*K*-increasing test in hydrogen and even in nitrogen. This difference is likely caused by the difference of the testing method. Indeed, the Δ*K*-increasing test was performed without stopping the test until the end of the test (when the maximum displacement of the loading rod reached the safety limit). On the other hand, in the Δ*K*-constant tests, the FCG test was regularly interrupted during the test to modify the loading parameters. During the interruption time, hydrogen may diffuse into the inside of the specimen. Because of this reason, in the Δ*K*-constant test, the amount of hydrogen concentration in the vicinity of the crack tip became higher compared to the case in the Δ*K*-increasing test. The higher amount of hydrogen concentration probably results in the higher FCGR. The mechanism of this higher hydrogen concentration effect will be discussed in Chapter 5.

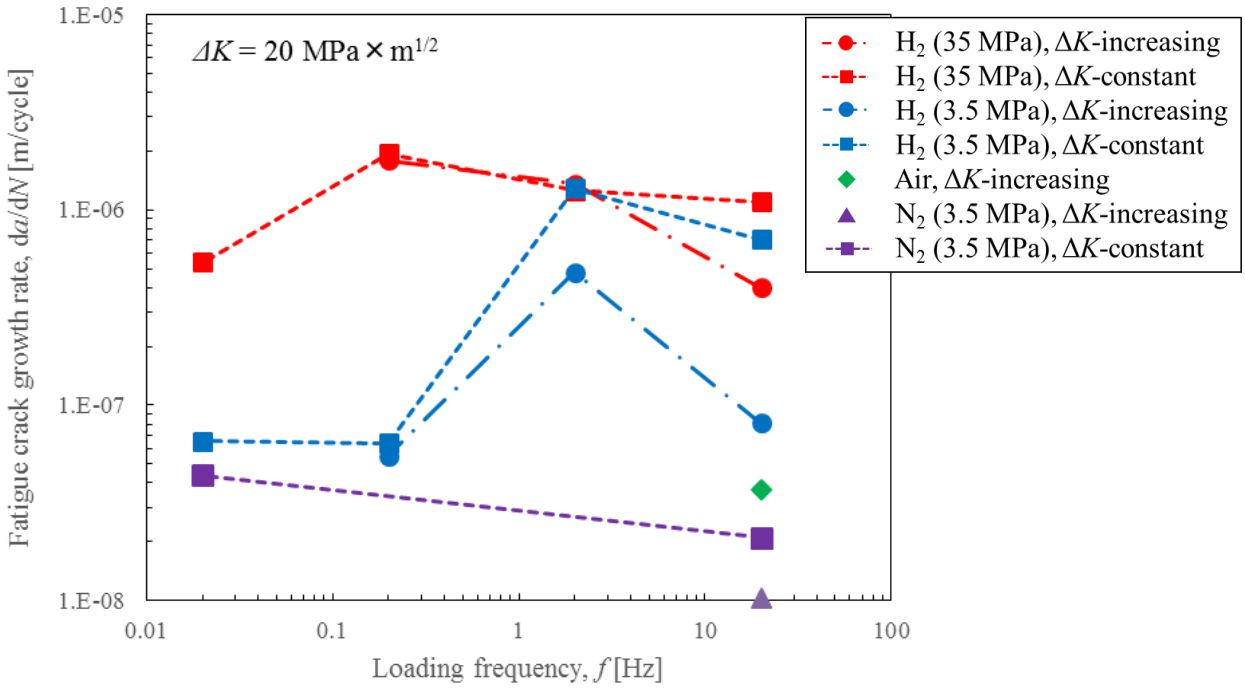

Figure 3 - 16 FCGR vs. ΔK curves of the ΔK-constant and ΔK-increasing tests at f = 0.02, 0.2, 2, and 20 Hz under gaseous hydrogen at P_{H2} = 3.5 and 35 MPa, as well as the tests in inert environments.

The fracture surfaces of tested specimens were observed by SEM to investigate the fracture mode associated with the attenuation of FCG enhancement at very low loading frequency. Figure 3 - 17 shows the fracture surfaces of the Δ*K*-constant tests in nitrogen at P_{N2} = 3.5 MPa and *f* = 0.02 (a) and 20 Hz (b). The fracture surfaces in nitrogen at both loading frequencies exhibit a ductile transgranular fracture.

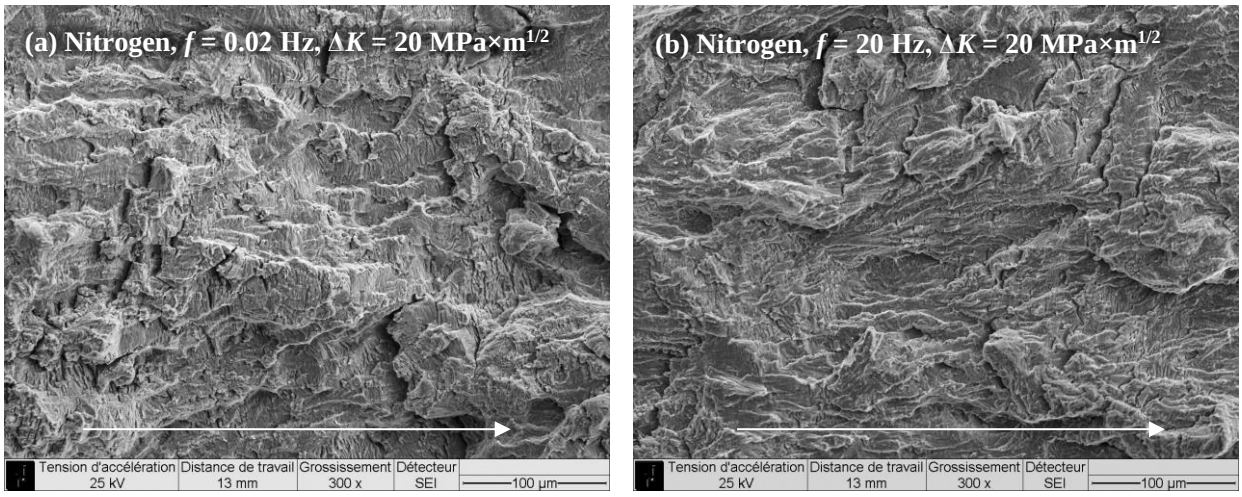

Figure 3 - 17 Fracture surfaces of the ΔK-constant tests (at ΔK = 20 MPa×$m^{1/2}$) in nitrogen at P_{N2} = 3.5 MPa and f = 0.02 (a) and 20 Hz (b). The crack propagation direction is from left to right.

On the other hand, Figure 3 - 18 shows the fracture surfaces of the Δ*K*-constant tests (at Δ*K* = 20 MPa×$m^{1/2}$) in hydrogen at P_{H2} = 35 MPa and *f* = 0.02 (a)(b), 0.2 (c)(d), 2 (e), and 20 Hz (f). From

this figure, it has been revealed that the fracture modes at all the loading frequencies are brittle QC fracture with some cleavage-like facets and many tear ridges. However, if one compares the fracture surfaces between f = 0.02 Hz (Figure 3 - 18a, b) and the other higher loading frequencies (Figure 3 - 18c-f), it can be seen that the amount of flat surface parts (i.e. cleavage-like facets) in the fracture surface at f = 0.02 Hz is higher compared to the other loading frequencies. The fracture surfaces at f = 0.2, 2, and 20 Hz (Figure 3 - 18c-f) are mostly covered by step-like surface morphology which is constituted by multiple cleavage planes. This difference in surface appearances between f = 0.02 Hz and higher f is likely related to the difference in FCGR (Figure 3 - 16), though both fracture modes are basically the same as the brittle QC fracture. The mechanism causing this difference will be discussed in Chapter 5.

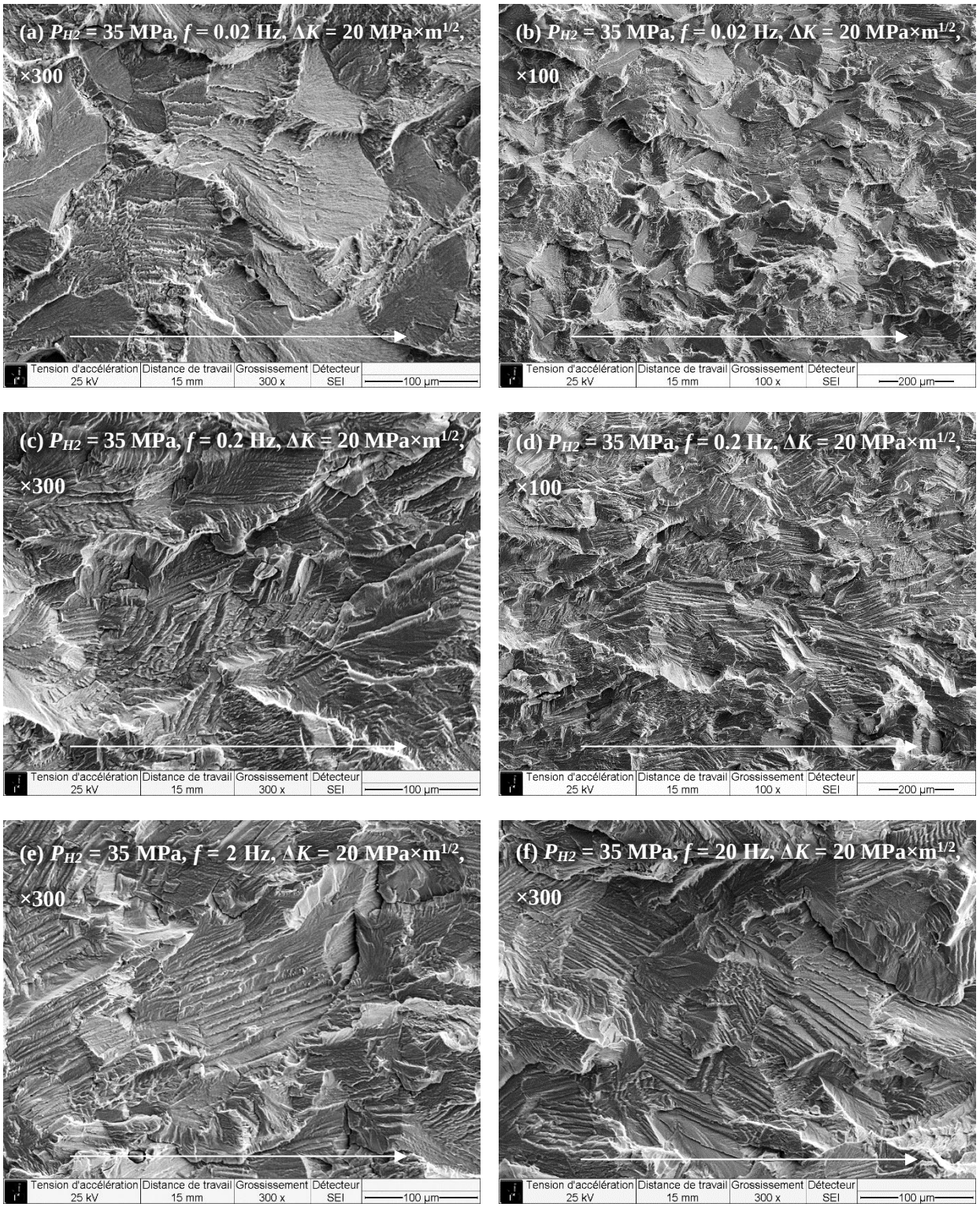

Figure 3 - 18 Fracture surfaces of the ΔK-constant tests (at ΔK = 20 MPa×m$^{1/2}$) in hydrogen at P_{H2} = 35 MPa and f = 0.02 (a)(b), 0.2 (c)(d), 2 (e), and 20 Hz (f). The crack propagation direction is from left to right.

Figure 3 - 19 shows fracture surfaces of the ΔK-constant tests (at ΔK = 20 MPa×m$^{1/2}$) in hydrogen at P_{H2} = 3.5 MPa and f = 0.02 (a), 0.2 (b), 2 (c), and 20 Hz (d). In the case of P_{H2} = 3.5 MPa, as shown in this figure, the fracture surfaces at f = 0.02 and 0.2 Hz exhibit a ductile fracture, while the fracture surfaces at f = 2 and 20 Hz exhibit a brittle QC fracture surface. Therefore, the drastic change in the fracture mode occurred accompanied by the drop of FCGRs by decreasing the loading frequency.

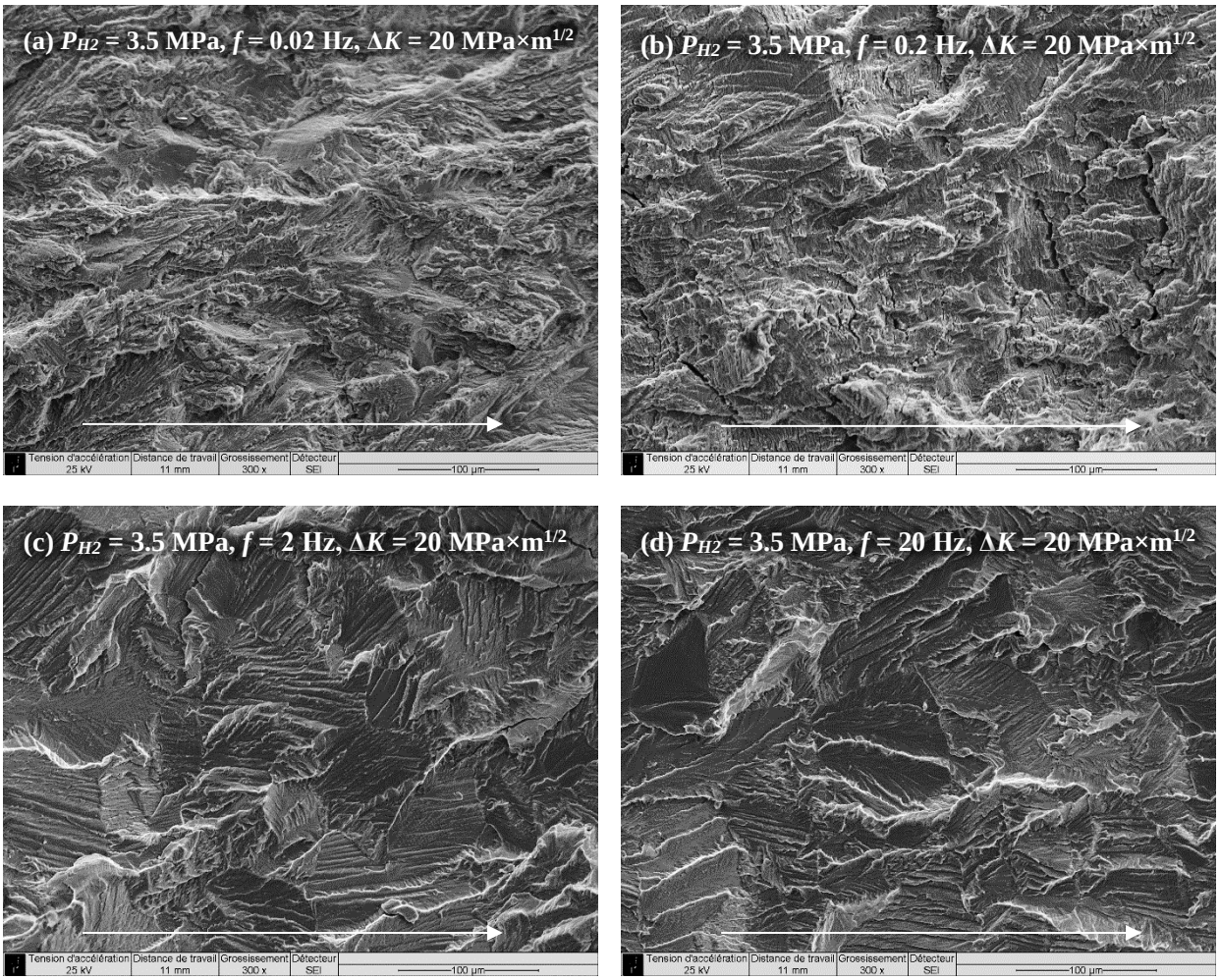

Figure 3 - 19 Fracture surfaces of the ΔK-constant tests (at ΔK = 20 MPa×m$^{1/2}$) in hydrogen at P_{H2} = 3.5 MPa and f = 0.02 (a), 0.2 (b), 2 (c), and 20 Hz (d). The crack propagation direction is from left to right.

3.5 Discussion

In the previous section, the FCG behavior in Armco iron under various gaseous environment including hydrogen has been investigated by means of the ΔK-increasing and ΔK-constant FCG tests with various hydrogen gas pressures and loading frequencies. In this section, based on the obtained experimental results of the FCG tests, the dependency of HAFCG on the testing conditions, the time-dependency of HAFCG, the change in the fracture mode by hydrogen and the attenuation of FCG enhancement at very low loading frequency are discussed.

3.5.1 Dependency of HAFCG rate on testing conditions

This sub-section firstly summarizes the obtained results of the HAFCG depending on the stress intensity factor range ΔK, the hydrogen gas pressure P_{H2}, and the loading frequency f. Figure 3 - 20 shows the schematic diagram of the influences of these testing parameters on the da/dN vs ΔK curves.

As mentioned in Sub-section 3.3.2, the HAFCG rate curves exhibit three different trends depending on ΔK. The three characteristic regimes are, from lower ΔK regime, (a) the non-accelerated regime, (b) the transition regime, and (c) the accelerated regime as indicated by Figure 3 - 20. The same type of FCGR trend has also been confirmed in pipeline steels [13, 153, 155, 158, 171, 172] which are composed of ferrite-perlite microstructure. This fact that Armco iron, i.e. a pure ferrite microstructure, exhibits the similar sensitivity to hydrogen as pipeline steels, suggests that the overall behavior is mainly contributed by the interaction between hydrogen and the ferrite microstructure, while a pearlite microstructure only plays a minor role.

For the dependency on hydrogen gas pressure, the value of ΔK_{tr} decreases by increasing P_{H2}, while the magnitude of FCGR enhancement in the accelerated regime does not change. On the other hand, the dependency on the loading frequency is that the magnitude of FCGR enhancement in the accelerated regime increases by decreasing f.

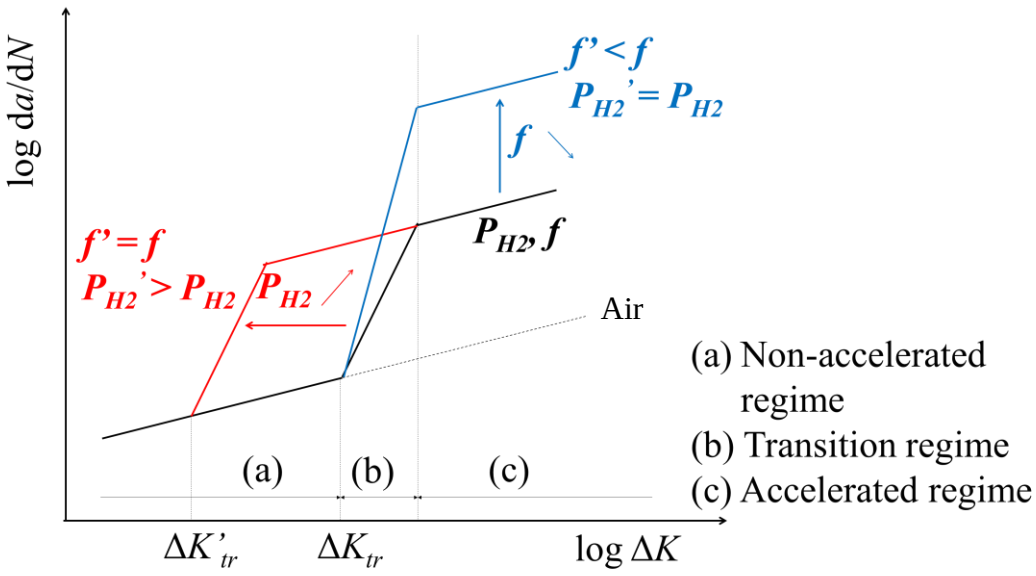

Figure 3 - 20 Schematic diagram of the influence of ΔK, hydrogen gas pressure and loading frequency on HAFCG rate curve.

The dependency of HAFCG rate on hydrogen gas pressure is generally described as the increment of FCGR enhancement by increasing hydrogen gas pressure. For example, Macadre et al. [72] have reported that the FCGR enhancement by hydrogen in Ni-Cr-Mo steel is proportional to the hydrogen gas pressure in double logarithmic scale as shown in Figure 3 - 21a. Besides, Yoshikawa et al. [142, 143] have investigated the hydrogen gas pressure effect on the FCGR in low carbon steel, and have found out that the FCGR increases by increasing P_{H2} until P_{H2} reaches a certain value. And then, the FCGR enhancement saturates as shown in Figure 3 - 21b. As far as these results are considered, the hydrogen gas pressure seems to influence the FCGR enhancement in the accelerated regime. However, if one considers the present results, the P_{H2}-dependency of FCGR at fixed ΔK shown in Figure 3 - 21 can be understood based on the shift of ΔK_{tr}. When the hydrogen gas pressure is low, the necessary value of ΔK to cause the FCGR enhancement (i.e. ΔK_{tr}) is high. So, as long as the applied ΔK is lower than the ΔK_{tr}, the FCGR is not enhanced. When the hydrogen gas pressure is increased, then the ΔK_{tr} value decreases. At some point, ΔK_{tr} becomes equal to the applied ΔK, and the FCGR enhancement is observed. The magnitude of FCGR enhancement increases as long as the applied ΔK is within the range of the transition regime. Once the applied ΔK reaches the accelerated regime, the increase in the FCGR stops and saturate in a higher hydrogen gas pressure as observed in Figure 3 - 21b.

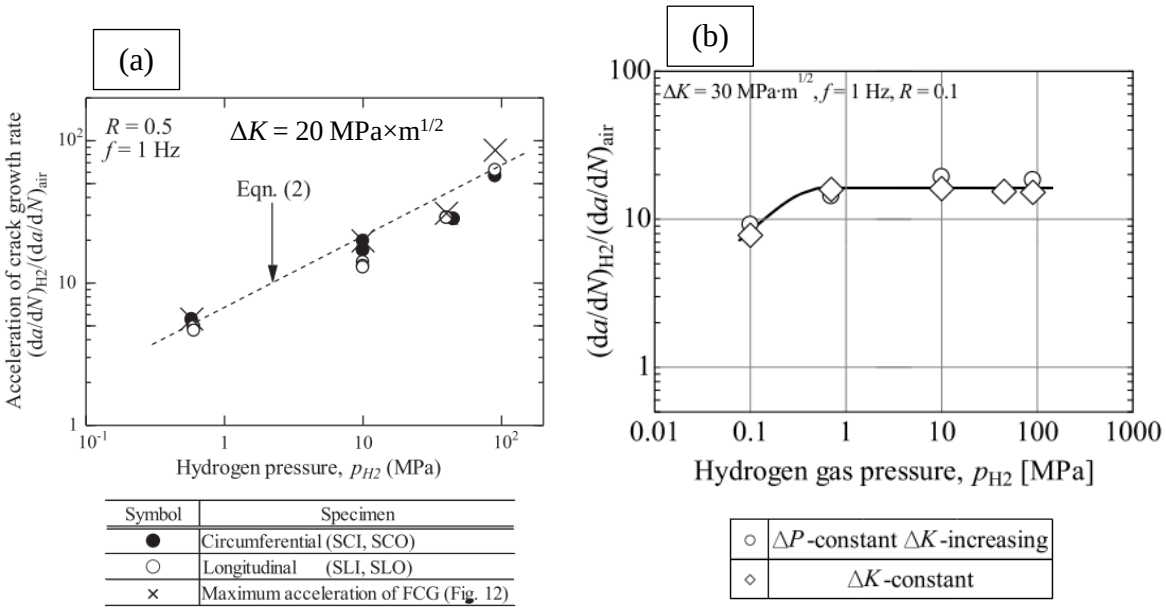

Figure 3 - 21 Dependency of FCGR enhancement on hydrogen gas pressure in Ni-Cr-Mo steel by Macadre et al. [72] (a) and in low carbon steel by Yoshikawa et al. [142, 143] (b).

3.5.2 Time-dependency of HAFCG

The obtained results from the FCG tests in Armco iron have been analyzed so far by fatigue crack growth rate per cycle da/dN, namely a cycle basis, which does not take into account the time. On the other hand, Bilotta et al. [25, 27] has revealed that the HAFCG enhancement in a precipitation-hardened martensitic stainless steel 15-5PH exhibits a time-dependency. Figure 3 - 22a and b respectively show the FCGR per cycle da/dN [m/cycle] versus ΔK and the crack growth rate per second da/dt [m/s] versus K_{max} of the FCG tests in 15-5PH at various loading frequency under air, nitrogen and gaseous hydrogen. As shown in Figure 3 - 22a, the HAFCG rates at P_{H2} = 9 MPa show the dependence on the loading frequency: a higher FCGR at a lower loading frequency. In Figure 3 - 22b, the FCGR data is rearranged by da/dt and K_{max}. This diagram shows that da/dt at P_{H2} = 9 MPa are almost the same in the accelerated regime regardless of the loading frequency. This diagram also includes the result of a sustained loading static crack propagation test at P_{H2} = 9 MPa (●), and it is consistent with the da/dt values of the FCG tests. This result suggests that the HAFCG enhancement in 15-5PH steel is mainly contributed by the static component of crack growth enhancement which depends on the time.

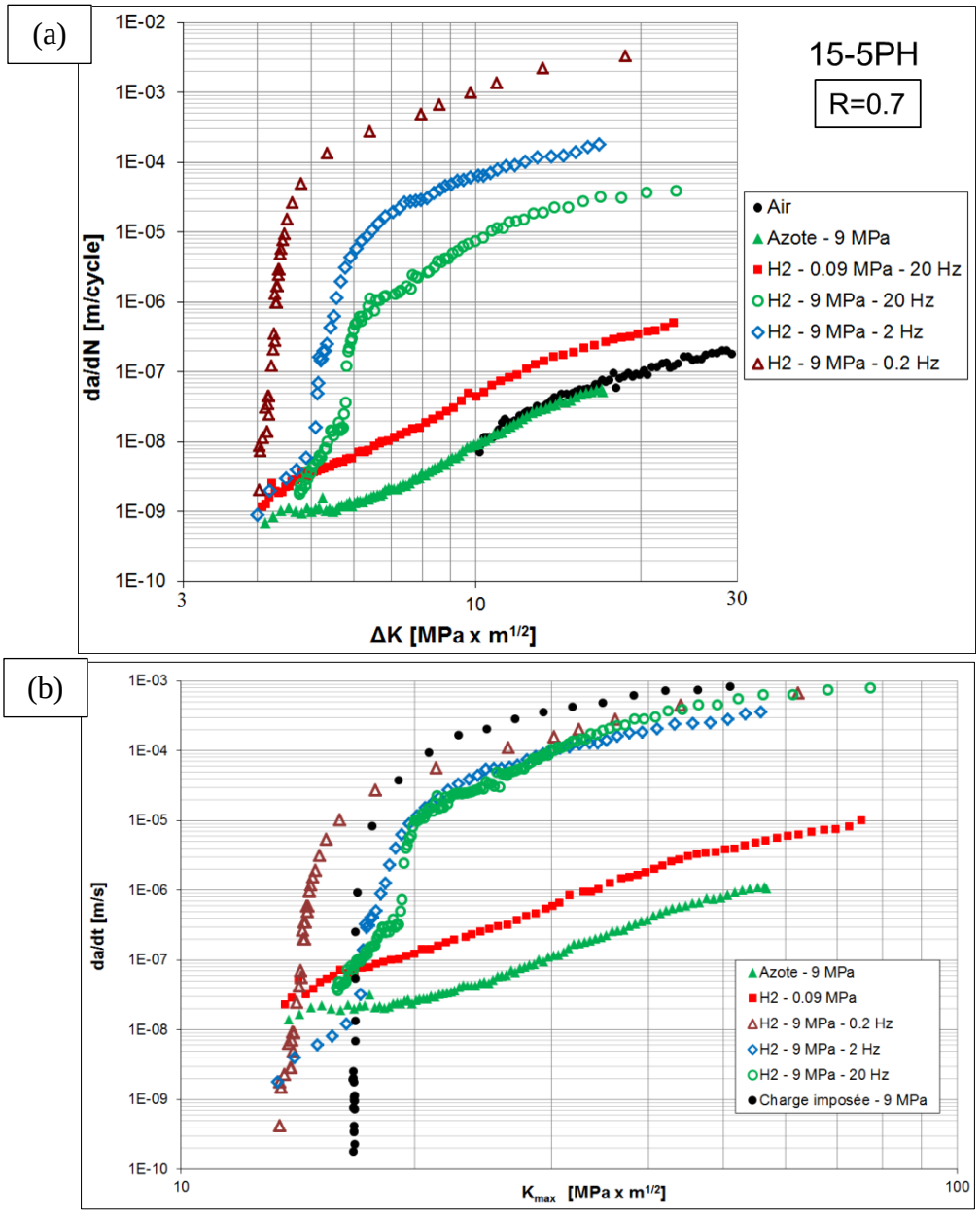

Figure 3 - 22 da/dN vs. ΔK (a) and da/dt vs. K or K_{max} (b) in 15-5PH steel obtained by Bilotta [27].

To investigate the time-dependency of HAFCG in Armco iron, the FCGR data was rearranged to display d*a*/d*t* versus K_{max} as shown in Figure 3 - 23. This diagram shows that the FCGRs in hydrogen at different loading frequencies are not consistent. This result clearly indicates that the HAFCG enhancement in Armco iron is not controlled by the time-dependent static component of crack growth as in the case of 15-5PH steel. In other words, hydrogen enhances the cyclic crack propagation in the case of Armco iron, while hydrogen enhances the static crack propagation in the case of 15-5PH steel.

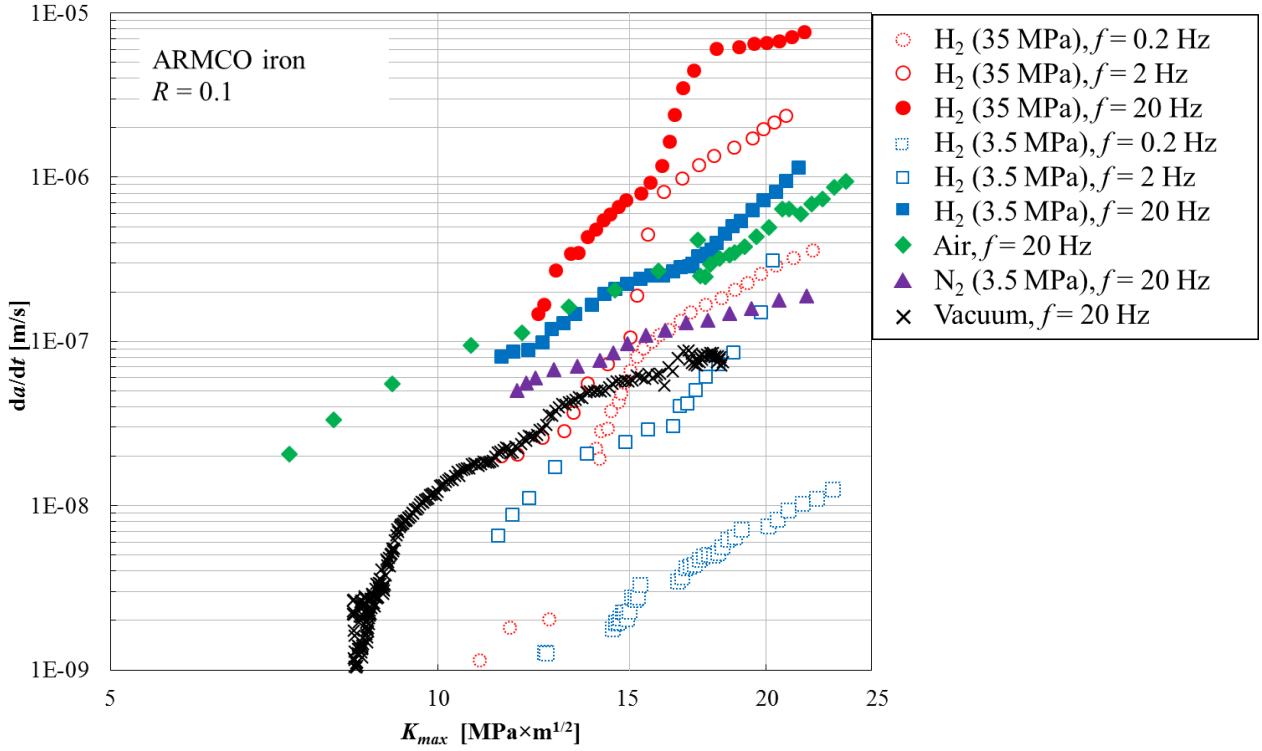

Figure 3 - 23 Static component of FCGR da/dt vs. K_{max} in Armco iron.

This difference in the hydrogen effect is likely related to the difference in yield strength σ_y: σ_y = 170 MPa for Armco iron and σ_y = 750 MPa for 15-5PH steel [27]. Nibur et al. [173] have studied a crack arrest threshold K_{TH} (K value when a static crack grwoth by constant dislpacement stops) and a crack initiation threshold K_{THi} (K value when a static crack grwoth starts by rising applied loading) in several kinds of steels in gaseous hydrogen P_{H2} = 103Mpa. They showed that both parameters are a function of the yield strength as shown in Figure 3 - 24. Both parameters decrease with the increase in the yield strength. Based on this diagram, the value of K_{THi} in 15-5PH steel can be predicted as about K_{THi} = 60 MPa×m$^{1/2}$ which is higher than the present case (~15 MPa as shown in Figure 3 - 22b). Also, according to Figure 3 - 24, the value of K_{THi} in Armco iron should be very high (around K_{THi} = 80 MPa×m$^{1/2}$ or more) which is equivalent to ΔK = 72 MPa×m$^{1/2}$ in the FCG test (R = 0.1). Since this value of ΔK is much higher than the investigated ΔK range in this study (< 20 MPa×m$^{1/2}$), therefore, this fact suggests that the investigated HAFCG rates in Armco iron do not involve the static cracking component, i.e. a time dependency. This difference in time-dependency of HAFCG in Armco iron and 15-5PH steel is a possible explanation of difference in the mechanism of HAFCG itself between a low strength material and a high strength material.

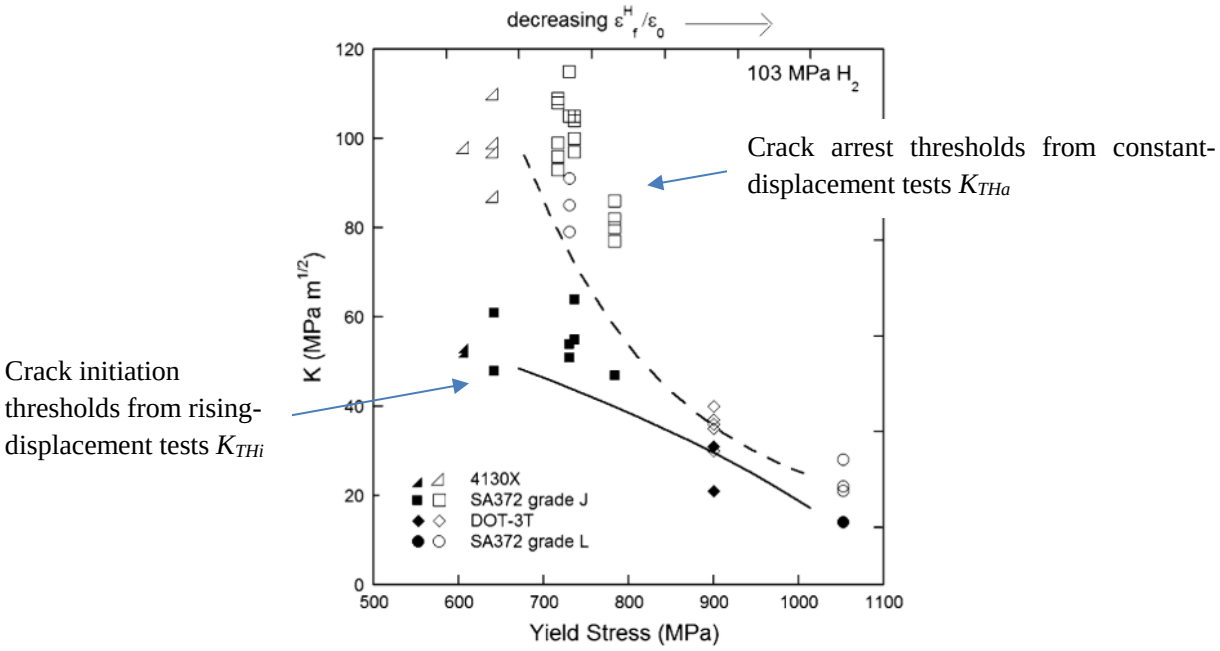

Figure 3 - 24 Crack arrest thresholds in 103 MPa H_2 gas from constant-displacement tests (K_{THa}, open symbols), and crack initiation thresholds from rising-displacement tests (K_{THi}, filled symbols), plotted as a function of yield strength, obtained by Nibur et al. [173].

3.5.3 Change in fracture mode induced by hydrogen

Since the change in FCGR behavior was discussed in the previous subsection, this sub-section presents the discussion about the fracture modes. The fracture mode in each characteristic regime is summarized in Table 3- 1. As shown in this table, the fracture modes corresponding to each regime at the two different P_{H2} are slightly different. In the non-accelerated regime, the fracture mode was the mix of intergranular and ductile fracture at P_{H2} = 3.5 MPa, while it was only the intergranular fracture at P_{H2} = 35 MPa. In the transition regime, the fracture mode was the QC fracture at P_{H2} = 3.5 MPa, while it was the mix of the intergranular and QC fracture at P_{H2} = 35 MPa.

Table 3- 1 Summary of fracture mode in each regime of ΔK-increasing tests (except the test at P_{H2} = 3.5 MPa and f = 0.2 Hz)

Characteristic regime	**P_{H2} = 3.5 MPa (except *f* = 0.2 Hz)**	**P_{H2} = 35 MPa**
Non-accelerated regime	Intergranular + Ductile transgranular	Intergranular
Transition regime	QC	Intergranular + QC
Accelerated regime	-	QC

The fracture surface transition from the intergranular to the transgranular QC fracture surfaces has been quantitatively investigated in a pure iron by Birenis et al. [157] and in Fe-Si alloy by Wan et

al. [174]. Both researches evaluated the coverage ratios of intergranular and transgranular fracture surfaces with respect to ΔK in FCG tests under gaseous hydrogen [157] and hydrogen-charged condition [174]. They commonly concluded that the intergranular and the ductile transgranular fracture surfaces are gradually replaced by the QC fracture surface during the transition regime accompanied by the FCGR enhancement, and the amount of the intergranular and the ductile transgranular fracture surfaces linearly decreases with the increase in ΔK.

Another interesting fact is that, although no FCGR acceleration in hydrogen was observed at low ΔK values, the significant change in the fracture mode from the transgranular fracture to the intergranular one occurred due to the presence of hydrogen. This phenomenon can be related to the fact that the intergranular facets present the formation of stripe-like markings on intergranular facets (Figure 3 - 10b, d, and f). This microscopic feature might be an important clue for understanding the mechanism of the hydrogen-induced intergranular fracture. To investigate this point, the spacing of the markings was measured at different test conditions and at different ΔK values. The spacing of the plastic markings was measured by counting the number of markings crossing a perpendicular gauge line of length from 5 to 20 μm in the SEM images of the fracture surface in each testing condition. An example of a gauge line of 10 μm is shown as the red line in Figure 3 - 10f. The inclination of the intergranular facet was not considered in this measurement. 5 to 12 measurements were performed for a given test condition. The result is presented in Figure 3 - 25. The black dot and the bar show the average value of the marking spacing and the standard deviation, respectively. As a result, the average values do not seem to depend on the test conditions (ΔK, the hydrogen gas pressure, or the loading frequency). The average value is approximately 0.65 μm which is one or two orders higher than the crack propagation distance per cycle (in the order of 10^{-9} - 10^{-8} m), indicating that the spacing of markings is not corresponding to the macroscopic FCGR. Hence, the stripe-like markings are unlikely striations.

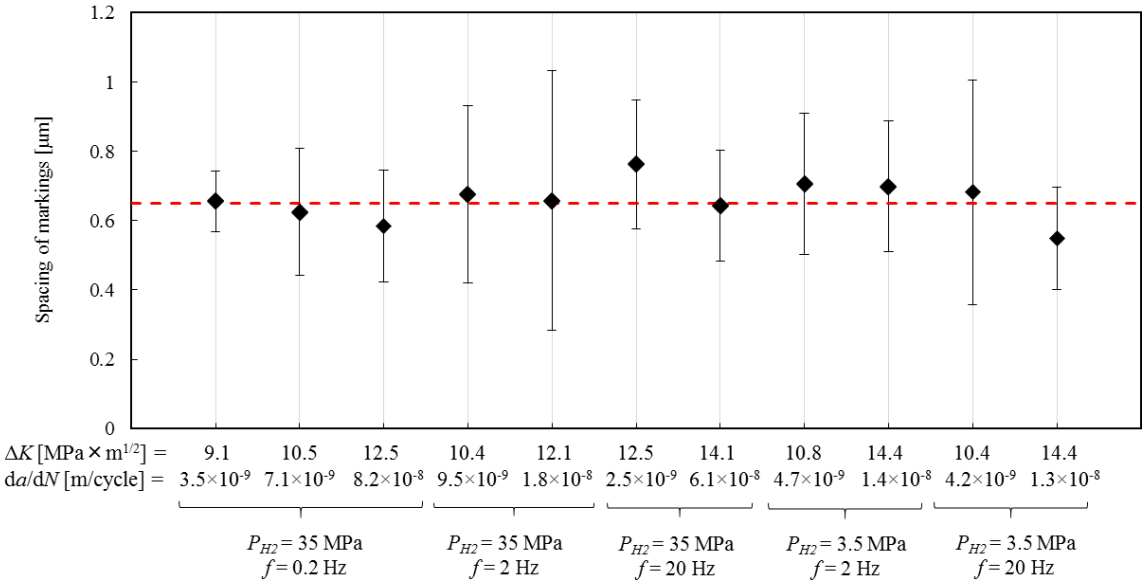

Figure 3 - 25 Spacing of stripe-like markings observed on the surface of intergranular facets at various ΔK values, loading frequencies, and hydrogen gas pressures.

These stripe-like markings have also been reported in some other researches interpreting that a cause of the markings is a crack tip blunting (i.e. a striation [175, 176]) or an emergence of slip activity on grain boundary (i.e. a slip marking [12, 73, 75, 77, 162]). On the other hand, Takahashi et al. [177] observed similar stripe-like markings on a QC fracture surface produced under static crack propagation in a single crystal Fe-Si alloy in a hydrogen atmosphere. They found out that the spacing of the markings is constant (≈ 0.4 μm) regardless of the increase in the value of K associated with the increase in crack propagation rate per second da/dt [m/s]. They concluded that the observed hydrogen-assisted cracking consists in a unit fracture process which is a rate-independent process. The increase of K (i.e. the expansion of plastic zone) reduces the incubation time for gathering solute hydrogen atoms toward the crack tip to initiate the unit fracture process.

Nevertheless the formation mechanism of the plastic markings is not clear, it is commonly accepted that the presence of the markings is an evidence of a certain degree of plastic strain introduced into the grains ahead of the crack tip during the hydrogen-induced intergranular fracture. The accumulation of plastic strain ahead of the intergranular crack has also been confirmed by an in-situ observation of intergranular fatigue crack propagation in low carbon steel under gaseous hydrogen [73] and the scanning transmission electron microscopy (STEM) observations of dislocation structure beneath intergranular facets in pure iron [77] and pure nickel [75, 178]. Therefore, even though the macroscopic feature of the intergranular fracture surface seems to be a brittle type of fracture, its microscopic feature shows some extent of plasticity. A dislocation structure in the interior of grains beneath the intergranular facets is also important to examine in the present case. Therefore, for this purpose, STEM observations of the intergranular facets are carried out in the next chapter.

3.5.4 Attenuation of HAFCG enhancement at very low loading frequency

In the previous section, the attenuation of HAFCG enhancement at very low f has been demonstrated in both ΔK-increasing and ΔK-constant tests. This influence of loading frequency can be summarized as follows: the HAFCG rate increases by decreasing the loading frequency down to a critical value depending on the hydrogen gas pressure (2 Hz for P_{H2} = 3.5 MPa and 0.2 Hz for P_{H2} = 35 MPa). Once the loading frequency becomes lower than the critical value, the HAFCG rate significantly decreases down to the same level as in nitrogen.

The f-dependency of HAFCG is also characterized by the presence of an upper limit of the FCGR enhancement. The upper limit of the FCGR has been highlighted by several researches [16, 72, 143, 172, 179]. The value of this upper limit and the loading frequency causing it are depending on hydrogen gas pressure [143] or pre-charged hydrogen content [72]. Furthermore, the research group at Kyushu University [72, 142, 143, 180, 181] has reported a similar decrease in HAFCG rate occurs at relatively low hydrogen gas pressure (P_{H2} < 10 MPa) in several types of steels, and the loading frequency causing this reduction of FCGR enhancement depends on the hydrogen gas pressure.

Another important feature of the attenuation of HAFCG enhancement by low f is that the apparent change in fracture mode occurred at the same time. The relationship between the fracture modes and the FCGRs at various f is shown in Figure 3 - 26. From this figure, it has been revealed that the ductile fracture is corresponding to the relatively low FCGR, while the QC fracture is corresponding to the relatively high FCGR (except the case at P_{H2} = 3.5 MPa, f = 20 Hz (indicated by *)). Therefore, this result elucidates that the brittle QC fracture is clearly associated with the FCGR enhancement effect even in the case of the attenuation of HAFCG enhancement by low f, as well as the HAFCG enhancement by increasing ΔK. A mechanism of this phenomenon is not clear from the present results. To elucidate the mechanism, a change in crack tip plasticity during this phenomenon is investigated in the next chapter. Based on the insights, the mechanism is discussed in Chapter 5.

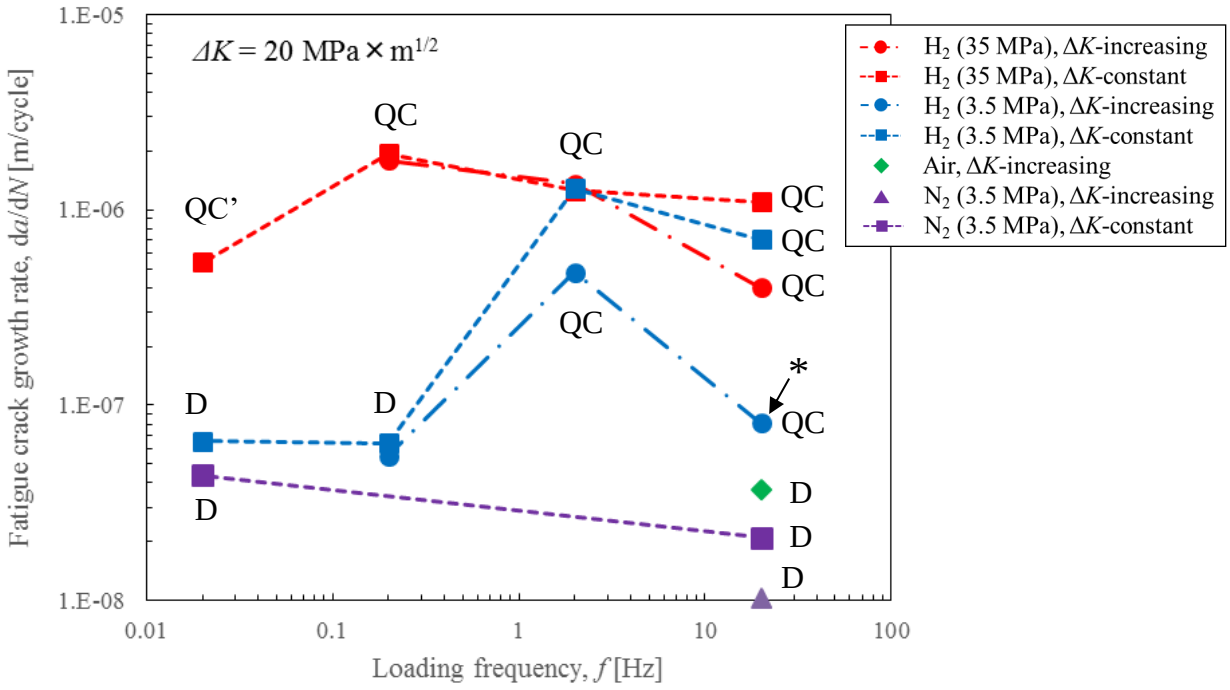

Figure 3 - 26 Summary of fracture modes corresponding to each result of FCGR. QC: brittle transgranular quasi-cleavage fracture, QC': quasi-cleavage fracture with a relatively high amount of cleavage-like facet, and D: ductile transgranular fracture.

3.6 Conclusion

This chapter studied the fatigue crack propagation properties with the influence of hydrogen by conducting FCG tests under gaseous hydrogen. The influence of hydrogen on the FCGR and the fracture mode have been identified. Moreover, the dependency of HAFCG on ΔK, hydrogen gas pressure and loading frequency has been characterized. The main conclusions of this chapter are summarized below.

1. HAFCG rate exhibits three distinct regimes: a non-accelerated regime at low ΔK values, a transition regime, and an accelerated regime at high ΔK values showing FCGR enhancement up to 50 times higher than the FCGR in the air.
2. In the non-accelerated regime, the FCGR in hydrogen is almost the same compared to the one in the air. Fracture mode in hydrogen is a brittle intergranular fracture, in contrast to transgranular in the air at the same ΔK value. Furthermore, stripe-like plastic marking has been observed on intergranular facets.
3. In the transition regime, fracture mode gradually changes from intergranular fracture to transgranular QC one, at the same time HAFCG rate highly increases. After the FCGR acceleration reaches a certain magnitude, the slope of HAFCG rate curve comes back to the same level as in the air, i.e. the accelerated regime. In the accelerated regime, fracture surface is fully covered by the QC fracture surface with brittle-like striations. The compositions of fracture mode in the non-accelerated regime and the transition regime are slightly different at lower hydrogen gas pressure (3.5 MPa).
4. The value of ΔK_{tr} (ΔK triggering the FCGR enhancement (i.e. the transition regime)) decreases by increasing hydrogen gas pressure.
5. The HAFCG rate increases by decreasing the loading frequency down to a critical value depending on the hydrogen gas pressure (2 Hz for P_{H2} = 3.5 MPa and 0.2 Hz for P_{H2} = 35 MPa). Once the loading frequency becomes lower than the critical value, the HAFCG rate significantly decreases down to the same level as in nitrogen. The fracture mode also changes with the attenuation of FCGR enhancement at low f.

Even though the significant change in fracture mode by hydrogen associated with the FCGR enhancement have been revealed, a mechanism of this hydrogen effect is not well understood yet. Since hydrogen influences the material plasticity as examined well in Chapter 1, an interaction between hydrogen and crack tip plasticity is expected to be a key factor to understand a mechanism of HAFCG. Therefore, the crack tip plasticity in the present FCG tests are investigated in the next chapter.

Chapter 4

Analysis of influence of gaseous hydrogen on crack tip plasticity

Résumé

Chapitre 4: Analyse de l'influence de l'hydrogène gazeux sur la plasticité du fond de fissure

R-4.1 Introduction

Le chapitre 4 vise à révéler l'influence de l'hydrogène sur la plasticité en pointe de fissure. Pour cet objectif, la déformation plastique près du trajet de la fissure ou sous la surface de rupture des éprouvettes testées a été évaluée. Afin d'analyser à la fois les zones plastiques monotones et cycliques, la plasticité en pointe de fissure a été analysée à plusieurs échelles allant de l'échelle macroscopique (quelques mm) à microscopique (quelques μm) au moyen de l'observation optique, de la mesure de déplacement hors du plan (« out-of-plane displacement (OPD) ») près du trajet de la fissure, et le « Scanning Transmission Electron Microscopy (STEM) » de la structure de dislocation sous la surface de rupture.

R-4.2 Résultat des analyses

À partir des résultats de la microscopie optique et de la microscopie interférométrique, les OPD de la surface latérale proches du trajet de la fissure ont été observés. Les tailles des zones plastiques monotones et cycliques sont comprises entre leurs valeurs théoriques en contrainte plane et en déformation plane.

Aucune dépendance claire de la taille et de l'OPD de la zone plastique monotone à la pression d'hydrogène et à la fréquence de chargement n'a été confirmée.

La Figure R - 3 montre les résultats de l'analyse de la zone plastique cyclique par STEM de la structure de dislocation située immédiatement sous la surface de rupture pour l'essai sous hydrogène (P_{H2} = 35 MPa, f = 2 Hz) en régime non-accéléré (ΔK = 12 MPa×m$^{1/2}$ (a)) et en régime accéléré (ΔK = 22 MPa×m$^{1/2}$ (b)). En régime non-accéléré (Figure R - 3a), la structure cellulaire de dislocations se développe immédiatement sous les facettes intergranulaires dans l'hydrogène, comme dans l'air et l'azote. Ce résultat indique qu'un cumul de déformation plastique cyclique équivalent est introduit dans les grains en avant du fond de fissure avant propagation.

En revanche, en régime accéléré (Figure R - 3b), il n'y a pas de structure de cellules de dislocation, mais les enchevêtrements de dislocation distribués aléatoirement, alors que pour un même niveau de sollicitation dans l'air la structure de cellules de dislocation est plus développée. On peut considérer que ces enchevêtrements constituent un état préliminaire à la structure cellulaire associée à la déformation plastique cyclique cumulée plus faible que dans l'air. Ceci indique que la plasticité cyclique de la pointe de la fissure sous hydrogène est fortement réduite par la présence d'hydrogène. La même réduction de la plasticité cyclique en pointe de fissure a été observée à des fréquences relativement élevées (≥ 0,2 Hz pour P_{H2} = 35 MPa, ≥ 2 Hz pour P_{H2} = 3,5 MPa) pour lesquelles une augmentation de la vitesse de propagation a été observée (sauf à P_{H2} = 3,5 MPa, f = 20 Hz).

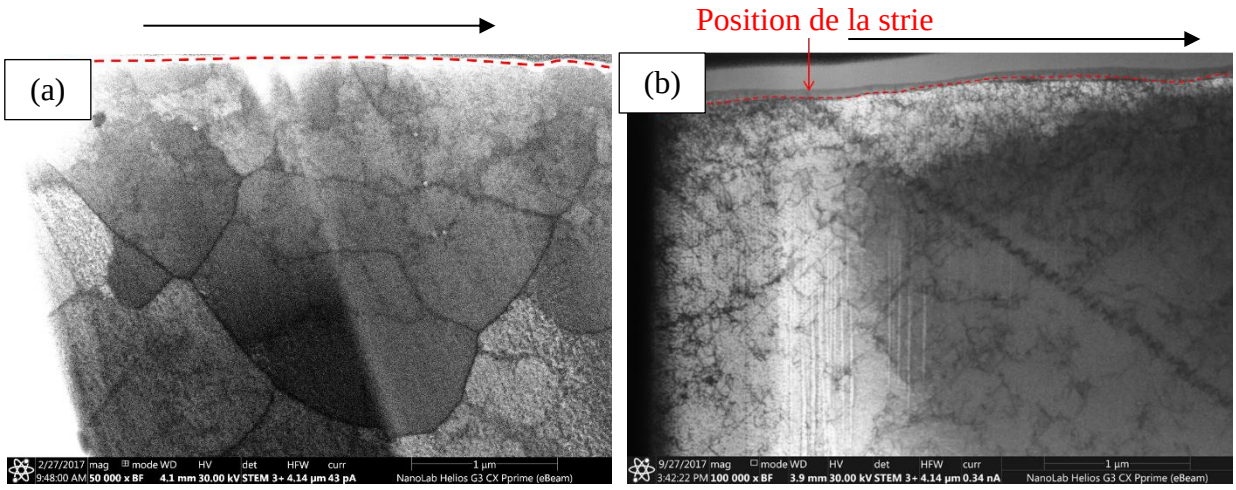

Figure R - 3 Observations STEM immédiatement sous la surface de rupture pour l'essai sous hydrogène (P_{H2} = 35 MPa, f = 2 Hz) à ΔK = 12 MPa×$m^{1/2}$ (a) et ΔK = 22 MPa×$m^{1/2}$ (b).

D'autre part, à des fréquences relativement basses (0,02 Hz pour P_{H2} = 35 MPa et 0,2, 0,02 Hz pour P_{H2} = 3,5 MPa) présentant une augmentation moindre ou nulle de la vitesse de propagation, la réduction de la plasticité cyclique ne se produit pas. Par conséquent, la réduction de la plasticité cyclique est fortement associée à la rupture fragile de type QC et à l'augmentation de la vitesse de propagation des fissures de fatigue.

L'influence de l'hydrogène sur la plasticité en pointe de fissure a été identifiée comme décrit ci-dessus. La plasticité étant clairement associée à la modification de la propagation des fissures de fatigue sous hydrogène gazeux, il est essentiel de comprendre le mécanisme de la propagation de la fissure de fatigue affectée par l'hydrogène décrit au chapitre 5.

----------(Fin du résumé)----------

4.1 Introduction

In the previous chapter, the FCG behavior in Armco iron under gaseous hydrogen in terms of the FCGR and the fracture surface have been investigated. Also, the dependency of HAFCG on the three parameters (the stress intensity factor ΔK, the hydrogen gas pressure P_{H2}, and the loading frequency f) has been identified. Besides, the peculiar drop of FCGR at very low loading frequency has been revealed. However, the mechanisms of these hydrogen effects are not clarified yet.

As revealed from the results of FCG tests, the brittle QC fracture mode is clearly associated with the FCGR enhancement. As mentioned in Chapter 1, some models proposed in the literature involve the modification of crack tip plasticity by hydrogen which is mainly or partially related to the FCGR enhancement. Therefore, the crack tip plasticity is expected as a key factor to understand a mechanism of HAFCG. Because of this, this chapter is aimed to investigate the influence of gaseous hydrogen on the plastic deformation in the vicinity of the crack tip in order to clarify a mechanism of HAFCG.

For this purpose, plastic deformation near the crack path was investigated because it is a trace of a crack tip plasticity during the FCG. The following three analyses were performed for this investigation: the optical observation of the crack path; the measurement of out-of-plane displacement (OPD); and the STEM (Scanning Transmission Electron Microscopy). The optical observation and the OPD measurement were aimed to analyze monotonic and cyclic plastic deformation formed ahead of the crack tip at the macroscopic scale (from a few hundred μm to a few mm). On the other hand, the STEM was applied to the microstructure beneath the fracture surface to directly observe the dislocation structure developed within few μm away from the crack tip.

4.2 Theoretical plastic zone size

Before analyzing the plastic deformation in the vicinity of the crack tip, the monotonic and cyclic plastic zone sizes were theoretically estimated. Figure 4 - 1 shows the schematic drawing of the monotonic and the cyclic plastic zones around the fatigue crack tip [182].

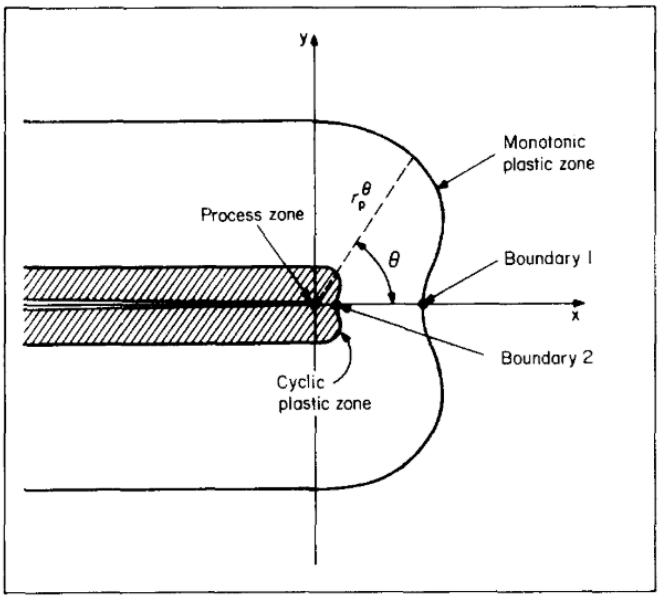

*Figure 4 - 1 Schematic drawing of monotonic and cyclic plastic zones around the fatigue crack tip [*182*].*

The monotonic plastic zone sizes r_p under plane stress and plane strain conditions are theoretically represented by [182–184]:

Plane stress condition: $r_p = \frac{1}{\pi}\left(\frac{K_{max}}{\sigma_y}\right)^2$; *4 - 1*

Plane strain condition: $r_p = \frac{1}{3\pi}\left(\frac{K_{max}}{\sigma_y}\right)^2$. *4 - 2*

On the other hand, according to Rice [183, 184], cyclic plastic zone sizes Δr_p under plane stress and plane strain conditions are expressed by:

Plane stress condition: $\Delta r_p = \frac{1}{\pi}\left(\frac{\Delta K}{2\sigma_y}\right)^2 = \frac{1}{\pi}\left(\frac{(1-R)K_{max}}{2\sigma_y}\right)^2 = \frac{(1-0.1)^2}{4}\frac{1}{\pi}\left(\frac{K_{max}}{2\sigma_y}\right)^2 = 0.2025 r_p$; *4 - 3*

Plane strain condition: $\Delta r_p = \frac{1}{3\pi}\left(\frac{\Delta K}{2\sigma_y}\right)^2 = 0.2025 r_p$. *4 - 4*

The cyclic plastic zone size is thus about 20 % of the monotonic one. If the minimum loading is 0 (R = 0), the cyclic plastic zone size is 1/4 (25 %) of the monotonic one. Figure 4 - 2 shows the evolution of the calculated plastic zone size as a function of ΔK. The plastic zone sizes are indicated as the half values $r_p/2$, $\Delta r_p/2$. It can be seen in this diagram that both plastic zone sizes increase by increasing ΔK.

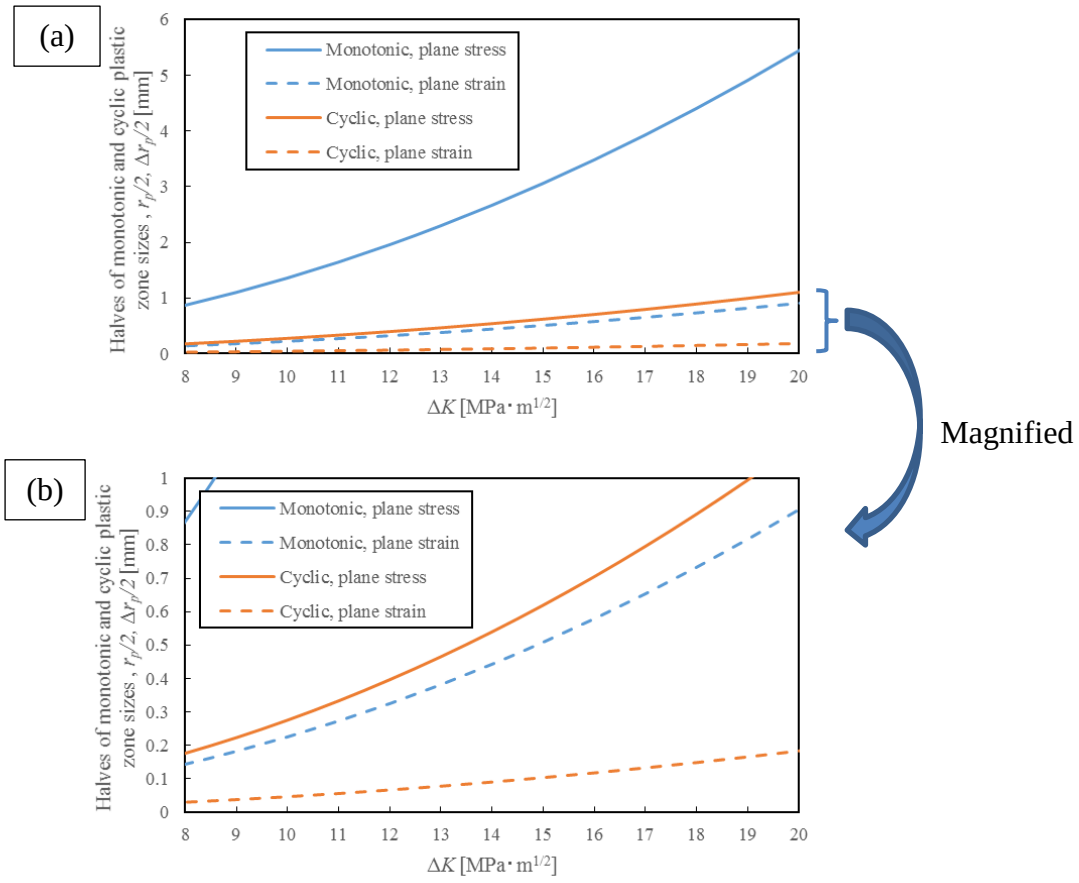

Figure 4 - 2 Evolution of monotonic and cyclic plastic zone sizes in plane stress condition with an increase in ΔK (a), and its magnification in low value part (b).

4.3 Optical observation of crack path

4.3.1 Observation result in Δ*K*-increasing tests

Firstly, the optical observation of the fatigue crack path on the side surface of the tested CT specimens has been conducted. For the observation, the optical microscope (ZEISS Imager Vario Z2) was used.

Figure 4 - 3 shows the optical observations in the tests under hydrogen at P_{H2} = 35 MPa with various loading frequencies f = 0.2 (a), 2 (b), and 20 Hz (c). At P_{H2} = 35 MPa, f = 0.2 Hz (Figure 4 - 3a). Only one side of the surface was observed because the other one was machined for different analyses. In this figure, the fatigue crack initiated from the notch in the left side of the image and propagated to right direction. In nitrogen and air, it can be noticed that the size of the plastically-deformed zone near the crack path gradually develops from left to right with increasing Δ*K*. These plastically-deformed zones are the monotonic plastic zone formed during the crack growth. Also, the monotonic plastic zone size suddenly increases near the end of the crack path. This is caused by the formation of the monotonic plastic zone in front of the crack tip reaching

the back surface of the CT specimen. Once it occurs, the entire ligament (the uncracked part) of the specimen is plastically deformed, and the monotonic plastic zone size is rapidly enlarged. This burst of plastic zone size always occurs in out of limitation of the LEFM defined by the ASTM standard [144] (Equation 3 - 3). This state does not satisfy anymore the small-scale yielding condition [144] which is required for considering the LEFM.

The monotonic plastic zone size is quite largely fluctuating along the crack path and between each side of the specimen. For example, at P_{H2} = 35 MPa, f = 20 Hz (Figure 4 - 3c), the monotonic plastic zone size decreases in some parts even with the increase in ΔK. Also, the monotonic plastic zone size of the lower side is much larger than the upper side.

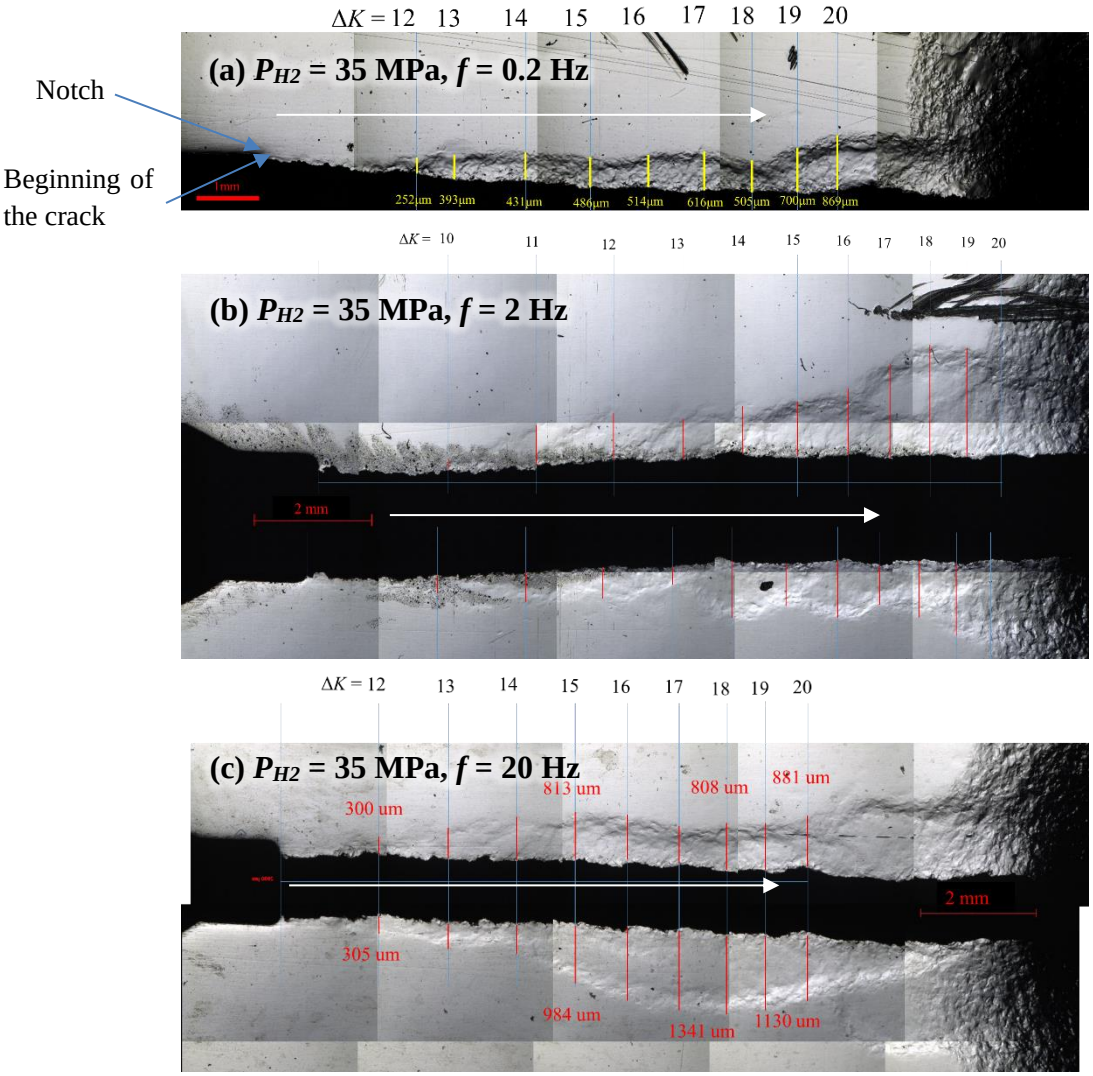

Figure 4 - 3 Crack path appearances of the FCG tests under hydrogen at P_{H2} = 35 MPa with various loading frequencies f = 0.2 (a), 2 (b), and 20 Hz (c). The crack propagation direction is from left to right.

The monotonic plastic zone sizes between in the inert environments and in hydrogen with various P_{H2} and f were compared (optical images in air, nitrogen and hydrogen at P_{H2} = 3.5 MPa are shown in Appendix). However, it was difficult to find clear difference in monotonic plastic zone size by qualitatively comparing the optical images. Thus, the monotonic plastic zone size was

evaluated by measuring the width of plastically-deformed parts at the positions corresponding to ΔK. The measured parts are indicated by yellow or red lines in Figure 4 - 3 for example. All four crack lips were measured for each specimen except the case of P_{H2} = 35 MPa, f = 0.2 Hz (Figure 4 - 3a) in which only two crack lips were measured.

The measurement result is shown in Figure 4 - 4. The measured values are indicated as a half value of the monotonic plastic zone size $r_p/2$. In this diagram, the plots show the averaged values and the uncertainty bars the maximum value and the minimum one. The values of $r_p/2$ in all the tests increased by increasing ΔK. Although there are some small differences in $r_p/2$ between the tests, they are likely a result of the fluctuation of $r_p/2$ because the fluctuation is so large as indicated by the uncertainty bar. Therefore, there is likely no influence of the testing parameters on monotonic plastic zone size. The black dotted lines in the diagram show the theoretical half value of the monotonic plastic zone sizes under the plane stress and the plane strain conditions calculated by Equations 4 - 1 and 4 - 2, respectively. By comparing the measured values with the theoretical ones, it has been confirmed that the measured values of $r_p/2$ are distributed between the theoretical values in plane stress and plane strain conditions. This indicates that the measured monotonic plastic zone size is resulted from a mix of the plane stress (i.e. an ideal condition at the surface) and the plane strain (i.e. an ideal condition in the middle-thick part) conditions.

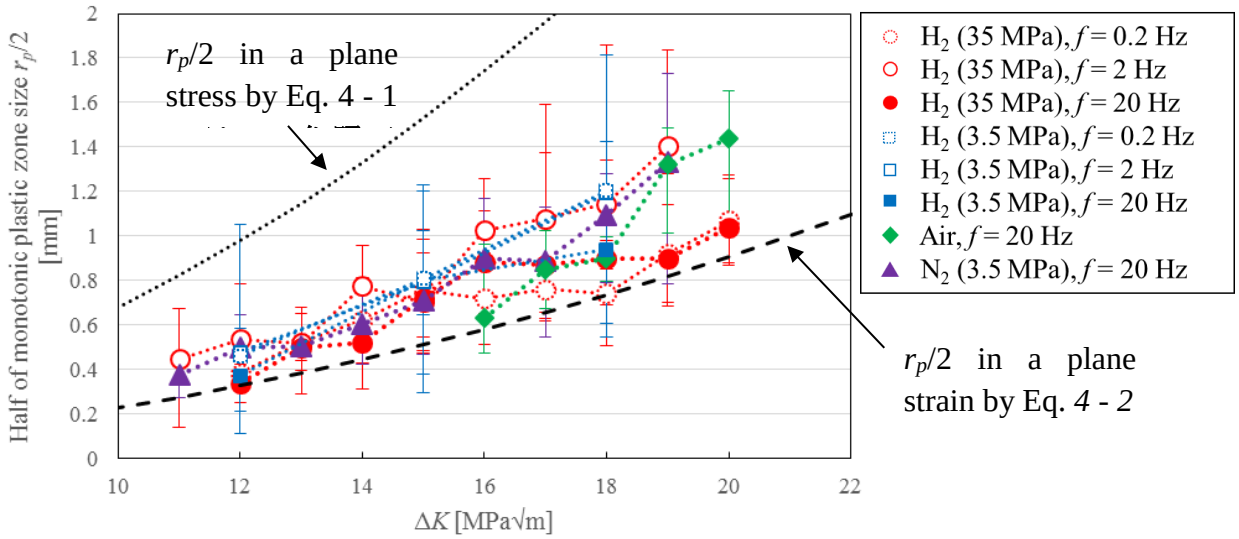

Figure 4 - 4 Evolution of monotonic plastic zone size $r_p/2$ with increasing ΔK in the ΔK-constant tests. The plots show the averaged values and the error bars show the maximum value and the minimum value. The black dashed lines indicate the theoretical values under a plane stress and a plane strain conditions calculated by Equations 4 - 1 and 4 - 2, *respectively.*

By seeing the overview images of the crack path, it is difficult to observe the cyclic plastic zone which is supposed to spread over a few hundred μm from the crack path. Thus, to observe the cyclic plastic deformation, the side surface near the crack path was optically observed with a higher magnification. Figure 4 – 5 shows the higher magnification images at ΔK = 12 MPa×m$^{1/2}$ in the ΔK-increasing tests under air (a), nitrogen (b), and hydrogen at P_{H2} = 35 (c), 3.5 MPa (d) with various loading frequencies. This figure shows that all the crack lips at ΔK = 12 MPa×m$^{1/2}$ (namely, in the non-accelerated regime) present a slight plastic deformation in the area very close

to the crack path. However, there is no clear difference in the extent of the plastic deformation by the difference in the testing conditions.

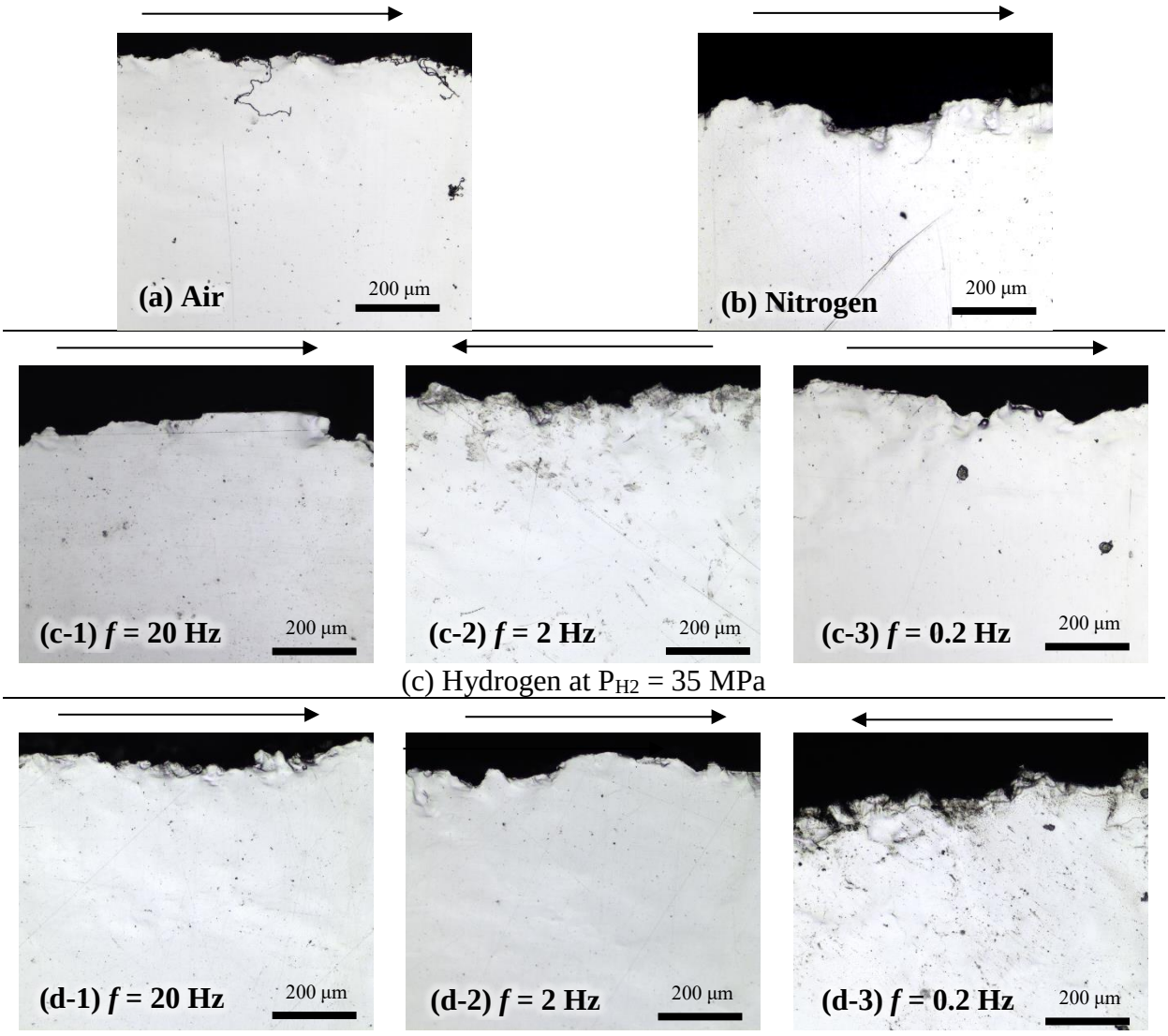

Figure 4 – 5 Higher magnification images of the side-surface near the crack path at ΔK = 12 MPa×m$^{1/2}$ in the ΔK-increasing tests under air (a), nitrogen (b), and hydrogen at P_{H2} = 35 (c) and 3.5 MPa (d). The crack propagation direction is indicated by the arrows.

Figure 4 - 6 shows the high magnification observations at ΔK = 18 MPa×m$^{1/2}$, namely in the accelerated regime. In the images in air and nitrogen (Figure 4 - 6a and b), the plastic deformation near the crack paths is more developed compared to that at ΔK = 12 MPa×m$^{1/2}$ (Figure 4 – 5a and b). The crack lip in nitrogen (Figure 4 - 6b) presents especially higher extent of the plastic deformation. The sizes of the plastic zone in air and in nitrogen are about 100 – 300 μm, which are ranged between the theoretical values of cyclic plastic zone size $\Delta r_p/2$ in plane stress and plane strain conditions. Therefore, these plastic zones are a cyclic plastic zone under a mix of plane stress and plane strain conditions.

On the other hand, the crack lips in the tests in hydrogen (Figure 4 - 6c and d), except the one at P_{H2} = 3.5 MPa, f = 0.2 Hz (Figure 4 - 6d-3), exhibit much less extent of cyclic plastic zone

compared to the ones in air and nitrogen. At P_{H2} = 3.5 MPa, f = 0.2 Hz (Figure 4 - 6d-3), the cyclic plastic zone is much more developed than the other tests in hydrogen and almost the same level as in air and nitrogen. As revealed in Chapter 3, this test at P_{H2} = 3.5 MPa, f = 0.2 Hz exhibited no FCGR enhancement due to the attenuation of the FCGR enhancement at a low loading frequency.

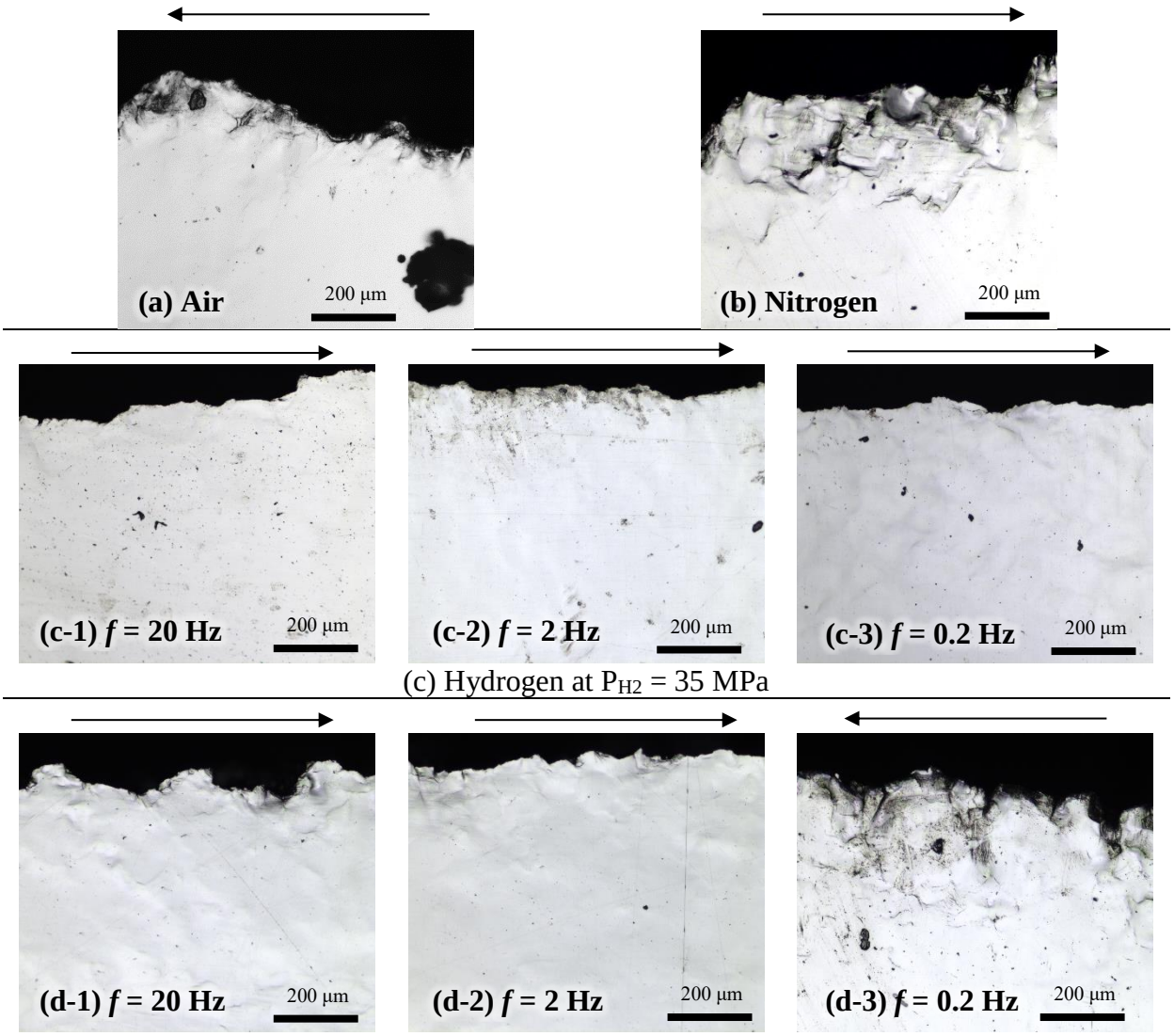

Figure 4 - 6 Higher magnification images of the side-surface near the crack path at ΔK = 18 MPa×m$^{1/2}$ in the ΔK-increasing tests under air (a), nitrogen (b), and hydrogen at P_{H2} = 35 (c) and 3.5 MPa (d). The crack propagation direction is indicated by the arrows.

4.3.2 Observation result in Δ*K*-constant tests

Next, the macroscopic plastic deformation around the crack path in the Δ*K*-constant tests was investigated. Figure 4 - 7 and Figure 4 - 8 show the crack path appearance of the Δ*K*-constant FCG tests (Δ*K* = 20 MPa×m$^{1/2}$) under hydrogen at P_{H2} = 35 and 3.5 MPa, respectively, with various loading frequencies f = 0.02, 0.2, 2, and 20 Hz. The plastic zone size increases from the

pre-crack in air to the crack in hydrogen because the value of ΔK was increased from 15 to 20 MPa×m$^{1/2}$. The monotonic plastic zone sizes $r_p/2$ in hydrogen seems randomly changing by a crack growth. For example, at P_{H2} = 35 MPa (Figure 4 - 7), $r_p/2$ rapidly increases from the middle of the step at f = 20 Hz, and also it decreases after the step at f = 2 Hz, however after the step at f = 0.02 Hz, $r_p/2$ increases again. There is no explanation for these changes in the monotonic plastic zone sizes but the random fluctuation, as same as the case of the ΔK-increasing tests. Because of the large fluctuation, the results of the monotonic plastic zone are not very reliable data.

On the other hand, the cyclic plastic zone exhibits a clear dependency on the loading frequency. At P_{H2} = 35 MPa (Figure 4 - 7), the extent of the cyclic plastic deformation along the crack path became larger by decreasing the loading frequency from 2 to 0.2 Hz. And then, it became even larger at f = 0.02 Hz than the one at f = 0.2 Hz. At P_{H2} = 3.5 MPa (Figure 4 - 8), no clear cyclic plastic deformation is visible at f = 20 Hz, while it is slightly enlarged after switching to f = 2 Hz. And then, the cyclic plastic deformation became prominent at f = 0.2 and 0.02 Hz. This enlargement of the cyclic plastic zone size is likely corresponding to the attenuation of the FCGR enhancement at a low loading frequency, as same as the ΔK-increasing test (Figure 4 - 6). The slight enlargement of the cyclic plastic zone size was observed at the loading frequency corresponding to the FCGR near the upper limit (at f = 0.2 Hz, P_{H2} = 35 MPa and at f = 2 Hz, P_{H2} = 3.5 MPa). Meanwhile, a plastic deformation near the crack path in nitrogen did not change by changing loading frequency from 20 to 0.02 Hz in which crack appearance is shown in Appendix.

The plastic deformation around the crack path formed during the HAFCG has also been examined for several kinds of steels by means of an optical microscopy by Murakami et al. [3, 17, 66, 67, 84, 179]. They also confirmed that the reduction of cyclic plastic deformation during the HAFCG occurs corresponding to the FCGR enhancement.

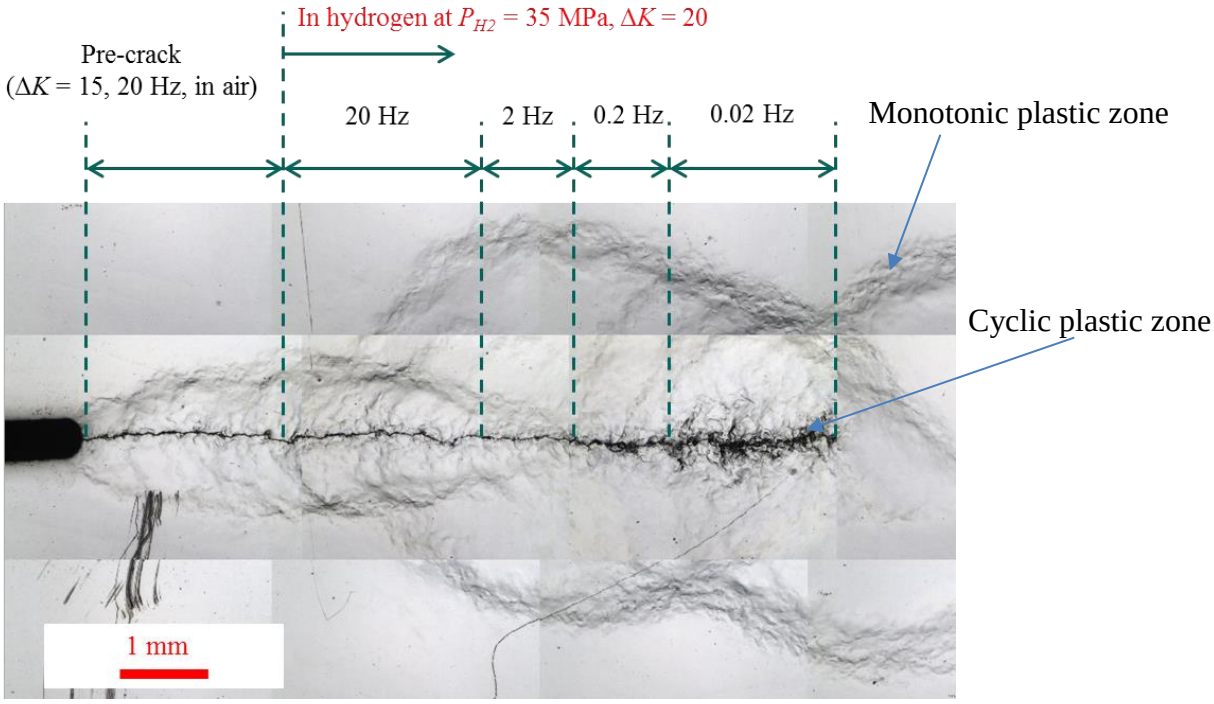

Figure 4 - 7 Crack path appearances of the ΔK-constant FCG test (ΔK = 20 MPa×m$^{1/2}$) under hydrogen at P_{H2} = 35 MPa with various loading frequencies f = 0.02, 0.2, 2, and 20 Hz. The crack propagation direction is from left to right.

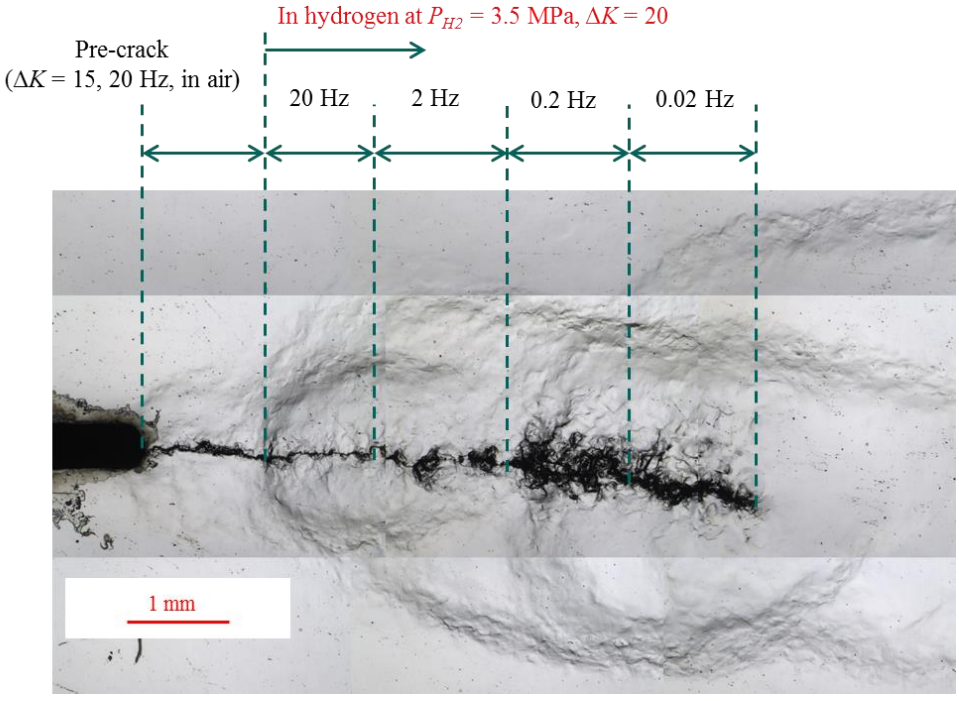

Figure 4 - 8 Crack path appearances of the ΔK-constant FCG test (ΔK = 20 MPa×m$^{1/2}$) under hydrogen at P_{H2} = 3.5 MPa with various loading frequencies f = 0.02, 0.2, 2, and 20 Hz. The crack propagation direction is from left to right.

4.4 Measurement of out-of-plane displacement

In the previous section, the monotonic and cyclic plastic zones around the crack path were optically observed in order to investigate the influence of hydrogen on the macroscopic plastic deformation. As a result, the reduction of cyclic plastic zone size in the vicinity of the crack tip is likely related to the hydrogen effect of FCGR enhancement. However, only the size of the plastically deformed zone was evaluated by means of the optical microscopy. To evaluate properly the extent of the plastic deformation near the crack path, it has to evaluate only the spread size of the plastic deformation, but also the intensity of plastic deformation which is represented by the surface displacement, i.e. OPD (Out-of-Plane Displacement), of the deformed zone. This section presents the measurement results of the OPD in the ΔK-increasing and ΔK-constant tests.

4.4.1 Measurement method

The OPD measurement is a method to evaluate plastic deformation at macroscopic scale (~ few mm) near the crack tip or near the crack path introduced by a fatigue crack propagation. The term "out-of-plane displacement" used in this study is defined as surface displacement in the perpendicular direction ("z" axis) to the plane composed by the crack propagation direction ("x" axis) and the loading direction ("y" axis) as indicated by Figure 4 - 9. The OPD near the crack tip is caused by a lateral shrinkage resulted from the development of plastic strain due to stress intensity near the crack tip.

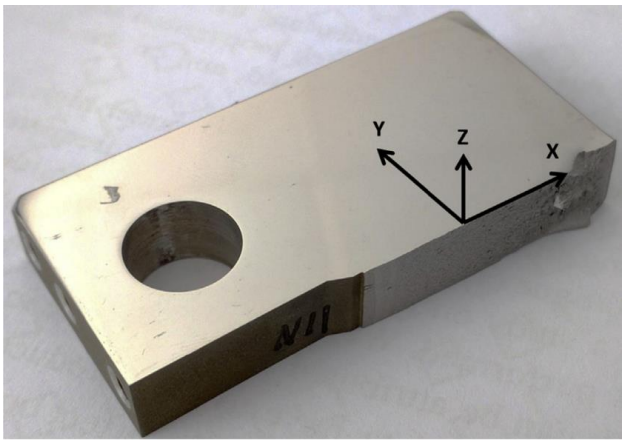

Figure 4 - 9 Definition of the axis: the crack propagation (x), the loading (y), and the out-of-plane displacement (z).

This method has been used by several researches [159, 185–187] for evaluating the extent of plastic deformation near the crack tip in fatigue test and fracture toughness test. The advantages of this method are as follows. The first advantage is that it is easy to perform the measurement since one has to measure only a surface shape. The second advantage is that it is capable to measure a wide area of the surface in mm scale. Generally, a stylus-type surface roughness tester and interferometry are used to measure the surface topography. As a stylus-type surface roughness tester measures the surface shape by touching and tracing the surface with a stylus, the

measurement by this equipment has a risk to damage the surface. On the other hand, interferometry is a method to measure the surface shape by applying coherent light. Its principle is as follows. A half mirror splits the coherent light emitted from one light source into two. The one light is reflected by the measured object and the other light is reflected by the reference mirror. These lights are converged again by the same half mirror. The converged light generates the interference fringes as shown in Figure 4 - 10. By observing the obtained interference fringes, it is possible to know the surface shape of the target object. This method is capable to measure the surface height variation with very high precision in the order of nm. Besides, as it is a non-contact method, there is no damage to the surface by the measurement.

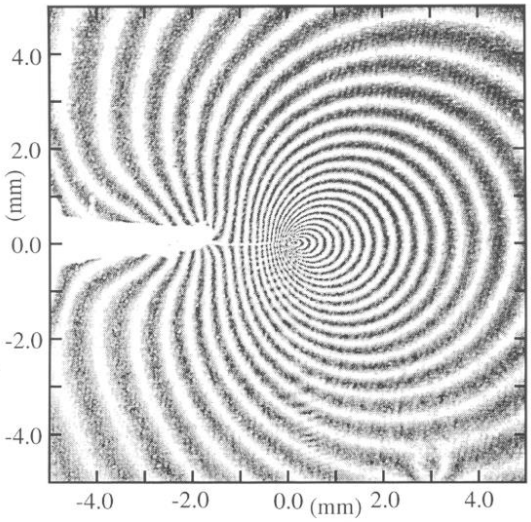

*Figure 4 - 10 Example of interference fringes around the crack shown in the literature [*185*].*

Because of these advantages, the interferometry was applied for the OPD measurement in this study. For the measurement, an interferometric microscope Talysurf CCI6000 (Taylor Hobson Corp., shown in Figure 4 - 11a, at Université de Poitiers) [188] was used. This microscope is capable to measure a surface topography in the principle of the interferometry, and automatically construct a three-dimensional (3D) surface topographic profile as shown in Figure 4 - 11b for example.

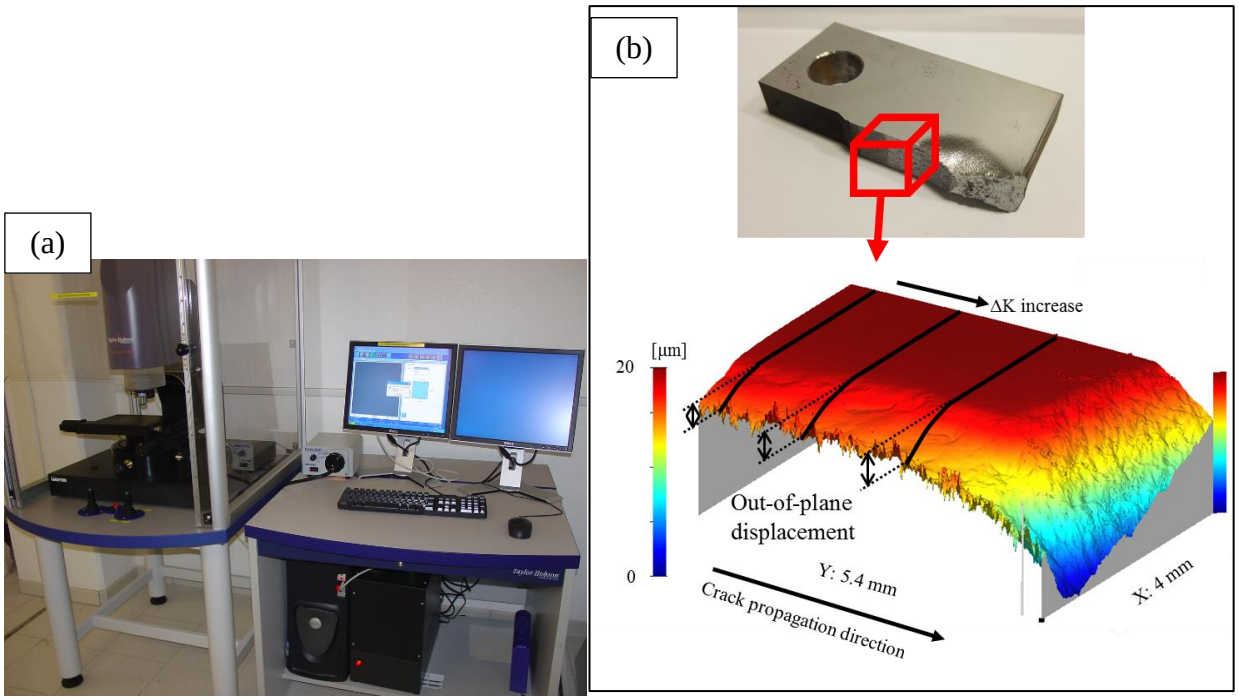

Figure 4 - 11 Appearance of the interferometric microscope Talysurf CCI6000 (a). (b) shows an example of the three-dimensional surface topographic profile obtained by the microscope.

The measurement resolution in z-direction mentioned by the supplier is theoretically 0.01 nm. But as it is influenced by vibration of the floor, it is practically 0.05 nm [188]. The x-y plane resolution depends on a magnification of the objective lens. The objective lenses of ×10 and ×50 were used for the measurements of monotonic and cyclic plastic zones, respectively, because of the difference in the interest area size. The x-y plane resolutions in the objective lens magnifications of ×10 and ×50 are 1.8 and 0.6 µm, respectively.

As it was not possible to measure in-situ the OPD during the FCG tests, the OPD around the crack path after the fracture was measured as a trace of the crack tip plasticity. The measurement area in y-direction (perpendicular to the crack path) was determined to have enough length to capture an actual spread of plastic deformation which was 3.5 – 4 mm for a monotonic plastic zone and 300 – 500 µm for a cyclic plastic zone.

The monotonic plastic deformation was evaluated by a two-dimensional (2D) OPD profile in y-direction at fixed ΔK which was extracted from the measured 3D surface topographic data as illustrated in Figure 4 - 11b, as same method as done by Bilotta [27, 159] for evaluating the monotonic plastic zone in the 15-5PH steel. On the other hand, the cyclic plastic deformation was directly evaluated by a 3D surface topographic image.

4.4.2 Measurement results of monotonic plastic zone

The measurement results of the OPD induced by crack tip plastic deformation in the Δ*K*-increasing and the Δ*K*-constant tests are presented below.

4.4.2.1 Measurement result in Δ*K*-increasing tests

Firstly, the results of the OPDs in the Δ*K*-increasing tests are presented. Figure 4 - 12 shows the OPDs at various values of Δ*K* in the tests under hydrogen at P_{H2} = 35 MPa, f = 0.2 Hz. In this figure, it can be confirmed that the surface near the crack path is displaced in out of plane direction due to the monotonic plastic deformation during the FCG. The amount and the width (which is the length of the deformed part from the crack path) of OPD increase as the value of Δ*K* increases. This figure represents an example of the evolution of OPD by increasing Δ*K*. Similar evolution of the OPD was also confirmed in the other Δ*K*-increasing tests.

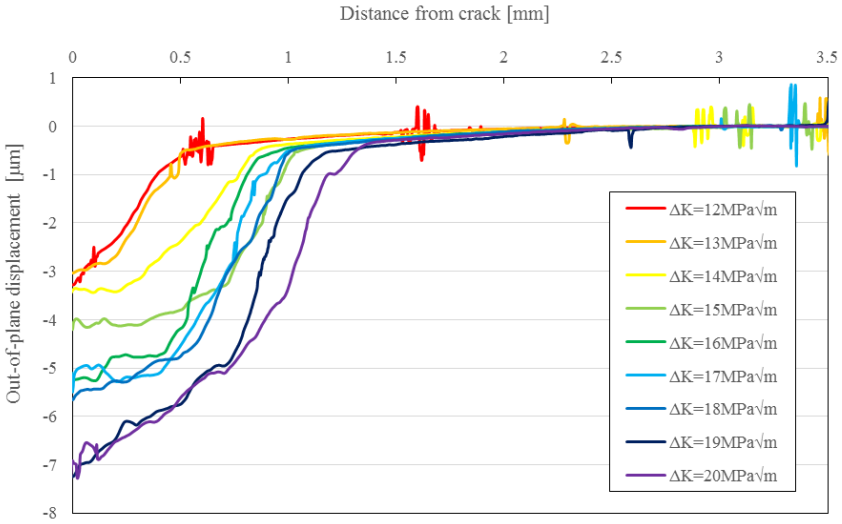

Figure 4 - 12 Evolution of the out-of-plane displacement near the crack path in the ΔK-increasing tests under hydrogen at P_{H2} = 35 MPa, f = 0.2 Hz.

Figure 4 - 13 shows the comparison of the OPDs among all the Δ*K*-increasing FCG tests with various testing conditions at Δ*K* = 12 (a) and 18 (b) MPa×m$^{1/2}$. Also, the black dashed line and the black dash-dot line in the diagrams indicate the halves of theoretical monotonic plastic zone sizes $r_p/2$ in plane stress and plane strain conditions, respectively. These diagrams show that the variation in the OPD curves is quite large even within one test (one specimen). For example, Figure 4 - 14 presents the OPD curves measured at three different positions on the crack lips of the specimen at P_{H2} = 3.5 MPa, f = 0.2 Hz. This diagram shows a large difference between each other although they were measured from the same specimen. The large fluctuation of the monotonic plastic zone size was also optically observed in the previous section. Despite the large fluctuation, most of the OPD curves exhibit a "knee" ranged between the values of $r_p/2$ in plane stress and plane strain. This indicates that the OPD is generated by the monotonic plastic deformation under the mix of plane stress and plane strain conditions.

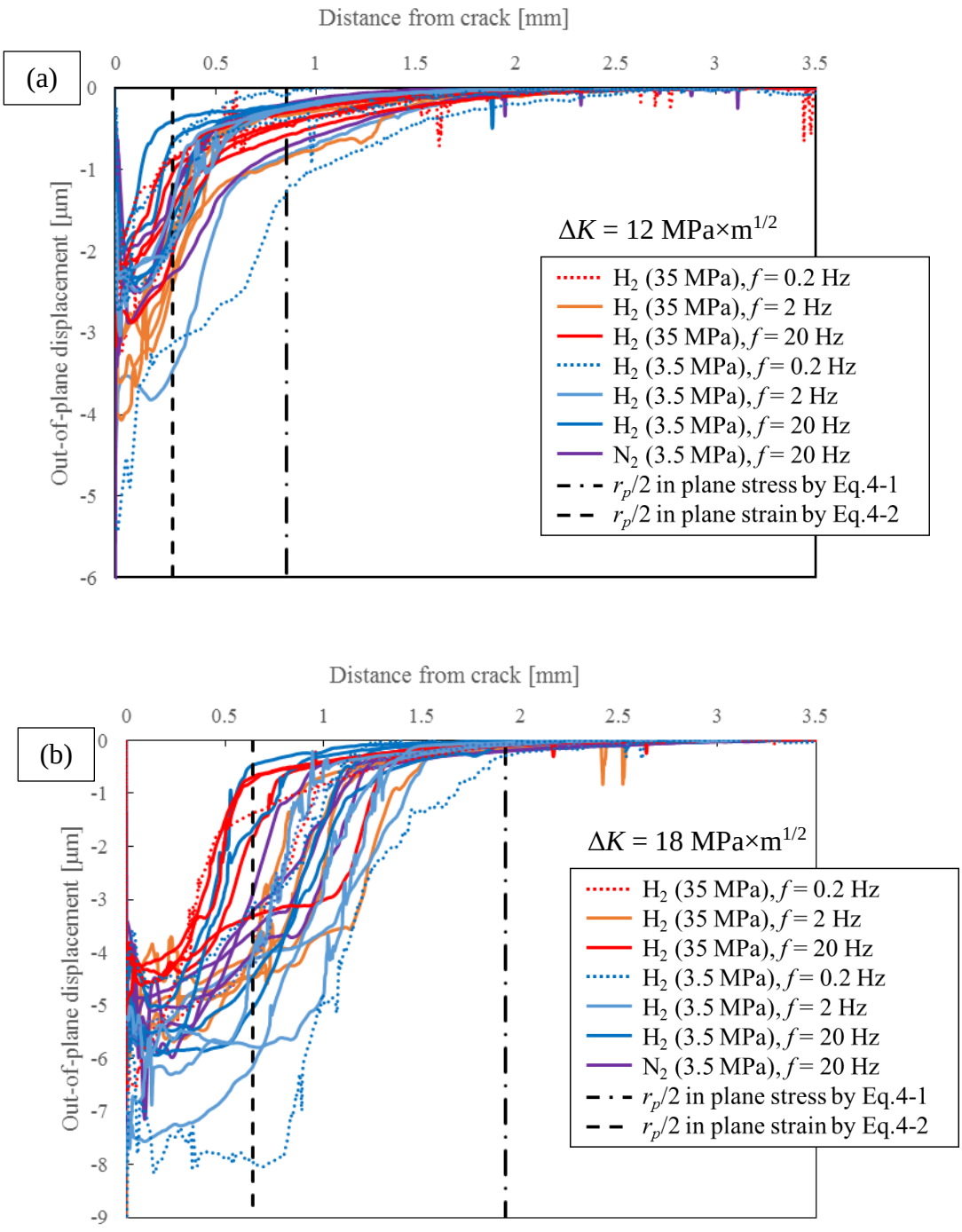

Figure 4 - 13 Comparison of OPDs among the ΔK-increasing FCG tests with various testing conditions at ΔK = 12 (a) and 18 (b) MPa×m$^{1/2}$.

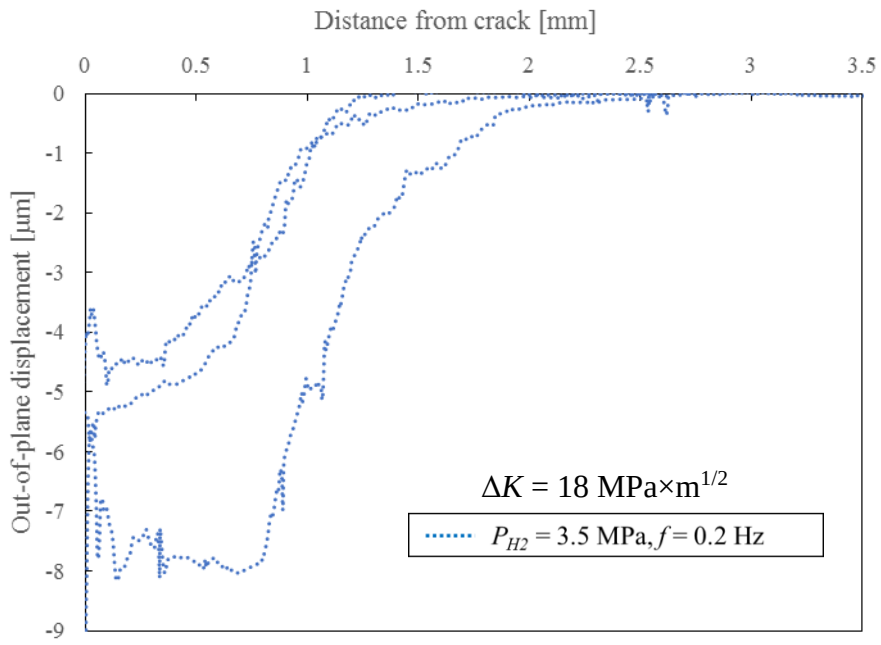

Figure 4 - 14 Example of large variation of the OPDs in one specimen (at P_{H2} = 3.5 MPa, f = 0.2 Hz, ΔK = 18 MPa×$m^{1/2}$).

Due to the large fluctuation, it is difficult to compare the OPDs among the different testing conditions in Figure 4 - 13. Thus, the maximum values of the OPDs were measured to quantitatively compare the OPDs in all the testing conditions. The results at ΔK = 12 and 18 MPa×$m^{1/2}$ are shown in Figure 4 - 15a and b, respectively. These diagrams show the averaged values of the maximum OPDs in each testing condition (each specimen) with the uncertainty bars showing the maximum value and the minimum value. At both ΔK = 12 and 18 MPa×$m^{1/2}$, the averaged values of maximum OPDs are slightly different among the testing conditions. However, as the fluctuations indicated by the uncertainty bars are large, it is difficult to see any clear dependency of the hydrogen gas pressure or the loading frequency on the maximum OPD.

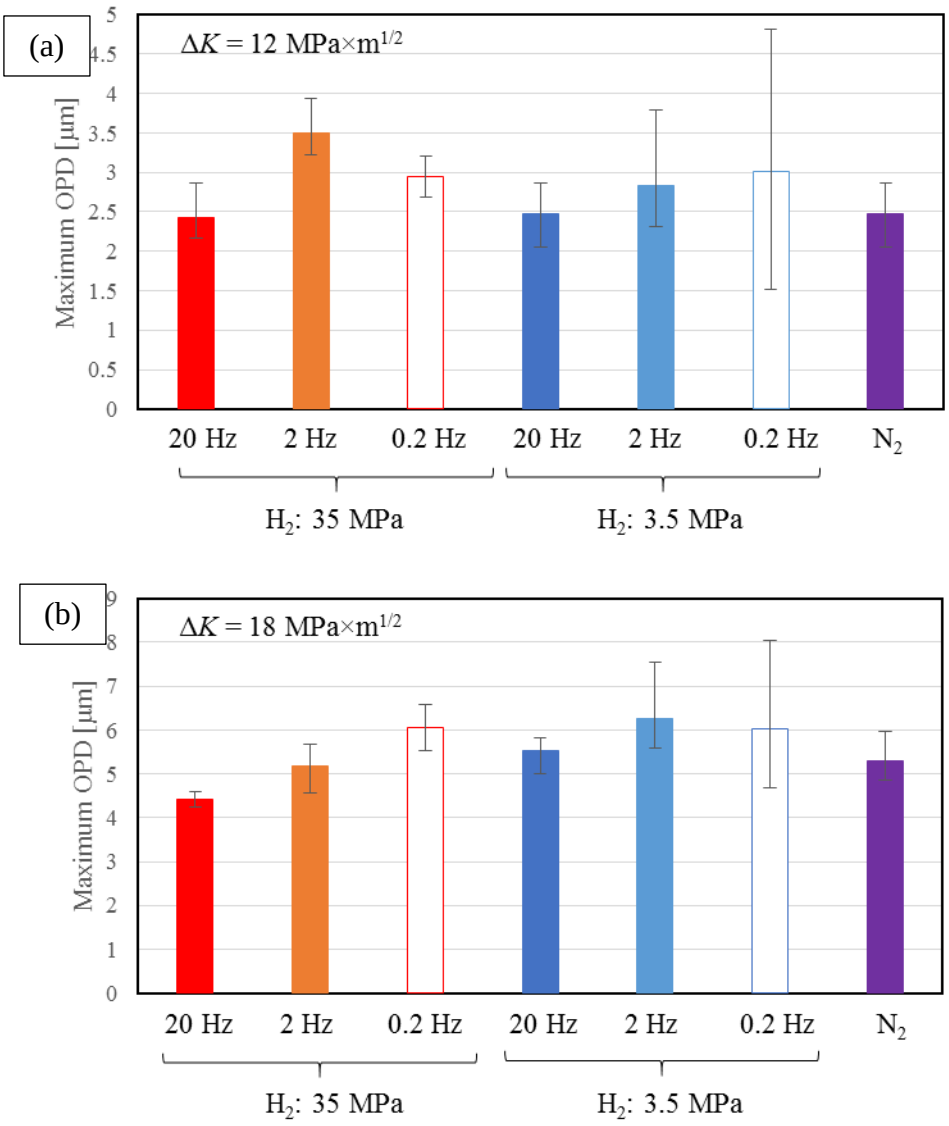

Figure 4 - 15 Maximum values of OPD of all the ΔK-increasing tests. The bar shows the averaged value, and the error bar shows the maximum value and the minimum value.

4.4.2.2 Measurement result in Δ*K*-constant tests

Next, the measurement results of OPDs in the Δ*K*-constant tests (Δ*K* = 20 MPa×m$^{1/2}$) are presented as follows. Most of the OPD measurements were performed before the final fracture of the specimen except for two of four crack lips in P_{H2} = 3.5 MPa, and all two crack lips in P_{H2} = 35 MPa (because only a half part of the specimen was available) in which cases the OPD measurements were performed after the final fracture. Some OPD results in these cases must be excluded from the consideration because they were affected by the plastic deformation during the final fracture of the specimen. Figure 4 - 16 shows the OPD curves at P_{H2} = 3.5 MPa, f = 0.2 (a) and 0.02 Hz (b), and at P_{H2} = 35 MPa, f = 0.2 and 0.02 Hz (c). In Figure 4 - 16a and b, the two of four curves (in blue) are the OPDs measured before the final fracture of the specimen, the other two of four curves (in green) are the OPDs measured after the final fracture of the specimen. In

Figure 4 - 16b, the green curves show larger values of OPD than the blue ones at f = 0.02 Hz. This difference in the OPDs is because the OPDs measured after the final fracture (the green curves) were likely changed by the large plastic deformation due to the final fracture. The large deformation due to the final fracture can be seen in the right part of the optical images in Figure 4 - 3. Though these images are the cases of ΔK-increasing tests, similar large deformation was also confirmed in the ΔK-constant tests. In contrast, in Figure 4 - 16a, there is no big difference in the OPDs between blue and green curves at f = 0.2 Hz. This is likely because the large final deformation does not reach the cracked part at f = 0.2 Hz which is a former step from the one at f = 0.2 Hz, hence, it is further away from the back-side of the specimen. In addition, in Figure 4 - 16c, the OPD curves at P_{H2} = 35 MPa, f = 0.02 Hz show a slightly larger displacement than that at f = 0.2 Hz, this is likely due to the influence of large plastic deformation due to final fracture, rather than a possibility of the dependency on the loading frequency. Therefore, because two of the four OPD curves at P_{H2} = 3.5 MPa, f = 0.02 Hz and the OPD curves at P_{H2} = 35 MPa, f = 0.02 Hz were possibly affected by the final fracture, these results were excluded from the following considerations.

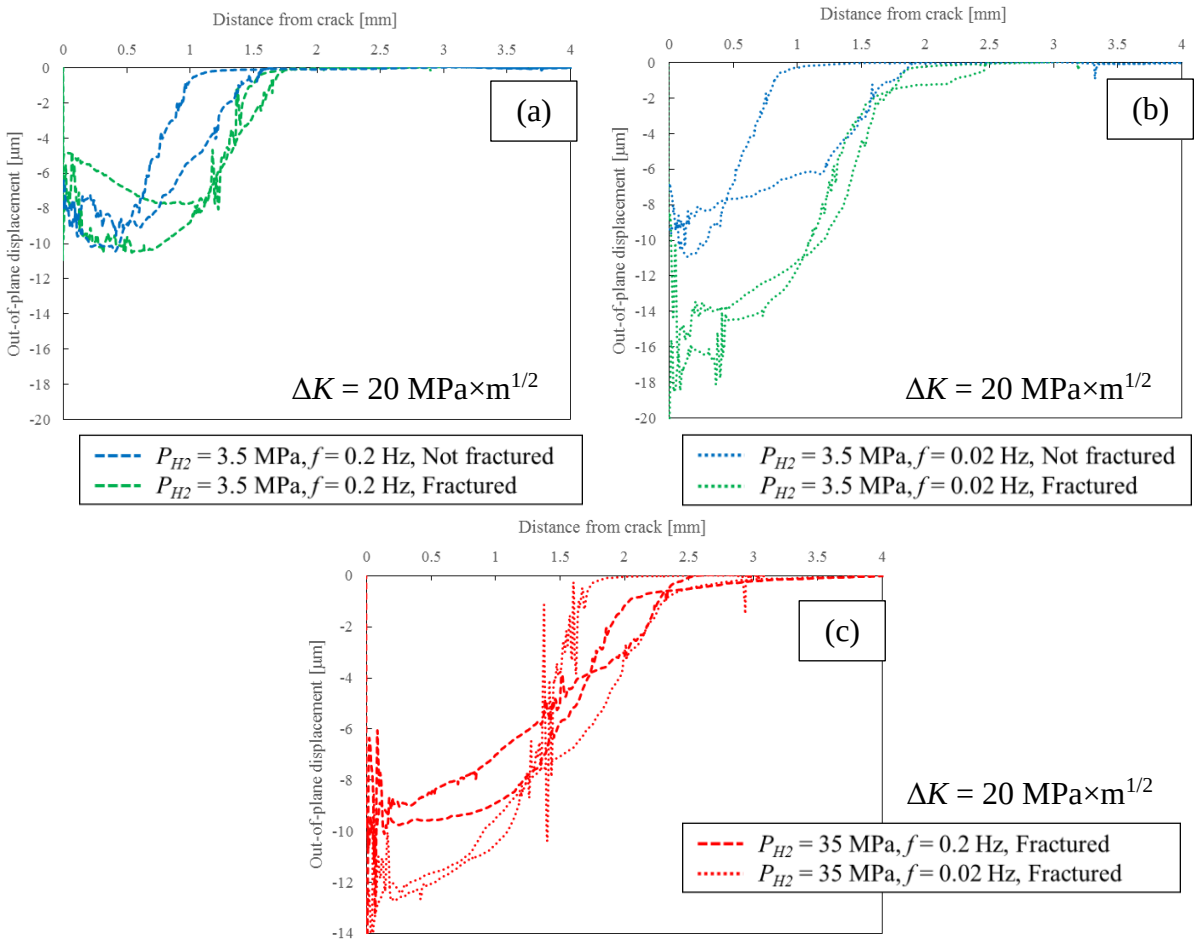

Figure 4 - 16 OPD curves of the ΔK-constant tests (ΔK = 20 MPa×m$^{1/2}$) at P_{H2} = 3.5 MPa, f = 0.2 (a) and 0.02 Hz (b), and at P_{H2} = 35 MPa, f = 0.2 and 0.02 Hz (c).

Figure 4 - 17 shows all the OPD curves of the Δ*K*-constant tests for a comparison of the OPDs among various testing conditions. The black dashed line and the black dash-dot line in the diagrams indicate the halves of theoretical monotonic plastic zone sizes $r_p/2$ in plane stress and plane strain conditions, respectively. It can be confirmed that the position of "knees" of the OPD curves (the beginning of the large displacement) are ranged between $r_p/2$ in plane stress and plane strain conditions, as well as the result in the Δ*K*-increasing tests. The number of the curves is too large to compare each other by only this diagram. Figure 4 - 18 and Figure 4 - 19 show the comparisons of the OPDs by the loading frequency and the environment (the hydrogen gas pressure), respectively. In Figure 4 - 18, one cannot find any clear difference in the OPDs by the different loading frequencies in all the environments: hydrogen at P_{H2} = 35 (a) and 3.5 (b) MPa; and nitrogen (c). One OPD curve in nitrogen at f = 0.02 Hz shows a larger displacement than the others, however, this is likely due to a fluctuation because the other OPDs at f = 0.02 Hz are the same level as the ones at f = 20 Hz.

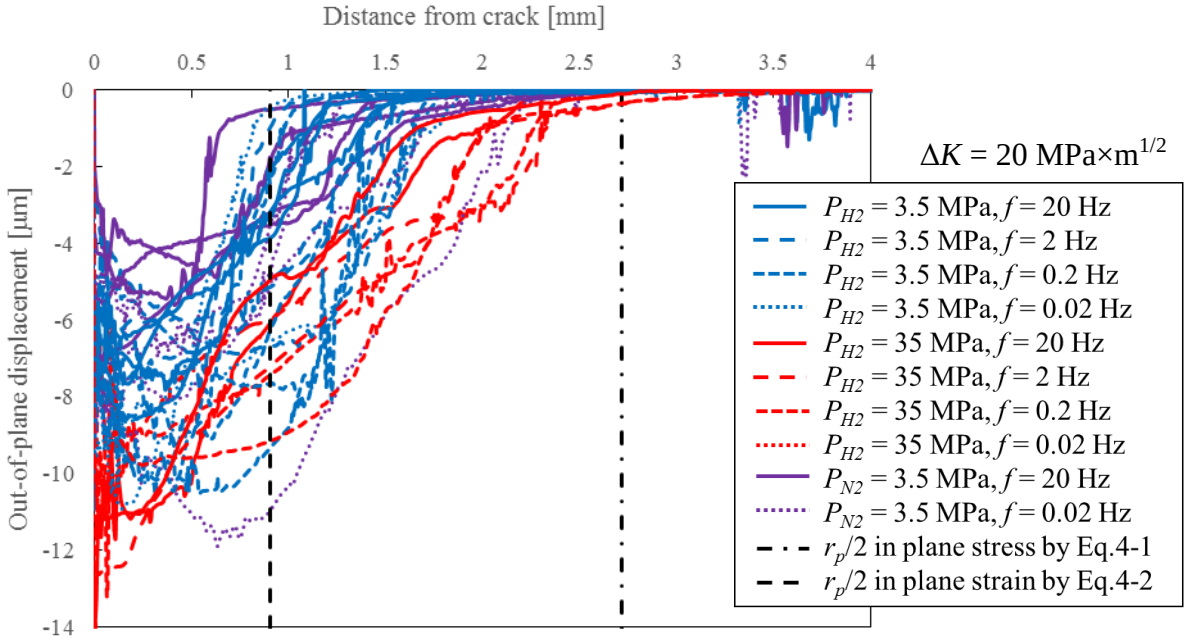

Figure 4 - 17 Comparison of OPDs among all the ΔK-constant FCG tests with various testing conditions at ΔK = 20 MPa×m$^{1/2}$.

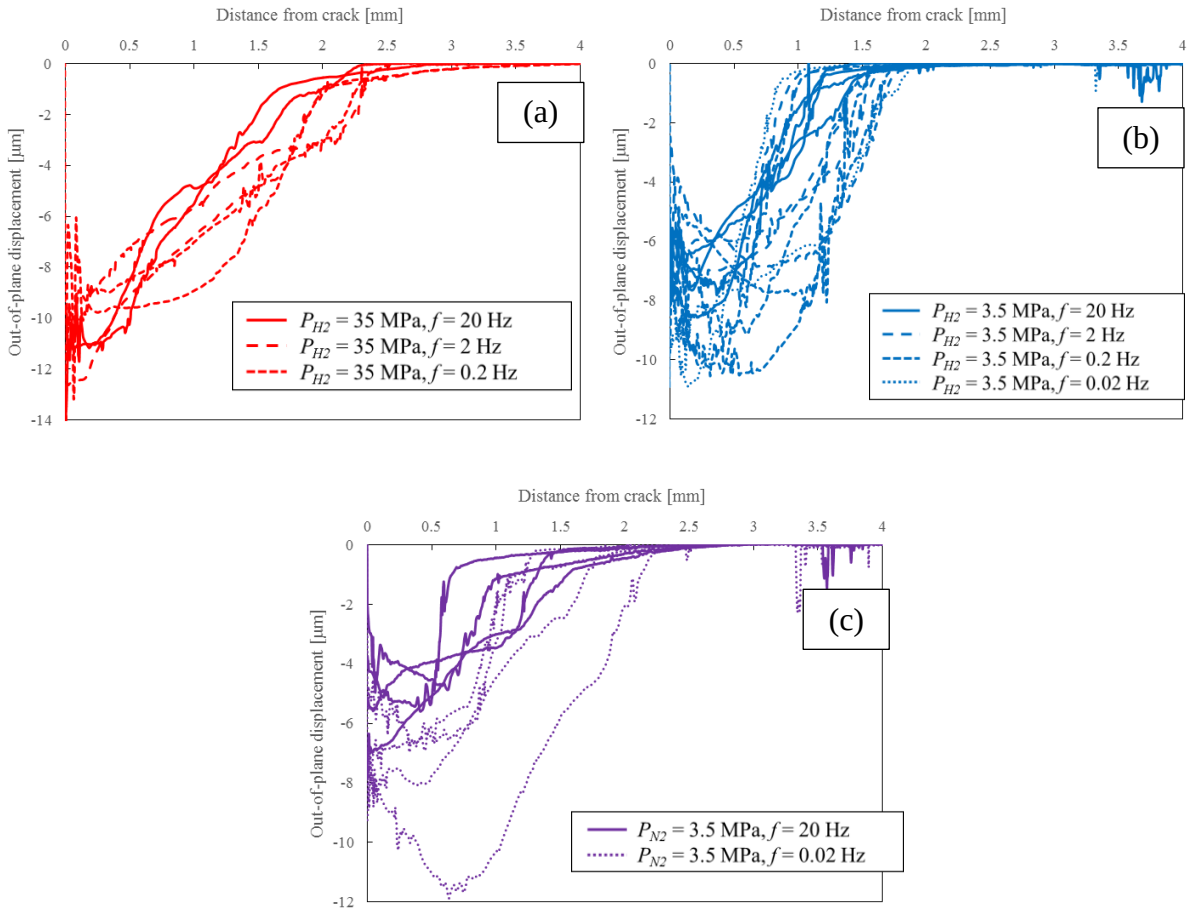

Figure 4 - 18 Comparison of the OPDs of the ΔK-constant FCG tests (ΔK = 20 MPa×m$^{1/2}$) by different loading frequencies in each environment: hydrogen at P_{H2} = 35 (a) and 3.5 (b) MPa; and nitrogen (c).

On the other hand, in Figure 4 - 19, the OPDs at f = 20 (a) and 2 (b) Hz are higher in the order of P_{H2} = 35, 3.5 MPa, and nitrogen. It seems that the OPDs depend on the environments. However, the OPDs in P_{H2} = 35 and 3.5 MPa at f = 0.2 Hz (c) and the OPDs in P_{H2} = 3.5 MPa and nitrogen at f = 0.02 Hz (d) are almost the same values, hence there is no clear difference in the OPDs by the environments.

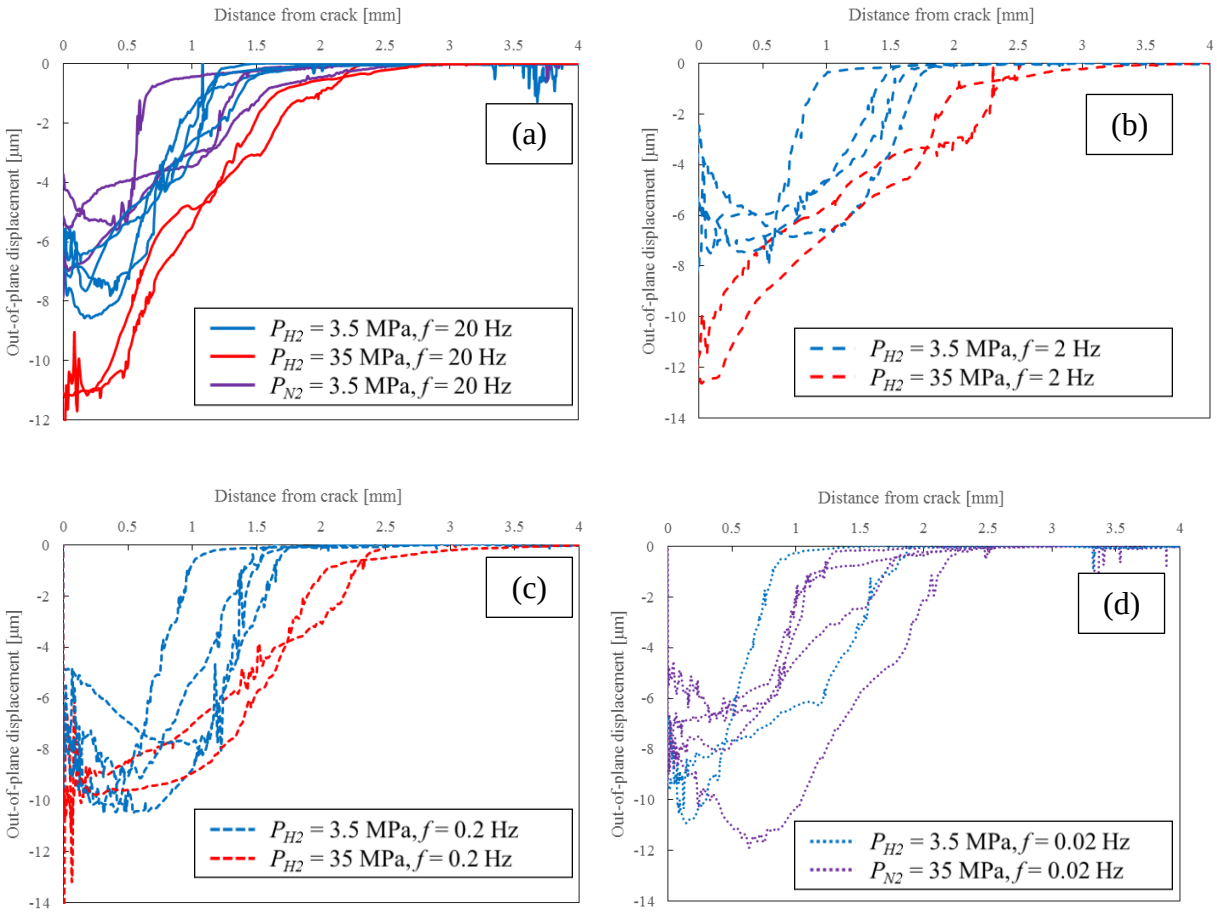

Figure 4 - 19 Comparison of the OPDs of the ΔK-constant FCG tests (ΔK = 20 MPa×m$^{1/2}$) by different environments at each loading frequency: f = 20 (a), 2 (b), 0.2 (c), and 0.02 (d) Hz.

In order to compare quantitatively the OPDs, the maximum values of the OPD curves were measured as shown in Figure 4 - 20. The relationship between the maximum OPDs and the testing conditions is consistent with the qualitative results mentioned above. There is not any clear dependency of the OPD on the loading frequency (i.e. the magnitude of FCGR enhancement). On the other hand, the OPD possibly depends on the environment (i.e. the hydrogen gas pressure). However, since the reliability of the result is doubtful due to its large fluctuations, it requires further investigation of the monotonic plastic zone to obtain solid conclusions.

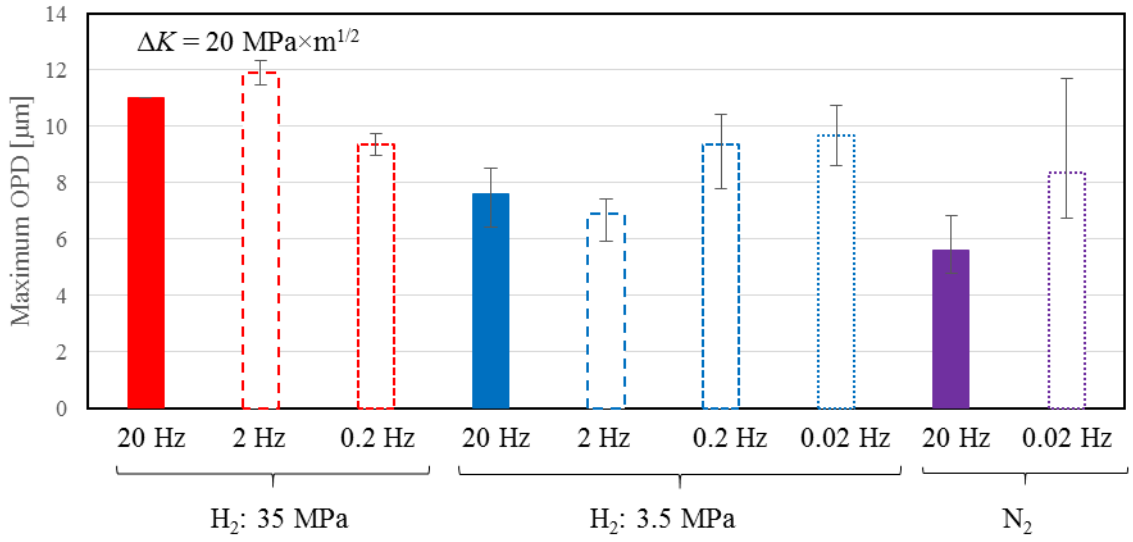

Figure 4 - 20 Maximum values of OPD of all the ΔK-constant tests (except P_{H2} = 35 MPa, f = 0.02 Hz). The bar shows the averaged value, and the error bar shows the maximum value and the minimum value.

4.4.3 Measurement results of cyclic plastic zone

Next, to investigate the cyclic plastic deformation in the vicinity of the crack tip during the FCG tests, the surface topographies in the cyclic plastic zone along the crack path of the specimens tested by the Δ*K*-increasing and Δ*K*-constant tests were measured and evaluated by comparing the surface topographic images.

4.4.3.1 Measurement result in Δ*K*-increasing tests

Firstly, the measurement results at low Δ*K* (Δ*K* = 12 MPa×m$^{1/2}$, corresponding to the non-accelerated regime) in the Δ*K*-increasing tests are presented below. Figure 4 - 21, Figure 4 - 22 and Figure 4 - 23 show the surface topographic images of the side-surface near the crack path at Δ*K* = 12 MPa×m$^{1/2}$ of the Δ*K*-increasing tests in nitrogen (P_{N2} = 3.5 MPa, f = 20 Hz) and hydrogen at P_{H2} = 35 and 3.5 MPa, respectively. In Figure 4 - 22 and Figure 4 - 23, the images (a)-(c) are the results for the different loading frequencies of f = 0.2, 2, and 20 Hz, respectively. In the presented surface topographic images, the surface height variation is indicated as a color gradation from blue to red. The green color part corresponds to the original surface height without any displacement. The blue vertical part in the middle of the images is the crack path. As shown in Figure 4 - 21, the surface topography in nitrogen is almost flat and shows only a slight displacement in the area very close to the crack path. Since the value of Δ*K* is low, the extent of cyclic plastic deformation introduced by the crack growth is small. From Figure 4 - 22 and Figure 4 - 23, it can be seen that the surface topography in hydrogen at both hydrogen gas pressures and all the loading frequencies exhibit very limited surface unevenness in the same manner as in

nitrogen. Therefore, the cyclic plastic deformation in the vicinity of the crack tip is small in both nitrogen and hydrogen. No clear modification of the cyclic crack tip plasticity by the presence of hydrogen was confirmed in the non-accelerated regime.

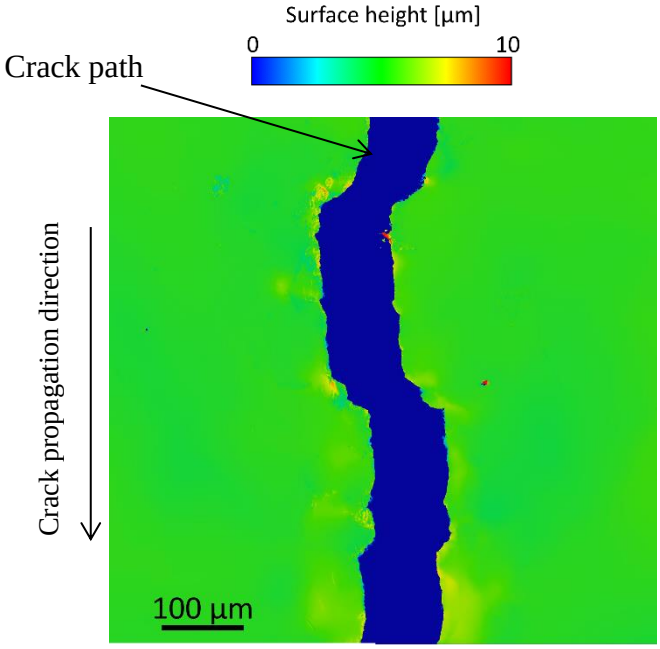

Figure 4 - 21 Surface topography (height variation) of the side-surface near the crack path at ΔK = 12 MPa×m$^{1/2}$ of the ΔK-increasing test in nitrogen (P_{N2} = 3.5 MPa, f = 20 Hz). Crack propagation direction is from top to bottom.

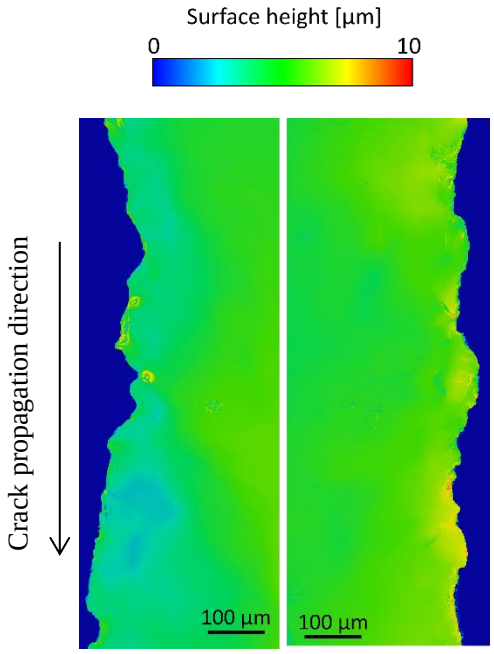

(a) P_{H2} = 35 MPa, f = 0.2 Hz

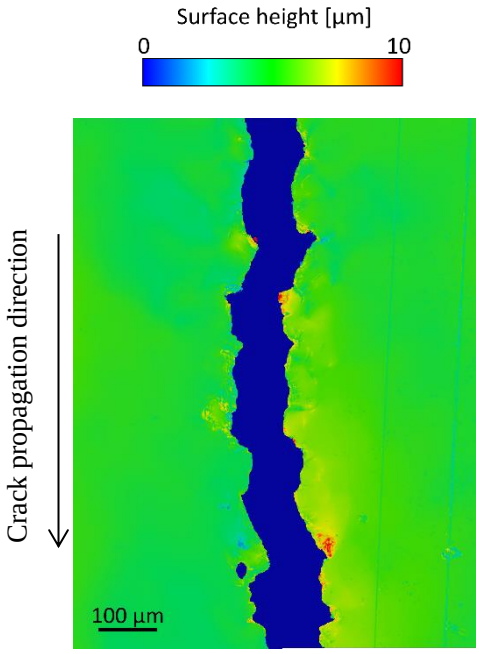

(b) P_{H2} = 35 MPa, f = 2 Hz

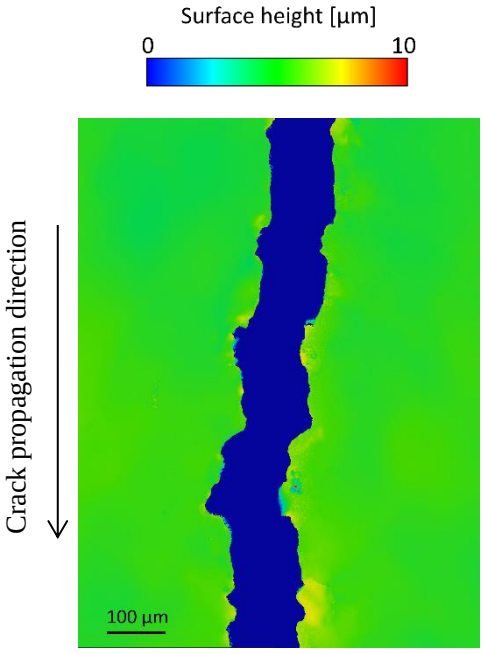

(c) P_{H2} = 35 MPa, f = 20 Hz

Figure 4 - 22 Surface topography (height variation) of the side-surface near the crack path at ΔK = 12 MPa×m$^{1/2}$ of the ΔK-increasing test in hydrogen at P_{H2} = 35 MPa and f = 0.2 (a), 2 (b), and 20 (c) Hz. Crack propagation direction is from top to bottom.

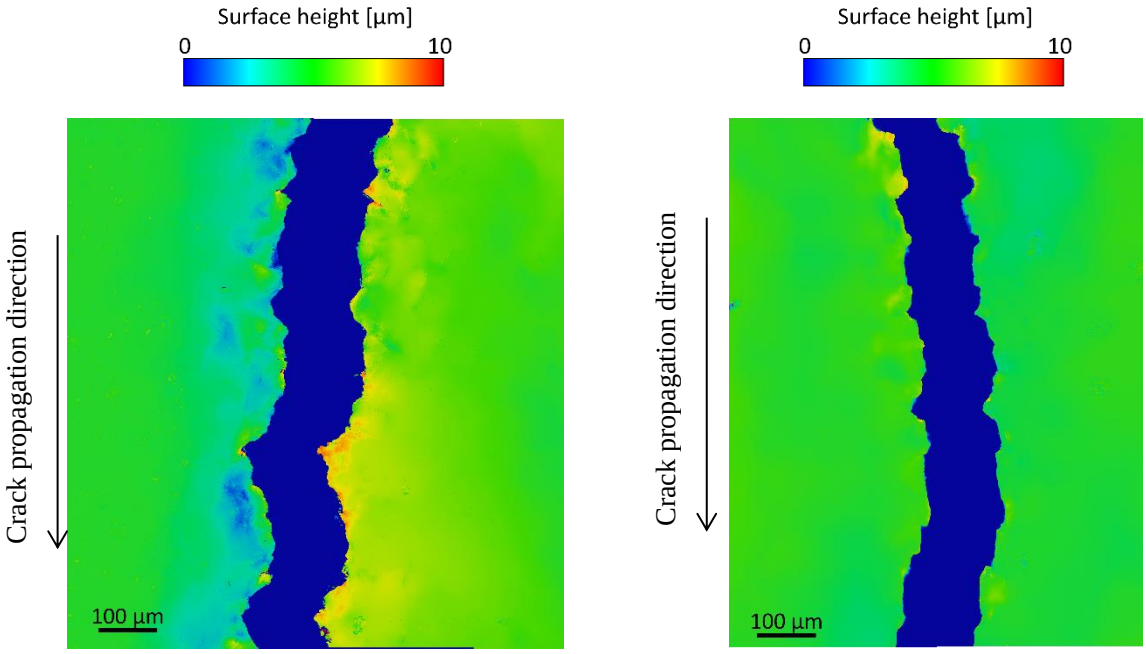

(a) P_{H2} = 3.5 MPa, f = 0.2 Hz

(b) P_{H2} = 3.5 MPa, f = 2 Hz

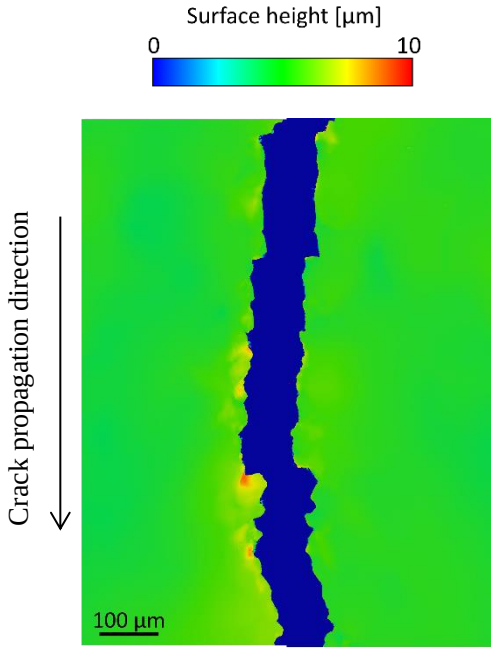

(c) P_{H2} = 3.5 MPa, f = 20 Hz

Figure 4 - 23 Surface topography (height variation) of the side-surface near the crack path at ΔK = 12 MPa×m$^{1/2}$ of the ΔK-increasing test in hydrogen at P_{H2} = 3.5 MPa and f = 0.2 (a), 2 (b), and 20 (c) Hz. Crack propagation direction is from top to bottom.

Next, Figure 4 - 24, Figure 4 - 25, and Figure 4 - 26 show the surface topographic images of the side-surface near the crack path at ΔK = 18 MPa×m$^{1/2}$ (corresponding to the accelerated regime) of the ΔK-constant tests in nitrogen (P_{N2} = 3.5 MPa) and hydrogen at P_{H2} = 35 and 3.5 MPa, respectively. In Figure 4 - 25 and Figure 4 - 26, the images (a)-(c) are the results for the different loading frequencies of f = 0.2, 2, and 20 Hz, respectively. In the case of P_{H2} = 35 MPa, f = 0.2 Hz (Figure 4 - 25a), because only a half part of the specimen was available for the measurement, the two crack lips of both sides of the half specimen are shown.

The surface topography in nitrogen (Figure 4 - 24) presents a large surface height variation. This heterogeneous surface uneveness was caused by an intense cyclic plastic deformation ahead of the crack tip during the tests. The spread size of the surface uneveness is about 100 to 300 µm which is in agreement with the cyclic plastic zone size optically observed in Section 4.3. On the other hand, all the surface topographies in hydrogen except the one at P_{H2} = 3.5 MPa, f = 0.2 Hz (Figure 4 - 26a) are almost flat without significant deformation. At P_{H2} = 3.5 MPa, f = 0.2 Hz, the surface unevenness is much more prominent than the others in hydrogen and it is the same level as in nitrogen. This result is consistent with the optical observations in Section 4.3.

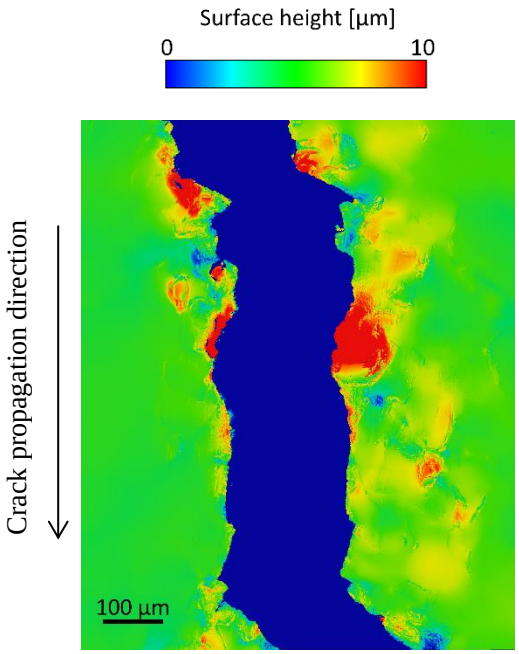

Figure 4 - 24 Surface topography (height variation) of the side-surface near the crack path at ΔK = 18 MPa×m$^{1/2}$ of the ΔK-increasing test in nitrogen (P_{N2} = 3.5 MPa, f = 20 Hz). Crack propagation direction is from top to bottom.

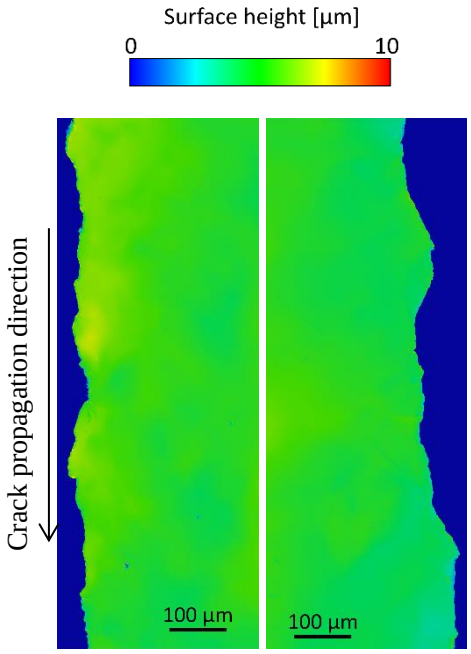

(a) P_{H2} = 35 MPa, f = 0.2 Hz

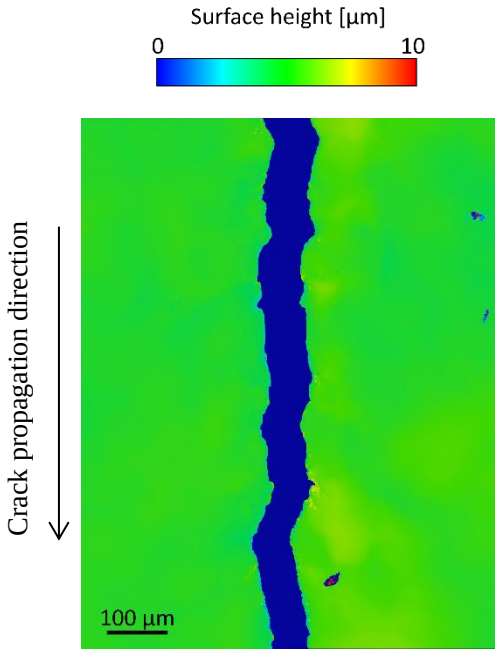

(b) P_{H2} = 35 MPa, f = 2 Hz

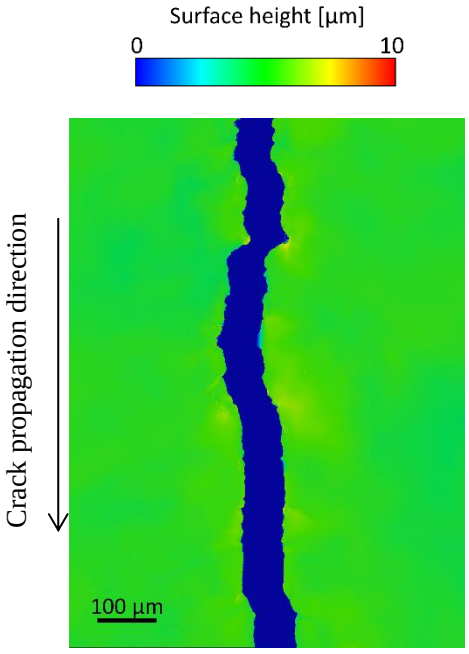

(c) P_{H2} = 35 MPa, f = 20 Hz

Figure 4 - 25 Surface topography (height variation) of the side-surface near the crack path at ΔK = 18 MPa×$m^{1/2}$ of ΔK-increasing the test in hydrogen at P_{H2} = 35 MPa and f = 0.2 (a), 2 (b), and 20 (c) Hz. Crack propagation direction is from top to bottom.

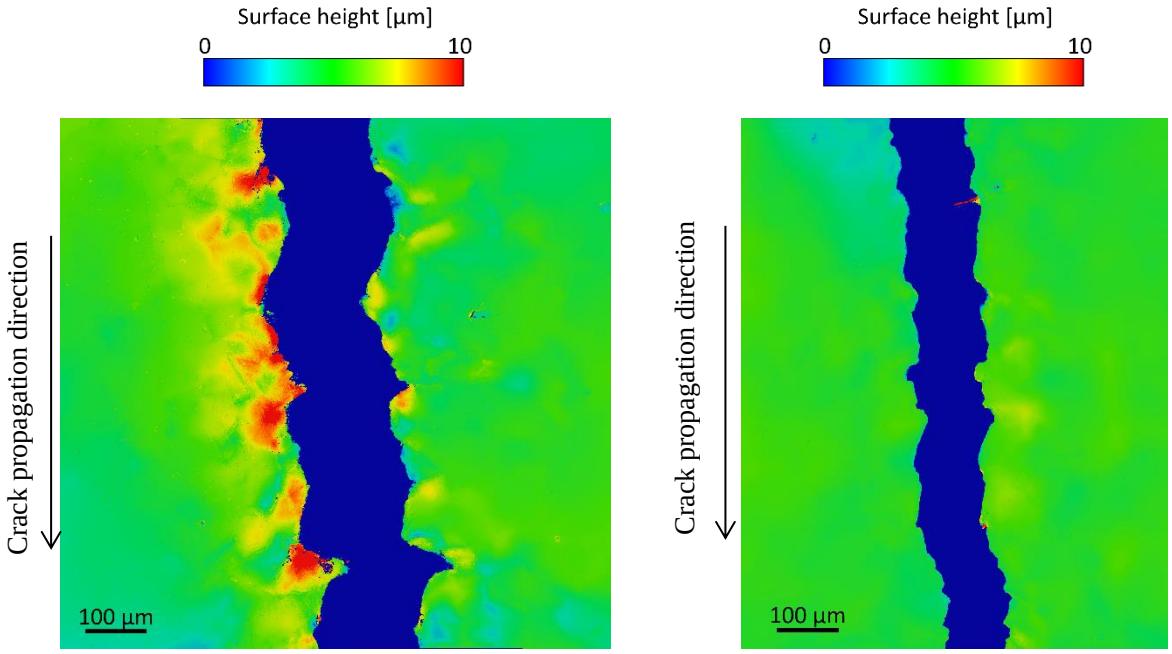

(a) P_{H2} = 3.5 MPa, f = 0.2 Hz

(b) P_{H2} = 3.5 MPa, f = 2 Hz

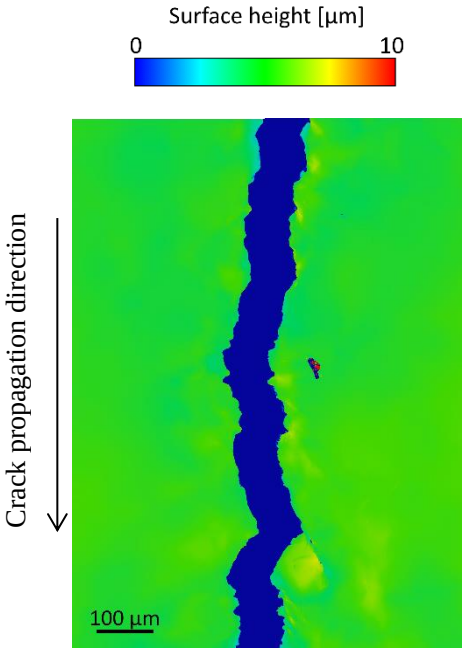

(c) P_{H2} = 3.5 MPa, f = 20 Hz

Figure 4 - 26 Surface topography (height variation) of the side-surface near the crack path at ΔK = 18 MPa×m$^{1/2}$ of the ΔK-increasing test in hydrogen at P_{H2} = 3.5 MPa and f = 0.2 (a), 2 (b), and 20 (c) Hz. Crack propagation direction is from top to bottom.

4.4.3.2 Measurement result in Δ*K*-constant tests

The measurement results in the Δ*K*-constant tests are presented below. Figure 4 - 27 shows the surface topographic images of the side-surface near the crack path of the Δ*K*-constant test (at Δ*K* = 20 MPa×m$^{1/2}$) in nitrogen (P_{N2} = 35 MPa) at *f* = 0.02 (a) and 20 (b) Hz. This figure shows that the heterogeneous surface unevenness is developed around the crack path at both loading frequencies. The extent of cyclic plastic deformation at 0.02 Hz seems slightly higher than that at 20 Hz.

On the other hand, Figure 4 - 28 and Figure 4 - 29 show the results of the tests in hydrogen at P_{H2} = 35 and 3.5 MPa, respectively. In these figures, each image from (a) to (d) corresponds to the loading frequency *f* = 0.02, 0.2, 2, and 20 Hz, respectively. At P_{H2} = 35 MPa (Figure 4 - 28), the surface unevenness is very small at the loading frequencies from 0.2 to 20 Hz (b)-(d), while some extent of surface unevenness exists at *f* = 0.02 Hz (a). At P_{H2} = 3.5 MPa (Figure 4 - 29), the surface unevenness is small at *f* = 20 Hz, while it is slightly developed at *f* = 2 Hz and it is significantly developed at *f* = 0.02 and 0.2 Hz. These observation results are consistent with the optical observation results obtained in Sub-section 4.3.2.

From the above results of OPD measurement, it has been confirmed that hydrogen greatly reduces the cyclic crack tip plasticity in the accelerated regime accompanied by the FCGR enhancement except the cases at very low loading frequency (at P_{H2} = 35 MPa, *f* = 0.02 Hz and at P_{H2} = 35 MPa, *f* = 0.2) showing the attenuation of the FCGR. Therefore, the reduction of cyclic crack tip plasticity is clearly associated with a mechanism of FCGR enhancement by hydrogen.

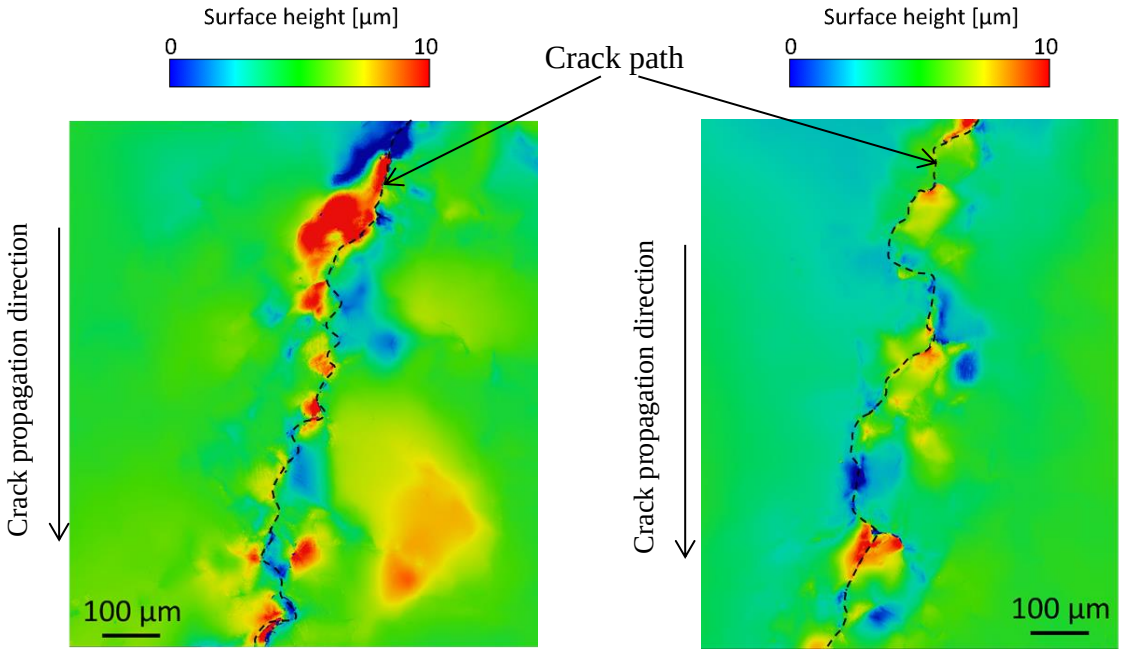

(a) Nitrogen, f = 0.02 Hz (b) Nitrogen, f = 20 Hz

Figure 4 - 27 Surface topography (height variation) of the side-surface near the crack path of the ΔK-constant test (at ΔK = 20 MPa×m$^{1/2}$) in nitrogen (P_{N2} = 35 MPa) at f = 0.02 (a) and 20 (b) Hz. Crack propagation direction is from top to bottom. The crack path is indicated by the black dashed line.

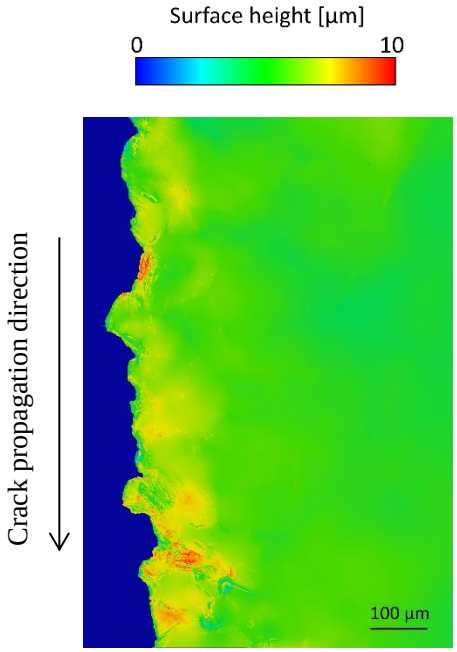

(a) P_{H2} = 35 MPa, f = 0.02 Hz

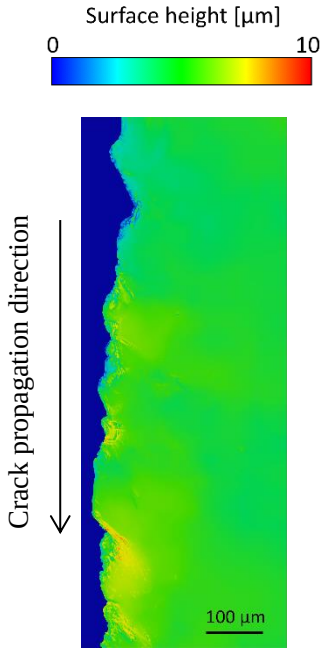

(b) P_{H2} = 35 MPa, f = 0.2 Hz

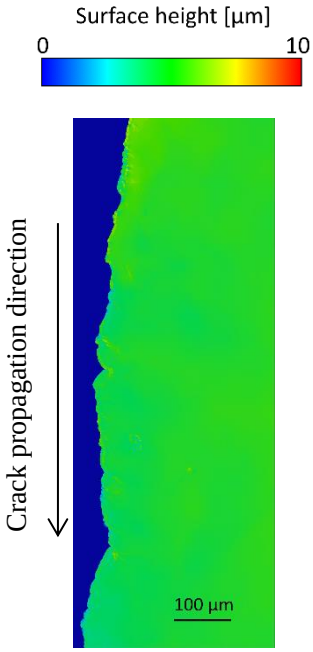

(b) P_{H2} = 35 MPa, f = 2 Hz

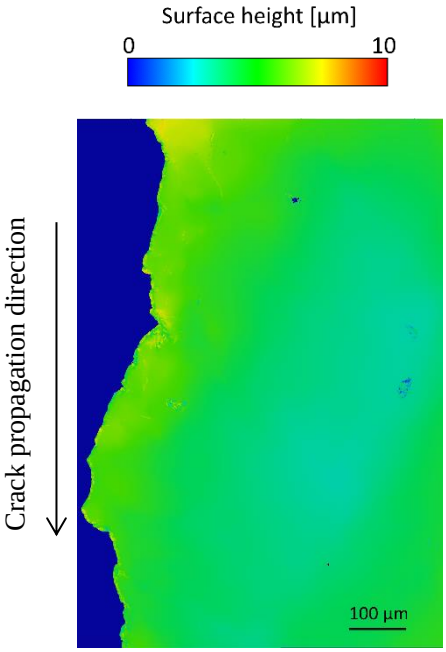

(b) P_{H2} = 35 MPa, f = 20 Hz

Figure 4 - 28 Surface topography (height variation) of the side-surface near the crack path of the ΔK-constant test (at ΔK = 20 MPa×m$^{1/2}$) in hydrogen at P_{H2} = 35 MPa and f = 0.02 (a), 0.2 (b), 2 (c), and 20 (d) Hz. Crack propagation direction is from top to bottom.

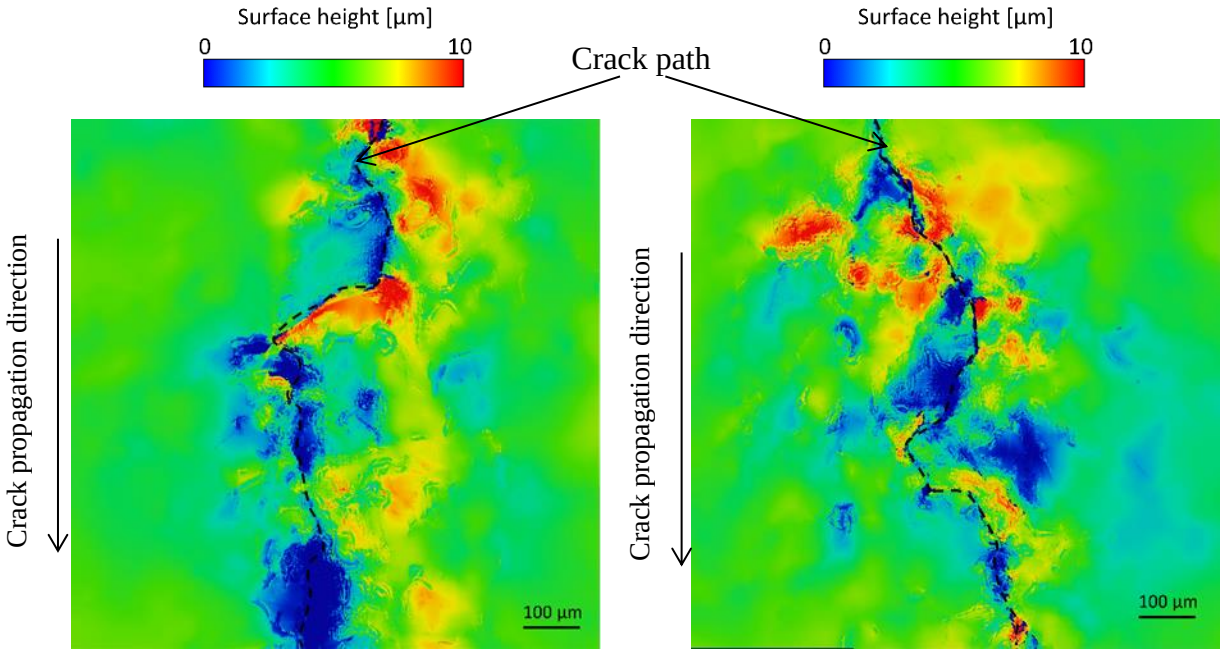

(a) P_{H2} = 3.5 MPa, f = 0.02 Hz

(b) P_{H2} = 3.5 MPa, f = 0.2 Hz

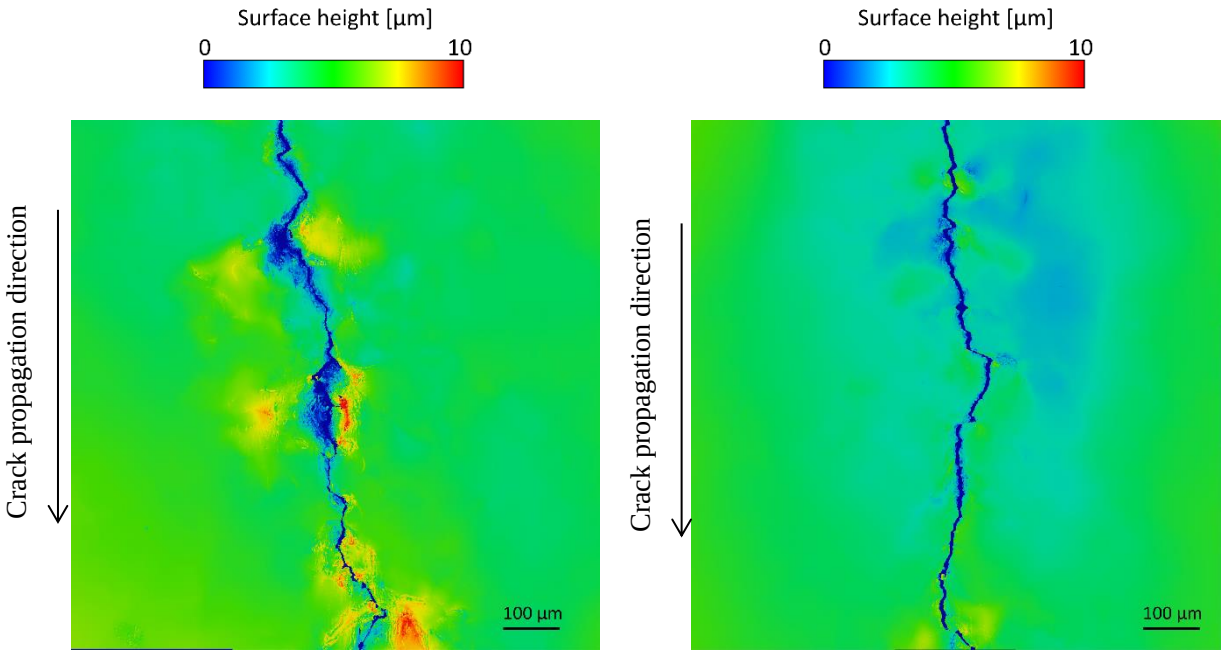

(a) P_{H2} = 3.5 MPa, f = 2 Hz

(a) P_{H2} = 3.5 MPa, f = 20 Hz

Figure 4 - 29 Surface topography (height variation) of the side-surface near the crack path of the ΔK-constant test (at ΔK = 20 MPa×m$^{1/2}$) in hydrogen at P_{H2} = 3.5 MPa and f = 0.02 (a), 0.2 (b), 2 (c), and 20 (d) Hz. Crack propagation direction is from top to bottom. The crack path is indicated by the black dashed line.

4.5 STEM observation of dislocation structure

From the above sections, the macroscopic plastic deformation in the vicinity of the crack tip has been investigated by means of optical microscopy and OPD measurement. As a result, it has been clarified that hydrogen influences the cyclic plastic deformation within a few hundred μm away from the crack path (i.e. the crack tip). The reduction of the cyclic plastic deformation is strongly associated with the FCGR enhancement effect of hydrogen. However, the mechanism of this hydrogen-plasticity interaction is not clear yet due to a lack of insight about the influence of hydrogen on the microscopic damage mechanism, specifically the dislocations. In order to elucidate this point, it is necessary to investigate the cyclic plasticity at microscopic scale in the vicinity of the crack tip in the presence of hydrogen. Because of this, this chapter is aimed to investigate the dislocation structure immediately beneath the fracture surface by means of STEM accompanied by a FIB technique.

4.5.1 Observation method

STEM is a microscopy technique which has a capacity to identify the microstructure with a very high resolution by detecting transmitted electrons through the materials [189]. The microscope observes a spatial distribution of the electron beam intensity transmitted by applying an electron beam to an observed object. Also, an atomic (lattice) structure of an observed object can be identified from an interference image generated as a result of electron diffraction due to a wave nature of electrons. Therefore, the STEM may visualize the distribution of the strain or defects (ex. dislocations) in the metallic materials because these microstructural features change the diffraction behavior of transmitted electrons.

There are several types of electron detector for the STEM as shown in Figure 4 - 30 [190]: the Bright-Field (BF); the Dark-Fields (DF); and the High-Angle Annular Dark-Field (HAADF). Each field detector detects the electrons diffracted with different angles and corresponds to different material characteristics [189, 191]. Firstly, The BF detector collects the electrons transmitted with a small angle (a collection angle $\beta < \sim 0.6$ deg.). The BF image represents the atomic density depending on an element, crystal structure, defect, dislocation, strain, etc. Secondly, the collection angle of DF is about $0.6 < \beta < 5$ deg. The DF detector collects the electron diffracted by an atomic lattice of the material. As the diffraction angle of the electron depends on the lattice orientation and the lattice structure, the DF image mainly represents the crystalline characteristics. Finally, the HAADF detector collects the electron scattered with a high angle ($\beta > \sim 5$ deg.) due to the atoms in the material, and very less diffracted electrons in contrast. This scattering is called as Rutherford-scatter which is a function of the atomic mass (= atomic number Z). Therefore, the HAADF image represents the element distribution composing the material based on the difference in the atomic number. In the case of this study, since the objective of the STEM is to observe the dislocation structure in the material, the DF was used to make the STEM image.

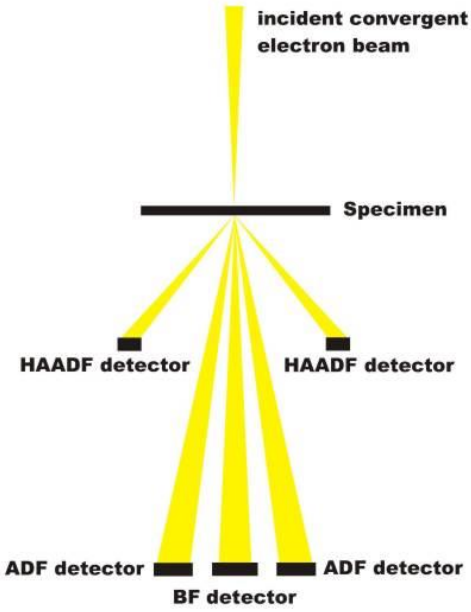

*Figure 4 - 30 Schematic outline of the arrangement of the various STEM detectors [*190*].*

As the microscope detects the transmitted electrons, it is necessary to prepare a very thin lamella (the thickness is about a few hundred nm) for the STEM observation. The lamellas were prepared from the selected locations of fracture surfaces by using a Focused Ion Beam (FIB, Helios NanoLab G3, FEI) at Université de Poitiers shown in Figure 4 - 31. The Helios NanoLab G3 is a microscope equipped with an electron gun and a gallium (Ga) ion gun [192]. This microscope is capable to characterize the microstructure of material by several techniques such as SEM, STEM, and EBSD with very high resolution in sub-nm order. Another feature of this microscope is the very accurate milling in the order of 10 nm by Ga ion beam. This microscope enables us to prepare the STEM lamella from the selected location on the material surface, and also perform the STEM on the lamella in the same vacuum chamber.

Figure 4 - 31 Focused Ion Beam microscope (Helios NanoLab G3, FEI).

The procedure of the preparation of the STEM lamella is explained as follows. Some example images of the preparation are shown in Figure 4 - 32. Firstly, the location to observe was chosen on the fracture surface for having a fixed value of ΔK and the specific features such as the

intergranular facet, the cleavage-like facet, etc. Also, the target location was carefully chosen not to be much undulated because if the surface is largely uneven, it is difficult to apply the FIB. Once the target location was decided, a platinum (Pt) protection layer was made on the fracture surface by Pt deposition for protecting the surface of target part from the ion beam as shown in Figure 4 - 32a. The dimension of the Pt layer was about 2 µm (perpendicular to crack propagation direction) × 15 – 20 µm (crack propagation direction) × 1 – 2 µm (thickness). The width direction of lamella was aligned to be parallel to the global crack propagation direction (i.e. specimen geometry), not to the local crack propagation direction which is often indicated by the striation. Secondly, the FIB was applied to remove (dig) the material beside the target position as shown in Figure 4 - 32b. The depth of the removed part is deeper at the place closer to the target position. Thirdly the tip of the micro-manipulator was attached to the top part of the lamella as shown in Figure 4 - 32c. Then, we have cut the surrounding part of the lamella by FIB and separated the lamella from the specimen. Finally, the lamella was attached on the half-moon stage as shown in Figure 4 - 32d. After that, we have applied the FIB on the lamella to reduce its thickness down to a few hundred nm.

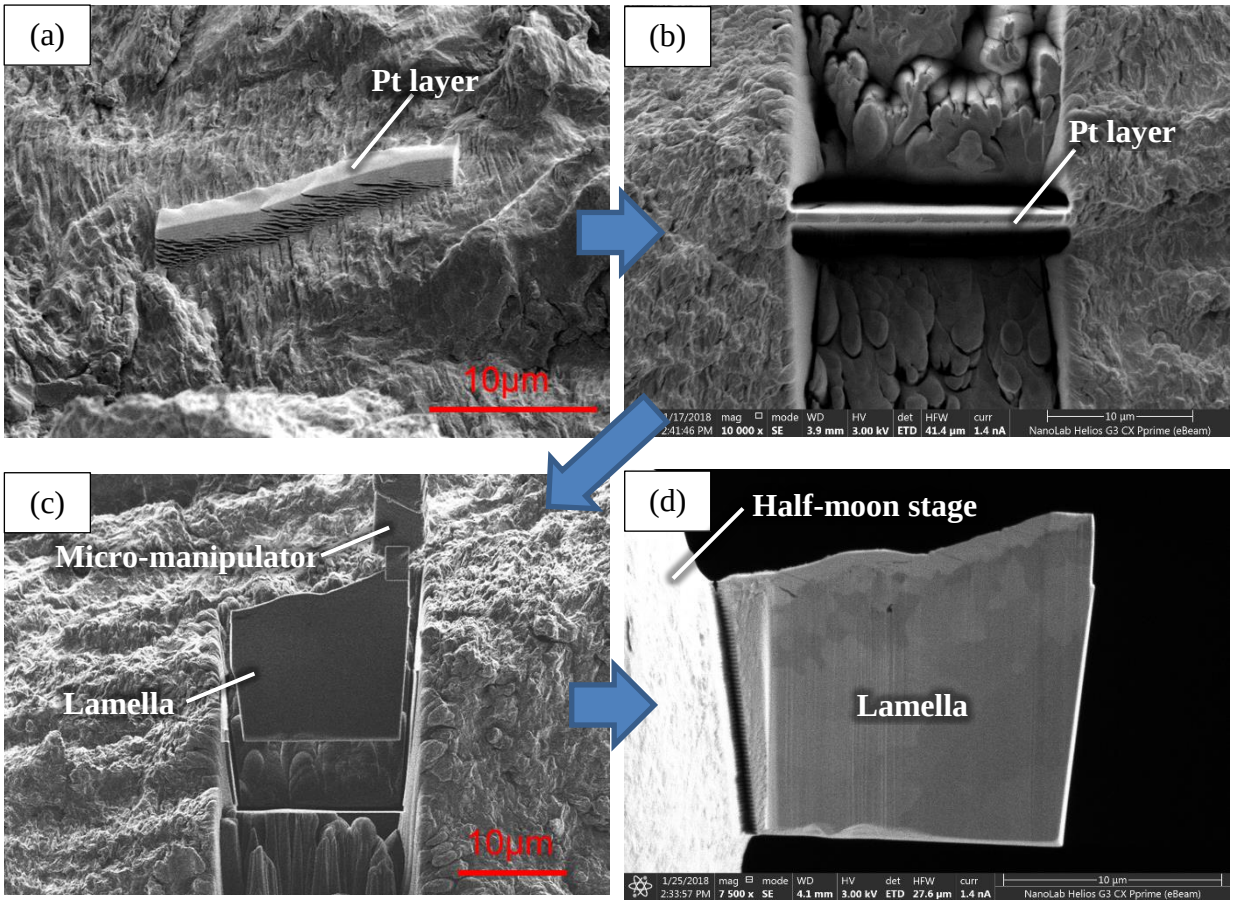

Figure 4 - 32 Example images showing the procedure of STEM lamella preparation by FIB: (a) putting Pt protection layer; (b) milling the fracture surface; (c) picking up the lamella by micromanipulator; and (d) attaching the lamella on the half-moon stage and thinning the lamella.

After preparing the lamella, the STEM and the transmission-EBSD (t-EBSD) were applied to identify the dislocation structure and the crystal orientation within the lamella, respectively. The t-EBSD is the analysis technique to characterize the crystal orientation in a thin sample by detecting transmitted electrons [193], while the standard EBSD measures back-scattered electrons. The advantage of the t-EBSD compared to the standard EBSD is a very high spatial resolution in the order of 10 nm. On the other hand, its disadvantage is a difficulty of preparing the sample which has to be sufficiently thin for the STEM. However, as the thin lamellas were prepared for the STEM, it was possible to perform the t-EBSD. For the STEM, the applied electron voltage was 30 kV, the electron beam current was adjusted between 0.34 and 1.4 nA depending on the thickness of the lamella.

4.5.2 Observation result in Δ*K*-increasing tests

First of all, the results of the STEM and t-EBSD observations for the Δ*K*-increasing tests at low Δ*K* corresponding to the non-accelerated regime are presented. Figure 4 - 33 shows the results of the Δ*K*-increasing test in air at f =20 Hz, ΔK = 12 MPa×m$^{1/2}$. This figure presents (a) the SEM image of the fracture surface around the location of the sample extraction indicated by red rectangle, (b) the STEM image of the entire view of the lamella (the red dashed-line indicates the position of the fracture surface), (c) the magnified image of the lamella close to the fracture surface indicated by red rectangle in (b), and (d) the Inverse Pole Figure (IPF) colored map of the lamella obtained by the t-EBSD. The fracture surface (Figure 4 - 33a) shows a ductile transgranular fracture surface. The STEM image (Figure 4 - 33b) shows that many black lines forming a cell-like structure spread over the entire lamella. These black lines are dislocation wall. The presence of dislocations induces distortion of the surrounding lattice, causing the diffraction of transmitted electrons. This effect is consequently observed as a dark color in the BF image. The diameter of the observed cell-like structure is ranged from 0.1 to 3 μm which is much smaller than the average grain size (90 μm) of this material. Thus, this microstructure is a dislocation cell structure (or sub-grains), not a grain boundary. In the magnified STEM image (Figure 4 - 33c), the dislocation cell structure continues until the fracture surface. There are many white vertical lines seen in the lamella. These markings indicate a thinner part than the other part caused by an ion channeling effect [194, 195]. The ion channeling effect occurs when a crystallographic axis of the target material is aligned with a direction of the incident ion beam. In this case, the interaction of the ion and the target material largely deviates depending on the position of impact of the incident ions. This causes the deviation of the sputtering intensity. This effect consequences the fluctuation of lamella thickness like seen in this observation.

The IPF colored map (Figure 4 - 33d) shows from blue to purple indicating the crystal orientation near the {111} plane. In this image, the white missing parts like a worm-hole are no data part due to too thin thickness. The small change in the crystal orientation exists corresponding to the dislocation cells, which means that the crystal lattice was slightly rotated inside the dislocation cell. As the crystal orientation of the entire lamella is nearly uniform, it can be concluded that the lamella consists of one grain. Nevertheless, the crystal orientation of the lamella was identified as {111} plane, the crack propagation plane which is angled by 90 degrees from the lamella plane cannot be identified by only seeing this IPF. This is because this type of IPF colored map indicated by the representative planes ({111}, {001}, and {101}) does not give the information of a rotation angle of crystal in the axis perpendicular to the lamella plane. For identifying the crystal orientation of crack propagation plane, it is necessary to obtain an original IPF (not colored for mapping) or a Selected-Area Diffraction Pattern (SADP) by TEM in the future. In this study, the obtained IPF colored maps mainly contribute for determining whether the lamella consists of one grain or several grains.

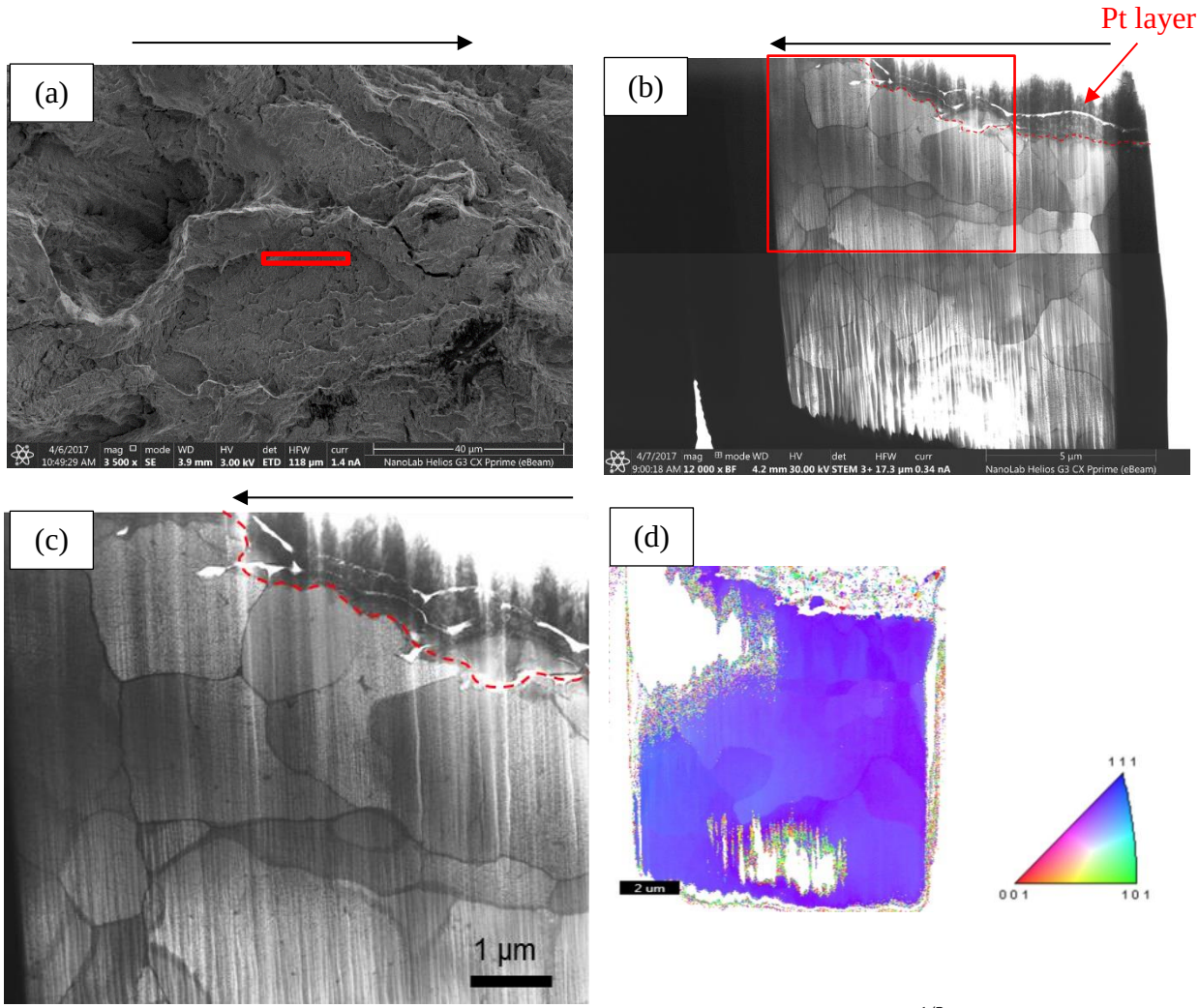

Figure 4 - 33 The ΔK-increasing test in air at f =20 Hz, ΔK = 12 MPa×m$^{1/2}$. (a) SEM image of the fracture surface around the location of the sample extraction indicated by the red rectangle. (b) STEM image of the entire view of the lamella. Red dashed-line indicates the position of fracture surface. (c) Magnified image of the lamella close to the fracture surface indicated by the red rectangle in (b). (d) t-EBSD mapping of the lamella.

Figure 4 - 34 shows the result of the Δ*K*-increasing test in nitrogen at *f* =20 Hz, Δ*K* = 12 MPa×m$^{1/2}$. The type of fracture surface (Figure 4 - 34a) is a ductile transgranular fracture as same as in air. The STEM images (Figure 4 - 34b and c) shows the presence of dislocation cell structure as same as in air. Though it is difficult to observe the middle part of lamella due to its severe damage, it seems that the size of dislocation cells near the fracture surface is smaller than the one in the bottom part of lamella. As high plastic strain forms smaller dislocation cells with a high dislocation density, it suggests that a higher amount of plastic strain was introduced to the material near the fracture surface. On the other hand, the dislocation cell size in air is relatively more homogeneous as shown in Figure 4 - 33b. However, since the area size of this observation is very small, the dislocation structure highly depends on the grain size, the crystal orientation, and so on. Thus, it is difficult to conclude that the observed difference in the dislocation cell size is globally consistent in the entire part.

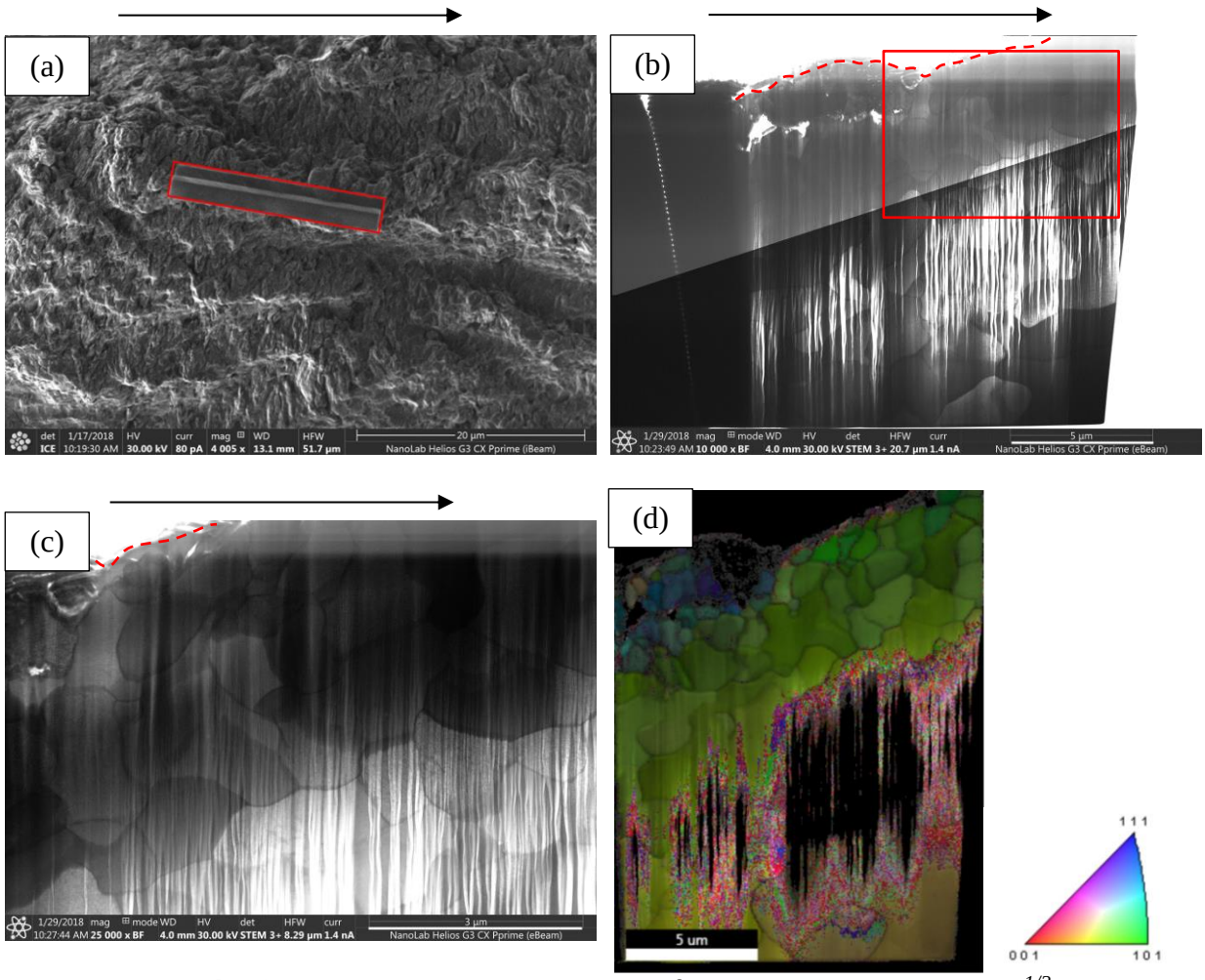

Figure 4 - 34 The ΔK-increasing test in nitrogen at f = 20 Hz, ΔK = 12 MPa×m$^{1/2}$. (a) SEM image of the fracture surface around the location of the sample extraction indicated by red rectangle. (b) STEM image of the entire view of the lamella. Red dashed-line indicates the position of fracture surface. (c) Magnified image of the lamella close to the fracture surface indicated by red rectangle in (b). (d) t-EBSD mapping of the lamella.

Two lamellas were prepared from two different locations in hydrogen at P_{H2} = 35 MPa, f = 2 Hz, ΔK = 12 MPa×m$^{1/2}$. Figure 4 - 35 and Figure 4 - 36 show the observation results of the first and second lamella, respectively. Both lamellas were taken from the surface of the intergranular facet as shown in Figure 4 - 35a and Figure 4 - 36a. The stripe-like markings exist on the intergranular facet within the extraction area as shown in Figure 4 - 35b. For the first lamella, the STEM images (Figure 4 - 35c – e) show that the dislocation cell structure is developed beneath the fracture surface. The dislocation cell size is approximately 1 μm near the fracture surface, while the size is larger (3 – 4 μm) in the bottom part of the lamella. Besides, the presence of some microvoids was confirmed near the fracture surface as shown in Figure 4 - 35d and e.

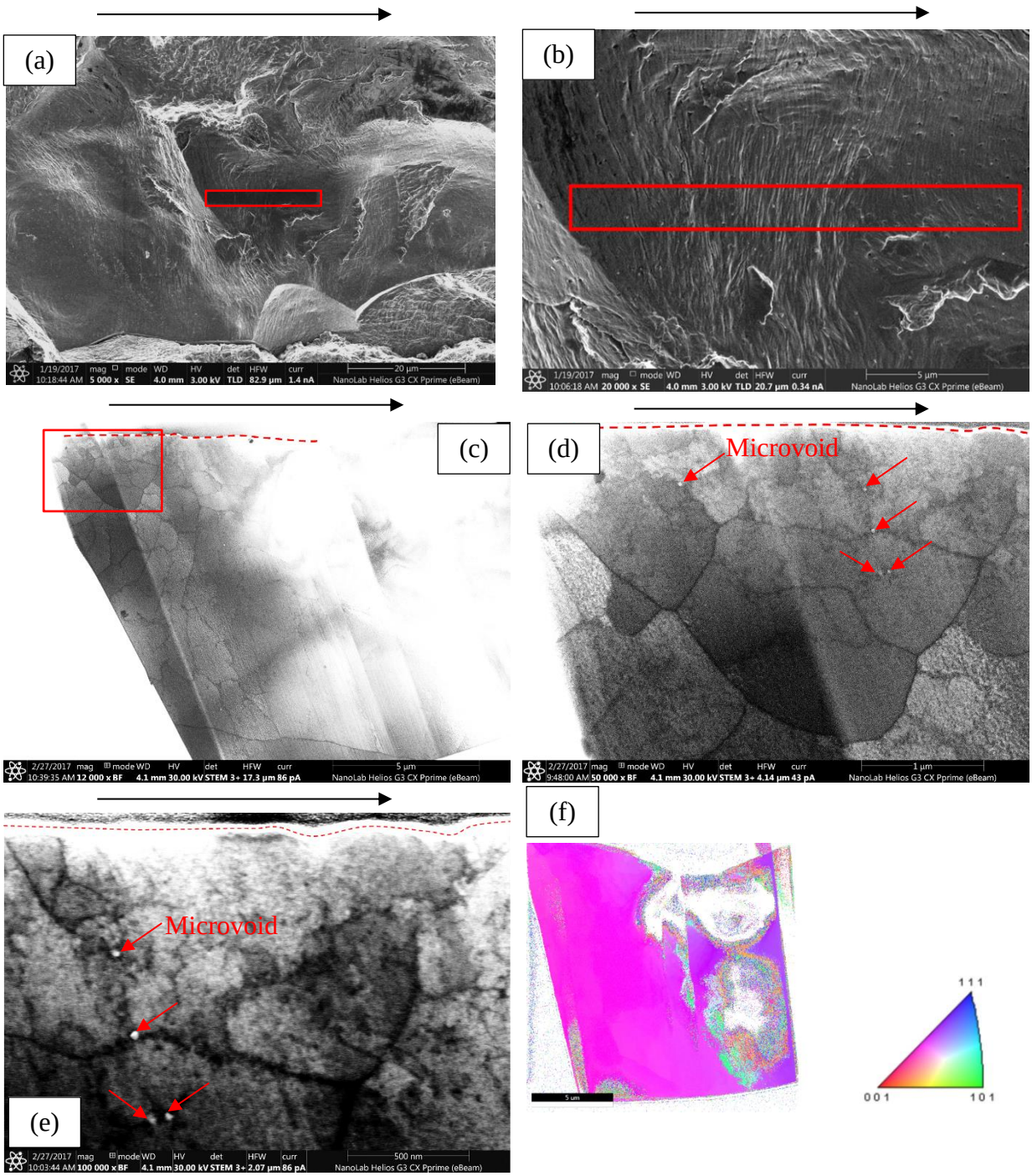

Figure 4 - 35 First observation for the ΔK-increasing test in hydrogen at P_{H2} = 35 MPa, f = 2 Hz, ΔK = 12 MPa×$m^{1/2}$. (a) SEM image of the fracture surface around the location of the sample extraction indicated by red rectangle. (b) Magnified image of (a). (c) STEM image of the entire view of the lamella. Red dashed-line indicates the position of fracture surface. (d) Magnified images of the lamella close to the fracture surface indicated by red rectangle in (c). (e) Further magnified image of (d). (f) t-EBSD mapping of the lamella.

For the second lamella, the STEM images (Figure 4 - 35b and c) show that the dislocation cell structure is formed near the fracture surface, while the dislocation cells are not well developed and the short dislocation walls (namely, dislocation tangles) are distributed in the bottom part of the lamella. Also, the top part of lamella close to the fracture surface shows a different contrast of the image (whiter) and fewer dislocation walls. This difference is likely due to its too much thin

thickness which can be also confirmed by the no-data part of the t-EBSD mapping (Figure 4 - 35d). The presence of the dislocation cell structure in the specimen tested in hydrogen (Figure 4 - 35 and Figure 4 - 36) indicates that the certain level of plastic strain has been introduced into the grains ahead of the intergranular crack tip as same as the transgranular crack tip in air. This result is surprising because the hydrogen-induced intergranular facet is macroscopically a sign of brittle fracture. The presence of high degree of plastic strain has also been suggested by the presence of stripe-like markings on the intergranular facet.

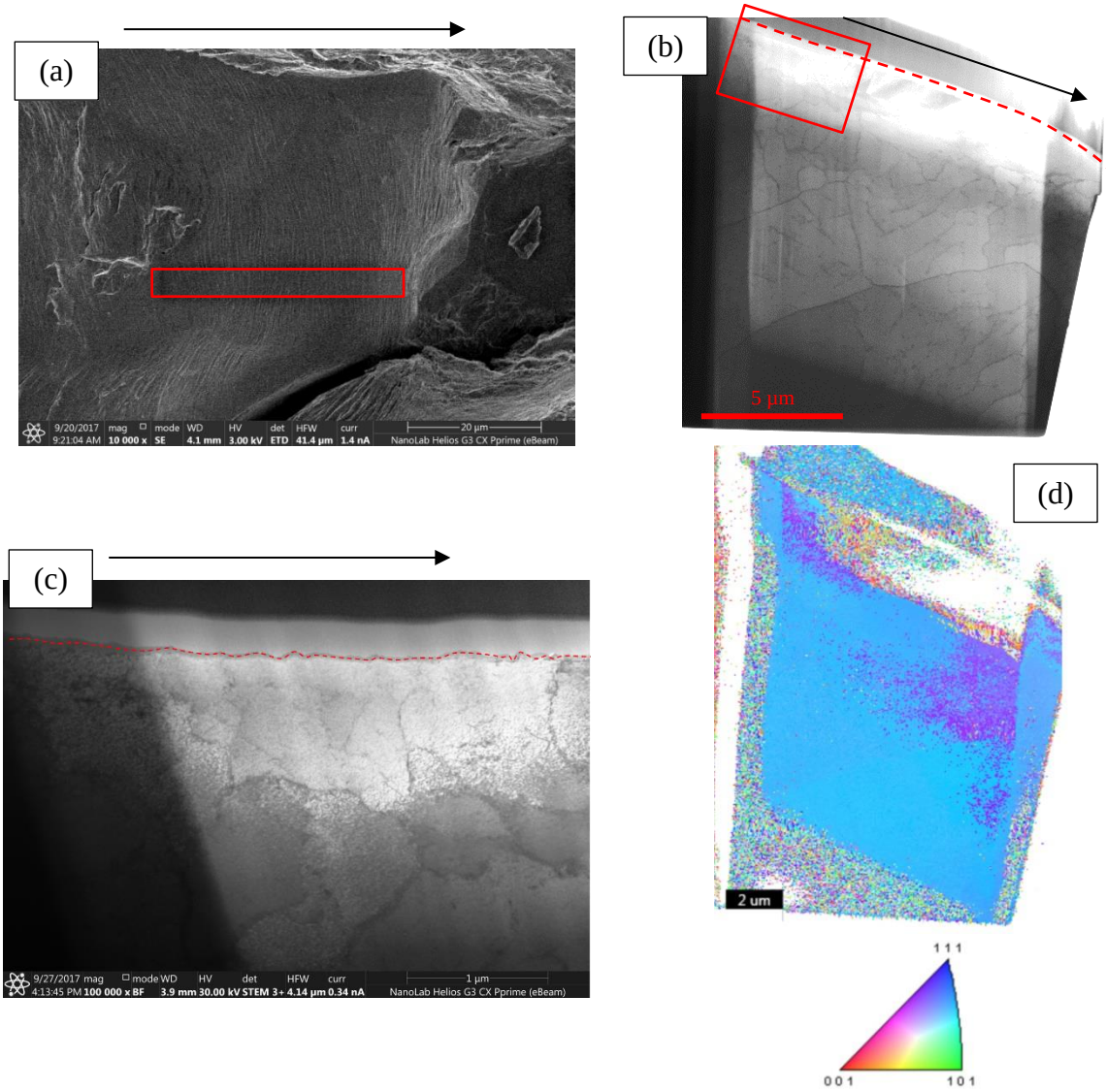

Figure 4 - 36 Second observation for the ΔK-increasing test in hydrogen at P_{H2} = 35 MPa, f = 2 Hz, ΔK = 12 MPa×$m^{1/2}$. (a) SEM image of the fracture surface around the location of the sample extraction indicated by red rectangle. (b) STEM image of the entire view of the lamella. Red dashed-line indicates the position of fracture surface. (c) Magnified image of the lamella close to the fracture surface indicated by red rectangle in (b). (d) t-EBSD mapping of the lamella.

Next, the observations of dislocation structure at higher ΔK corresponding to the accelerated regime are presented below. Figure 4 - 37 shows the results of the ΔK-increasing test in air at f = 20 Hz, ΔK = 22 MPa×m$^{1/2}$. The fracture mode is a ductile transgranular fracture (Figure 4 - 37a). The dislocation structure is fully a cell structure (Figure 4 - 37b and c) as same as at low ΔK (Figure 4 - 33). In the magnified image (Figure 4 - 37c), a fine surface uneveness of the fracture surface can be seen at the top edge of the lamella. And, there are very small dislocation cells corresponding to the fine surface uneveness. The differences in the contrast of image indicated by the red arrows in Figure 4 - 37b are likely due to a slight difference in the crystal orientation of dislocation cells because the different contrast parts seem corresponding to the difference in the IPF color indicated by the red arrows in Figure 4 - 37d.

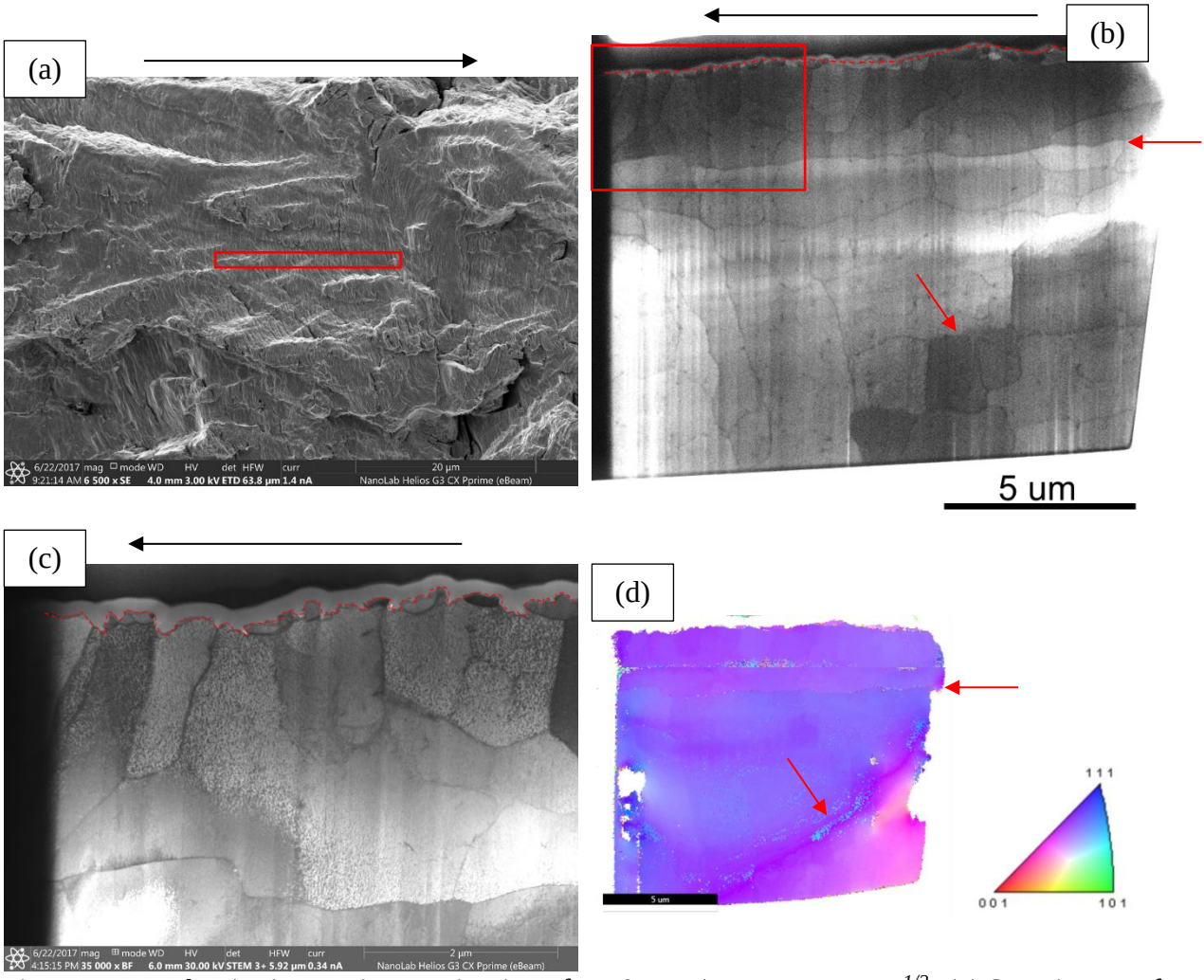

Figure 4 - 37 The ΔK-increasing test in air at f = 20 Hz, ΔK = 22 MPa×m$^{1/2}$. (a) SEM image of the fracture surface around the location of the sample extraction indicated by red rectangle. (b) STEM image of the entire view of the lamella. Red dashed-line indicates the position of fracture surface. (c) Magnified image of the lamella close to the fracture surface indicated by red rectangle in (b). (d) t-EBSD mapping of the lamella.

Figure 4 - 38 and Figure 4 - 39 show the observations of first and second lamellas of the ΔK-increasing test in hydrogen at P_{H2} = 35 MPa, f = 2 Hz, ΔK = 22 MPa×m$^{1/2}$, respectively. For the first lamella, the extraction location is the cleavage-like facets with the brittle striations as shown in Figure 4 - 38a. The STEM observation of the first lamella (Figure 4 - 38b and c) revealed that

the dislocation structure is not a cell structure, but many short dislocation tangles are randomly distributed in the material. The positions of striation are indicated by red arrows in Figure 4 - 38b and c. There are also two long winding dislocation walls connecting to the center position of striation. This dislocation wall might be induced by a crack tip blunting forming the striation markings. However, no such dislocation wall was observed for the other two positions of striations. Besides, some microvoids were observed as indicated by white arrows in Figure 4 - 38c.

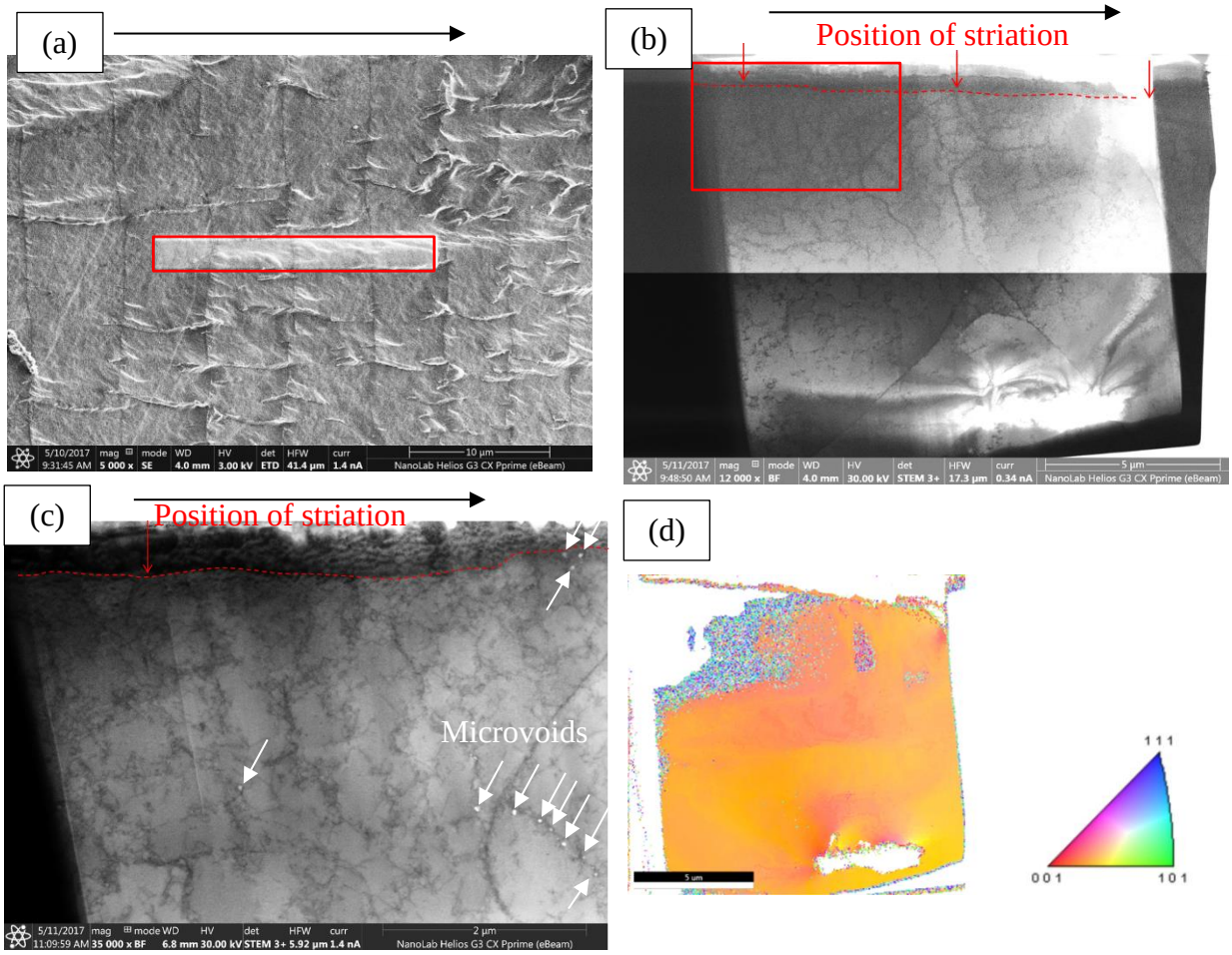

Figure 4 - 38 First observation for the ΔK-increasing test in hydrogen at P_{H2} = 35 MPa, f = 2 Hz, ΔK = 22 MPa×$m^{1/2}$. (a) SEM image of the fracture surface around the location of the sample extraction indicated by red rectangle. (b) STEM image of the entire view of the lamella. Red dashed-line indicates the position of fracture surface. (c) Magnified image of the lamella close to the fracture surface indicated by red rectangle in (b). (d) t-EBSD mapping of the lamella.

For the second lamella, the extraction location is also on the cleavage-like facet with the brittle striations (Figure 4 - 39a). The dislocation structure (Figure 4 - 39b and c) is a random distribution of dislocation tangles without a cell structure in the same way as for the first lamella. There is a straight dislocation wall angled by 45 degrees from the crack propagation direction as shown in the images. This line connects to the position of striation. The feature of this dislocation wall agrees with that of a slip line formed during a crack tip blunting. However, no such dislocation wall was observed for the other two positions of striation.

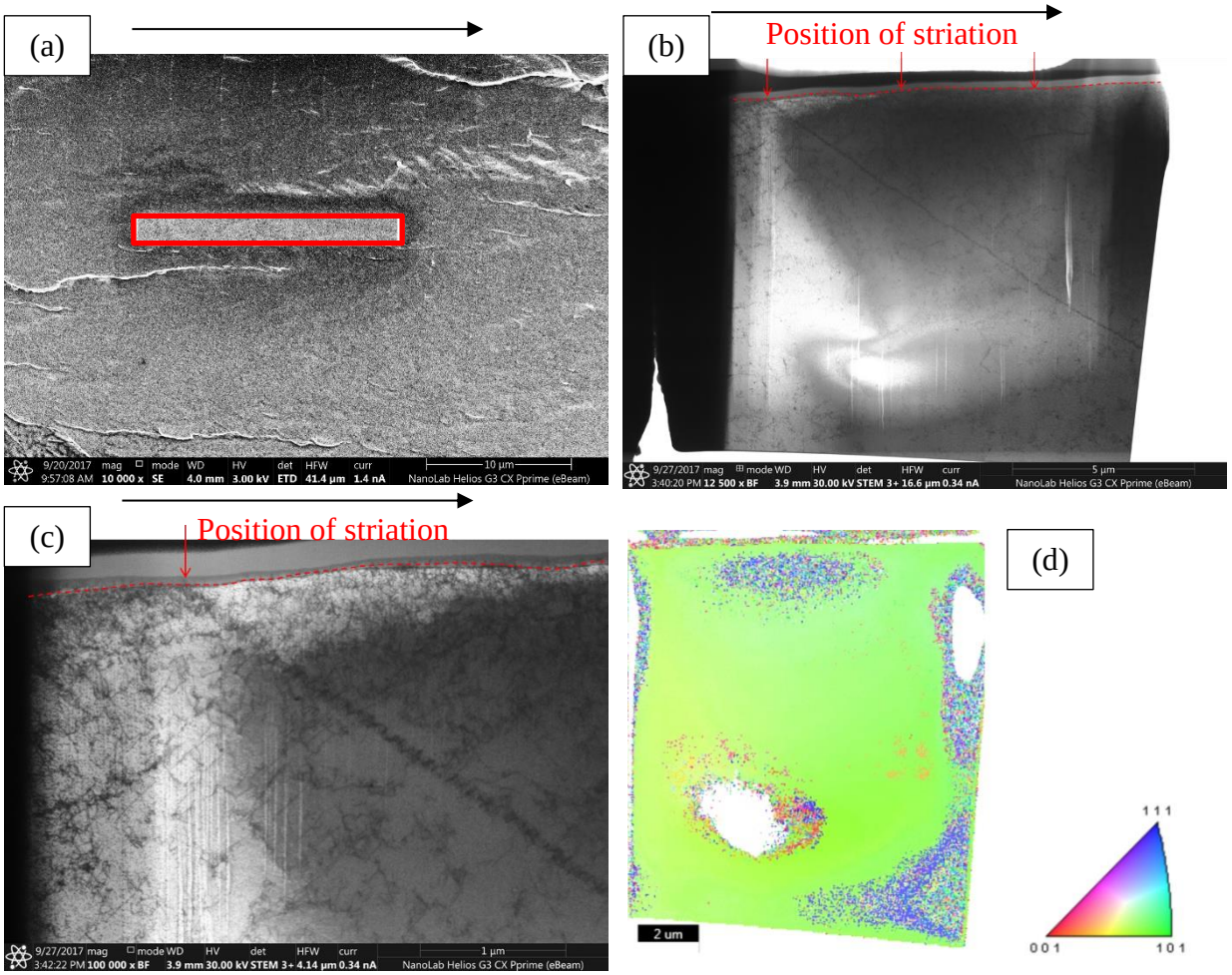

Figure 4 - 39 Second observation for the ΔK-increasing test in hydrogen at P_{H2} = 35 MPa, f = 2 Hz, ΔK = 22 MPa×m$^{1/2}$. (a) SEM image of the fracture surface around the location of the sample extraction indicated by red rectangle. (b) STEM image of the entire view of the lamella. Red dashed-line indicates the position of fracture surface. (c) Magnified image of the lamella close to the fracture surface indicated by red rectangle in (b). (d) t-EBSD mapping of the lamella.

From the IPF colored maps obtained by t-EBSD, it has been confirmed that all the lamellas consist of one grain, except the one in nitrogen at ΔK = 12 MPa×m$^{1/2}$ (Figure 4 - 34d) which shows {101} grain in most part of the lamella and a small {111} grain on the left top of lamella.

The observed type of dislocation structure (a random distribution of dislocation tangles) in hydrogen is a preliminary state before the formation of cell structure, indicating that less plastic strain was introduced into the material during the FCG, compared to the case in air. This fact agrees with the presence of the brittle striation which is an indication of low crack tip plasticity.

4.5.3 Observation result in Δ*K*-constant tests

In the previous sub-section, the dislocation structures in the vicinity of the crack tip in various environments and values of ΔK have been observed. Next, aiming to investigate the influence of hydrogen gas pressure and the loading frequency on the dislocation structure, the STEM

observation in the Δ*K*-constant tests were performed. This sub-section presents the results of the observations. Figure 4 - 40 and Figure 4 - 41 show the results of the Δ*K*-constant tests (Δ*K* = 20 MPa×m$^{1/2}$) in hydrogen of P_{H2} = 35 MPa at *f* = 20 and 0.02 Hz, respectively. The extraction location at *f* = 20 Hz (Figure 4 - 40a) is on a cleavage-like facet with brittle striations. The dislocation structure beneath it (Figure 4 - 40b) is a random distribution of dislocation tangles with a low density and also the two dislocation walls indicated by red arrows in the image. At 0.02 Hz, the fracture surface of the extraction location (Figure 4 - 41a) is a ductile transgranular fracture surface. The dislocation structure (Figure 4 - 41b) is a cell structure, but the cell walls are not very solid and some cell walls are not connecting.

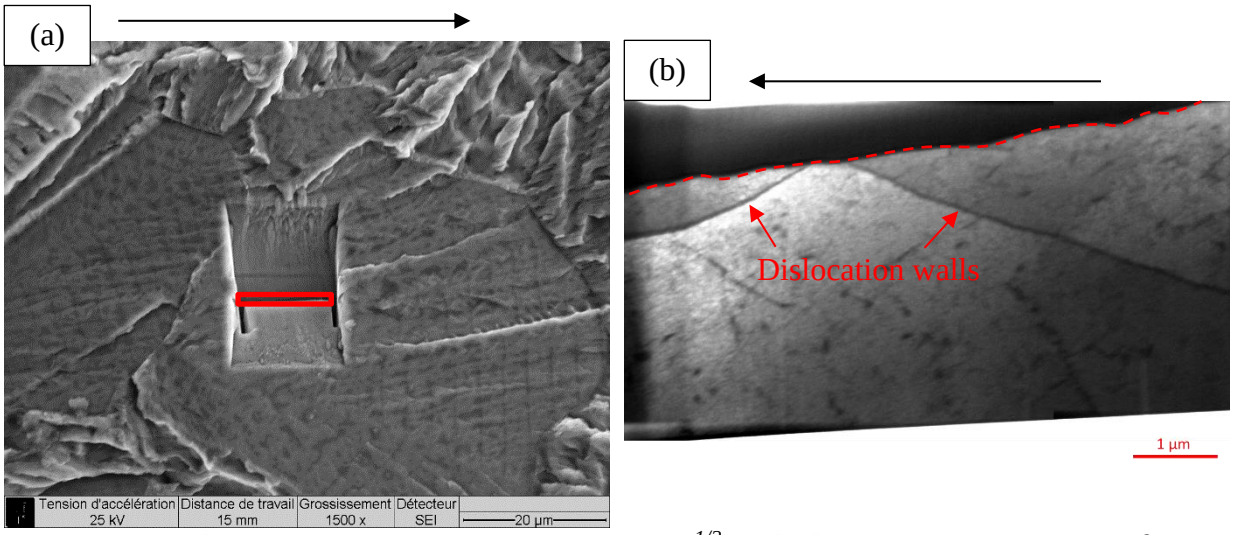

Figure 4 - 40 The ΔK-constant test (ΔK = 20 MPa×m$^{1/2}$) in hydrogen at P_{H2} = 35 MPa, f = 20 Hz. (a) SEM image of the fracture surface around the location of the sample extraction after the extraction. (b) STEM image of the entire view of the lamella. Red dashed-line indicates the position of fracture surface.

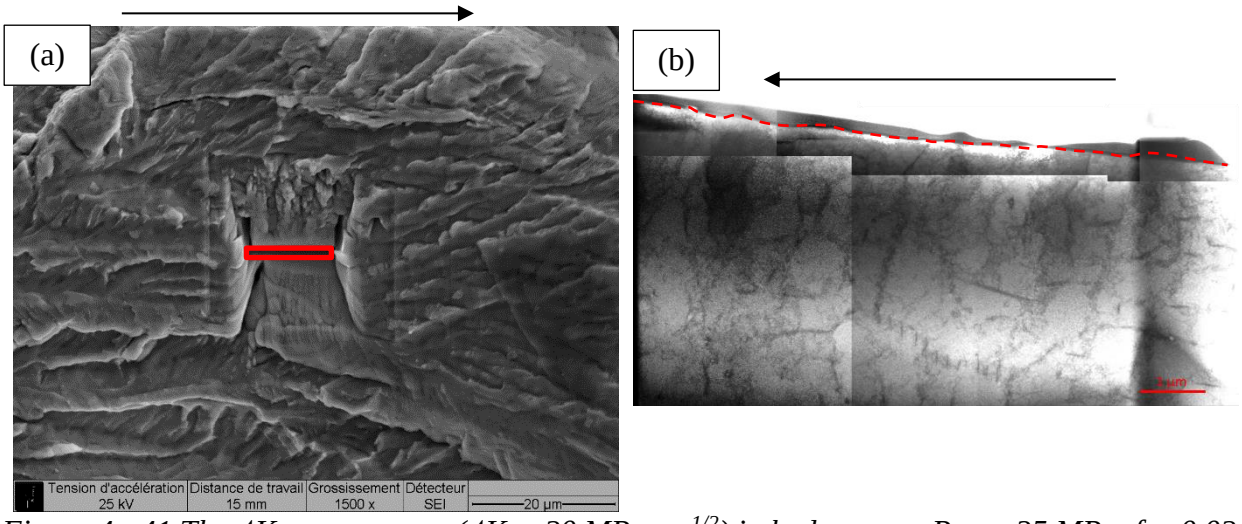

Figure 4 - 41 The ΔK-constant test (ΔK = 20 MPa×m$^{1/2}$) in hydrogen at P_{H2} = 35 MPa, f = 0.02 Hz. (a) SEM image of the fracture surface around the location of the sample extraction after the extraction. (b) STEM image of the entire view of the lamella. Red dashed-line indicates the position of fracture surface.

Figure 4 - 42 and Figure 4 - 43 present the observations of dislocation structure of the specimens tested at a lower hydrogen gas pressure (P_{H2} = 3.5 MPa), f = 20 and 0.02 Hz, respectively. The extraction location at f = 20 Hz (Figure 4 - 42a) is on a cleavage-like facet with striations. The dislocation structure (Figure 4 - 42b) is a distribution of dislocation tangles without a cell structure. Besides, it can be seen that there is a mountain-like marking with a darker contrast indicated by the blue arrows. The right edges of the mountain-like markings seem corresponding to the positions of striations indicated by the red arrows. On the other hand, at f = 0.02 Hz, the extraction location (Figure 4 - 43a) is on the ductile transgranular fracture surface. The clear dislocation cell structure was observed in the entire area of the lamella as shown in Figure 4 - 43b.

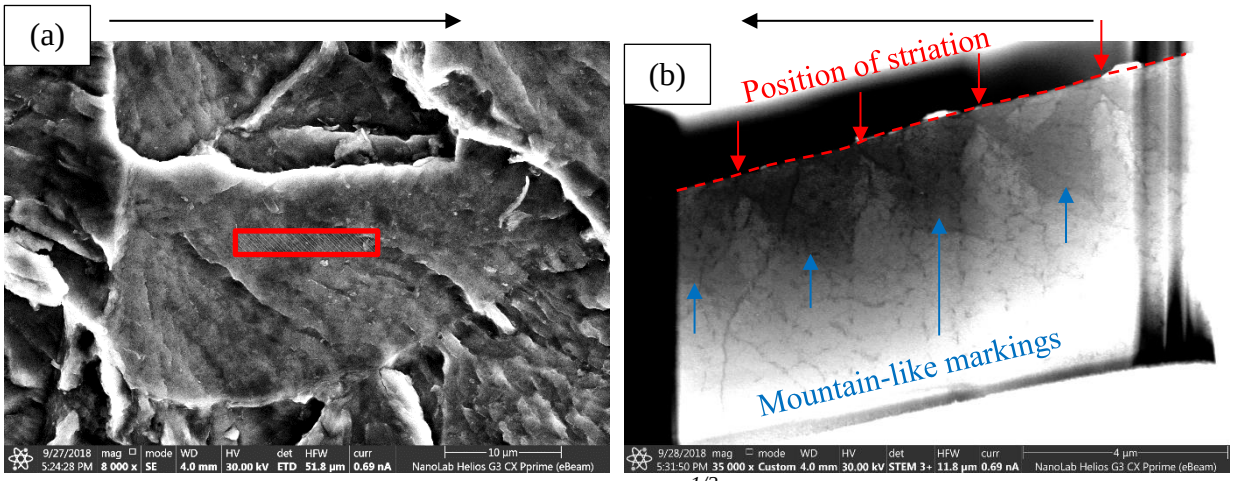

Figure 4 - 42 The ΔK-constant test (ΔK = 20 MPa×m$^{1/2}$) in hydrogen at P_{H2} = 3.5 MPa, f = 20 Hz. (a) SEM image of the fracture surface around the location of the sample extraction indicated by red rectangle. (b) STEM image of the entire view of the lamella. Red dashed-line indicates the position of fracture surface.

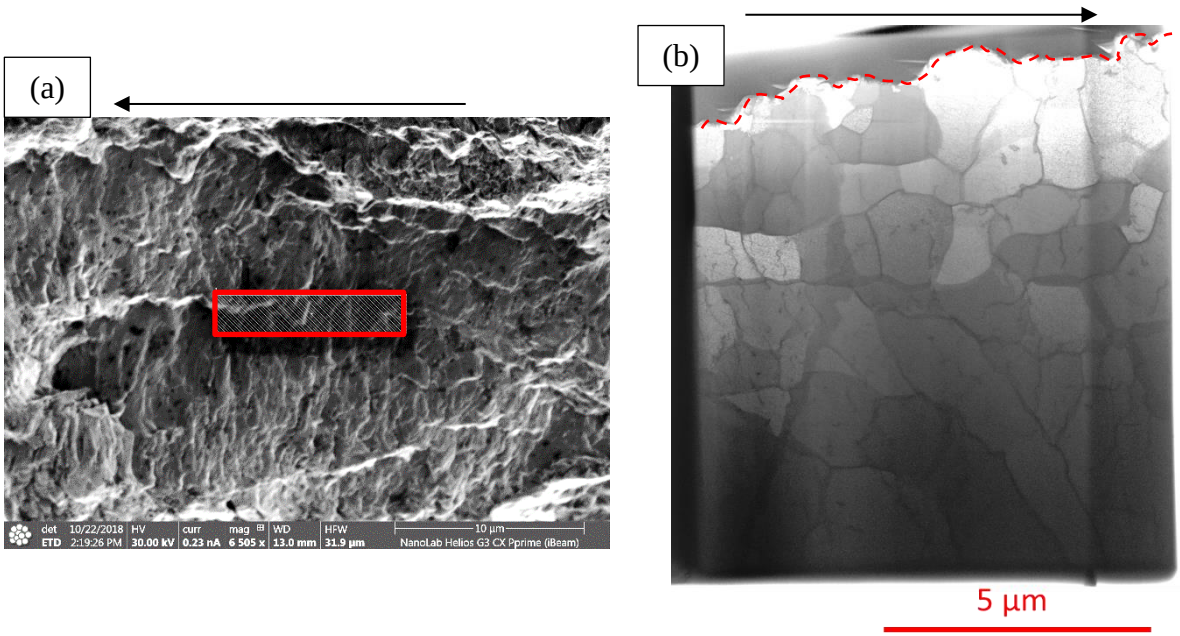

Figure 4 - 43 The ΔK-constant test (ΔK = 20 MPa×m$^{1/2}$) in hydrogen at P_{H2} = 3.5 MPa, f = 0.02 Hz. (a) SEM image of the fracture surface around the location of the sample extraction indicated by red rectangle. (b) STEM image of the entire view of the lamella. Red dashed-line indicates the position of fracture surface.

At both hydrogen gas pressures, the two types of dislocation structure, namely a dislocation tangles distribution and a dislocation cell structure, clearly correspond to the two fracture modes, a brittle QC fracture and a ductile fracture, respectively. Additionally, the low level of microscopic crack tip plasticity is associated with the FCG enhancement, as same as the macroscopic cyclic crack tip plasticity as observed in the previous section.

4.5.4 Comparison of dislocation cell size

As the dislocation cell size represents a level of local plastic strain, it was measured in the obtained STEM images to compare the test conditions. The measurement was done by using an image analysis software ImageJ. The average dislocation cell sizes of all the lamellas exhibiting the dislocation cell structure are shown in Figure 4 - 44. In this diagram, the uncertainty bar indicates the standard deviation of measured values. The average dislocation cell sizes of all the testing conditions are almost the same, ranging from 1 to 2 µm. Though there are differences in the average dislocation cell size by the testing conditions, these differences are probably just a fluctuation. The reason for this is that the standard deviations indicated by the uncertainty bars are large. The dislocation cell size at ΔK = 22 MPa×m$^{1/2}$ in air is larger than that at ΔK = 12 MPa×m$^{1/2}$ in air. But this is supposed to be the opposite because the introduced plastic strain in the vicinity of the crack tip should be higher at a higher ΔK. A reason of this fluctuation of dislocation cell size (i.e. local plastic strain) is possibly that since its observation window is very small, a result highly depends on local microstructural conditions such as a grain orientation, a grain size, a crack path, etc.

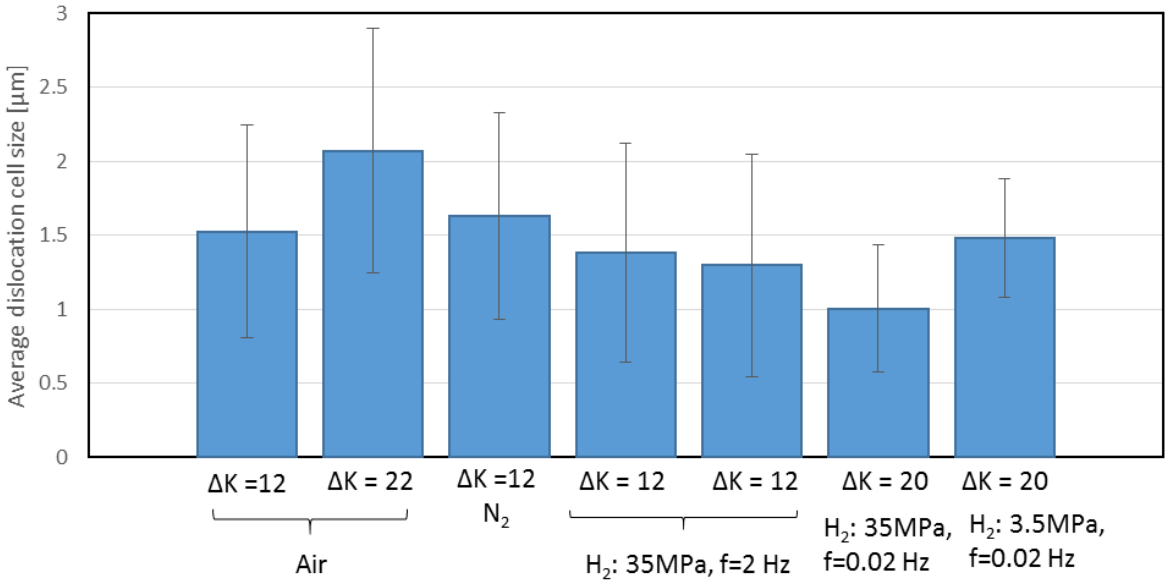

Figure 4 - 44 Comparison of average dislocation cell size among various test conditions.

Bilotta [27] has investigated the dislocation structure of a cyclically-deformed Armco iron. He conducted low cycle fatigue tests on cylindrical specimens of Armco iron with a strain amplitude of 0.2 and 0.8 % and a cumulated strain of 0 (non-deformed), 8 and 32. After the tests, he has cut the specimens into small pieces and observed a dislocation structure by TEM conducted by a collaboration with Professor X. Feaugas at Université de La Rochelle [27]. His results of the average dislocation structure in each test and the comparison with the present results are shown in Figure 4 - 45. As shown in the diagram, the dislocation cell size of the non-deformed specimen ($\varepsilon_{p,cum}$ = 0) is the highest. A dislocation cell structure was observed even in the non-deformed specimen, while it was not observed beneath some fracture surfaces in hydrogen. The dislocation cell structure in the non-deformed specimen might be caused by the preparation process of sample (machining to make a cylindrical specimen and cutting of the specimen into small piece for STEM). From the results for the fatigue specimens, the dislocation cell size depends on the amount of the cumulated plastic strain, but not on the strain amplitude. The dislocation cell sizes in the present FCG tests and the low cycle fatigue by Bilotta are ranged in the same level. Therefore, the level of cumulated cyclic plastic strain introduced into the vicinity of the crack tip during the FCG is possibly in the order of $\varepsilon_{p,cum}$ = 8 – 32.

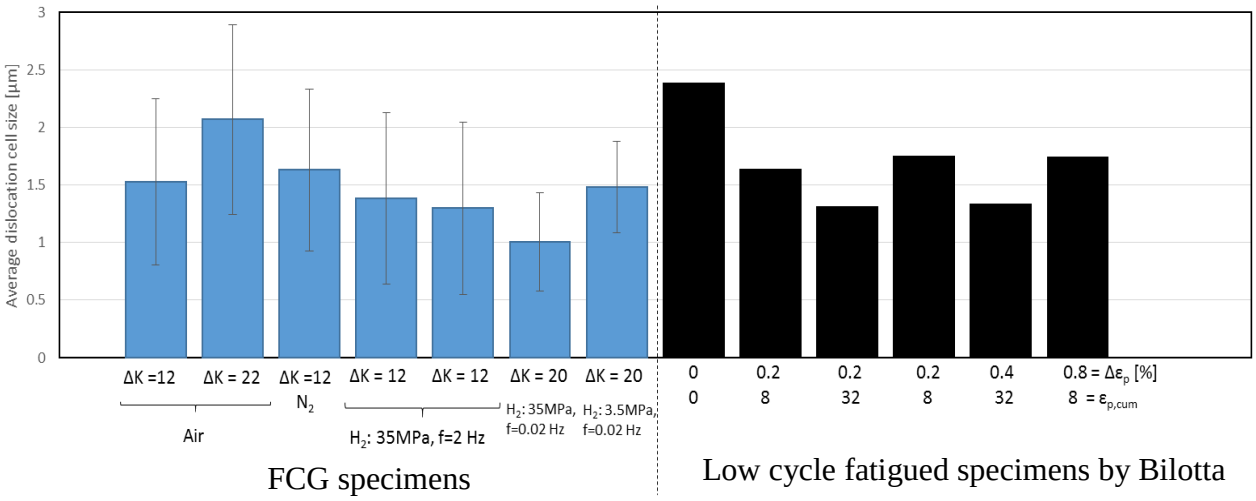

Figure 4 - 45 Comparison of average dislocation cell size between the present FCG specimens and the low cycle fatigued ones in Armco iron obtained by Bilotta [27].

4.6 Discussion

In the above sections, the macroscopic and microscopic plastic deformation near the crack path of the tested specimens was investigated by means of the optical microscopy, the interferometric microscopy, and the STEM. This section presents discussions aiming to compare the present results with literature to see a consistency of experimental results. The mechanism of the hydrogen effects on crack tip plasticity and the dependency on the testing parameters are not discussed in this chapter but are presented in the next chapter within the framework of a discussion on the mechanism of HAFCG.

4.6.1 Influence of hydrogen on monotonic plastic zone

The results of the OPD measurement obtained in Section 4.4 have to be compared to the ones in 15-5PH steel obtained by Bilotta et al. [27, 159]. They performed the OPD measurement for the monotonic plastic zone formed during a cyclic and static cracking under gaseous hydrogen by the same method as this study. Their results show a clear enhancement of OPD near the crack path by hydrogen. The values of OPD were increased by hydrogen but the width of the deformed part does not change. Besides, the degree of OPD enhancement increases as the hydrogen gas pressure increases, and also it is almost the same degree between the cyclic and static crack propagations. These results are not consistent with the present results which do not confirm a clear modification of the monotonic plastic zone by hydrogen in Armco iron. This inconsistency in the hydrogen effect on the monotonic plastic zone between Armco iron and 15-5PH steel is possibly related to their difference in the time-dependency of FCG as mentioned in Sub-section 3.5.2. The time-independent HAFCGR (da/dN) in Armco iron depends on ΔK, while the time-dependent HAFCGR (da/dt) in 15-5PH steel depends on K_{max}. On the other hand, as expressed by Equations 4 - 1 to 4 - 4, the cyclic and the monotonic plastic zone sizes depend on ΔK and K_{max}, respectively. These facts suggest that whether hydrogen influences the cyclic crack tip plasticity or monotonic one depends on the material (probably the yield strength as mentioned in Sub-section 3.5.2). And because of this, the HAFCG in Armco iron exhibits the time-independence, meanwhile, the one in 15-5PH steel exhibits the time-dependence. However, the reason why the hydrogen effect depends on the yield strength is not clear. This point should be pursued in a prospective research.

4.6.2 Cyclic crack tip plasticity in the non-accelerated regime

In the non-accelerated regime (ΔK = 12 MPa×m$^{1/2}$), no clear plastic deformation was observed in both nitrogen and hydrogen by the OPD measurement. This is because the spread of cyclic crack tip plasticity in such low ΔK regime is not enough to produce detectable surface unevenness. On the other hand, by means of STEM, the development of dislocation cell structure was observed immediately beneath the intergranular fracture surface in hydrogen (Figure 4 - 35 and Figure 4 - 36) as well as in air and nitrogen. This indicates a surprising fact that a high degree of plastic strain was introduced into grains. Nevertheless, it has also to be reminded that in this regime the

fracture is a intergranular while the presence of stripe-like markings on the intergranular facets is also an indication of plastic strain in the grains.

The dislocation structure beneath the hydrogen-induced intergranular fracture surface has been investigated by several studies [75, 77, 163, 167, 176]. Ogawa et al. [163, 167] observed a dislocation structure beneath intergranular fatigue fracture surface in pure iron by STEM in the same way as this study and confirmed the presence of dislocation cell structures and microvoids which are consistent with the present result. Wang et al. [75, 77] observed the dislocation cell structure beneath the fracture surface produced by tensile loading in pure iron and pure nickel. Both Ogawa et al. and Wang et al. argued that the dislocation cell size in hydrogen is smaller than the one in air, indicating that dislocation mobility and local plastic strain are enhanced by hydrogen.

Besides, Robertson et al. [12, 23, 95] have studied in detail the interaction between hydrogen and mobile dislocations by conducting an in-situ STEM observation during plastic deformation of hydrogen-charged materials. Their observations revealed that hydrogen has an effect enhancing dislocation mobility and local crack tip plasticity. The dislocation dynamics analysis by Birnbaum et al. [8] also supports the plasticity enhancement effect of hydrogen.

However, the change in the dislocation cell size by hydrogen was not clearly confirmed by the present STEM observations as shown in Figure 4 - 44. In fact, it is difficult to conclude a global characteristic of dislocation structure by referring to only few STEM observations because of the small size of STEM observation area. The dislocation structure observed within very limited area (normally within one grain) highly depends on the grain orientation, the grain size, and so on. Since both Ogawa et al. and Wang et al. obtained only few STEM images, it should be careful to conclude that the hydrogen effect enhancing the crack tip plasticity (dislocation density) occurs during the intergranular fatigue cracking. Ogawa et al. [163, 167] also provide the Grain Reference Orientation Deviation (GROD) mapping near the crack path by means of the EBSD analysis which technique is capable to analyze the plastic strain distribution in the scale of hundred μ m. Their GROD results have shown that the extent of plastic strain distribution near the intergranular crack path in hydrogen is almost the same as in air, and not clearly greater. Nishikawa et al. [73] confirmed the development of slip bands ahead of the intergranular crack tip by means of in-situ optical observation during FCG test in low carbon steel under gaseous hydrogen. This result is also an evidence of the presence of plastic strain accumulated in the grains during the intergranular cracking. However, this result did not evidence the hydrogen-enhanced plasticity. Therefore, as far as considering all the available experimental evidences, it is still difficult to conclude that hydrogen enhances the crack tip plasticity during the intergranular cracking.

Another noteworthy feature of microstructure in the non-accelerated regime is the presence of microvoids observed in Figure 4 - 35e. Experimental studies by Nagumo et al. [10, 106] have revealed that the highly accumulated hydrogen atoms trapped by defects may stabilize and enhance a vacancy nucleation during straining. A high density of vacancies agglomerate to form microvoids, degrading material strength. They named this process by "hydrogen-enhanced strain-induced vacancy (HESIV)". Nishikawa et al. [18] reported that the microvoid formation due to

the HESIV process may occur in front of the fatigue crack tip. They proposed the crack growth model based on microvoids coalescence by the HESIV. The observed microvoids in the present study are also likely induced by hydrogen due to HESIV process.

4.6.3 Cyclic crack tip plasticity in the accelerated regime

By means of the optical microscopy, Murakami and his colleagues at Kyushu University [3, 17, 66, 67, 84, 142, 143, 179] have actively applied this method to investigate the cyclic plastic deformation near the crack path in the HAFCG. They have revealed that the FCGR enhancement by a hydrogen environment or a hydrogen-charged state is mostly accompanied by the localization of the plastic deformation near the crack path in austenitic stainless steel [17, 66, 67], Cr-Mo steel [84], and low carbon steel [16, 142, 143]. It has to be noted that the plastic deformation investigated by them is the cyclic plastic deformation, not the monotonic one. They also confirmed the localization of crack tip plasticity from the changes in the fracture surface morphology [17, 67]. Specifically, they measured the fracture surface morphology exhibiting the striations in austenitic stainless steels by means of a stereographic SEM analysis. As a result, it has been revealed that the presence of hydrogen reduces the surface undulation of striations due to a less crack tip blunting. Besides, Birenis et al. [108, 157] performed the STEM observation of the dislocation structure immediately beneath the fracture surface in the accelerated regime, and observed dislocation tangles and individual dislocations without any dislocation cell structure, which is consistent with the present observations. They also evidenced the great reduction of crack tip plasticity by visualizing the plastic strain distribution near the crack path by the GROD mapping.

This plasticity reduction effect by hydrogen may be understood by referring to the hydrogen effects suppressing dislocation emission [196] and mobility [197, 198]. The suppression of dislocation emission by hydrogen has been confirmed by molecular dynamics simulations by Song et al. [196] demonstrating that in hydrogen-rich regions, dislocation emission is blocked on the crack surface, and brittle cleavage occurs after increasing the applied loading. On the other hand, molecular dynamics simulations by Taketomi et al. [197, 198] have confirmed that hydrogen induces the dislocation mobility reduction resulting in a hardening effect. These analytical results have been confirmed experimentally by the tensile test of hydrogen-charged pure iron by Kimura et al. [56–58] and microcantilever bending test in hydrogen charged-Fe-3%Si alloy by Hajilou et al. [199].

Based on the hydrogen-reduced crack tip plasticity, Murakami and Matsuoka [3, 16, 17] have proposed the HESFCG suggesting that the FCG enhancement occurs by localized crack tip plasticity inducing a less crack tip blunting and a successive advancement of the crack front during crack mouth opening. It has to be noted that they argue that the hydrogen effect is the “localization” of plastic strain ahead of the crack tip, not the “reduction” of plastic strain. The localization of plastic strain means that the hydrogen reduces the plastically deformed zone size meanwhile enhances the local plastic strain within the limited zone, as suggested by the HELP mechanism.

The HESFCG model suggests that the fracture mechanism is basically a shearing fracture due to the enhanced-localized slip activity at the crack tip.

However, their assumption that "the hydrogen effect on the crack tip plasticity is a "localization", not a "reduction", has to be revisited because the present results in this chapter did not confirm the enhanced-localized plastic deformation or slip activity. In the present results, both the optical observation and the OPD measurement with high magnification have evidenced that the extent of the cyclic plastic deformation in the tests in hydrogen exhibiting the FCGR enhancement is dramatically reduced, even in the part very close to the crack path. In addition to this, the critical fact is that the reduction of plastic strain by hydrogen has been confirmed immediately beneath the fracture surface by the STEM observations. This has also been confirmed by Birenis et al. [108, 157]. These present results strongly evidence that hydrogen does "reduce" the crack tip plasticity but does not "localize" it. In fact, Murakami and Matsuoka have not offered a critical experimental proof for the presence of the "enhanced-localized" plasticity in their literature [3, 16, 17].

Wang et al. [200] also argued that hydrogen may "localize" the crack tip plasticity. They applied STEM for directly observing the dislocation structure beneath the fracture surface in low carbon steel. In fact, they observed similar dislocation structure to the present one, disordered dislocation arrangement without any solid cell structure immediately beneath the fracture surface (within a few μm). However, they interpreted this type of dislocation structure as a result of the higher plastic strain inducing higher dislocation density. Therefore, the difference in conclusion between theirs and the present study is attributed to the difference in the interpretation of dislocation structure. Regarding this issue: "is the hydrogen effect on a crack tip plasticity a "reduction" or a "localization"?", the opinions of the researchers are not yet unified. This point must be furthermore pursued because it is critical to elucidate the mechanism of HAFCG.

Another noteworthy fact is that the peculiar mountain-like markings (darker contrast area) were observed beneath the brittle QC fracture surface in the accelerated regime (Figure 4 - 42b). The difference in the contrast of STEM image is caused by a lattice distortion due to local plastic strain. Thus, the mountain-like markings are the area with higher plastic strain compared to the other part. Similar marking has been reported by Nishikawa et al. [19]. They performed the STEM beneath the fracture surface of low carbon steel fatigued in gaseous hydrogen, and observed a similar type of mountain-like marking corresponding to the striation as well as the present result. In addition to the mountain-like marking, they also found a slip band (line-like marking connecting to striation) and a thin layer along the fracture surface showing high dislocation density which were not confirmed in the present observation. They argued that these features of plastic strain distribution beneath the striations are evidence of the hydrogen-induced microvoid coalescence fracture model as mentioned in Chapter 1.

4.7 Conclusion

The main conclusions obtained in this chapter are listed below.

(1) A clear OPD of the side-surface near the crack path due to the monotonic and cyclic plastic zones were observed by means of the optical microscopy and the interferometric microscopy. Both the monotonic and cyclic plastic zone sizes were ranged between their theoretical values in a plane stress and a plane strain conditions, indicating that the surface displacement is generated under the mix of plane stress and plane strain conditions.

(2) No clear dependency of the size and OPD of the monotonic plastic zone on the hydrogen gas pressure and the loading frequency were confirmed in the ΔK-increasing tests, meanwhile, their slight dependencies on the hydrogen gas pressure were observed in the ΔK-constant tests. However, due to the large fluctuation in the size and the OPD of the monotonic plastic zone, it is difficult to draw a reliable conclusion from the present results. Further investigation into the monotonic plastic zone is still necessary to clarify the influence of hydrogen on the monotonic plastic zone.

(3) In the non-accelerated regime (at ΔK = 12 MPa×m$^{1/2}$), the extent of the cyclic plastic zone was too small to be analyzed by optical observation and OPD measurement. The STEM observations revealed that the dislocation cell structure is developed immediately beneath the intergranular facets in hydrogen as same as in air and nitrogen. This result indicates that a certain degree of plastic strain is introduced in the grains ahead of the crack tip.

(4) In the accelerated regime (at ΔK = 18 or 20 MPa×m$^{1/2}$), the cyclic crack tip plasticity in hydrogen is greatly reduced at relatively high loading frequencies ($\geq$ 0.2 Hz for P_{H2} = 35 MPa, $\geq$ 2 Hz for P_{H2} = 3.5 MPa) exhibiting the FCGR enhancement (except at P_{H2} = 3.5 MPa, f = 20 Hz). At relatively low loading frequencies (0.02 Hz for P_{H2} = 35 MPa and 0.2, 0.02 Hz for P_{H2} = 3.5 MPa) exhibiting less or no FCGR enhancement in hydrogen, the reduction of the cyclic crack plasticity does not occur. Therefore, the reduction of cyclic crack tip plasticity is strongly associated with the brittle QC fracture and the FCGR enhancement.

In this chapter, the influence of hydrogen on crack tip plasticity has been identified as described by the above conclusions. As the crack tip plasticity is clearly associated with the modification of FCG behavior by gaseous hydrogen, it is a key factor to understand the HAFCG mechanism which is discussed in the next chapter.

Chapter 5

Discussion on hydrogen-affected fatigue crack growth mechanisms

Résumé

Chapitre 5: Discussion sur les mécanismes de propagation des fissures de fatigue affecté par l'hydrogène

R-5.1 Introduction

Au chapitre 2, les influences de l'hydrogène gazeux sur la déformation plastique monotone et la rupture par traction ont été identifiées. Le fait remarquable obtenu est que l'influence de l'hydrogène sur la propagation des fissures est beaucoup plus importante que celle sur la déformation plastique uniforme. En outre, le gradient de concentration en hydrogène est important pour la fragilisation par l'hydrogène. Le chapitre 3 présentait les résultats des essais de fissuration sous hydrogène gazeux révélant les influences de l'hydrogène sur la vitesse de propagation de la fissure de fatigue et le mode de fracture. De plus, la dépendance de propagation de fissure de fatigue affecté par l'hydrogène sur ΔK, la pression de l'hydrogène et la fréquence de chargement a été identifiée. Le chapitre 4 a révélé que l'hydrogène influe de manière significative sur la plasticité cyclique du fond de fissure fortement associée à l'augmentation de vitesse de propagation de la fissure de fatigue.

Sur la base des résultats obtenus, ce chapitre propose une discussion dans le but d'élucider le mécanisme de propagation des fissures de fatigue sous hydrogène gazeux et sa dépendance aux paramètres d'essai.

R-5.2 Mécanisme de rupture intergranulaire induite par l'hydrogène en régime non-accéléré

Sur la base de les faits expérimentaux, un scénario de rupture intergranulaire induite par l'hydrogène est proposé comme suit et indiqué schématiquement par Figure R - 4.

1) Lors de l'application d'une charge cyclique, les atomes d'hydrogène sont absorbés et entraînés par la nucléation de dislocation à la surface de la fissure. Les atomes d'hydrogène en solution sont entraînés par des dislocations mobiles le long des plans de glissement et diffusent en avant du fond de la fissure (Figure R - 4a).
2) Les dislocations accumulées en avant du fond de fissure forment une structure cellulaire. En même temps, étant donné que le joint de grain peut constituer une barrière à la mobilité de la dislocation [201], les dislocations mobiles portant des atomes d'hydrogène s'arrêtent et s'accumulent au joint de grain et s'accompagnent d'une augmentation de la concentration en hydrogène (Figure R - 4b).

3) Les dislocations et les atomes d'hydrogène fortement accumulés induisent la nucléation de microvides au joint de grain par le mécanisme HESIV, comme en témoignent analytiquement [10, 106, 202] et expérimentalement [18] (Figure R - 4c).
4) Enfin, les microvides et les atomes d'hydrogène fortement accumulés aux joints de grains affaiblissent l'énergie de liaison, entraînant une séparation du joint des grains par décohésion et coalescence des microvides. Les simulations atomiques de plusieurs auteurs [203–205] ont bien démontré ce type de processus de décohésion des joints de grains. Les microvides sont supposés être disposés linéairement dans le sens de la profondeur car l'intersection du plan de glissement et du joint des grains est une ligne dans le sens de la profondeur. Par conséquent, la trace des microvides est peut-être observée sous forme de marques en forme de bandes sur les facettes intergranulaires (Figure R - 4d).

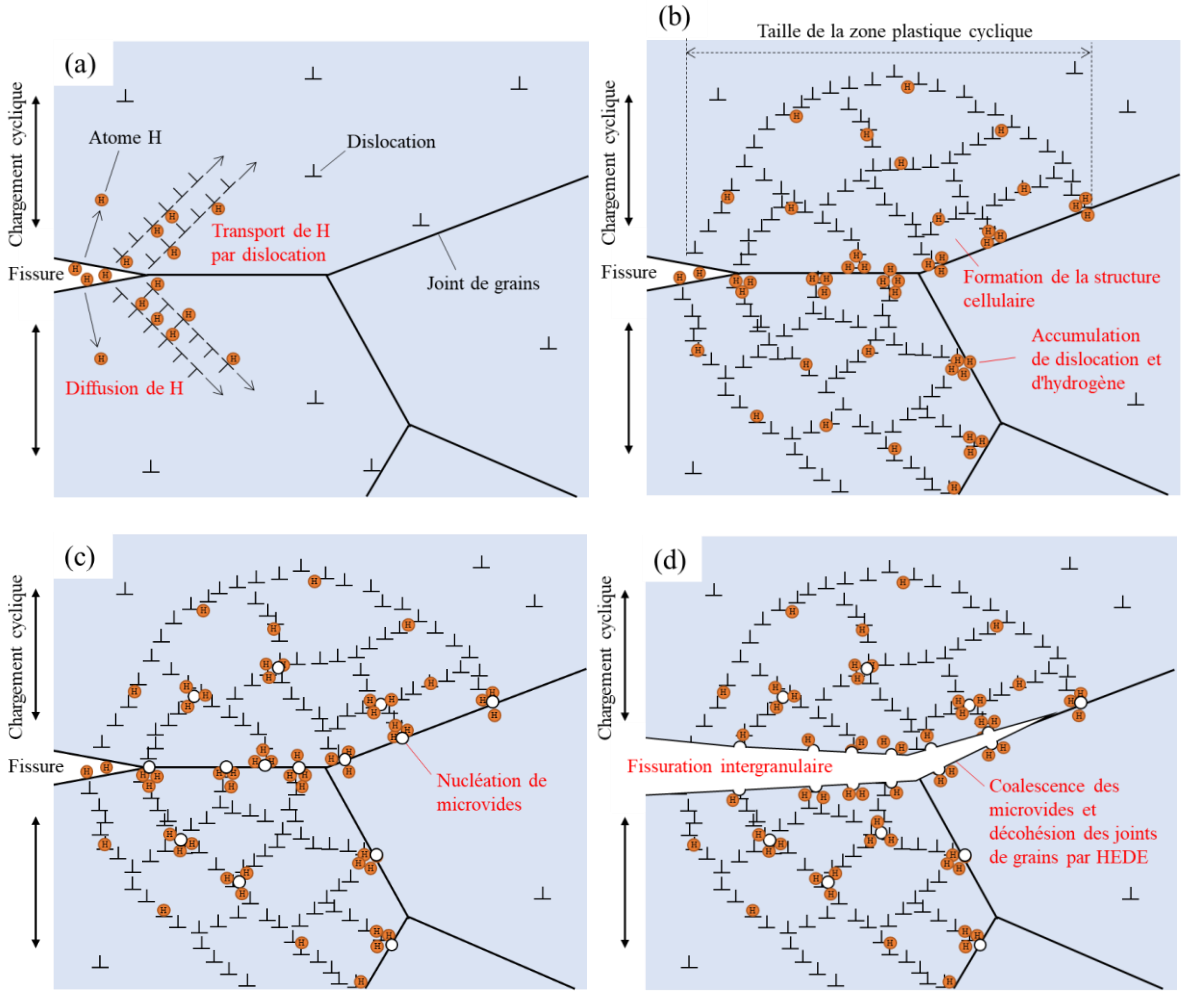

Figure R - 4 Illustration schématique du modèle actuel du mécanisme de rupture intergranulaire induite par l'hydrogène.

R-5.3 Mécanisme de rupture de QC induit par l'hydrogène en régime accéléré

Sur la base des faits expérimentaux, un scénario de rupture fragile de type QC en régime accéléré est proposé comme suit et indiqué schématiquement par Figure R - 5.

1) Avant que la charge augmente, les atomes d'hydrogène sont absorbés par la surface de la fissure et diffusent en avant du fond de la fissure (Figure R - 5(b-1)).
2) Une fois que le chargement a commencé à augmenter, dans le cas sous air, la forte déformation plastique provoque l'émoussement du fond de fissure accompagné d'une zone déformée plastiquement en avant du fond de fissure (Figure R - 5(a-2)). En présence d'hydrogène, les atomes d'hydrogène dissous localisés dans le champ de contrainte hydrostatique élevé [206] inhibent la déformation plastique au fond de la fissure, supprimant ainsi la nucléation [196, 199] et la mobilité [56–58, 197–199] des dislocations (Figure R - 5(b-2)). Le fond de fissure est également maintenu aigu en raison de la réduction de la plasticité du fond de fissure. L'intensité de la contrainte hydrostatique en avant du fond de fissure est encore accrue en raison de son extrémité pointue, induisant une concentration d'hydrogène plus élevée. On observe donc une synergie entre la contrainte et la concentration en hydrogène.
3) Lorsque l'intensité de la contrainte et la concentration en hydrogène atteignent un niveau critique, la rupture de type clivage se produit par le mécanisme HEDE [6], dans lequel l'hydrogène réduit l'énergie de liaison des atomes de la matrice (Figure R - 5(b-3)). Ce mécanisme est mis en évidence par une simulation de dynamique moléculaire réalisée par Matsumoto et al. [207]. La rupture de clivage a lieu le long du plan {100} dans le cas d'un réseau CC, car il s'agit du plan le plus faible. Il continue jusqu'à ce que le fond de la fissure avance vers l'endroit contenant une concentration insuffisante d'hydrogène pour maintenir la décohésion atomique.

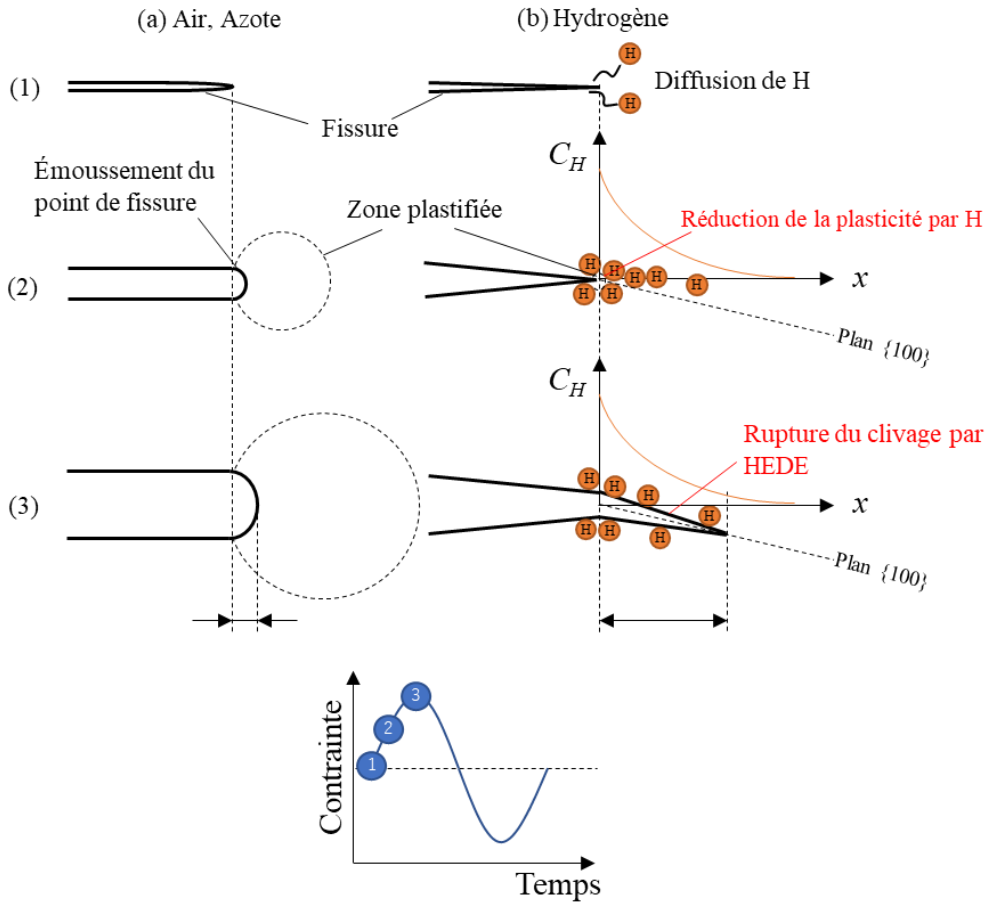

Figure R - 5 Illustration schématique du modèle actuel du mécanisme de fracture par clivage cyclique induit par l'hydrogène.

R-5.4 Dépendance à ΔK, P_{H2}, et f

La dépendance de ΔK_{tr} à la pression d'hydrogène peut être interprétée dans le cadre du modèle de clivage proposé en supposant que l'effet de l'hydrogène sur l'activité des dislocations change en fonction de la concentration en hydrogène et du niveau de contrainte, comme suggéré par Taketomi et al. [197, 198]. Plus précisément, l'augmentation de la vitesse des dislocations (adoucissement) se produit à des concentrations d'hydrogène plus faibles ou à des conditions de contrainte appliquées plus faibles, tandis que la diminution de la vitesse des dislocations (durcissement) se produit à des concentrations plus élevées en hydrogène ou des conditions de contraintes appliquées plus élevées. Par conséquent, si la pression d'hydrogène est élevée (c'est-à-dire une concentration élevée d'hydrogène au fond de la fissure), la réduction de l'activité des dislocations par l'hydrogène peut se produire même à un niveau de contrainte faible, à savoir un faible ΔK_{tr}.

D'autre part, la dépendance à la fréquence de chargement peut être interprétée par la profondeur de pénétration de l'hydrogène et/ou l'équilibre entre la vitesse de diffusion de l'hydrogène et la vitesse des dislocations mobiles, comme suggéré par Takai et al. [106, 208]. Dans ce contexte, la

limite supérieure de la vitesse de propagation est probablement atteinte lorsque la vitesse de diffusion de l'hydrogène et la vitesse des dislocations mobiles sont équilibrées. De plus, l'atténuation de l'augmentation la vitesse de propagation à une fréquence de charge très faible peut s'expliquer par le fait que l'interaction entre l'hydrogène et les dislocations devient faible lorsque la vitesse des dislocations devient inférieure à la vitesse de diffusion l'hydrogène, par réduction de la fréquence de chargement.

R-5.5 Critères caractéristiques de la fissuration affectées par l'hydrogène

À partir des analyses des propriétés de propagation des fissures de fatigue affectées par l'hydrogène en fonction des paramètres influents (ΔK, P_{H2}, and f), trois critères caractéristiques ont été identifiés comme suit:

i. $\boldsymbol{\Delta K_{tr}}$: facteur d'intensité de contrainte nécessaire pour provoquer une rupture de clivage induite par l'hydrogène. Il dépend de P_{H2} car c'est une combinaison de ces deux paramètres qui doit satisfaire à une condition critique pour activer un effet de l'hydrogène réduisant l'activité des dislocations, ce qui entraîne une réduction de la plasticité en fond de fissure et une rupture de type clivage. Ce critère permet de déterminer un niveau de contrainte maximal admissible de fonctionnement en fonction de la pression d'hydrogène gazeux, sans dégradation de la durée de vie en fatigue.

ii. $\boldsymbol{(P_{H2} \times f)^{1/2}}$: gradient de concentration d'hydrogène nécessaire pour provoquer une rupture de type clivage induite par l'hydrogène. Sous un certain niveau de gradient, les atomes d'hydrogène peuvent interagir avec les dislocations mobiles. Leur interaction déclenche un effet réduisant l'activité des dislocations, ce qui entraîne une plasticité en pointe de fissure et une rupture du clivage. Ce critère nous permet de déterminer une plage de sécurité reliant la pression d'hydrogène et la fréquence de chargement appliquée.

iii. **Limite supérieure de da/dN**: maximum possible de la vitesse de propagation de fissure. Cette valeur correspond à un équilibre entre l'action de l'hydrogène et les vitesses de dislocations. L'interaction entre l'hydrogène et les dislocations est alors maximisée. Ce critère peut être considéré comme un maximum possible de la vitesse de propagation de la fissure de fatigue à toute fréquence de chargement sous environnement hydrogène, ce qui nous aide à estimer la durée de vie des produits soumis à cet environnement.

L'application pratique de ces critères peut améliorer la conception en fatigue et la fiabilité des équipements liés à l'hydrogène et ainsi contribuer à une économie fondée sur l'hydrogène.

----------(Fin du résumé)----------

5.1 Introduction

In Chapter 2, the influence of gaseous hydrogen on monotonic plastic deformation and tensile fracture has been identified. The obtained noteworthy fact is that the influence of hydrogen on crack propagation is much more important than the one on uniform plastic deformation. Besides, the gradient of hydrogen concentration is likely important for the hydrogen embrittlement. Chapter 3 presented the results of FCG tests under gaseous hydrogen revealing the influence of hydrogen on FCGR and fracture mode. Furthermore, the dependency of HAFCG on ΔK, hydrogen gas pressure, and loading frequency has been identified. Chapter 4 revealed that hydrogen significantly influences the cyclic crack tip plasticity which is strongly associated with the FCGR enhancement. The obtained results of fatigue crack properties under gaseous hydrogen are summarized by Table 5 - 1 organizing the results in terms of various ΔK, P_{H2} and f. The unknown parts are shown as blank in this table.

Based on these results, this chapter provides a discussion by integrating the facts and insights, aiming to elucidate the mechanisms of fatigue crack propagation under gaseous hydrogen and its dependency on the testing parameters.

Table 5 - 1 Summary of fatigue crack properties under gaseous hydrogen at various ΔK, P_{H2} and f.

(a) P_{H2} = 35 MPa

Regime (ΔK range [MPa×m$^{1/2}$])	Non-accelerated (ΔK < 12)	Transition (12 < ΔK < 15)	Accelerated (15 < ΔK)	
			$f \geq$ 0.2 Hz	f = 0.02 Hz
FCGR	Not enhanced (or slightly enhanced)	Enhanced	Enhanced	Less enhanced
Fracture mode	IG	IG + QC	QC	QC with larger cleavage-like facets
Cyclic crack tip plasticity (compared to the one in the inert environment)	-	Reduced	Reduced	No change
Dislocation structure	Cell structure (2 Hz)	-	Dislocation tangles + Dislocation walls connected to striation (20, 2 Hz)	Cell structure

(a) P_{H2} = 3.5 MPa

Regime (ΔK range [MPa×m$^{1/2}$])	Non-accelerated (ΔK < 15)	Transition (15 < ΔK < Unknown)		Accelerated (Unknown < ΔK)
		$f \geq$ 2 Hz	$f \leq$ 0.2 Hz	
FCGR	Not or slightly enhanced	Enhanced	Not or slightly enhanced	-
Fracture mode	IG + Ductile TG	QC	Ductile TG	-
Cyclic crack tip plasticity (compared to the one in the inert environment)	-	Reduced	No change	-
Dislocation structure	-	Dislocation tangles + Dislocation walls connected to striation (20 Hz)	Cell structure (0.02 Hz)	-

(IG: Intergranular, QC: Quasi-cleavage, TG: Transgranular, -: Unknown)

5.2 Mechanism of hydrogen-induced intergranular fracture in the non-accelerated regime

Firstly, the mechanism of hydrogen-induced intergranular fracture in the non-accelerated regime is discussed in this section. The important features of this fracture mode are noted as follows.

- The intergranular fracture occurs in relatively low ΔK range depending on the hydrogen gas pressure (Sub-section 3.3.3).
- The FCGR is the same level as the one in air (Figure 3 - 8).
- High degree of plastic strain is accumulated in the grains beneath the intergranular facets as same level as ductile fracture in air. This has been evidenced by the presences of stripe-like markings on the intergranular facets (Figure 3 - 10), the dislocation cell structure and microvoids (Figure 4 - 35) immediately beneath the fracture surface.

Based on these experimental facts, a scenario of the hydrogen-induced intergranular fracture is proposed as follows and schematically represented in Figure 5 - 1.

1) During cyclic loading, hydrogen atoms are absorbed and/or swept-in by dislocation nucleation from the crack surface. Solute hydrogen atoms are dragged by mobile dislocations along slip planes as well as they diffuse ahead of the crack tip (Figure 5 - 1a).
2) The dislocations accumulated ahead of the crack tip form a characteristic cell structure. At the same time, since the grain boundaries may act as a barrier for the dislocation mobility [201], the mobile dislocations carrying hydrogen atoms stop and pile-up at the intersections of the dislocation walls and the grain boundary, accompanied by hydrogen concentration (Figure 5 - 1b).
3) The highly accumulated dislocations and hydrogen atoms induce the nucleation of vacancies at the grain boundary by the HESIV mechanism [10]. An aggregation of the vacancies produces microvoids as evidenced analytically [10, 106, 202] and experimentally [18] (Figure 5 - 1c).
4) Finally, the highly accumulated microvoids and hydrogen atoms at the grain boundaries weaken the bonding energy of the grain boundary, triggering a separation of grain boundary by decohesion and microvoid coalescence. Atomistic simulations by several authors [203–205] have demonstrated well this type of grain boundary decohesion process. The microvoids are supposed to be linearly arranged in the depth-direction of this illustration since the intersection of slip plane and grain boundary would be a line parallel to the crack front edge. Therefore, the trace of the microvoids is possibly observed as stripe-like markings perpendicular to the crack growth direction on the intergranular facets (Figure 5 - 1d).

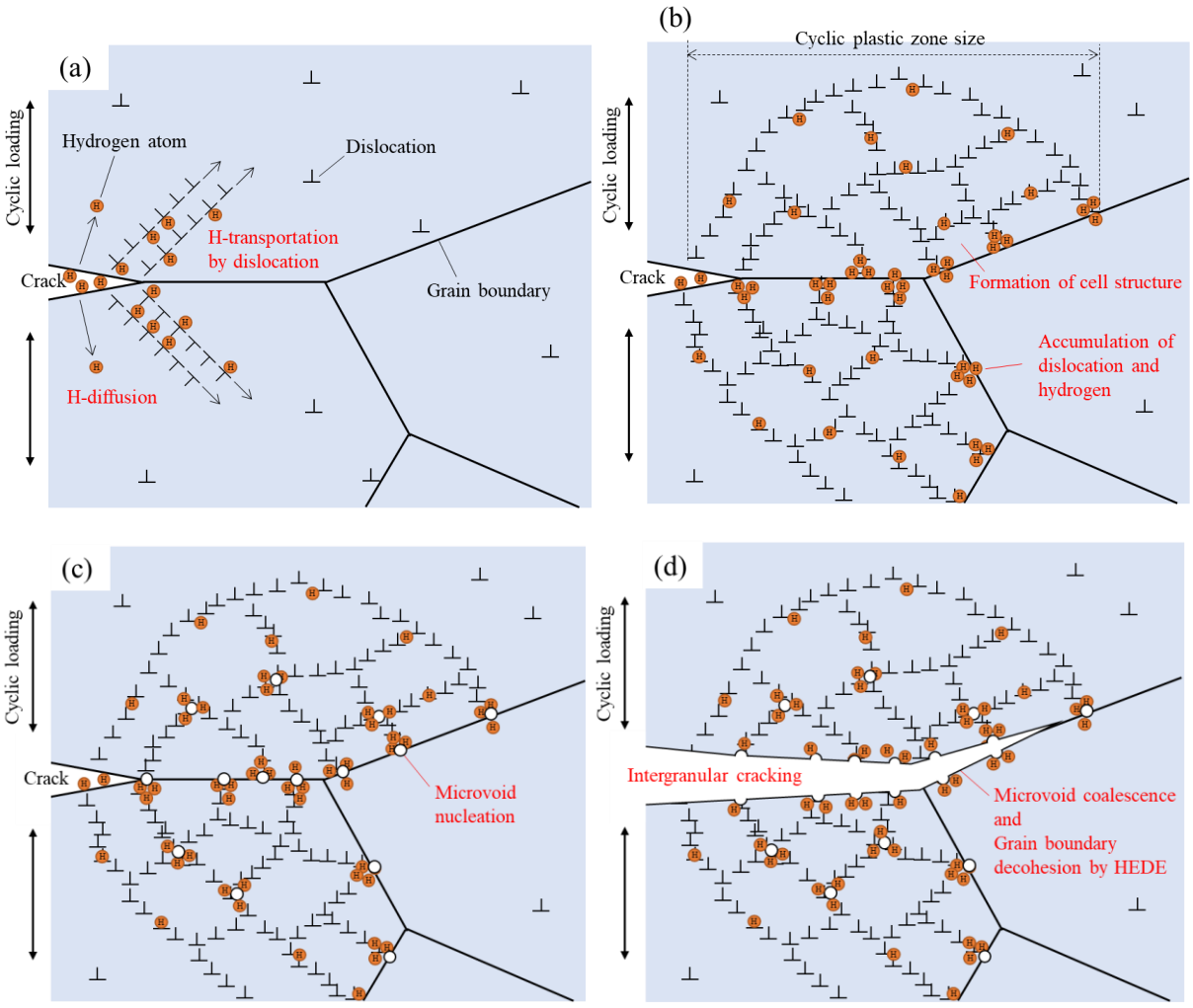

Figure 5 - 1 Schematic illustration of the present model of hydrogen-induced intergranular fracture mechanism.

A model similar to the present one has been recently proposed by Ogawa et al. [167]. They obtained experimental evidences in pure iron which are mostly consistent with this study as already mentioned in Sub-section 4.6.2. They also found the presence of microvoids formed along the grain boundary ahead of the intergranular crack tip in a pure iron which is a direct evidence of this type of fracture model. However, their model is not totally the same as the present model. The main difference is that their model emphasizes that hydrogen enhances the emission and mobility of dislocations inside of the grains ahead of the crack tip, playing an important role for a high amount of accumulation of dislocation and hydrogen at the grain boundary. Since the hydrogen effect of plasticity enhancement in the intergranular cracking has not been clearly confirmed by any experimental evidence as explained in Sub-section 4.6.2, thus, this hydrogen effect is not involved in the present model.

Wang et al. [77] have observed the dislocation cell structure in the intergranular tensile fracture in hydrogen-charged pure iron. They also proposed the fracture model based on plasticity-mediated intergranular decohesion. They also confirmed the presence of stripe-like markings on the intergranular facets which is similar to the one observed in this study (Figure 3 - 10). They argued that the stripe-like markings are produced as a result of extrusions at the grain surface due

to slip band formation, that is different from the present argument and Ogawa's one. As the present STEM observation did not confirm a presence of ladder-like dislocation structure which is a typical microstructure of the persistent slip bands (PSBs), the assumption by Wang et al. is not convincing in this case. Even though, the general concept of "hydrogen-induced plasticity-mediated intergranular decohesion process" seems to hold true for both cases of cyclic and monotonic loadings.

One question remains: despite such a drastic change in the fracture mode from transgranular to intergranular due to the presence of hydrogen, the FCGR was not changed. One possible explanation for this is that the same level of strain energy might be required for triggering both types of cracking. The TEM observation of dislocation structure [30] has revealed that the size of dislocation cells formed beneath the fracture surface in air and hydrogen is almost the same, indicating that the same degree of plastic strain was imparted to the material during the crack propagation. This suggests that the same level of strain energy is consumed for plastic deformation during the transgranular crack propagation in air and the intergranular one in hydrogen. Thus, because the remaining available energy for crack advancement is the same for both cases, so the crack growth rate becomes almost the same. On the other hand, Ogawa et al. [167] explained this issue by referring a competition of two different effects of hydrogen: material softening (resulting in FCG deceleration) and material hardening (resulting in FCG acceleration), occurring at the same time. Currently, either explanation is possible. Further investigation on this point is necessary.

5.3 Mechanism of hydrogen-induced QC fracture in the accelerated regime

The mechanism of hydrogen-induced QC fracture in the accelerated regime is discussed in this section. The important features of this fracture mode are noted as follows.

- The brittle QC fracture occurs in relatively high ΔK range, depending on the hydrogen gas pressure (Sub-section 3.3.3).
- The FCGR in hydrogen is highly enhanced from the one in air (Figure 3 - 8).
- Significant reduction of cyclic crack tip plasticity occurs with the FCGR enhancement. This has been evidenced by the reduced plastic deformation near the crack path (Section 4.4) and the dislocation structure (random distribution of dislocation tangles, Figure 4 - 38) immediately beneath the fracture surface.

Based on these experimental facts, a scenario of brittle QC fracture in the accelerated regime is proposed as follows and schematically described by Figure 5 - 2.

1) Before the loading increases, hydrogen atoms are absorbed from the crack surface and diffuses ahead of the crack tip (Figure 5 - 2(b-1)).
2) After the loading starts increasing, in air, intense slip deformation of the crack tip causes crack tip blunting accompanied by plastically deformed zone ahead of the crack tip (Figure 5 - 2(a-2)) [209]. In contrast, with the presence of hydrogen, the solute hydrogen atoms concentrated in high hydrostatic stress field [206] inhibit the plastic deformation at the crack tip by the hydrogen effect suppressing dislocation nucleation [196, 199] and mobility [56–58, 197–199] (Figure 5 - 2(b-2)). The crack tip is maintained as sharp due to the crack tip plasticity reduction. The hydrostatic stress intensity ahead of the crack tip is further enhanced due to the sharp crack tip, inducing higher hydrogen concentration. In a synergy effect, hydrostatic stress and hydrogen concentration rapidly enhance each other.
3) When both stress intensity and hydrogen concentration reach a critical level, cleavage fracture occurs by the HEDE mechanism [6] in which the hydrogen reduces bonding energy of matrix atoms (Figure 5 - 2(b-3)). This mechanism is supported by a molecular dynamics simulation by Matsumoto et al. [207]. The cleavage fracture takes place along {100} plane in case of BCC lattice because it is the weakest plane. It continues until the crack tip advances to the place containing insufficient amount of hydrogen concentration to maintain the atomic decohesion.

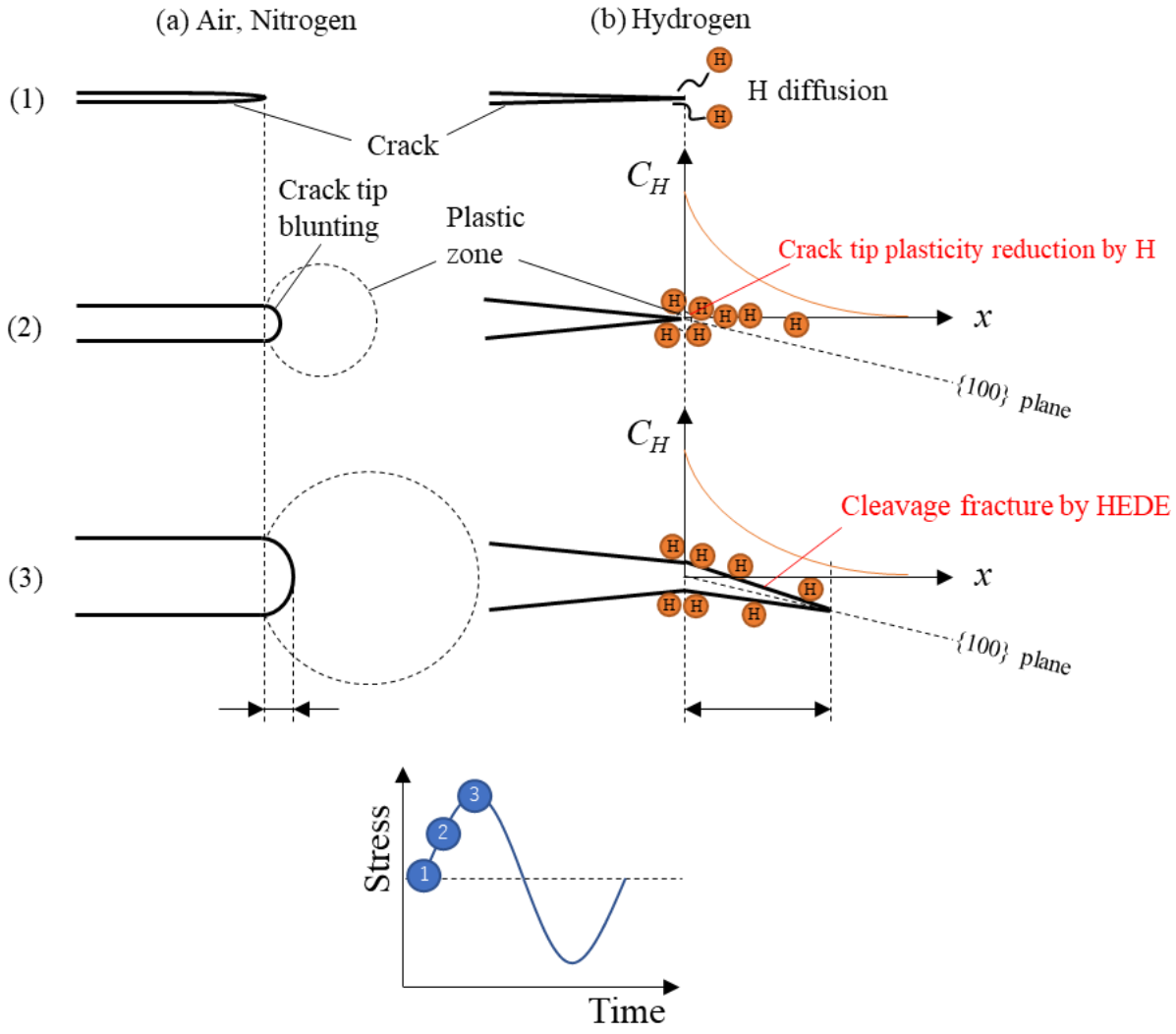

Figure 5 - 2 Schematic illustration of typical FCG model in air or nitrogen (a) and the present model of hydrogen-induced cyclic cleavage fracture mechanism (b).

Several past works have proposed some different models of the hydrogen-induced QC fracture as summarized in Sub-section 1.7.5 (Figure 1 - 12). In order to examine the validity of the present model, the three models in literature (Figure 1 - 12b-d) are revisited and compared with the present one. Nevertheless, the dominant mechanism for each proposed model is different, the common argument of these models in literature is that all the models involve the intense plasticity ahead of the crack tip accompanied by a high density of dislocation and defects. However, the present study did not confirm the intense plasticity near the crack path even immediately beneath the fracture surface. Besides, the fracture mechanisms assumed by the literature models are a localized slip deformation for the HESFCG model, and a microvoid coalescence for the hydrogen-induced void coalescence model, which are not cleavage fracture. Thus, these two models cannot explain the presence of the cleavage-like facets on the fracture surface. Because of these reasons, these two explanations are unlikely the case for Armco iron.

Although the hydrogen-induced cyclic cleavage model by Marrow et al. [15] involves the same fracture process, i.e. a cleavage, it assumes the plastically deformed zone with high density of dislocation ahead of the crack tip as a trapping site of hydrogen which contradicts the observation in this study.

On the other hand, Birenis et al. [108, 157] have recently proposed a hydrogen-induced cyclic cleavage model driven by the reduction of crack tip plasticity, which is very similar to the present one. They identified the crack tip plasticity reduction due to hydrogen by a fractography and analyses of plastic strain distribution around the crack by EBSD and STEM. The main difference between their model and the present one is that their model does not involve the bonding energy reduction of matrix atoms by the HEDE mechanism while the present one does. At the moment, it cannot be clearly concluded whether the HEDE mechanism is operating or not. Since the activation of HEDE mechanism requires very high hydrogen concentration and stress concentration [50], in order to clarify the involvement of the HEDE mechanism, it may be effective to investigate quantitatively whether such condition is satisfied at the actual fatigue crack tip.

5.4 Transition from intergranular to transgranular fracture

Although the mechanisms of two types of HAFCG have been proposed in the previous sections, an inevitable question is: why does the fracture mode drastically change from the intergranular fracture to the transgranular one by increasing ΔK? A possible clue to answer this question is the presence of two different hydrogen effects: in the non-accelerated regime, no clear modification of the crack tip plasticity by hydrogen was observed whereas, in the accelerated regime, a drastic reduction of the crack tip plasticity by hydrogen resulting in the absence of dislocation cell structure was observed. Regarding this issue, a noteworthy finding from the molecular dynamics simulations by Taketomi et al. [197, 198] is that the hydrogen effect on dislocation activity changes depending on the hydrogen concentration and stress level. Specifically, the increase in dislocation velocity (resulting in softening) occurs at lower hydrogen concentration or lower applied stress conditions. In contrast, the decrease in dislocation velocity (resulting in hardening) occurs at higher hydrogen concentration or higher applied stress conditions. This fact gives a good explanation to the transition from the intergranular fracture mode to the transgranular one as follows. When ΔK is lower than ΔK_{tr} (i.e. in the non-accelerated regime), as the crack tip stress intensity is low, the solute hydrogen atoms in the vicinity of the crack tip enhance the dislocation mobility (which might be a little effect because it is not clearly confirmed in the present study). Consequently, the interaction between the enhanced dislocation activity and solute hydrogen atoms leads to the intergranular fracture process as proposed. When ΔK reaches ΔK_{tr} (i.e. the beginning of the transition regime), the crack tip stress intensity becomes sufficiently high to allow the solute hydrogen to decrease the dislocation mobility. This inhibits the crack tip blunting and induces the synergetic increases in the hydrostatic stress intensity and the hydrogen concentration ahead of the crack tip. This results in the cleavage fracture as assumed by the present model of the hydrogen-induced QC fracture.

5.5 Dependencies of HAFCG on ΔK and hydrogen gas pressure

The dependency of HAFCG on the testing parameters, ΔK, the hydrogen gas pressure P_{H2}, and the loading frequency f, is here discussed. Since the testing parameters strongly affect the hydrogen diffusion behavior in the material, it is important to consider the hydrogen diffusion and concentration ahead of the crack tip under various testing conditions to investigate the mechanisms of the dependencies. For this purpose, to study a cause and effect relationship between the testing conditions and the diffused hydrogen concentration C_H ahead of the crack tip, the hydrogen diffusion from the crack tip during one loading cycle has been estimated by the following calculations. The hydrogen concentration C_H in the material was calculated by the one-dimensional Fick's diffusion law in a semi-infinite plane surface subjected to a hydrogen concentration C_s at its boundary as [40]:

$$C_H(x,t) = C_s\left\{1 - erf\left(\frac{x}{2\sqrt{Dt}}\right)\right\} \qquad 5\text{ - }1$$

where x is the distance from the surface of the semi-infinite plane, t the time, and erf the error function. This equation is the approximated function of Fick's diffusion law by the error function. The value of D was 2.5×10^{-10} m^2/s, as the one used in Chapter 2. The evolution of C_H is considered for one loading cycle period, *i.e.* for t ranging from 0 to $1/f$ [s]. The saturated hydrogen concentration at the surface C_s is obtained by the Sievert's law (Equation 1 - 6).

Figure 5 - 3 shows the calculated hydrogen concentration ahead of the crack tip after one loading cycle. In this figure, the hydrogen concentration was indicated by a ratio of C_H to the saturated hydrogen content at P_{H2} = 35 MPa, $C_{s,\,PH2=35}$, allowing us to compare the values between different hydrogen gas pressures. It has to be noted that these calculations neglect the factors influencing the hydrogen diffusion, such as the hydrostatic stress field and defects trapping hydrogen atoms as evidenced by Sofronis et al. [39, 86]. Meanwhile, Moriconi [26] confirmed that the influence of hydrostatic stress on the hydrogen diffusion is limited within only few μm away from the crack tip. The purpose of the calculations is here to compare different testing configurations by reliable orders of hydrogen concentration, with the same assumptions, and not to calculate precisely the hydrogen concentration.

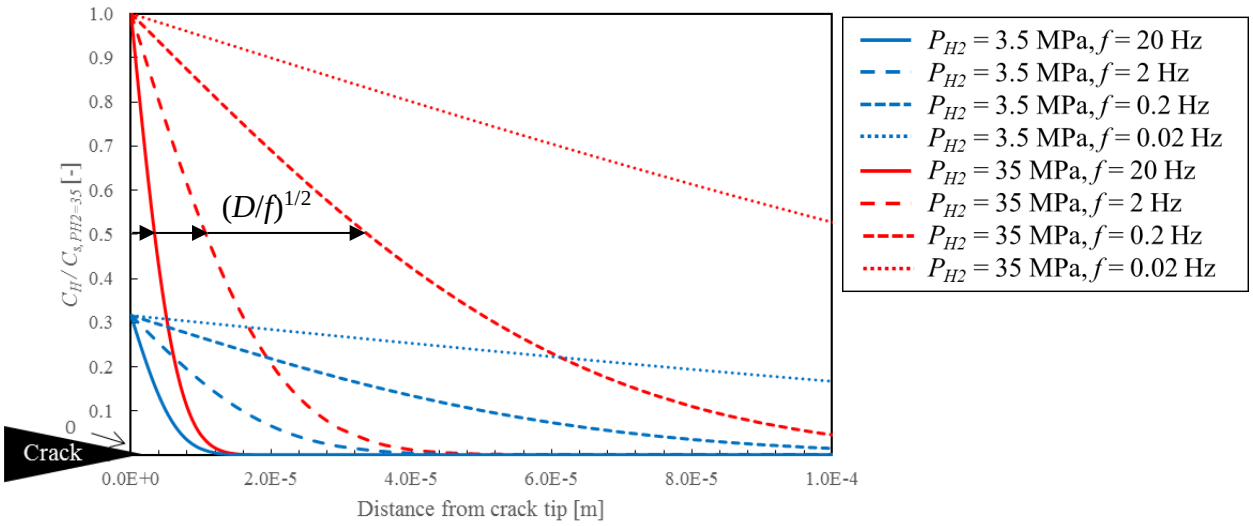

Figure 5 - 3 Comparison of the hydrogen concentration profile ahead of the crack tip after one loading cycle.

In terms of the influence of hydrogen gas pressure, as revealed in Chapter 3, the value of ΔK triggering the FCGR enhancement (i.e. ΔK_{tr}) decreases by increasing the hydrogen gas pressure. Equation 1 - 6 expresses that the saturated hydrogen content C_s depends on the hydrogen gas pressure P_{H2} (also as shown in Figure 5 - 3). Since ΔK_{tr} depends on hydrogen gas pressure, C_s is considered as an influential factor acting on the shift of ΔK_{tr}. This dependence of ΔK_{tr} on the hydrogen gas pressure can be explained by the assumption mentioned in Section 5.4. If hydrogen gas pressure is high, the hydrogen concentration at the crack tip (C_s) also becomes high, hence the hydrogen-induced QC fracture is easily activated even in the case of a low level of stress intensity at the crack tip. On the contrary, if hydrogen gas pressure is low, the hydrogen concentration at the crack tip (C_s) becomes low, hence a high level of stress intensity at the crack tip might be required to activate the hydrogen-induced QC fracture. A similar interpretation has also been suggested recently by Ogawa et al. [167].

5.6 Dependency of HAFCG on loading frequency

In terms of the influence of loading frequency f on the FCGR in the accelerated regime, the following two important features have been revealed by the present study:

- the magnitude of FCGR enhancement in the accelerated regime increases by decreasing f until a certain value; and
- the magnitude of FCGR enhancement reaches the upper limit by decreasing f down to a certain value. If f is further decreased, the FCGR rapidly decreases as same level as in air. At the same time, the crack tip plasticity and the fracture mode also change.

If the first feature is considered from the viewpoint of hydrogen concentration ahead of the crack tip, the penetration depth $(D/f)^{1/2}$, which is defined as the distance from the crack tip where the value of C_H/C_s becomes 0.5 C_s, increases with the decrease in loading frequency (as shown in Figure 5 - 3). This is because a longer period of one loading cycle allows hydrogen to diffuse

deeper from the crack tip at lower loading frequency. According to the present model of hydrogen-induced QC fracture, deeper hydrogen penetration ahead of the crack tip allows a longer crack advancement due to the continuous cleavage fracture, resulting in higher FCGR.

Regarding the second feature, a possible explanation is the importance of the relationship between hydrogen diffusing velocity and dislocation velocity as suggested by Takai et al. [106, 208]. They examined the hydrogen desorption behavior of pure iron and Inconel 625 during tensile deformation with various strain rates of $d\varepsilon/dt = 4.2\times10^{-5}$/s, 4.2×10^{-4}/s and 4.2×10^{-3}/s. As a result, in pure iron, the amount of desorbed hydrogen increased by increasing the strain rate from 4.2×10^{-5}/s to 4.2×10^{-4}/s, and reached the maximum amount (16% of the initial hydrogen content) at the strain rate of 4.2×10^{-4}/s. And then, the amount of desorbed hydrogen decreased by increasing the strain rate from 4.2×10^{-4}/s to 4.2×10^{-3}/s. This result implies that, when the velocities of hydrogen and dislocation are balanced, their interaction is maximized, hence the maximum amount of hydrogen are transported by dislocations.

This mechanism may explain the dependency of HAFCG on loading frequency as follows. When the loading frequency is high (e.g. 20 Hz in the case of P_{H2} = 35 MPa), since the crack tip straining rate is high, the dislocation velocity emitted from the crack may be much higher than hydrogen diffusing velocity. Thus, the interaction between hydrogen and dislocation is still weak. When the loading frequency decreases (e.g. 2 Hz), the dislocation velocity decreases and approaches the hydrogen diffusing velocity. As the hydrogen and dislocation velocities are getting close to each other, their interaction becomes strong, reducing the dislocation activity. This effect leads to the crack growth enhancement by the proposed cleavage fracture model. Finally, when the hydrogen and dislocation velocities are balanced by decreasing *f* down to a certain level (e.g. 0.2 Hz), their interaction is maximized, exhibiting the maximum FCGR enhancement. When *f* is further decreased (e.g. 0.02 Hz), the dislocation velocity becomes slower than the hydrogen velocity, the connection between hydrogen and dislocation becomes weak again. Consequently, the influence of hydrogen on dislocation disappears. As mentioned above, this theory explains well the second feature of the *f*-dependency of HAFCG (the presence of the upper limit of enhanced FCGR and the attenuation of hydrogen effects of the FCGR enhancement, the crack tip plasticity, and the fracture mechanism), in fact, as well as the first feature (the increase in FCGR by decreasing *f*). Therefore, the two possible explanations exist for the first feature.

However, the dislocation and hydrogen velocities in the vicinity of the crack tip in the present case of FCG tests have not been quantitatively examined yet, since it is difficult to precisely estimate them due to the complexity of the crack tip stress field under cyclic loading. The quantitative investigation on this issue is necessary in the prospective work in order to verify the above assumption and to clarify the interaction between hydrogen and dislocation.

In addition to the above qualitative interpretation for the second feature based on the relationship between hydrogen and dislocation velocities, another important quantitative finding for the attenuation of the hydrogen effects has been made by Yoshikawa et al. [142, 143] based on their experimental results of FCG tests in low carbon steel with a wide range of hydrogen gas pressure and loading frequency. Their obtained relationship between HAFCG rate and loading frequency is shown in Figure 5 - 4a. As shown in this diagram, the FCGRs at relatively low hydrogen gas

pressures exhibit a reversal effect of loading frequency similar to the one observed in this study (Figure 3 - 16). Yoshikawa et al. have estimated the hydrogen distribution ahead of the crack tip by means of the same method as explained in the previous section, and calculated the gradient of hydrogen concentration in the vicinity of the crack tip expressed by:

$$\text{Hydrogen gradient: } \left(\frac{P_{H2}\times f}{2D}\right)^{1/2} \propto (P_{H2}\times f)^{1/2} \qquad 5\text{ - }2$$

The definition of this term is a gradient of hydrogen concentration between the crack tip ($x = 0$) and the position in which C_H becomes $0.5C_s$ (i.e. the penetration depth $(D/f)^{1/2}$). Yoshikawa et al. have found out that, by rearranging the FCGR data in the function of $(P_{H2} \times f)^{1/2}$ as shown by Figure 5 - 4b, it can be seen that the attenuation of FCGR enhancement at ΔK = 30 MPa×m$^{1/2}$ occurs when $(P_{H2} \times f)^{1/2}$ is lower than 0.2 (MPa/s)$^{1/2}$ regardless of the hydrogen gas pressure.

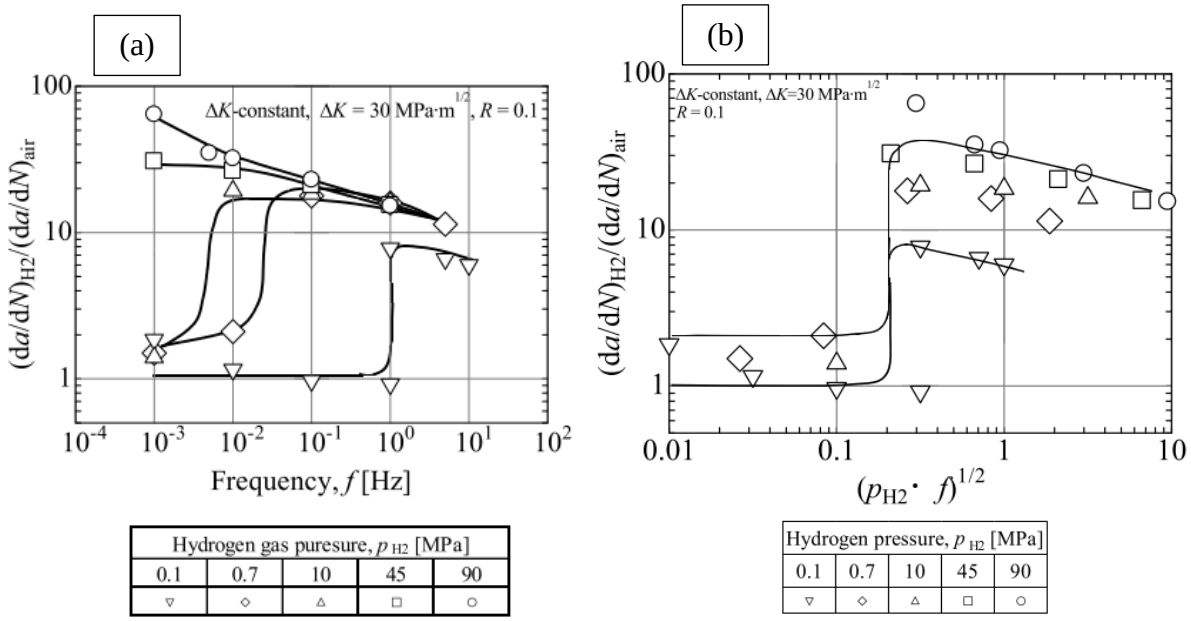

*Figure 5 - 4 Dependencies of HAFCGR enhancement on loading frequency (a) and hydrogen gradient $(P_{H2} \times f)^{1/2}$ (b) in low carbon steel under various hydrogen gas pressures at ΔK = 30 MPa×m$^{1/2}$ by Yoshikawa et al. [*142, 143*].*

To investigate the validity of the criterion $(P_{H2} \times f)^{1/2}$ for the present results, the relationship between the FCGRs in hydrogen and $(P_{H2} \times f)^{1/2}$ is shown in Figure 5 - 5. This diagram clearly demonstrates that the onsets of FCGR enhancement by increasing loading frequency at both hydrogen gas pressures occur at the same value of $(P_{H2} \times f)^{1/2} \sim 2$ (MPa/s)$^{1/2}$. This result indicates that the hydrogen gradient $(P_{H2} \times f)^{1/2}$ is likely a valid criterion for the onset of HAFCGR enhancement of the present case in Armco iron.

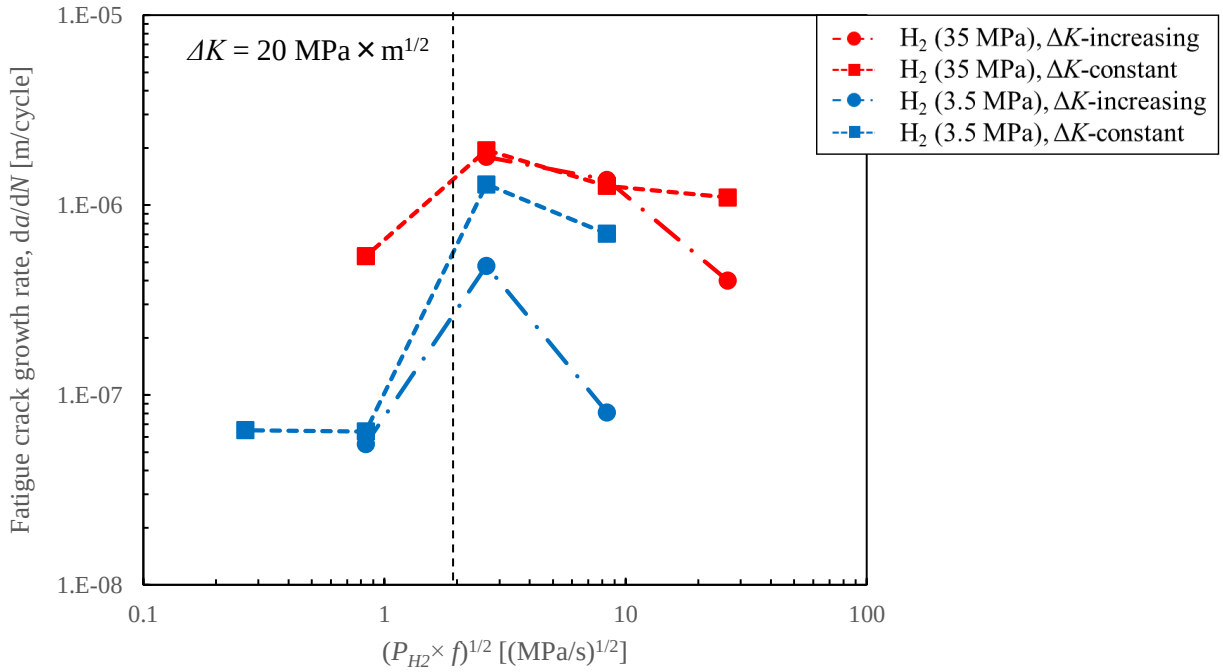

Figure 5 - 5 Relationship between HAFCGR and hydrogen gradient $(P_{H2} \times f)^{1/2}$ at ΔK = 20 MPa×m$^{1/2}$.

Yoshikawa et al. [142, 143] also observed that a clear reduction of the extent of plastic deformation near the crack tip occurred during the enhanced FCG with a high level of hydrogen gradient. On the other hand, at low level of hydrogen gradient without the FCG enhancement, the extent of crack tip plasticity was the same level as in air, which is consistent with the present results. However, they did not provide any clear explanation why the hydrogen gradient is so important for the activation of hydrogen effects in their literature.

The reason why the hydrogen gradient controls the HAFCG enhancement may be understood by the framework of the above-mentioned theory of the balance between hydrogen and dislocation velocities. Theoretically, the hydrogen flux J is a function of the hydrogen gradient ∇C_H as defined by Equation 1 - 7. Therefore, a higher hydrogen gradient induces a higher hydrogen flux ahead of the crack tip, namely a higher number of hydrogen atoms diffusing. As described above, the mobile dislocations and the diffusing hydrogen atoms might interact when their velocities are close. Therefore, it is considered that a movement of large number of hydrogen atoms driven by a high hydrogen concentration gradient is a necessary condition for the interaction between hydrogen and dislocation. If the hydrogen concentration gradient is small (i.e. a hydrogen-saturated state), the diffusion of hydrogen atoms does not occur, and as a result, the interaction between hydrogen and dislocation does not occur. This assumption may explain well the importance of hydrogen gradient as one of the key factors to activate the HAFCG enhancement. This assumption is in a good agreement with the results of tensile tests in Chapter 2 that the hydrogen embrittlement effect under a saturated hydrogen concentration is weaker than the one under less hydrogen concentration but with higher gradient. Furthermore, another conclusion, that hydrogen does not influence uniform deformation while it does influence crack growth with stress gradient, can also be interpreted as follows: hydrogen intensively diffuses to the crack tip due to

stress concentration (stress gradient) at the crack tip. As a result, a hydrogen concentration gradient is generated, and it may activate the crack growth enhancement effect by hydrogen.

In contrast, Somerday et al. [172] suggested that the attenuation of the hydrogen effect at very low loading frequency is caused by an oxidation of crack surface near the crack tip impeding an absorption of hydrogen from the crack surface. They argued that the amount of oxygen in a hydrogen gas may be a controlling factor of *f*-dependency. Their FCG tests exhibited that the attenuation of hydrogen effect occurs by even very small amount of oxygen of 10 ppm which is the same level as the hydrogen gas used in this study. Thus, it is possible that the influence of impurities such as oxygen contained in the hydrogen atmosphere exists in the present case. However, Matsunaga et al. [180] have denied this explanation by referring their experimental results of the FCG tests in hydrogen-charged 304 stainless steel which have demonstrated the attenuation of the hydrogen effect at very low loading frequency without an influence of oxygen.

The dependency of HAFCG on hydrogen gas pressure and loading frequency elucidated from this study is summarized in Figure 5 - 6. If the hydrogen gradient ahead of the crack tip is below a critical level due to a low hydrogen gas pressure or a low loading frequency, the fracture mode becomes ductile in the same way as in air and the FCGR enhancement does not occur. On the other hand, once the hydrogen gradient exceeds the critical level by increasing the hydrogen gas pressure or the loading frequency, the hydrogen effect is activated and leads to brittle QC fracture and FCGR enhancement. At the same time, the FCGR depends on the hydrogen gas pressure and the loading frequency. If the loading frequency is decreased, the crack advancement per cycle increases by the two possible mechanisms: (i) the hydrogen atoms may penetrate deeper from the crack tip, which allows the cleavage fracture to continue over longer distance; and/or (ii) the dislocation velocity decreases and becomes closer to hydrogen diffusing velocity, which induces their stronger interaction. This enhances the cleavage crack growth. On the other hand, when the hydrogen gas pressure is increased, as the hydrogen concentration at the crack tip increases, the necessary stress intensity (ΔK_{tr}) triggering the QC fracture decreases. In other words, the FCGR enhancement may occur from lower ΔK.

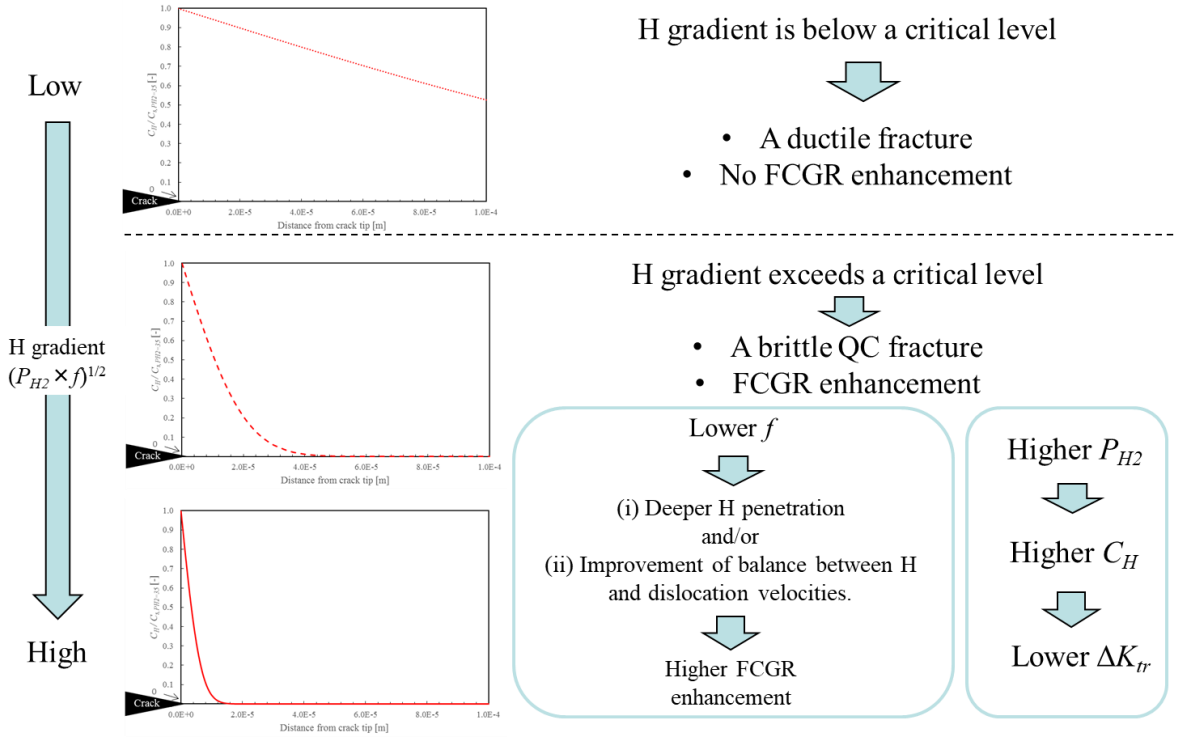

Figure 5 - 6 Summary of dependencies of HAFCG on hydrogen gradient $(P_{H2} \times f)^{1/2}$, hydrogen gas pressure, and loading frequency.

5.7 Criteria for HAFCG enhancement

From the discussions so far, one of the important findings is the presence of the three criteria for the HAFCGR enhancement: the upper limit of HAFCGR; ΔK_{tr}; and $(P_{H2} \times f)^{1/2}$ as indicated in Figure 5 - 7.

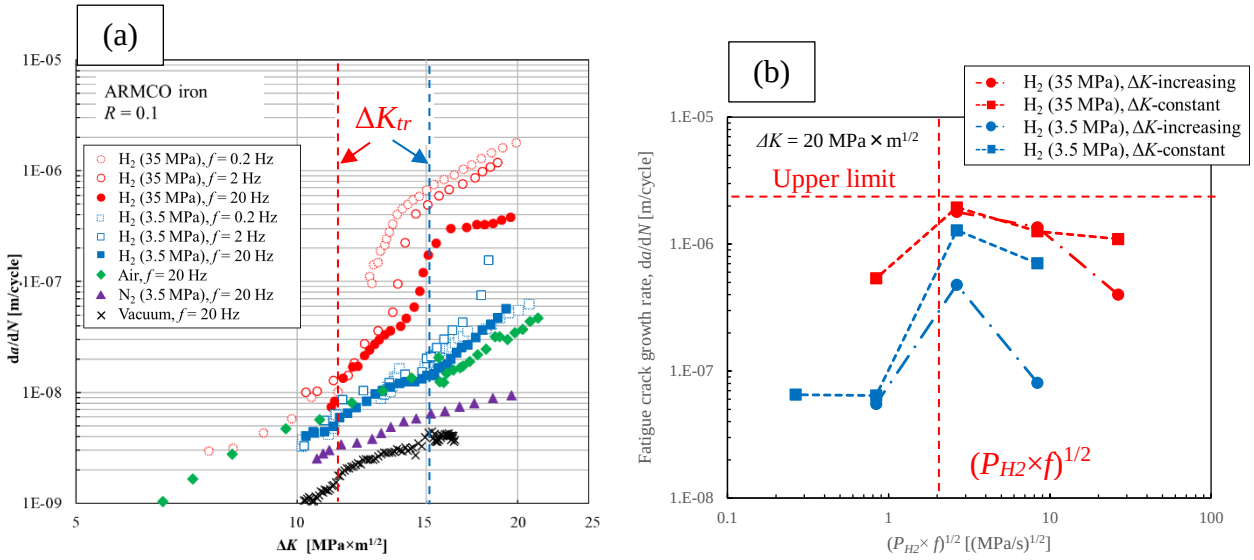

Figure 5 - 7 Three criteria for hydrogen-induced FCGR enhancement: ΔK_{tr} indicated in the diagram of FCGR vs. ΔK (a); the upper limit of FCGR enhancement; and hydrogen gradient $(P_{H2} \times f)^{1/2}$ indicated in the diagram of FCGR vs. hydrogen gradient (b).

The physical meanings of the criteria interpreted by the above discussions are:

i. ΔK_{tr}: a necessary crack tip stress intensity to occur a hydrogen-induced cleavage fracture. It depends on P_{H2} (i.e. C_s) because a combination of both parameters must satisfy a critical condition to activate a hydrogen effect reducing dislocation activity, which results in crack tip plasticity reduction and cleavage fracture.

ii. $(P_{H2} \times f)^{1/2}$: a necessary hydrogen concentration gradient ahead of a crack tip to occur a hydrogen-induced cleavage fracture. Under a certain level of hydrogen gradient, diffusing hydrogen atoms may interact with mobile dislocations. Their interaction triggers a hydrogen effect reducing dislocation activity, which results in crack tip plasticity and cleavage fracture.

iii. Upper limit of FCGR: a possible maximum FCGR enhanced by hydrogen which is roughly 50 times higher than the one in air in the present case. This value is determined by a crack advancement per cycle when hydrogen and dislocation velocities are balanced, and the interaction between hydrogen and dislocation is maximized.

Even though both ΔK_{tr} and $(P_{H2} \times f)^{1/2}$ are the criteria of the onset of HAFCG enhancement, the phenomena represented by these parameters are different. This can be confirmed by two experimental evidences. The first evidence is that the fracture mode in the condition not satisfying the criterion is different between ΔK_{tr} and $(P_{H2} \times f)^{1/2}$: the fracture mode in the non-accelerated regime ($\Delta K < \Delta K_{tr}$) is intergranular, meanwhile the one in low hydrogen gradient ($(P_{H2} \times f)^{1/2} <$ 2) is ductile transgranular (and QC). The second evidence is the shift of ΔK_{tr} cannot be explained

by $(P_{H2} \times f)^{1/2}$. For example, the two testing conditions P_{H2} = 35 MPa, f = 0.2 Hz and P_{H2} = 3.5 MPa, f = 2 Hz are characterized by the same value of $(P_{H2} \times f)^{1/2}$ = 2 $(\text{MPa/s})^{1/2}$, but the values of ΔK_{tr} are different, as shown in Figure 5 - 7. These values of ΔK_{tr} should be consistent if ΔK_{tr} was also controlled by $(P_{H2} \times f)^{1/2}$. Therefore, the physical phenomena triggering the hydrogen-induced QC fracture by satisfying ΔK_{tr} and $(P_{H2} \times f)^{1/2}$ are different.

The three criteria are expected to be useful for a fatigue design and a fatigue life prediction of hydrogen-related equipment. The upper limit of HAFCG rate can be considered as a maximum possible FCGR at any loading frequency under hydrogen environment. This value would enable us to estimate a minimum fatigue life of products and to determine the periods of usage and replacement of products. Besides, ΔK_{tr} and $(P_{H2} \times f)^{1/2}$ could be considered as criteria for degradation of fatigue life. These criteria are useful to determine the usage condition of materials under hydrogen environment avoiding a critical degradation of fatigue life. Identification and application of the criteria is expected to greatly contribute to the improvement of reliability of hydrogen-related equipment.

5.8 Conclusion

In this chapter, the mechanisms of influence of hydrogen on fatigue crack growth have been discussed based on the experimental results obtained in the previous chapters. The obtained main conclusions are summarized as follows.

1) A model of hydrogen-induced intergranular fracture mechanism has been proposed as follows. Under cyclic loading, hydrogen atoms diffuse and are swep-in by mobile dislocations ahead of the crack tip. The mobile dislocations carrying hydrogen atoms stop and pile-up at the intersections of the dislocation walls and the grain boundary, accompanied by hydrogen concentration. The highly accumulated dislocations and hydrogen atoms induce the nucleation of microvoids at the grain boundary by the HESIV mechanism. Finally, the highly accumulated microvoids and hydrogen atoms at the grain boundaries weaken the bonding energy of the grain boundary, triggering a separation of grain boundary by decohesion and microvoid coalescence.
2) A model of hydrogen-induced cyclic cleavage fracture mechanism has been proposed as follows. Solute hydrogen atoms concentrated in high hydrostatic stress field inhibit the plastic deformation at the crack tip by the hydrogen effects suppressing dislocation emission and mobility. The hydrostatic stress intensity ahead of the crack tip is further enhanced by the sharpened crack tip due to the crack tip plasticity reduction, inducing higher hydrogen concentration as a synergy effect. When both stress intensity and hydrogen concentration reach a critical level, cleavage fracture occurs by the HEDE mechanism.
3) The dependency of ΔK_{tr} on hydrogen gas pressure can be interpreted by the proposed cleavage fracture model assuming that a combination of high hydrogen concentration and high crack tip stress intensity is required to trigger the cleavage fracture.
4) The dependency of HAFCG on loading frequency can be interpreted by referring the hydrogen penetration depth and/or the balance between hydrogen diffusing velocity and

mobile dislocation velocity which is likely important for their interaction inducing the crack tip plasticity reduction by hydrogen.

5) The upper limit of HAFCG rate is likely achieved when hydrogen diffusing velocity and mobile dislocation velocity are balanced.
6) The attenuation of HAFCG enhancement at very low loading frequency can be explained as a result of the weak interaction between hydrogen and dislocation when dislocation velocity becomes smaller than hydrogen velocity by decreasing the loading frequency.
7) Three criteria for HAFCG (ΔK_{tr}, $(P_{H2} \times f)^{1/2}$, and Upper limit of HAFCG rate) have been identified. These criteria are expected to be useful for improving a reliability of hydrogen-related equipment.

Conclusion

At the end of the thesis, this part addresses an overview of this study aiming to provide a general conclusion and prospects.

Numerous theories have been proposed to explain the mechanism of hydrogen embrittlement. In particular, the following three theories are today considered as the most important ones: HEDE (Hydrogen-Enhanced DEcohesion) [6, 7], HELP (Hydrogen-Enhanced Localized Plasticity) [8], AIDE (Adsorption-Induced Dislocation Emission) [9] and HESIV (Hydrogen-Enhanced Strain-Induced Void) [10]. These representative models were described in Chapter 1.

In order to be able to predict the fatigue life of hydrogen-related equipment, the advancement of the understandings for the influence of hydrogen gas pressure and loading frequency on the FCG mechanism in hydrogen is strongly required. Thus, the recent studies by Pprime Institute [28–30] have put the emphasis on FCG tests in a commercially pure iron, Armco iron, aiming to investigate the fracture mechanism under various hydrogen gas pressures and loading frequencies. Armco iron was selected as a sample material because of its simple ferrite structure allowing us to analyze the interaction between hydrogen and bcc microstructure. From the previous studies by Bilotta et al. [27, 28], it has been demonstrated that the FCGR at hydrogen gas pressure P_{H2} = 35 MPa is highly enhanced in this material. Besides, the clear dependence of HAFCG rate on the loading frequency has been observed. Nevertheless, the mechanism of FCG enhancement by hydrogen and its dependency on testing parameters are still unclear. This is because of a shortage of understandings for the interaction between hydrogen and plasticity of the material and the characteristics of FCG in hydrogen under wide range of testing parameters (hydrogen gas pressure, loading frequency etc.).

Therefore, the objective of this study is to deepen the understanding for the mechanism of FCG in the presence of hydrogen by mainly clarifying the following two issues:

- interaction between hydrogen and crack tip plasticity;
- the influence of testing parameters on hydrogen-affected FCG in Armco iron.

For the first step, in order to clarify the influence of hydrogen on the tensile deformation and fracture behavior in Armco iron, the tensile tests under high pressure gaseous hydrogen (35 MPa) have been performed with changing the strain rate and the exposure time.

As a result, it has been revealed that the elastic deformation (i.e. Young's modulus) and uniform plastic deformation before the necking (i.e. yield strength and tensile strength) are not influenced by hydrogen. Fracture elongation and reduction of area (*RA*) are decreased (up to 10 %) due to the presence of hydrogen. Hydrogen clearly changes the fracture mode from ductile void coalescence fracture to brittle QC fracture with many surface and secondary cracks. Fracture elongation decreases by decreasing strain rate in both hydrogen and nitrogen. This strain rate dependency is likely related to the material, not to the influence of hydrogen. Fracture elongations at short and very long hydrogen exposure time were as large as in air and nitrogen. Besides, at long hydrogen exposure time, the *RA* was larger than that at the intermediate one and a ductile fracture surface was observed in the central part of the fracture surface. This result suggests that

the saturated hydrogen concentration does not induce intense hydrogen embrittlement despite of the high hydrogen amount inside the specimen.

In these experimental insights, the following two facts are particularly important for considering the influence of hydrogen on FCG:

- hydrogen does not influence uniform deformation behavior of the material, while it does influence the cracking process during the necking deformation. This fact points out that the hydrogen effect on crack propagation is a core issue of hydrogen embrittlement, and this emphasizes the importance of the investigation of hydrogen effect on crack propagation;
- a saturated hydrogen concentration does not necessarily cause a severe hydrogen embrittlement effect. In contrast the importance of the hydrogen gradient on crack propagation has been evidenced. This is related to the mechanism of the onset of hydrogen effect on FCG.

The FCG properties with the influence of hydrogen have been studied by conducting FCG tests under gaseous hydrogen. The influence of hydrogen on the FCGR and the fracture mode were examined. Moreover, the HAFCG was analyzed as a function of ΔK, hydrogen gas pressure and loading frequency.

As a result, the HAFCG rate exhibits three distinct regimes, namely: a non-accelerated regime at low ΔK values, a transition regime, and an accelerated regime at high ΔK values showing FCGR enhancement up to 50 times higher than the FCGR in air. In the non-accelerated regime, the FCGR in hydrogen is almost the same compared to the one in air. Fracture mode in hydrogen is a brittle intergranular fracture, in contrast to transgranular in air at the same ΔK value. Furthermore, stripe-like plastic marking has been observed on intergranular facets. On the other hand, in the transition regime, fracture mode gradually changes from intergranular fracture to transgranular QC one, at the same time HAFCG rate highly increases. After the FCGR acceleration reaches a certain magnitude, the slope of HAFCG rate curve comes back to the same level as in air. In this accelerated regime, fracture surface is fully covered by QC patterns with brittle-like striations.

The value of ΔK_{tr} (the minimum value of ΔK triggering the FCGR enhancement, i.e. the transition regime) decreases by increasing hydrogen gas pressure. In addition, the HAFCG rate increases by decreasing the loading frequency down to a critical value depending on the hydrogen gas pressure. Once the loading frequency becomes lower than the critical value, the HAFCG rate significantly decreases down to the same level as in nitrogen. The fracture mode also changes with the attenuation of FCGR enhancement at low f.

Even though a significant change in fracture mode by hydrogen associated with the FCGR enhancement has been revealed, the mechanism controlling this hydrogen effect was not understood by considering only these results. Since the interaction between hydrogen and crack tip plasticity was expected to be a key factor to understand the mechanism of HAFCG, therefore, the crack tip plasticity in the present FCG tests were investigated. To elucidate the influence of hydrogen on the crack tip plasticity, the plastic deformation near the crack path or beneath the fracture surface of the tested specimens was investigated. The crack tip plasticity was analyzed in multiple scales from macroscopic scale (few mm) to microscopic one (few μm) by means of

optical observations, OPD measurements near the crack path, and STEM observations of dislocation structure immediately beneath the fracture surface.

From the results of optical microscopy and interferometric microscopy, the OPD of the side-surface near the crack path due to the monotonic and cyclic plastic zones were observed. No clear dependency of the size and OPD of the monotonic plastic zone on the hydrogen gas pressure and the loading frequency was confirmed.

On the other hand, the analysis of cyclic plastic zone in the non-accelerated regime by the STEM observations revealed that the dislocation cell structure is developed immediately beneath the intergranular facets in hydrogen as same as in air and nitrogen. This result indicates that a certain degree of plastic strain is accumulated in the grains ahead of the crack tip. In the accelerated regime, the cyclic crack tip plasticity in presence of hydrogen is greatly reduced at relatively high loading frequencies inducing the FCGR enhancement. Meanwhile, at relatively low loading frequencies inducing less or no FCGR enhancement in hydrogen, the reduction of the cyclic crack plasticity does not occur. Therefore, the reduction of cyclic crack tip plasticity is strongly associated with the brittle QC fracture and the FCGR enhancement.

The influence of hydrogen on crack tip plasticity has been identified as described above. As the crack tip plasticity is clearly associated with the modification of FCG behavior by gaseous hydrogen, it is a key factor to understand the HAFCG mechanism. The two mechanism models of hydrogen-induced intergranular FCG and hydrogen-induced QC FCG have been discussed and proposed based on the experimental results obtained in the previous chapters. The proposed scenario of hydrogen-induced intergranular FCG mechanism is as follows:

1) Under cyclic loading, hydrogen atoms diffuse and are swept-in by mobile dislocations ahead of the crack tip.
2) The mobile dislocations carrying hydrogen atoms stop and pile-up at the intersections of the dislocation walls and the grain boundaries, accompanied by hydrogen concentration.
3) The highly accumulated dislocations and hydrogen atoms induce the nucleation of microvoids at the grain boundary by the HESIV mechanism.
4) Finally, the highly accumulated microvoids and hydrogen atoms at the grain boundaries weaken the bonding energy of the grain boundary, triggering a separation of grain boundary by decohesion and microvoid coalescence.

The proposed scenario of hydrogen-induced QC FCG mechanism is as follows:

1) Solute hydrogen atoms concentrated in high hydrostatic stress field inhibit the plastic deformation at the crack tip by limiting dislocation emission and mobility.
2) The hydrostatic stress intensity ahead of the crack tip is further enhanced by the sharpened crack tip due to the plasticity reduction, inducing higher hydrogen concentration as a synergy effect.
3) When both stress intensity and hydrogen concentration reach a critical level, cleavage fracture occurs by the HEDE mechanism.

For the hydrogen-induced QC fracture accompanied by the FCGR enhancement, several different models have been proposed in the past literature as described in Sub-section 1.7.5 (Figure 1 - 12):

Although the cracking mechanisms proposed in these models are different (local slip deformation, atomic decohesion and microvoids coalescence, respectively), they commonly assume the intense plastic strain with a high density of dislocations and defects ahead of the crack tip as a preliminary step of fracture. However, the present STEM observations revealed that the dislocation structure immediately beneath the QC fracture surface consists in a random distribution of individual dislocation tangles without development of cell structure. This indicates that a very small amount of plastic strain was accumulated in the vicinity of the crack tip during the FCG, which casts doubt on the models commonly admitted in the literature.

The dependency of ΔK_{tr} on hydrogen gas pressure can be interpreted in the framework of the proposed cleavage model by assuming that the hydrogen effect on dislocation activity changes depending on the hydrogen concentration and stress level as suggested by Taketomi et al. [197, 198]. Specifically, the increase in dislocation velocity (softening) occurs at lower hydrogen concentration or lower applied stress conditions, while, the decrease in dislocation velocity (hardening) occurs at higher hydrogen concentration or higher applied stress conditions. Therefore, if the hydrogen gas pressure is high (i.e. high hydrogen concentration at the crack tip), the reduction of dislocation activity by hydrogen may occurs even at low stress level, namely a low ΔK_{tr}.

On the other hand, the dependency of HAFCG on loading frequency can be interpreted by the hydrogen penetration depth and/or the balance between hydrogen diffusing velocity and mobile dislocation velocity. The balance of velocities of hydrogen and dislocation is likely important for their interaction inducing the crack tip plasticity reduction by hydrogen as suggested by Takai et al. [106, 208]. In this context, the upper limit of HAFCG rate is likely achieved when hydrogen diffusion rate and mobile dislocation velocity are balanced. Moreover, the attenuation of HAFCG enhancement at very low loading frequency can be explained as a result of weak interaction between hydrogen and dislocation when dislocation velocity becomes smaller than hydrogen velocity by decreasing the loading frequency.

From the analyses of HAFCG rate property as a function of the influential parameters (ΔK, P_{H2}, and f), three characteristic criteria for the HAFCG have been identified as follows:

i. $\boldsymbol{\Delta K_{tr}}$: hydrogen-induced cleavage fracture is driven by crack tip stress intensity. This parameter depends on P_{H2} because a combination of ΔK and P_{H2} must satisfy a critical condition to activate the hydrogen effect reducing dislocation activity, which results in crack tip plasticity reduction and cleavage fracture. This criterion is capable to determine a usage condition of equipment according to the allowable maximum stress level as a function of hydrogen gas pressure at which degradation of fatigue life does not occur.
ii. $\boldsymbol{(P_{H2} \times f)^{1/2}}$: hydrogen-induced cleavage fracture is driven by hydrogen concentration gradient ahead of crack tip. Under a certain level of hydrogen gradient, diffusing hydrogen atoms may interact with mobile dislocations. Their interaction triggers a hydrogen effect reducing dislocation activity, which results in crack tip plasticity and cleavage fracture. This criterion allows us to determine a safe range of hydrogen gas pressure of usage environment not causing the degradation of fatigue life at a given frequency of applied loads.

iii. **Upper limit of FCGR**: possible maximum FCGR enhanced by hydrogen. This value is determined by the crack advancement per cycle when hydrogen and dislocation velocities are balanced, and the interaction between hydrogen and dislocation is maximized. This criterion can be considered as a maximum possible FCGR at any loading frequency under hydrogen environment which helps us to estimate an available lifetime of products subjected to hydrogen without having detrimental effects of hydrogen.

Practical application of these criteria may improve fatigue design and reliability of hydrogen-related equipment. This improvement is expected to greatly contribute for a realization of the hydrogen-based society.

Prospects

The experimental dispersion of the tensile tests in Chapter 2 has to be further investigated. Because of the large dispersion, a reliable conclusion about the influence of very long exposure time could not be obtained as mentioned in Sub-section 2.3.6. A cause of this large experimental dispersion might be related to the work hardened layer of the specimen. Since Armco iron is a ductile material, machining may easily introduce a large amount of plastic strain in the sub-surface. The extent of the work hardened layer may fluctuate due to the severity of machining (feed rate, rotation rate of lathe, etc.) and the layer thickness removed by the polishing. These preparation conditions were not well controlled in this study. Since it is known that the work hardened layer influences the hydrogen embrittlement property [130], the fluctuation of the work hardened layer might be a cause of the experimental dispersion. Therefore, the tensile deformation behavior in Armco iron under gaseous hydrogen should be revisited with a removal or a control of work hardened layer.

The influence of strain rate on hydrogen embrittlement was confirmed by Wu et al. [81], but not in the present result. A reason of this inconsistency may be a difference in the composition of materials (between pressure vessel steel and pure iron), the testing methods (in particular, between a cathodic charging and gaseous atmosphere), or the above-mentioned issue of experimental dispersion of the present tests. This reason should also be investigated because this might lead to an elucidation of influence of material composition or a hydrogen-charging method.

Since this study conducted the FCG tests at only one condition of stress ratio (R = 0.1), the crack closure behavior was not considered. However, as the hydrogen clearly influences the crack tip plasticity, the crack closure behavior is possibly affected by hydrogen. Even though, the influence of hydrogen on the crack closure has not been well investigated even in literature, so it would be interesting to study on this point in the future.

Due to the large dispersion of the maximum OPD and the monotonic plastic zone size, no reliable conclusion about the influence of hydrogen on the monotonic plastic zone was obtained. This dispersion might be due to the ductility of Armco iron. The OPD of monotonic plastic zone was also studied in a 15-5PH steel by Bilotta et al. [27, 159]. In the case of 15-5PH steel which has much higher strength, the size of plastic zone near the crack path is much smaller (< 300 μm) compared to Armco iron. For 15-5PH steel, a clear influence of hydrogen on the OPD has been observed as well as its dependency on hydrogen gas pressure with small dispersion of the results. Thus, the dispersion of monotonic plastic zone size in Armco iron might be an inevitable intrinsic problem. Even though, this difficulty may be overcome by a large amount of experimental data.

As demonstrated in Sub-section 3.5.2 and Sub-section 4.6.1, the HAFCG in Armco iron exhibits time-independence, meanwhile, the one in 15-5PH steel exhibits the time-dependence. However, the difference in time-dependence or time-independence (cycle-dependence) from the view point of the HAFCG mechanism is not clear yet. As mentioned in Sub-section 3.5.2, the difference in the time-dependency between Armco iron and 15-5PH steel is likely because of the difference in yield strength as suggested by Nibur et al. [173]. In order to deeply understand the time-dependency in Armco iron, it is effective to perform static crack growth tests by applying

sustained loading and sustained displacement, as well as the same type of tests in 15-5PH performed by Bilotta et al. [25, 27, 159].

The identification of crystal plane of hydrogen-induced QC cracking as mentioned in Sub-section 4.5.2 has also to be addressed. Although the crystal orientations of the lamellas were identified by the IPF figures obtained by t-EBSD analysis, the crack propagation plane which is angled by 90 degrees from the lamella plane cannot be identified by only seeing this IPF. This is because this type of IPF colored map indicated by the representative planes ({111}, {001}, and {101}) does not give the information of a rotation angle of crystal in the axis perpendicular to the lamella plane. However, as this study proposes the model of hydrogen-induced cyclic cleavage fracture, it is very important to identify and prove the cracking plane is {100} plane which is a typical cleavage plane of bcc material. For identifying the crystal orientation of cracking plane, it is necessary to obtain an original IPF (not colored for mapping) or a Selected-Area Diffraction Pattern (SADP) by TEM in the future.

In addition to the STEM, the microstructure near the crack path should be analyzed by means of EBSD technique to characterize the crystal orientation of cracking plane. Besides, the crack tip plasticity can be further identified by the Grain Reference Orientation Deviation (GROD) analysis which can be obtain by treating the EBSD data. The GROD analysis displays the local deviation (gradient) of crystal orientation inside the grain allowing us to know the distribution of plastic strain in the scale over few grains (few hundreds μm). This analysis is capable to visualize detailed distribution of cyclic plastic strain near the crack path in the scale between the STEM (dislocation structure) and the OPD or optical microscopy (few mm). This technique has been used by Ogawa et al. [108, 157, 163, 167] for example.

Finally, the relevance of the interaction between hydrogen and dislocations and their velocity deserves to be further discussed. The identification and the comparison of the dislocation and hydrogen velocities in the vicinity of the crack tip are necessary in order to verify the credibility of the proposed FCG mechanism and to deepen the understanding of the interaction between hydrogen and dislocation. The formulation for the Crack Tip Strain Rate (CTSR) has been attempted by several literatures [210, 211]. These formulas of CTSR might be applicable to estimate the strain rate ahead of the crack tip and the mobile dislocation velocity in the present case.

Appendix

A. Supplementary results of optical observation of plastic deformation near crack path

A-1 Observation result in Δ*K*-increasing tests

Since the optical images of the crack appearance of the Δ*K*-increasing FCG tests under air and hydrogen at P_{H2} = 3.5 MPa were omitted in Sub-section 4.3.1, they are presented here. Figure A - 1 shows the optical images for the tests under air (f = 20 Hz) (a) and under nitrogen (P_{N2} = 3.5 MPa, f = 20 Hz) (b). Also, Figure A - 2 shows the optical image for the tests under hydrogen at P_{H2} = 3.5 MPa with various loading frequencies f = 0.2 (a), 2 (b), and 20 Hz (c). A noteworthy fact is that, under hydrogen at P_{H2} = 3.5 MPa and f = 0.2 Hz (Figure A - 2a), the cyclic plastic deformation along the crack path is more prominently developed compared to the other loading frequencies, which is consistent with the result of surface topography measurement (Figure 4 - 26).

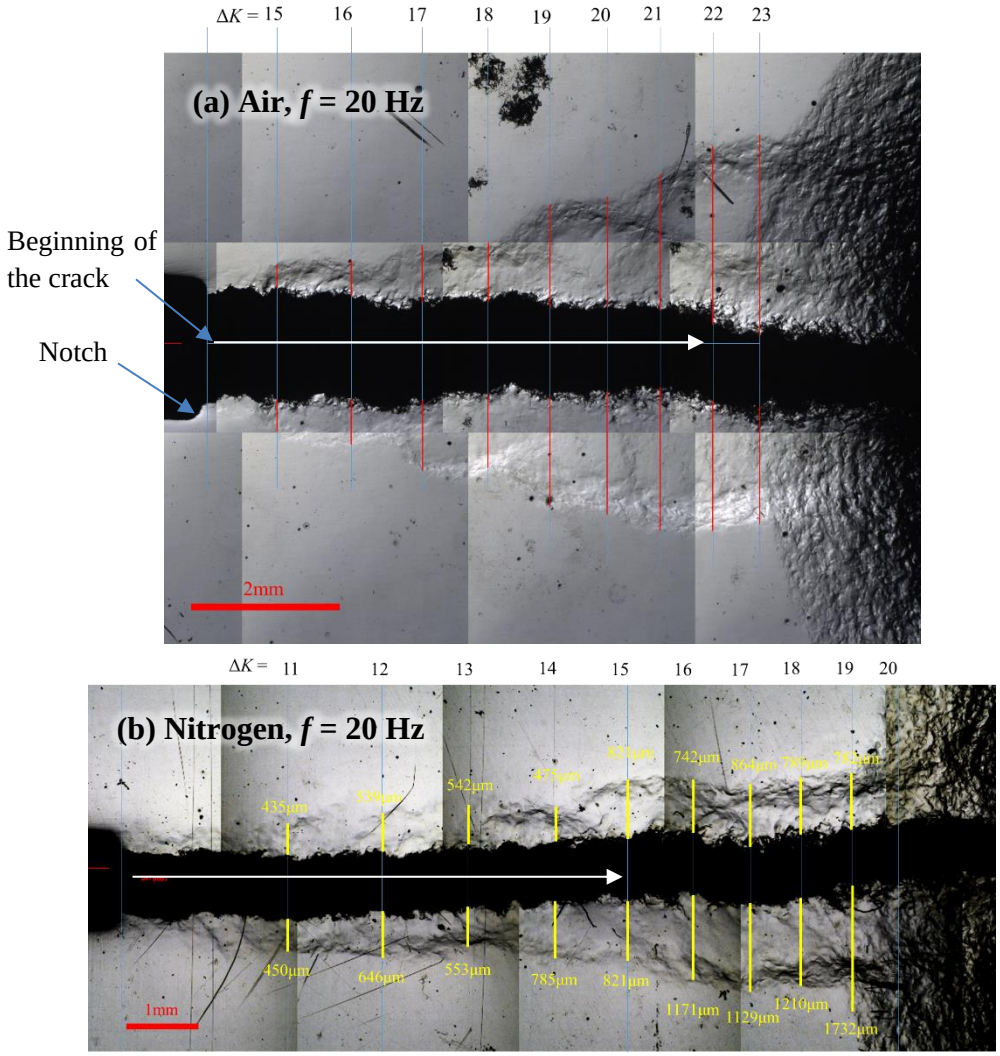

Figure A - 1 Crack path appearances of the FCG tests under air (f = 20 Hz) (a) and under nitrogen (P_{N2} = 3.5 MPa, f = 20 Hz) (b). The crack propagation direction is from left to right.

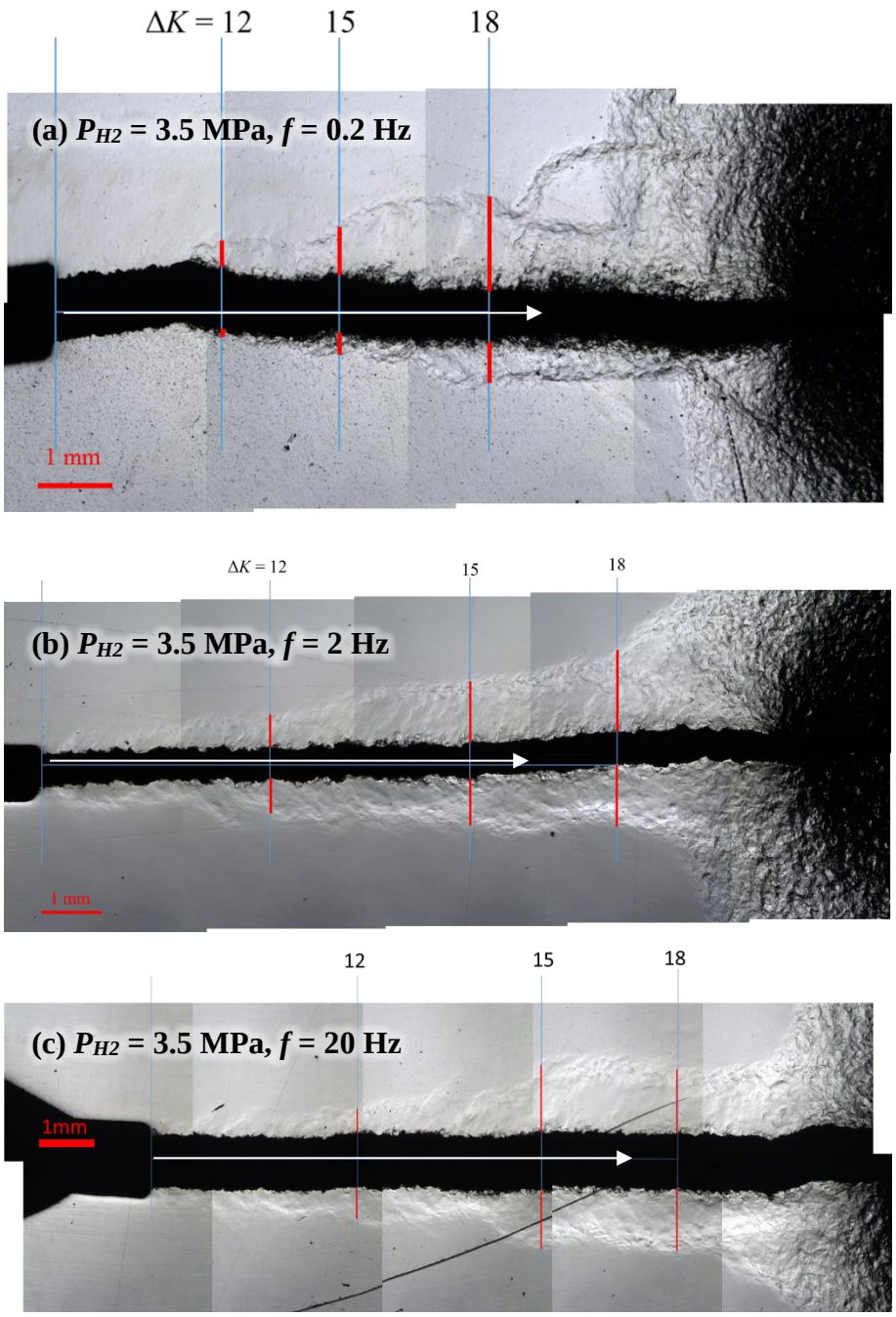

Figure A - 2 Crack path appearances of the ΔK-increase FCG tests under hydrogen at P_{H2} = 3.5 MPa with various loading frequencies f = 0.2 (a), 2 (b), and 20 Hz (c). The crack propagation direction is from left to right.

A-2 Observation result in Δ*K*-constant tests

Since the optical images of the crack appearance of the Δ*K*-constant FCG tests under nitrogen was omitted in Sub-section 4.3.2, it is presented here. Figure A - 3 shows the crack path appearances of the Δ*K*-constant FCG test (Δ*K* = 20 MPa×m$^{1/2}$) under nitrogen (P_{N2} = 3.5 MPa) with various loading frequencies of *f* = 0.2 and 20 Hz. From this image, it can be confirmed that the monotonic plastic zone is formed around the crack path as same as in the Δ*K*-increasing tests. The plastic zone size increases from the pre-crack in the air to the crack in nitrogen because the value of Δ*K* was increased from 15 to 20 MPa×m$^{1/2}$. By comparing the plastic zone sizes between *f* = 20 and 0.2 Hz, the monotonic plastic zone size seems slightly larger at *f* = 0.2 Hz than that at *f* = 20 Hz. Besides, the cyclic plastic zone (black color part along the crack path) at *f* = 0.2 Hz is slightly wider than that at *f* = 20 Hz. As confirmed in Figure 3 - 16, the slight increase in the FCGR in nitrogen by decreasing the loading frequency from 20 to 0.2 Hz might be related to the slight enlargement of the plastic zone size.

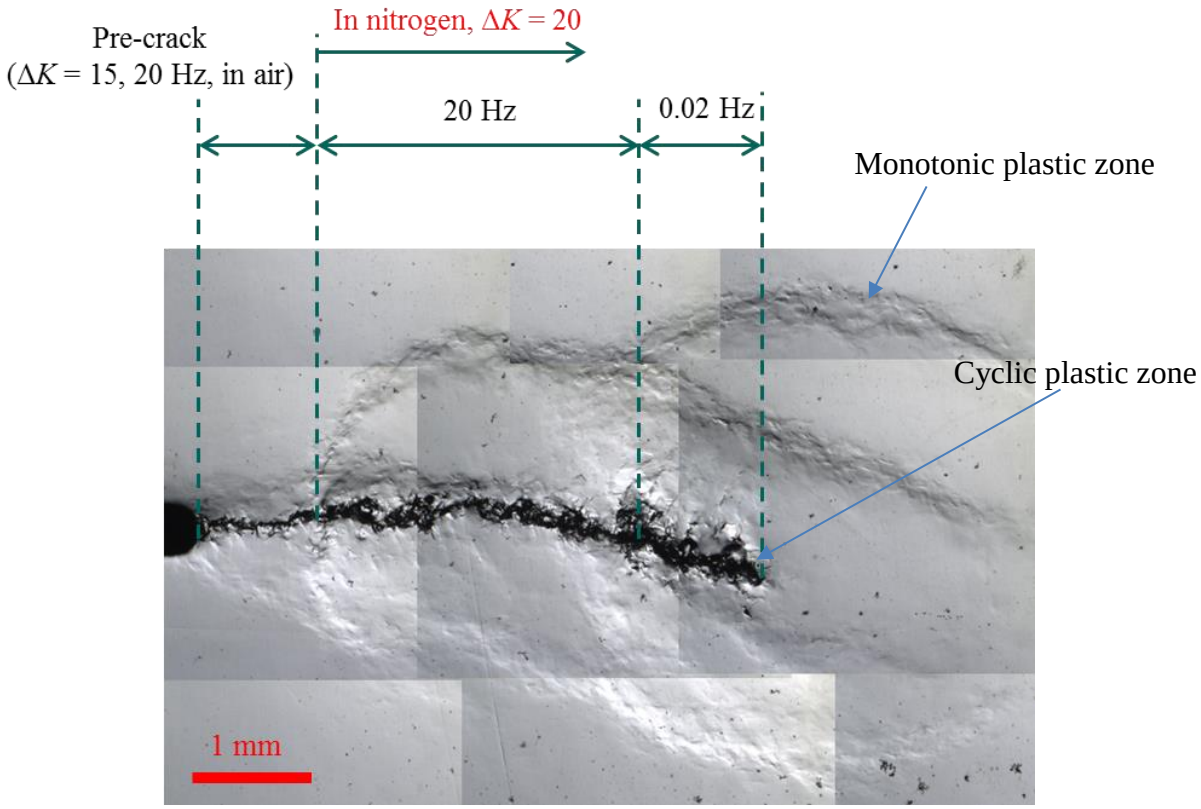

Figure A - 3 Crack path appearances of the ΔK-constant FCG test (ΔK = 20 MPa×m$^{1/2}$) under nitrogen at P_{N2} = 3.5 MPa with various loading frequencies f = 0.2 and 20 Hz. The crack propagation direction is from left to right.

References

[1] T. Yoshida and K. Kojima, “Toyota MIRAI Fuel Cell Vehicle and Progress Toward a Future Hydrogen Society,” *Interface Mag.*, vol. 24, no. 2, pp. 45–49, 2015, DOI:10.1149/2.F03152if.

[2] G. Hénaff, G. Odemer, and A. Tonneau-Morel, “Environmentally-assisted fatigue crack growth mechanisms in advanced materials for aerospace applications,” *Int. J. Fatigue*, vol. 29, no. 9–11, pp. 1927–1940, 2007, DOI:10.1016/j.ijfatigue.2007.03.014.

[3] Y. Murakami and S. Matsuoka, “Effect of hydrogen on fatigue crack growth of metals,” *Eng. Fract. Mech.*, vol. 77, no. 11, pp. 1926–1940, 2010, DOI:10.1016/j.engfracmech.2010.04.012.

[4] S. P. Lynch, “Mechanisms and Kinetics of Environmentally Assisted Cracking: Current Status, Issues, and Suggestions for Further Work,” *Metall. Mater. Trans. A*, vol. 44, no. 3, pp. 1209–1229, 2012, DOI:10.1007/s11661-012-1359-2.

[5] W. H. Johnson, “On Some Remarkable Changes Produced in Iron and Steel by the Action of Hydrogen and Acids,” *Proc. R. Soc. London*, vol. 23, no. 156–163, pp. 168–179, 1874, DOI:10.1098/rspl.1874.0024.

[6] R. A. Oriani and P. H. Josephic, “Testing of the decohesion theory of hydrogen-induced crack propagation,” *Scr. Metall.*, vol. 6, no. 8, pp. 681–688, 1972, DOI:10.1016/0036-9748(72)90126-3.

[7] R. A. Oriani, “A Mechanistic Theory of Hydrogen Embrittlement of Steels,” *Berichte der Bunsengesellschaft, Technol. Asp.*, vol. 76, no. 8, pp. 848–857, 1972, DOI:https://doi.org/10.1002/bbpc.19720760864.

[8] H. K. Birnbaum and P. Sofronis, “Hydrogen-enhanced localized plasticity-a mechanism for hydrogen-related fracture,” *Mater. Sci. Eng. A*, vol. 176, no. 1–2, pp. 191–202, 1994, DOI:10.1016/0921-5093(94)90975-X.

[9] S. P. Lynch and N. E. Ryan, “Mechanisms of Hydrogen Embrittlement - Crack Growth in a Low-Alloy Ultra-High-Strength Steel Under Cyclic and Sustained Stresses in Gaseous Hydrogen,” *Proc. Second Int. Congr. Hydrog. Met.*, pp. 369–376, 1977.

[10] M. Nagumo, “Function of hydrogen in embrittlement of high-strength steels,” *ISIJ Int.*, vol. 41, no. 6, pp. 590–598, 2001, DOI:10.2355/isijinternational.41.590.

[11] O. Takakuwa, J. Yamabe, H. Matsunaga, S. Matsuoka, and Y. Furuya, “Comprehensive Understanding of Ductility Loss Mechanisms in Various Steels with External and Internal Hydrogen,” *Metall. Mater. Trans. A Phys. Metall. Mater. Sci.*, vol. 48, no. 11, pp. 5717–5732, 2017, DOI:10.1007/s11661-017-4323-3.

[12] I. M. Robertson, P. Sofronis, A. Nagao, M. L. Martin, S. Wang, D. W. Gross, and K. E. Nygren, “Hydrogen Embrittlement Understood,” *Metall. Mater. Trans. A Phys. Metall. Mater. Sci.*, vol. 46, no. 6, pp. 2323–2341, 2015, DOI:10.1007/s11661-015-2836-1.

[13] N. Nanninga, A. Slifka, Y. Levy, and C. White, “A review of fatigue crack growth for pipeline steels exposed to hydrogen,” *J. Res. Natl. Inst. Stand. Technol.*, vol. 115, no. 6, p. 437, 2010, DOI:10.6028/jres.115.030.

[14] Z. Sun, C. Moriconi, G. Benoit, D. Halm, and G. Henaff, "Fatigue Crack Growth under High Pressure of Gaseous Hydrogen in a 15-5PH Martensitic Stainless Steel: Influence of Pressure and Loading Frequency," *Metall. Mater. Trans. A*, vol. 44, no. 3, pp. 1320–1330, 2012, DOI:10.1007/s11661-012-1133-5.

[15] T. J. Marrow, P. J. Cotterill, and J. E. King, "Temperature effects on the mechanism of time independent hydrogen assisted fatigue crack propagation in steels," *Acta Metall. Mater.*, vol. 40, no. 8, pp. 2059–2068, 1992, DOI:10.1016/0956-7151(92)90192-H.

[16] S. Matsuoka, N. Tsutsumi, and Y. Murakami, "Effects of Hydrogen on Fatigue Crack Growth and Stretch Zone of 0.08mass%C Low Carbon Steel Pipe," *Trans. Japan Soc. Mech. Eng. Ser. A (in Japanese)*, vol. 74, no. 748, pp. 1528–1537, 2008, DOI:10.1299/kikaia.74.1528.

[17] Y. Murakami, T. Kanezaki, Y. Mine, and S. Matsuoka, "Hydrogen Embrittlement Mechanism in Fatigue of Austenitic Stainless Steels," *Metall. Mater. Trans. A*, vol. 39, no. 6, pp. 1327–1339, Jun. 2008, DOI:10.1007/s11661-008-9506-5.

[18] H. Nishikawa, Y. Oda, and H. Noguchi, "Investigation of the Mechanism for Brittle-Striation Formation in Low Carbon Steel Fatigued in Hydrogen Gas," *J. Solid Mech. Mater. Eng.*, vol. 5, no. 8, pp. 370–385, 2011, DOI:10.1299/jmmp.5.370.

[19] H. Nishikawa, Y. Oda, Y. Takahashi, and H. Noguchi, "Microscopic Observation of the Brittle-Striation Formation Mechanism in Low Carbon Steel Fatigued in Hydrogen Gas," *J. Solid Mech. Mater. Eng.*, vol. 5, no. 4, pp. 179–190, 2011, DOI:10.1299/jmmp.5.179.

[20] Y. Takahashi, J. Sakamoto, M. Tanaka, K. Higashida, and H. Noguchi, "Effect of hydrogen on dislocation structures around a mixed-mode fatigue crack tip in a single-crystalline iron-silicon alloy," *Scr. Mater.*, vol. 64, no. 8, pp. 721–724, 2011, DOI:10.1016/j.scriptamat.2010.12.032.

[21] Y. Takahashi, M. Tanaka, K. Higashida, and H. Noguchi, "Hydrogen-induced slip localization around a quasi-brittle fatigue crack observed by high-voltage electron microscopy," *Scr. Mater.*, vol. 61, no. 2, pp. 145–148, 2009, DOI:10.1016/j.scriptamat.2009.03.020.

[22] M. L. Martin, P. Sofronis, I. M. Robertson, T. Awane, and Y. Murakami, "A microstructural based understanding of hydrogen-enhanced fatigue of stainless steels," *Int. J. Fatigue*, vol. 57, pp. 28–36, 2013, DOI:10.1016/j.ijfatigue.2012.08.009.

[23] M. L. Martin, I. M. Robertson, and P. Sofronis, "Interpreting hydrogen-induced fracture surfaces in terms of deformation processes: A new approach," *Acta Mater.*, vol. 59, no. 9, pp. 3680–3687, May 2011, DOI:10.1016/j.actamat.2011.03.002.

[24] C. Moriconi, G. Hénaff, and D. Halm, "Cohesive zone modeling of fatigue crack propagation assisted by gaseous hydrogen in metals," *Int. J. Fatigue*, vol. 68, pp. 56–66, 2014, DOI:10.1016/j.ijfatigue.2014.06.007.

[25] G. Bilotta, G. Hénaff, G. Benoit, C. Moriconi, D. Halm, and M. Arzaghi, "Cohesive Zone Modeling Of Hydrogen Assisted Cracking In A 15-5 PH Steel And Comparison With Experiments," *ASME 2015 Press. Vessel. Pip. Conf.*, pp. 1–8, 2015, DOI:10.1115/PVP201545631.

[26] C. Moriconi, “Modélisation de la propagation de fissure de fatigue assistée par l’hydrogène gazeux dans les matériaux métalliques,” PhD thesis of École nationale supérieure de mécanique et d’aérotechnique, 2012.

[27] G. Bilotta, “Influence de l’hydrogène gazeux sur la vitesse de propagation d’une fissure de fatigue dans les métaux : approche expérimentale et modélisation,” PhD thesis of École nationale supérieure de mécanique et d’aérotechnique, 2016.

[28] G. Bilotta, M. Arzaghi, G. Hénaff, G. Benoit, and D. Halm, “Hydrogen Induced Intergranular Failure in Armco Iron Under Fatigue Crack Propagation,” *Vol. 6B Mater. Fabr.*, p. V06BT06A026, Jul. 2016, DOI:10.1115/PVP2016-63338.

[29] G. Bilotta, M. Arzaghi, G. Benoit, D. Halm, G. Henaff, and T. Shinko, “Environmentally-Assisted Fatigue Crack Growth in ARMCO Iron Under High Pressure of Gaseous Hydrogen,” *Proc. Int. Hydrog. Conf. (IHC 2016) Mater. Perform. Hydrog. Environ.*, pp. 1–10, 2016, DOI:10.1115/1.861387_ch21.

[30] T. Shinko, G. Hénaff, D. Halm, and G. Benoit, “Influence of gaseous hydrogen on plastic strain in vicinity of fatigue crack tip in Armco pure iron,” *MATEC Web Conf.*, vol. 165, no. MATEC Web Conf., p. 03006, May 2018, DOI:10.1051/matecconf/201816503006.

[31] H. Z. Hassan, “Energy Analysis and Performance Evaluation of the Adsorption Refrigeration System,” *ISRN Mech. Eng.*, vol. 2013, pp. 1–14, 2013, DOI:10.1155/2013/704340.

[32] S. Serebrinsky, E. A. Carter, and M. Ortiz, “A quantum-mechanically informed continuum model of hydrogen embrittlement,” *J. Mech. Phys. Solids*, vol. 52, no. 10, pp. 2403–2430, 2004, DOI:10.1016/j.jmps.2004.02.010.

[33] W. W. Gerberich, T. L1vne, X. F. Chen, and M. Kaczorowski, “Crack growth from internal hydrogen-temperature and microstructural effects in 4340 steel,” *Metall. Trans. A*, vol. 19, no. 5, pp. 1319–1334, 1988, DOI:10.1007/BF02662593.

[34] J. P. Hirth, “Effects of hydrogen on the properties of iron and steel,” *Metall. Trans. A*, vol. 11, no. 6, pp. 861–890, Jun. 1980, DOI:10.1007/BF02654700.

[35] D. E. Jiang and E. A. Carter, “Diffusion of interstitial hydrogen into and through bcc Fe from first principles,” *Phys. Rev. B - Condens. Matter Mater. Phys.*, vol. 70, no. 6, pp. 1–9, 2004, DOI:10.1103/PhysRevB.70.064102.

[36] A. Sieverts and W. Krumbhaar, “Über die Löslichkeit von Gasen in Metallen und Legierungen,” *Berichte der Dtsch. Chem. Gesellschaft*, vol. 43, no. 1, pp. 893–900, Jan. 1910, DOI:10.1002/cber.191004301152.

[37] R. Broudeur, J. P. Fidelle, M. Rapin, C. Roux, and P. Tison, “Influence de l’hydrogene sur le comportement des metaux, 4 : permeation, diffusion, dissolution du deuterium et du tritium dans les aciers austenitiques Z 5 NCTD 26-15 et Z 3 CN 18-10,” *Saclay Commis. Energ. At. Cent. Etud.*, p. 188, 1976.

[38] J. C. M. Li, R. A. Oriani, and L. S. Darken, “The Thermodynamics of Stressed Solids,” *Zeitschrift für Phys. Chemie*, vol. 49, no. 3_5, pp. 271–290, May 1966, DOI:10.1524/zpch.1966.49.3_5.271.

[39] P. Sofronis and R. M. McMeeking, "Numerical analysis of hydrogen transport near a blunting crack tip," *J. Mech. Phys. Solids*, vol. 37, no. 3, pp. 317–350, 1989, DOI:10.1016/0022-5096(89)90002-1.

[40] J. Crank, *The mathematics of diffusion*, Second edi. 1975.

[41] C. San Marchi and B. P. Somerday, "Technical Reference On Hydrogen Compatibility Of Materials," *Sand2008-1163*, no. code 4001, p. 292, 2012.

[42] V. Olden, C. Thaulow, and R. Johnsen, "Modelling of hydrogen diffusion and hydrogen induced cracking in supermartensitic and duplex stainless steels," *Mater. Des.*, vol. 29, no. 10, pp. 1934–1948, 2008, DOI:10.1016/j.matdes.2008.04.026.

[43] L. Coudreuse, J. Chêne, and A. M. Brass, "Fragilisation des aciers par l ' hydrogène : étude et prévention," *Tech. l'ingénieur*, vol. M175, no. Corrosion et vieillissement: phénomènes et mécanismes, pp. 1–24, 2000.

[44] G. M. Pressouyre, "A classification of hydrogen traps in steel," *Metall. Trans. A*, vol. 10, no. 10, pp. 1571–1573, 1979, DOI:10.1007/BF02812023.

[45] M. Koyama, M. Rohwerder, C. C. Tasan, A. Bashir, E. Akiyama, K. Takai, D. Raabe, and K. Tsuzaki, "Recent progress in microstructural hydrogen mapping in steels: quantification, kinetic analysis, and multi-scale characterisation," *Mater. Sci. Technol.*, no. March, pp. 1–16, 2017, DOI:10.1080/02670836.2017.1299276.

[46] F. Vucko, "ETUDE EXPERIMENTALE ET MODELISATION DES EFFETS DE L'HYDROGENE SUR LES PROPRIETES MECANIQUES ET LE COMPORTEMENT EN FATIGUE D'UN ACIER A HAUTE LIMITE D'ELASTICITE," PhD thesis of l'École Nationale Supérieure des Mines de Saint-Étienne, 2014.

[47] A. J. Kumnick and H. H. Johnson, "Deep Trapping for Hydrogen Iron," *Acta Metall.*, vol. 28, pp. 33–39, 1980, DOI:10.1021/acs.organomet.7b00855.

[48] A. Metsue, A. Oudriss, and X. Feaugas, "Trapping/detrapping kinetic rates of hydrogen around a vacancy in nickel and some consequences on the hydrogen-vacancy clusters thermodynamic equilibrium," *Comput. Mater. Sci.*, vol. 151, no. April, pp. 144–152, 2018, DOI:10.1016/j.commatsci.2018.05.013.

[49] A. Metsue, A. Oudriss, and X. Feaugas, "Hydrogen solubility and vacancy concentration in nickel single crystals at thermal equilibrium: New insights from statistical mechanics and ab initio calculations," *J. Alloys Compd.*, vol. 656, pp. 555–567, 2016, DOI:10.1016/j.jallcom.2015.09.252.

[50] R. A. Oriani, "The diffusion and trapping of hydrogen in steel," *Acta Metall.*, vol. 18, no. 1, pp. 147–157, 1970, DOI:10.1016/0001-6160(70)90078-7.

[51] I. Moro, "Fragilisation par l'oxygène gazeux d'un acier ferrito-perlitique de grade API X80," PhD thesis of Université de Toulouse, 2009.

[52] D. Hardie, E. A. Charles, and A. H. Lopez, "Hydrogen embrittlement of high strength pipeline steels," *Corros. Sci.*, vol. 48, no. 12, pp. 4378–4385, 2006, DOI:10.1016/j.corsci.2006.02.011.

[53] S. P. Trasatti, E. Sivieri, and F. Mazza, "Susceptibility of a X80 steel to hydrogen embrittlement," *Mater. Corros.*, vol. 56, no. 2, pp. 111–117, Feb. 2005, DOI:10.1002/maco.200403821.

[54] H. J. Cialone and J. H. Holbrook, "Sensitivity of Steels to Degradation in Gaseous Hydrogen," in *Hydrogen Embrittlement: Prevention and Control*, 100 Barr Harbor Drive, PO Box C700, West Conshohocken, PA 19428-2959: ASTM International, pp. 134-134–19.

[55] V. G. Gavriljuk, V. N. Shivanyuk, and J. Foct, "Diagnostic experimental results on the hydrogen embrittlement of austenitic steels," *Acta Mater.*, vol. 51, no. 5, pp. 1293–1305, 2003, DOI:10.1016/S1359-6454(02)00524-4.

[56] H. Matsui, H. Kimura, and S. Moriya, "The effect of hydrogen on the mechanical properties of high purity iron I. Softening and hardening of high purity iron by hydrogen charging during tensile deformation," *Mater. Sci. Eng.*, vol. 40, no. 2, pp. 207–216, 1979, DOI:10.1016/0025-5416(79)90191-5.

[57] S. Moriya, H. Matsui, and H. Kimura, "The effect of hydrogen on the mechanical properties of high purity iron II. Effect of quenched-in hydrogen below room temperature," *Mater. Sci. Eng.*, vol. 40, no. 2, pp. 217–225, 1979, DOI:10.1016/0025-5416(79)90192-7.

[58] H. Matsui, H. Kimura, and A. Kimura, "The effect of hydrogen on the mechanical properties of high purity iron III. The dependence of softening in specimen size and charging current density," *Mater. Sci. Eng.*, vol. 40, no. 2, pp. 227–234, 1979, DOI:10.1016/0025-5416(79)90193-9.

[59] P. S. Lam, R. L. Sindelar, A. J. Duncan, and T. M. Adams, "Literature Survey of Gaseous Hydrogen Effects on the Mechanical Properties of Carbon and Low Alloy Steels," *J. Press. Vessel Technol.*, vol. 131, no. 4, p. 041408, 2009, DOI:10.1115/1.3141435.

[60] D. G. Ulmer and C. J. Altstetter, "Hydrogen-induced strain localization and failure of austenitic stainless steels at high hydrogen concentrations," *Acta Metall. Mater.*, vol. 39, no. 6, pp. 1237–1248, Jun. 1991, DOI:10.1016/0956-7151(91)90211-I.

[61] Y. Murakami and H. Matsunaga, "The effect of hydrogen on fatigue properties of steels used for fuel cell system," *Int. J. Fatigue*, vol. 28, no. 11, pp. 1509–1520, 2006, DOI:10.1016/j.ijfatigue.2005.06.059.

[62] G. Bilotta, M. Arzaghi, G. Hénaff, G. Benoit, C. Moriconi, and D. Halm, "Hydrogen Assisted Fatigue Crack Growth in a Precipitation-Hardened Martensitic Stainless Steel Under Gaseous Hydrogen," in *Volume 6B: Materials and Fabrication*, 2014, p. V06BT06A014.

[63] Z. Sun, G. Benoit, C. Moriconi, F. Hamon, D. Halm, F. Hamon, and G. Hénaff, "Fatigue crack propagation under gaseous hydrogen in a precipitation-hardened martensitic stainless steel," *Int. J. Hydrogen Energy*, vol. 36, no. 14, pp. 8641–8644, Jul. 2011, DOI:10.1016/j.ijhydene.2011.04.094.

[64] H. Nishikawa, Y. Oda, and H. Noguchi, "Loading-Frequency Effects On Fatigue Crack Growth Behavior Of A Low Carbon Steel JIS S10C In Hydrogen Gas Environment," *J. Solid Mech. Mater. Eng.*, vol. 5, no. 2, pp. 104–116, 2011, DOI:10.1299/jmmp.5.104.

[65] R. L. Amaro, E. S. Drexler, and A. J. Slifka, "Fatigue crack growth modeling of pipeline steels in high pressure gaseous hydrogen," *Int. J. Fatigue*, vol. 62, pp. 249–257, 2014, DOI:10.1016/j.ijfatigue.2013.10.013.

[66] Y. Murakami, T. Kanezaki, and Y. Mine, "Hydrogen Effect against Hydrogen Embrittlement," *Metall. Mater. Trans. a-Physical Metall. Mater. Sci.*, vol. 41A, no. 10, pp. 2548–2562, 2010, DOI:10.1007/s11661-010-0275-6.

[67] T. Kanezaki, C. Narazaki, Y. Mine, S. Matsuoka, and Y. Murakami, "Effects of hydrogen on fatigue crack growth behavior of austenitic stainless steels," *Int. J. Hydrogen Energy*, vol. 33, no. 10, pp. 2604–2619, May 2008, DOI:10.1016/j.ijhydene.2008.02.067.

[68] K. Kawamoto, K. Ochi, Y. Oda, and H. Noguchi, "Effects of Hydrogen Gas Environment on Fatigue Strength at 107 cycles in Plain Specimen of Type 316L Stainless Steel," *J. Solid Mech. Mater. Eng.*, vol. 3, no. 1, pp. 72–83, 2009, DOI:10.1299/jmmp.3.72.

[69] K. Kawamoto, Y. Oda, H. Noguchi, H. Fujii, T. Izumi, and G. Itoh, "Investigation of Local Hydrogen Distribution Around Fatigue Crack Tip of a Type 304 Stainless Steel with Secondary Ion Mass Spectrometry and Hydrogen Micro-Print Technique," *J. Solid Mech. Mater. Eng.*, vol. 3, no. 6, pp. 898–909, 2009, DOI:10.1299/jmmp.3.898.

[70] A. Nagao, C. D. Smith, M. Dadfarnia, P. Sofronis, and I. M. Robertson, "The role of hydrogen in hydrogen embrittlement fracture of lath martensitic steel," *Acta Mater.*, vol. 60, no. 13–14, pp. 5182–5189, 2012, DOI:10.1016/j.actamat.2012.06.040.

[71] H. Tanaka, N. Honma, S. Matsuoka, and Y. Murakami, "Effect of hydrogen and frequency on fatigue behaviour of SCM435 steel for storage cylinder of hydrogen station," *Trans. japan Soc. Mech. Eng.*, vol. A 73, pp. 1358–1365, 2007.

[72] A. Macadre, M. Artamonov, S. Matsuoka, and J. Furtado, "Effects of hydrogen pressure and test frequency on fatigue crack growth properties of Ni-Cr-Mo steel candidate for a storage cylinder of a 70MPa hydrogen filling station," *Eng. Fract. Mech.*, vol. 78, no. 18, pp. 3196–3211, 2011, DOI:10.1016/j.engfracmech.2011.09.007.

[73] H. Nishikawa, Y. Oda, and H. Noguchi, "Investigation of Mechanism for Intergranular Fatigue Crack Propagation of Low Carbon Steel JIS S10C in Hydrogen Gas Environment," *J. Solid Mech. Mater. Eng.*, vol. 5, no. 6, pp. 263–278, 2011, DOI:10.1299/jmmp.5.263.

[74] J. Kameda and C. J. Mcmahon, "Solute segregation and hydrogen-induced intergranular fracture in an alloy steel," *Metall. Trans. A*, vol. 14, no. 4, pp. 903–911, 1983, DOI:10.1007/BF02644295.

[75] M. L. Martin, B. P. Somerday, R. O. Ritchie, P. Sofronis, and I. M. Robertson, "Hydrogen-induced intergranular failure in nickel revisited," *Acta Mater.*, vol. 60, no. 6–7, pp. 2739–2745, 2012, DOI:10.1016/j.actamat.2012.01.040.

[76] R. H. Jones, "Analysis of hydrogen-induced subcritical intergranular crack growth of iron and nickel," *Acta Metall. Mater.*, vol. 38, no. 9, pp. 1703–1718, 1990, DOI:10.1016/0956-7151(90)90013-7.

[77] S. Wang, M. L. Martin, P. Sofronis, S. Ohnuki, N. Hashimoto, and I. M. Robertson, "Hydrogen-induced intergranular failure of iron," *Acta Mater.*, vol. 69, pp. 275–282, 2014, DOI:10.1016/j.actamat.2014.01.060.

[78] S. Bechtle, M. Kumar, B. P. Somerday, M. E. Launey, and R. O. Ritchie, “Grain-boundary engineering markedly reduces susceptibility to intergranular hydrogen embrittlement in metallic materials,” *Acta Mater.*, vol. 57, no. 14, pp. 4148–4157, 2009, DOI:10.1016/j.actamat.2009.05.012.

[79] J. Kameda, “a Microscopic Model of Hydrogen-Induced Intergranular Equilibrium,” vol. 34, no. 5, pp. 867–882, 1986.

[80] P. Novak, R. Yuan, B. P. Somerday, P. Sofronis, and R. O. Ritchie, “A statistical, physical-based, micro-mechanical model of hydrogen-induced intergranular fracture in steel,” *J. Mech. Phys. Solids*, vol. 58, no. 2, pp. 206–226, 2010, DOI:10.1016/j.jmps.2009.10.005.

[81] X. Q. Wu and I. S. Kim, “Effects of strain rate and temperature on tensile behavior of hydrogen-charged SA508 Cl.3 pressure vessel steel,” *Mater. Sci. Eng. A*, vol. 348, no. 1–2, pp. 309–318, 2003, DOI:10.1016/S0921-5093(02)00737-2.

[82] M. L. Martin, J. A. Fenske, G. S. Liu, P. Sofronis, and I. M. Robertson, “On the formation and nature of quasi-cleavage fracture surfaces in hydrogen embrittled steels,” *Acta Mater.*, vol. 59, no. 4, pp. 1601–1606, 2011, DOI:10.1016/j.actamat.2010.11.024.

[83] A. T. Yokobori, “The mechanism of hydrogen embrittlement: The stress interaction between a crack, a hydrogen cluster, and moving dislocations,” *Int. J. Fract.*, vol. 128, no. 1, pp. 121–131, 2004, DOI:10.1023/B:FRAC.0000040974.59017.55.

[84] T. Matsuo, S. Matsuoka, and Y. Murakami, “Fatigue crack growth properties of quenched and tempered Cr-Mo steel in 0.7 MPa hydrogen gas,” in *18th European Conference on Fracture*, 2010, pp. 1–8.

[85] A. T. Yokobori, Y. Chinda, T. Nemoto, K. Satoh, and T. Yamada, “The characteristics of hydrogen diffusion and concentration around a crack tip concerned with hydrogen embrittlement,” *Corros. Sci.*, vol. 44, no. 3, pp. 407–424, 2002, DOI:10.1016/S0010-938X(01)00095-6.

[86] A. Taha and P. Sofronis, “A micromechanics approach to the study of hydrogen transport and embrittlement,” *Eng. Fract. Mech.*, vol. 68, no. 6, pp. 803–837, 2001, DOI:10.1016/S0013-7944(00)00126-0.

[87] J. K. Tien, R. J. Richards, O. Buck, and H. L. Marcus, “Model of dislocation sweep-in of hydrogen during fatigue crack growth,” *Scr. Metall.*, vol. 9, no. 10, pp. 1097–1101, 1975, DOI:10.1016/0036-9748(75)90287-2.

[88] M. Dadfarnia, M. L. Martin, A. Nagao, P. Sofronis, and I. M. Robertson, “Modeling hydrogen transport by dislocations,” *J. Mech. Phys. Solids*, vol. 78, pp. 511–525, 2014, DOI:10.1016/j.jmps.2015.03.002.

[89] J. Tien, A. W. Thompson, I. M. Bernstein, and R. J. Richards, “Hydrogen transport by dislocations,” *Metall. Trans. A*, vol. 7, no. 6, pp. 821–829, 1976, DOI:10.1007/BF02644079.

[90] N. Saintier, T. Awane, J. M. Olive, S. Matsuoka, and Y. Murakami, “Analyses of hydrogen distribution around fatigue crack on type 304 stainless steel using secondary ion mass spectrometry,” *Int. J. Hydrogen Energy*, vol. 36, no. 14, pp. 8630–8640, 2011, DOI:10.1016/j.ijhydene.2011.03.111.

[91] A. R. Troiano, "The Role of Hydrogen and Other Interstitials in the Mechanical Behavior of Metals," *Metallogr. Microstruct. Anal.*, vol. 5, no. 6, pp. 557–569, Dec. 2016, DOI:10.1007/s13632-016-0319-4.

[92] D. Tromans, "On surface energy and the hydrogen embrittlement of iron and steels," *Acta Metall. Mater.*, vol. 42, no. 6, pp. 2043–2049, Jun. 1994, DOI:10.1016/0956-7151(94)90029-9.

[93] S. Lynch, "Mechanisms of hydrogen assisted cracking-A review," *Hydrog. Eff. Mater. Behav. Corros. Deform. Interact.*, pp. 449–466, 2003.

[94] C. D. Beachem, "A new model for hydrogen-assisted cracking (hydrogen 'embrittlement')," *Metall. Trans.*, vol. 3, no. 2, pp. 441–455, 1972, DOI:10.1007/BF02642048.

[95] I. M. Robertson, "The effect of hydrogen on dislocation dynamics," *Eng. Fract. Mech.*, vol. 68, no. 6, pp. 671–692, 2001, DOI:10.1016/S0013-7944(01)00011-X.

[96] P. J. Ferreira, I. M. Robertson, and H. K. Birnbaum, "Hydrogen effects on the character of dislocations in high-purity aluminum," *Acta Mater.*, vol. 47, no. 10, pp. 2991–2998, Aug. 1999, DOI:10.1016/S1359-6454(99)00156-1.

[97] H. Birnbaum, "Mechanisms of hydrogen related fracture of metals," *ILLINOIS UNIV URBANA DEPT Mater. Sci. Eng.*, Feb. 1989.

[98] S. Lynch and N. Ryan, "Mechanisms of Hydrogen Embrittlement-Crack Growth in a Low-Alloy Ultra-High-Strength Steel Under Cyclic and Sustained Stresses in Gaseous Hydrogen," DTIC Document, 1978.

[99] S. P. Lynch, "Hydrogen embrittlement and liquid-metal embrittlement in nickel single crystals," *Scr. Metall.*, vol. 13, no. 11, pp. 1051–1056, 1979, DOI:10.1016/0036-9748(79)90202-3.

[100] S. P. Lynch, "Environmentally assisted cracking: Overview of evidence for an adsorption-induced localised-slip process," *Acta Metall.*, vol. 36, no. 10, pp. 2639–2661, Oct. 1988, DOI:10.1016/0001-6160(88)90113-7.

[101] S. P. Lynch, "Metallographic contributions to understanding mechanisms of environmentally assisted cracking," *Metallography*, vol. 23, no. 2, pp. 147–171, 1989, DOI:10.1016/0026-0800(89)90016-5.

[102] M. S. Daw and M. I. Baskes, "Application of the Embedded Atom Method to Hydrogen Embrittlement," in *Chemistry and Physics of Fracture*, Dordrecht: Springer Netherlands, 1987, pp. 196–218.

[103] A. Barnoush and H. Vehoff, "Recent developments in the study of hydrogen embrittlement: Hydrogen effect on dislocation nucleation," *Acta Mater.*, vol. 58, no. 16, pp. 5274–5285, 2010, DOI:10.1016/j.actamat.2010.05.057.

[104] A. Barnoush and H. Vehoff, "Hydrogen embrittlement of aluminum in aqueous environments examined by in situ electrochemical nanoindentation," *Scr. Mater.*, vol. 58, no. 9, pp. 747–750, 2008, DOI:10.1016/j.scriptamat.2007.12.019.

[105] A. Barnoush, "Hydrogen embrittlement , revisited by in situ electrochemical nanoindentation," p. 288, 2007.

[106] K. Takai, H. Shoda, H. Suzuki, and M. Nagumo, "Lattice defects dominating hydrogen-related failure of metals," *Acta Mater.*, vol. 56, pp. 5158–5167, 2008, DOI:10.1016/j.actamat.2008.06.031.

[107] M. Nagumo, M. Nakamura, and K. Takai, "Hydrogen thermal desorption relevant to delayed-fracture susceptibility of high-strength steels," *Metall. Mater. Trans. A*, vol. 32, no. 2, pp. 339–347, Feb. 2001, DOI:10.1007/s11661-001-0265-9.

[108] D. Birenis, Y. Ogawa, H. Matsunaga, O. Takakuwa, J. Yamabe, Ø. Prytz, and A. Thøgersen, "Interpretation of hydrogen-assisted fatigue crack propagation in BCC iron based on dislocation structure evolution around the crack wake," *Acta Mater.*, vol. 156, pp. 245–253, 2018, DOI:10.1016/j.actamat.2018.06.041.

[109] C. E. Jackson, *Metallurgy and Weldability of Steels*. 1978.

[110] J. M. Radzikowska, "Effect of specimen preparation on evaluation of cast iron microstructures," *Mater. Charact.*, vol. 54, no. 4–5, pp. 287–304, 2005, DOI:10.1016/j.matchar.2004.08.019.

[111] E. Bonnot, A. L. Helbert, F. Brisset, and T. Baudin, "Microstructure and texture evolution during the ultra grain refinement of the Armco iron deformed by accumulative roll bonding (ARB)," *Mater. Sci. Eng. A*, vol. 561, pp. 60–66, 2013, DOI:10.1016/j.msea.2012.11.017.

[112] Astm Standard, "E112-12:Standard Test Methods for Determining Average Grain Size," *ASTM Int.*, vol. E112-12, pp. 1–27, 2012, DOI:10.1520/E0112-12.1.4.

[113] R. Hielscher and H. Schaeben, "A novel pole figure inversion method: Specification of the MTEX algorithm," *J. Appl. Crystallogr.*, vol. 41, no. 6, pp. 1024–1037, 2008, DOI:10.1107/S0021889808030112.

[114] L. Priester, *Grain Boundaries: From Theory to Engineering*, vol. 172. Dordrecht: Springer Netherlands, 2013.

[115] A. Oudriss, J. Creus, J. Bouhattate, E. Conforto, C. Berziou, C. Savall, and X. Feaugas, "Grain size and grain-boundary effects on diffusion and trapping of hydrogen in pure nickel," *Acta Mater.*, vol. 60, no. 19, pp. 6814–6828, 2012, DOI:10.1016/j.actamat.2012.09.004.

[116] ASTM Int., "ASTM E8 / E8M-13a, Standard Test Methods for Tension Testing of Metallic Materials, ASTM International," *Astm*, no. C, pp. 1–27, 2013, DOI:10.1520/E0008_E0008M-13A.

[117] J. M. Gere, *Mechanics of Materials*. 2008.

[118] AK steel International, "ARMCO Pure Iron, Product Information 8-10." pp. 1–12.

[119] R. W. Armstrong and S. M. Walley, "High strain rate properties of metals and alloys," *Int. Mater. Rev.*, vol. 53, no. 3, pp. 105–128, 2008, DOI:10.1179/174328008X277795.

[120] S. Castagnet, J. C. Grandidier, M. Comyn, and G. Benoît, "Hydrogen influence on the tensile properties of mono and multi-layer polymers for gas distribution," *Int. J. Hydrogen Energy*, vol. 35, no. 14, pp. 7633–7640, 2010, DOI:10.1016/j.ijhydene.2010.04.155.

[121] Z. Sun, G. Benoit, C. Moriconi, F. Hamon, D. Halm, F. Hamon, and G. Hénaff, "Fatigue crack propagation under gaseous hydrogen in a precipitation- hardened martensitic stainless steel," *Int. J. Hydrogen Energy*, vol. 36, no. 14, pp. 8641–8644, 2011, DOI:10.1016/j.ijhydene.2011.04.094.

[122]Kyowa Electronic Instruments Co. Ltd., "Foil Strain Gage for Hydrogen Gas Environment." [Online]. Available: http://www.kyowa-ei.com/eng/product/category/strain_gages/kfv/index.html.

[123] R. J. Fields, T. Weerasooriya, and M. F. Ashby, "Fracture-mechanisms in pure iron, two austenitic steels, and one ferritic steel," *Metall. Trans. A*, vol. 11, no. 2, pp. 333–347, 1980, DOI:10.1007/BF02660638.

[124] V. Tvergaard and A. Needleman, "Analysis of the Cup-Cone Round Tensile Fracture," *Acta Metall.*, vol. 32, no. 1, pp. 157–169, 1984, DOI:10.1016/0001-6160(84)90213-X.

[125] M. Möser, "Fractography with the SEM (Failure Analysis)," in *Electron Microscopy in Solid State Physics (Materials Science Monographs)*, H. Bethge and J. Heydenreich, Eds. Amsterdam–New York–Tokyo: Elsevier, 1987, pp. 366–385.

[126] G. R. Johnson and W. H. Cook, "Fracture characteristics of three metals subjected to various strains, strain rates, temperatures and pressures," *Eng. Fract. Mech.*, vol. 21, no. 1, pp. 31–48, 1985, DOI:10.1016/0013-7944(85)90052-9.

[127] CEN, "ISO 2566-1:1999, Steel. Conversion of elongation values. Carbon and low alloy steels," 1999.

[128] H. Matsunaga, M. Yoshikawa, R. Kondo, J. Yamabe, and S. Matsuoka, "Slow strain rate tensile and fatigue properties of Cr-Mo and carbon steels in a 115 MPa hydrogen gas atmosphere," *Int. J. Hydrogen Energy*, vol. 40, no. 16, pp. 5739–5748, 2015, DOI:10.1016/j.ijhydene.2015.02.098.

[129] I. Moro, L. Briottet, P. Lemoine, E. Andrieu, C. Blanc, and G. Odemer, "Hydrogen embrittlement susceptibility of a high strength steel X80," *Mater. Sci. Eng. A*, vol. 527, no. 27–28, pp. 7252–7260, 2010, DOI:10.1016/j.msea.2010.07.027.

[130] S. Wang, S. Ohnuki, N. Hashimoto, and K. Chiba, "Hydrogen effects on tensile property of pure iron with deformed surface," *Mater. Sci. Eng. A*, vol. 560, pp. 332–338, 2013, DOI:10.1016/j.msea.2012.09.075.

[131] N. E. Nanninga, Y. S. Levy, E. S. Drexler, R. T. Condon, A. E. Stevenson, and A. J. Slifka, "Comparison of hydrogen embrittlement in three pipeline steels in high pressure gaseous hydrogen environments," *Corros. Sci.*, vol. 59, pp. 1–9, 2012, DOI:10.1016/j.corsci.2012.01.028.

[132] S. Matsuoka, J. Yamabe, and H. Matsunaga, "Criteria for determining hydrogen compatibility and the mechanisms for hydrogen-assisted, surface crack growth in austenitic stainless steels," *Eng. Fract. Mech.*, vol. 153, pp. 103–127, Mar. 2016, DOI:10.1016/j.engfracmech.2015.12.023.

[133] Y. Katz, N. Tymiak, and W. W. Gerberich, "Nanomechanical probes as new approaches to hydrogen/deformation interaction studies," *Eng. Fract. Mech.*, vol. 68, no. 6, pp. 619–646, 2001, DOI:10.1016/S0013-7944(00)00119-3.

[134] G. Bertolino, G. Meyer, and J. Perez Ipiña, "In situ crack growth observation and fracture toughness measurement of hydrogen charged Zircaloy-4," *J. Nucl. Mater.*, vol. 322, no. 1, pp. 57–65, 2003, DOI:10.1016/S0022-3115(03)00305-2.

[135] Y. Wada and R. Ishigaki, "Evaluation of metal materials for hydrogen fuel stations," *Proc. Int. Conf. Hydrog. Saf.*, 2005.

[136] E. V. Chatzidouros, V. J. Papazoglou, T. E. Tsiourva, and D. I. Pantelis, "Hydrogen effect on fracture toughness of pipeline steel welds, with in situ hydrogen charging," *Int. J. Hydrogen Energy*, vol. 36, no. 19, pp. 12626–12643, 2011, DOI:10.1016/j.ijhydene.2011.06.140.

[137] L. Briottet, I. Moro, and P. Lemoine, "Quantifying the hydrogen embrittlement of pipeline steels for safety considerations," *Int. J. Hydrogen Energy*, vol. 37, no. 22, pp. 17616–17623, 2012, DOI:10.1016/j.ijhydene.2012.05.143.

[138] T. Matsumoto, H. Itoga, S. Hirabayashi, M. Kubota, and S. Matsuoka, "Effect of Displacement Velocity on Elastic Plastic Fracture Toughness of SM490B Carbon Steel Plate in 0.7 MPa Hydrogen Gas (in Japanese)," *Nihon Kikai Gakkai Ronbunshu, A Hen/Transactions Japan Soc. Mech. Eng. Part A*, vol. 79, pp. 1210–1225, 2013, DOI:10.1299/kikaia.79.1210.

[139] T. Matsumoto, M. Kubota, S. Matsuoka, P. Ginet, J. Furtado, and F. Barbier, "Threshold stress intensity factor for hydrogen-assisted cracking of CR-MO steel used as stationary storage buffer of a hydrogen refueling station," *Int. J. Hydrogen Energy*, vol. 42, no. 11, pp. 7422–7428, 2017, DOI:10.1016/j.ijhydene.2016.05.124.

[140] Y. Ogawa, H. Matsunaga, J. Yamabe, M. Yoshikawa, and S. Matsuoka, "Unified evaluation of hydrogen-induced crack growth in fatigue tests and fracture toughness tests of a carbon steel," *Int. J. Fatigue*, vol. 103, pp. 223–233, 2017, DOI:10.1016/j.ijfatigue.2017.06.006.

[141] J. Stoer and R. Bulirsch, *Introduction to Numerical Analysis*. New York, NY: Springer New York, 2002.

[142] M. Yoshikawa, T. Matsuo, N. Tsutsumi, H. Matsunaga, and S. Matsuoka, "Effects of hydrogen gas pressure and test frequency on fatigue crack growth properties of low carbon steel in 0.1-90 MPa hydrogen gas," *Trans. JSME (in Japanese)*, vol. 80, no. 817, pp. SMM0254-SMM0254, 2014, DOI:10.1299/transjsme.2014smm0254.

[143] J. Yamabe, M. Yoshikawa, H. Matsunaga, and S. Matsuoka, "Effects of hydrogen pressure, test frequency and test temperature on fatigue crack growth properties of low-carbon steel in gaseous hydrogen," *Procedia Struct. Integr.*, vol. 2, no. 817, pp. 525–532, 2016, DOI:10.1016/j.prostr.2016.06.068.

[144] ASTM, *E 647 – 05: Standard Test Method for Measurement of Fatigue Crack Growth Rates*, no. July. 2005.

[145] ELBER W, "Fatigue Crack Closure Under Cyclic Tension," *Eng. Fract. Mech.*, vol. 2, no. 1, pp. 37–45, 1970, DOI:10.1016/0013-7944(70)90028-7.

[146] R. Pippan, "Threshold and effective threshold of fatigue crack propagation in ARMCO iron I: The influence of grain size and cold working," *Mater. Sci. Eng. A*, vol. 138, no. 1, pp. 1–13, May 1991, DOI:10.1016/0921-5093(91)90671-9.

[147] R. Pippan, "Threshold and effective threshold of fatigue crack propagation in ARMCO iron II: The influence of environment," *Mater. Sci. Eng. A*, vol. 138, no. 1, pp. 15–22, May 1991, DOI:10.1016/0921-5093(91)90672-A.

[148] P. C. Paris, M. P. Gomez, and W. E. Anderson, "A rational analytic theory of fatiuge," *The Trend in Engineering*, vol. 13, no. 4. pp. 9–14, 1961.

[149] R. O. Ritchie, "Mechanisms of fatigue crack propagation in ductile and brittle solids," *Int. J. Fract.*, vol. 100, no. 1, pp. 55–83, 1999, DOI:10.1023/A:1018655917051.

[150] R. M. N. Pelloux, "Crack extension by alternating shear," *Eng. Fract. Mech.*, vol. 1, no. 4, 1970, DOI:10.1016/0013-7944(70)90008-1.

[151] J. Petit, G. Hénaff, and C. Sarrazin-Baudoux., "Environmentally Assisted Fatigue in the Gaseous Atmosphere," in *Comprehensive structural integrity, volume 6*, 2003, pp. 211–280.

[152] A. K. Vasudevan and K. Sadananda, "Classification of environmentally assisted fatigue crack growth behavior," *Int. J. Fatigue*, vol. 31, no. 11–12, pp. 1696–1708, 2009, DOI:10.1016/j.ijfatigue.2009.03.019.

[153] E. S. Drexler, A. J. Slifka, R. L. Amaro, N. Barbosa, D. S. Lauria, L. E. Hayden, and D. G. Stalheim, "Fatigue crack growth rates of API X70 pipeline steel in a pressurized hydrogen gas environment," *Fatigue Fract. Eng. Mater. Struct.*, vol. 37, no. 5, pp. 517–525, 2014, DOI:10.1111/ffe.12133.

[154] A. J. Slifka, E. S. Drexler, N. E. Nanninga, Y. S. Levy, J. D. McColskey, R. L. Amaro, and A. E. Stevenson, "Fatigue crack growth of two pipeline steels in a pressurized hydrogen environment," *Corros. Sci.*, vol. 78, pp. 313–321, 2014, DOI:10.1016/j.corsci.2013.10.014.

[155] J. A. Ronevich and B. P. Somerday, "Hydrogen Effects on Fatigue Crack Growth Rates in Pipeline Steel Welds," *Vol. 6B Mater. Fabr.*, p. V06BT06A035, Jul. 2016, DOI:10.1115/PVP2016-63669.

[156] K. Tazoe, S. Hamada, and H. Noguchi, "Fatigue crack growth behavior of JIS SCM440 steel near fatigue threshold in 9-MPa hydrogen gas environment," *Int. J. Hydrogen Energy*, vol. 42, no. 18, pp. 13158–13170, 2017, DOI:10.1016/j.ijhydene.2017.03.223.

[157] D. Birenis, Y. Ogawa, H. Matsunaga, O. Takakuwa, J. Yamabe, Ø. Prytz, and A. Thøgersen, "Hydrogen-assisted fatigue crack propagation in a pure BCC iron. Part II: Accelerated regime manifested by quasi-cleavage fracture at relatively high stress intensity range values," *MATEC Web Conf.*, vol. 165, p. 03010, May 2018, DOI:10.1051/matecconf/201816503010.

[158] J. A. Ronevich, B. P. Somerday, and C. W. San Marchi, "Effects of microstructure banding on hydrogen assisted fatigue crack growth in X65 pipeline steels," *Int. J. Fatigue*, vol. 82, pp. 497–504, 2015, DOI:10.1016/j.ijfatigue.2015.09.004.

[159] G. Bilotta, G. Henaff, D. Halm, and M. Arzaghi, "Experimental measurement of out-of-plane displacement in crack propagation under gaseous hydrogen," *Int. J. Hydrogen Energy*, vol. 42, no. 15, pp. 10568–10578, 2017, DOI:10.1016/j.ijhydene.2017.02.084.

[160] J. Yamabe, M. Yoshikawa, H. Matsunaga, and S. Matsuoka, "Hydrogen trapping and fatigue crack growth property of low-carbon steel in hydrogen-gas environment," *Int. J. Fatigue*, 2017, DOI:10.1016/j.ijfatigue.2017.04.010.

[161] Y. Takeo and S. Kiyoshi, "The effect of frequency on fatigue crack propagation rate and striation spacing in 2024-T3 aluminium alloy and SM-50 steel," *Eng. Fract. Mech.*, vol. 8, no. 1, 1976, DOI:10.1016/0013-7944(76)90078-3.

[162] Y. Ogawa, D. Birenis, H. Matsunaga, A. Thøgersen, Ø. Prytz, O. Takakuwa, and J. Yamabe, "Multi-scale observation of hydrogen-induced, localized plastic deformation in fatigue-crack propagation in a pure iron," *Scr. Mater.*, vol. 140, pp. 13–17, 2017, DOI:10.1016/j.scriptamat.2017.06.037.

[163] Y. Ogawa, D. Birenis, H. Matsunaga, O. Takakuwa, J. Yamabe, Ø. Prytz, and A. Thøgersen, "Hydrogen-assisted fatigue crack propagation in a pure BCC iron. Part I: Intergranular crack propagation at relatively low stress intensities," *MATEC Web Conf.*, vol. 165, p. 03011, May 2018, DOI:10.1051/matecconf/201816503011.

[164] J. Yamabe, T. Matsumoto, S. Matsuoka, and Y. Murakami, "A new mechanism in hydrogen-enhanced fatigue crack growth behavior of a 1900-MPa-class high-strength steel," *Int. J. Fract.*, vol. 177, no. 2, pp. 141–162, 2012, DOI:10.1007/s10704-012-9760-9.

[165] M. Dadfarnia, A. Nagao, S. Wang, M. L. Martin, B. P. Somerday, and P. Sofronis, "Recent advances on hydrogen embrittlement of structural materials," *Int. J. Fract.*, pp. 1–21, 2015, DOI:10.1007/s10704-015-0068-4.

[166] S. K. Banerji, C. J. McMahon, and H. C. Feng, "Intergranular fracture in 4340-type steels: Effects of impurities and hydrogen," *Metall. Trans. A*, vol. 9, no. 2, pp. 237–247, 1978, DOI:10.1007/BF02646706.

[167] Y. Ogawa, D. Birenis, H. Matsunaga, O. Takakuwa, J. Yamabe, Ø. Prytz, and A. Thøgersen, "The role of intergranular fracture on hydrogen-assisted fatigue crack propagation in pure iron at a low stress intensity range," *Mater. Sci. Eng. A*, vol. 733, pp. 316–328, Aug. 2018, DOI:10.1016/j.msea.2018.07.014.

[168] Z. F. Zhang and Z. G. Wang, "Dependence of intergranular fatigue cracking on the interactions of persistent slip bands with grain boundaries," *Acta Mater.*, vol. 51, no. 2, pp. 347–364, 2003, DOI:10.1016/S1359-6454(02)00399-3.

[169] H. Cai and A. J. McEvily, "On striations and fatigue crack growth in 1018 steel," *Mater. Sci. Eng. A*, vol. 314, no. 1–2, pp. 86–89, 2001, DOI:10.1016/S0921-5093(00)01925-0.

[170] S. Lynch and S. Lynch, "Some fractographic contributions to understanding fatigue crack growth," *Int. J. Fatigue*, vol. 104, pp. 12–26, 2017, DOI:10.1016/j.ijfatigue.2017.06.036.

[171] A. J. Slifka, E. S. Drexler, D. G. Stalheim, R. L. Amaro, D. S. Lauria, A. E. Stevenson, and L. E. Hayden, "The Effect of Microstructure on the Hydrogen-Assisted Fatigue of Pipeline Steels," *Vol. 6B Mater. Fabr.*, p. V06BT06A009, Jul. 2013, DOI:10.1115/PVP2013-97217.

[172] B. P. Somerday, P. Sofronis, K. A. Nibur, C. S. Marchi, and R. Kirchheim, "Elucidating the variables affecting accelerated fatigue crack growth of steels in hydrogen gas with low oxygen concentrations," *Acta Mater.*, vol. 61, no. 16, pp. 6153–6170, 2013, DOI:10.1016/j.actamat.2013.07.001.

[173] K. A. Nibur, B. P. Somerday, C. S. Marchi, J. W. Foulk III, M. Dadfarnia, and P. Sofronis, "The Relationship Between Crack-Tip Strain and Subcritical Cracking Thresholds for Steels in High-Pressure Hydrogen Gas," *Metall. Mater. Trans. a-Physical Metall. Mater. Sci.*, vol. 44A, no. 1, pp. 248–269, 2013, DOI:10.1007/s11661-012-1400-5.

[174] D. Wan, A. Alvaro, V. Olden, and A. Barnoush, "Hydrogen-assisted fatigue crack growth in ferritic steels – a fractographic study," *MATEC Web Conf.*, vol. 165, p. 03004, May 2018, DOI:10.1051/matecconf/201816503004.

[175] J. Pokluda and J. Siegl, "Mixed Fatigue Fracture Morphology of Ferritic Ductile Iron," *Fatigue Fract. Eng. Mater. Struct.*, vol. 13, no. 4, pp. 375–385, Jul. 1990, DOI:10.1111/j.1460-2695.1990.tb00608.x.

[176] M. Koyama, Y. Onishi, and H. Noguchi, "Characteristics of hydrogen-assisted intergranular fatigue crack growth in interstitial-free steel: role of plastic strain localization," *Int. J. Fract.*, vol. 206, no. 1, pp. 123–130, 2017, DOI:10.1007/s10704-017-0205-3.

[177] Y. Takahashi, K. Yamaguchi, M. Tanaka, K. Higashida, and H. Noguchi, "On the micromechanism of hydrogen-assisted cracking in a single-crystalline iron-silicon alloy thin sheet," *Scr. Mater.*, vol. 64, no. 6, pp. 537–540, 2011, DOI:10.1016/j.scriptamat.2010.11.035.

[178] D. H. Lassila and H. K. Birnbaum, "Intergranular fracture of nickel: the effect of hydrogen-sulfur co-segregation," *Acta Metall.*, vol. 35, no. 7, pp. 1815–1822, Jul. 1987, DOI:10.1016/0001-6160(87)90127-1.

[179] S. Matsuoka, H. Tanaka, N. Homma, and Y. Murakami, "Influence of hydrogen and frequency on fatigue crack growth behavior of Cr-Mo steel," *Int. J. Fract.*, vol. 168, no. 1, pp. 101–112, 2011, DOI:10.1007/s10704-010-9560-z.

[180] H. Matsunaga, T. Nakashima, K. Yamada, T. Matsuo, J. Yamabe, and S. Matsuoka, "Effect of Test Frequency on Hydrogen-Enhanced Fatigue Crack Growth in Type 304 Stainless Steel and Ductile Cast Iron," *Vol. 6B Mater. Fabr.*, p. V06BT06A031, Jul. 2016, DOI:10.1115/PVP2016-63536.

[181] H. Matsunaga, O. Takakuwa, J. Yamabe, and S. Matsuoka, "Hydrogen-enhanced fatigue crack growth in steels and its frequency dependence," *Philos. Trans. R. Soc. A Math. Phys. Eng. Sci.*, vol. 375, no. 2098, p. 20160412, Jul. 2017, DOI:10.1098/rsta.2016.0412.

[182] L. Guerra-Rosa, C. Moura Branco, and J. C. Radon, "Monotonic and cyclic crack tip plasticity," *Int. J. Fatigue*, vol. 6, no. 1, pp. 17–24, 1984, DOI:10.1016/0142-1123(84)90004-5.

[183] J. R. Rice, "Mechanics of Crack Tip Deformation and Extension by Fatigue," *Fatigue Crack Propag.*, vol. ASTM STP 4, no. October, pp. 247–309, 1967, DOI:10.1520/STP47234S.

[184] R. C. McClung, "Crack Closure and Plastic Zone Sizes in Fatigue," *Fatigue Fract. Eng. Mater. Struct.*, vol. 14, no. 4, pp. 455–468, 1991, DOI:10.1111/j.1460-2695.1991.tb00674.x.

[185] R. D. Pfaff, P. D. Washabaugh, and W. G. Knauss, "An interpretation of Twyman-Green interferograms from static and dynamic fracture experiments," *Int. J. Solids Struct.*, vol. 32, no. 6–7, pp. 939–955, 1995, DOI:10.1016/0020-7683(94)00170-2.

[186] L. Humbert, V. Valle, and M. Cottron, “Experimental determination and empirical representation of out-of-plane displacements in a cracked elastic plate loaded in mode I,” *Int. J. Solids Struct.*, vol. 37, no. 39, pp. 5493–5504, 2000, DOI:10.1016/S0020-7683(99)00210-3.

[187] L. D. Paolinelli, G. E. Carr, N. Gubeljak, J. Predan, and M. D. Chapetti, “Fracture toughness analysis of a ductile steel by means of 3D surface displacements,” *Eng. Fract. Mech.*, vol. 98, no. 1, pp. 109–121, 2013, DOI:10.1016/j.engfracmech.2012.12.006.

[188] Taylor Hobson, “Talysurf CCI 6000.” [Online]. Available: http://blogs.univ-poitiers.fr/surfacestopo/files/2014/01/Talysurf_CCI6000.pdf.

[189] J. Titchmarsh, *Transmission Electron Microscopy*. 2009.

[190] ETH Zürich and the authors, “STEM Detectors.” [Online]. Available: http://www.microscopy.ethz.ch/STEM.htm.

[191] K. Saitoh, “High-resolution Z-contrast Imaging by the HAADF-STEM Method,” *Nihon Kessho Gakkaishi (in japanese)*, vol. 47, no. 1, pp. 9–14, 2005, DOI:10.5940/jcrsj.47.9.

[192] FEI, “Helios NanoLab G3 - Electron Microscopy Center.” [Online]. Available: http://mtrmika.technion.ac.il/wp-content/uploads/2016/07/Helios_NanoLab_G3_Datasheet.pdf.

[193] S. Suzuki, “Features of transmission EBSD and its application,” *Jom*, vol. 65, no. 9, pp. 1254–1263, 2013, DOI:10.1007/s11837-013-0700-6.

[194] C. A. Volkert and A. M. Minor, “Focused Ion Beam Microscopy and Micromachining,” *MRS Bull.*, vol. 32, no. 05, pp. 389–399, May 2007, DOI:10.1557/mrs2007.62.

[195] B. W. Kempshall, S. M. Schwarz, B. I. Prenitzer, L. A. Giannuzzi, R. B. Irwin, and F. A. Stevie, “Ion channeling effects on the focused ion beam milling of Cu,” *J. Vac. Sci. Technol. B Microelectron. Nanom. Struct.*, vol. 19, no. 3, p. 749, 2001, DOI:10.1116/1.1368670.

[196] J. Song and W. a Curtin, “Atomic mechanism and prediction of hydrogen embrittlement in iron.,” *Nat. Mater.*, vol. 12, no. 2, pp. 145–51, 2013, DOI:10.1038/nmat3479.

[197] S. Taketomi, R. Matsumoto, and N. Miyazaki, “Atomistic study of the competitive relationship between edge dislocation motion and hydrogen diffusion in alpha iron,” *J. Mater. Res.*, vol. 26, no. 10, pp. 1269–1278, 2011, DOI:10.1557/jmr.2011.106.

[198] N. Taketomi, S., Imanishi, S., Matsumoto, R., Miyazaki, “Dislocation dynamics analysis of hydrogen embrittlement in alpha iron based on atomistic investigations,” *13th Int. Conf. Fract.*, pp. 16–21, 2013.

[199] T. Hajilou, Y. Deng, B. R. Rogne, N. Kheradmand, and A. Barnoush, “In situ electrochemical microcantilever bending test: A new insight into hydrogen enhanced cracking,” *Scr. Mater.*, vol. 132, pp. 17–21, 2017, DOI:10.1016/j.scriptamat.2017.01.019.

[200] S. Wang, A. Nagao, P. Sofronis, and I. M. Robertson, “Hydrogen-modified dislocation structures in a cyclically deformed ferritic-pearlitic low carbon steel,” *Acta Mater.*, vol. 144, pp. 164–176, 2018, DOI:10.1016/j.actamat.2017.10.034.

[201] J. Kacher and I. M. Robertson, "Quasi-four-dimensional analysis of dislocation interactions with grain boundaries in 304 stainless steel," *Acta Mater.*, vol. 60, no. 19, pp. 6657–6672, Nov. 2012, DOI:10.1016/j.actamat.2012.08.036.

[202] R. Matsumoto, M. Riku, S. Taketomi, and N. Miyazaki, "Hydrogen–Grain Boundary Interaction in Fe, Fe–C, and Fe–N Systems," *Prog. Nucl. Sci. Technol.*, vol. 2, no. 0, pp. 9–15, Oct. 2011, DOI:10.15669/pnst.2.9.

[203] S. Wang, M. L. Martin, I. M. Robertson, and P. Sofronis, "Effect of hydrogen environment on the separation of Fe grain boundaries," *Acta Mater.*, vol. 107, pp. 279–288, 2016, DOI:10.1016/j.actamat.2016.01.067.

[204] M. Riku, R. Matsumoto, S. Taketomi, and N. Miyazaki, "Atomistic simulation study of cohesive energy of grain boundaries in alpha iron under gaseous hydrogen environment," *Zair. Soc. Mater. Sci. Japan*, vol. 59, no. 8, pp. 589–595, 2010, DOI:10.2472/jsms.59.589.

[205] L. Wan, W. Tong, A. Ishii, J. Du, and N. Ishikawa, "Hydrogen embrittlement controlled by reaction of dislocation with grain boundary in alpha-iron," *Int. J. Plast.*, no. July, pp. 1–26, 2018, DOI:10.1016/J.IJPLAS.2018.08.013.

[206] R. A. Oriani and P. H. Josephic, "Equilibrium aspects of hydrogen-induced cracking of steels," *Acta Metall.*, vol. 22, no. 9, pp. 1065–1074, 1974, DOI:10.1016/0001-6160(74)90061-3.

[207] R. Matsumoto, S. Seki, S. Taketomi, and N. Miyazaki, "Hydrogen-related phenomena due to decreases in lattice defect energies - Molecular dynamics simulations using the embedded atom method potential with pseudo-hydrogen effects," *Comput. Mater. Sci.*, vol. 92, pp. 362–371, 2014, DOI:10.1016/j.commatsci.2014.05.029.

[208] H. Shoda, H. Suzuki, K. Takai, and Y. Hagihara, "Hydrogen Desorption Behavior of Pure Iron and Inconel 625 during Elastic and Plastic Deformation," *Tetsu-to-Hagane*, vol. 95, no. 1, pp. 573–581, 2009, DOI:10.2355/tetsutohagane.95.573.

[209] R. Pippan, C. Zelger, E. Gach, C. Bichler, and H. Weinhandl, "On the mechanism of fatigue crack propagation in ductile metallic materials," *Fatigue Fract. Eng. Mater. Struct.*, vol. 34, no. 1, pp. 1–16, 2011, DOI:10.1111/j.1460-2695.2010.01484.x.

[210] Q. J. Peng, J. Kwon, and T. Shoji, "Development of a fundamental crack tip strain rate equation and its application to quantitative prediction of stress corrosion cracking of stainless steels in high temperature oxygenated water," *J. Nucl. Mater.*, vol. 324, no. 1, pp. 52–61, 2004, DOI:10.1016/j.jnucmat.2003.09.008.

[211] M. M. Hall, "An alternative to the Shoji crack tip strain rate equation," *Corros. Sci.*, vol. 50, no. 10, pp. 2902–2905, 2008, DOI:10.1016/j.corsci.2008.07.011.

Caractérisation expérimentale de l'influence de l'hydrogène gazeux sur la propagation et la plasticité en pointe de fissure de fatigue dans le fer pur Armco

Résumé: L'objectif de cette étude est de caractériser expérimentalement la propagation de fissures de fatigue affectée par l'hydrogène (Hydrogen-Affected Fatigue Crack Growth, HAFCG) dans diverses conditions et de clarifier le mécanisme impliqué en se concentrant sur la plasticité en pointe de fissures. Pour cet objectif, dans une première étape, l'influence de l'hydrogène sur la déformation plastique a été étudiée à l'aide d'essais de traction effectués sur un fer commercialement pur, le fer Armco, sous hydrogène gazeux. Les résultats ont montré que l'effet de l'hydrogène sur la propagation des fissures après apparition de la striction est plus important que celui sur la déformation plastique uniforme. Le HAFCG a ensuite été étudié au moyen d'essais de fissuration pour diverses valeurs de l'amplitude de facteur d'intensité de contrainte ΔK, de pression d'hydrogène (P_{H2} = 3,5 et 35 MPa) et de fréquence de chargement (f = 0,02 - 20 Hz). Il a été révélé que les vitesses de propagation dans un régime à ΔK élevé étaient fortement augmentées par l'hydrogène, jusqu'à 50 fois plus élevé que celles dans l'air. Le mode de rupture est une rupture intergranulaire fragile dans un régime de propagation à faible ΔK, alors qu'on observe une rupture transgranulaire de type quasi-clivage dans un régime à ΔK élevé. La valeur de ΔK_{tr} (valeur de ΔK déclenchant l'augmentation de la vitesse de fissuration) diminue en augmentant la pression P_{H2}. En outre, la vitesse augmente en diminuant la fréquence f. Une fois que la fréquence devient inférieure à une valeur critique, la vitesse de fissuration diminue considérablement jusqu'au même niveau que celle sous azote. La plasticité en pointe de fissure a été analysée à plusieurs échelles par microscopie optique, par mesure de déplacement hors plan et par microscopie électronique à balayage par transmission de la structure de dislocation située immédiatement sous la surface de rupture (FIB/STEM). Aucune modification claire de la zone plastique monotone en pointe de fissure sous hydrogène n'a été observée, alors qu'une réduction drastique de la plasticité cyclique associée à l'augmentation de la vitesse a été identifiée. Sur la base des observations expérimentales, des modèles de mécanisme de fissuration intergranulaire induit par l'hydrogène impliquant la coalescence des micro-vides le long de joints de grain et de mécanisme de fissuration transgranulaire induit par l'hydrogène impliquant un clivage cyclique dû à la réduction de la plasticité en pointe de fissure ont été proposés. Trois critères caractéristiques de fissuration assistée par hydrogène (ΔK_{tr}, gradient d'hydrogène $(P_{H2} \times f)^{1/2}$ etlimite supérieure de vitesse de fissuration) ont été établis. Ces critères devraient être utiles pour améliorer la conception en fatigue et la fiabilité des équipements exposés à l'hydrogène gazeux.

Mots clés: Métaux--Fatigue, Matériaux--Fissuration, Métaux--Fragilisation par l'hydrogène, Fer, Plasticité, Dislocations dans les métaux

Experimental characterization of influence of gaseous hydrogen on fatigue crack propagation and crack tip plasticity in Armco pure iron

Abstract: The objective of this study is to experimentally characterize Hydrogen-Affected Fatigue Crack Growth (HAFCG) behavior under various conditions and clarify the mechanism by focusing on crack tip plasticity. For this objective, as a first step, the influence of hydrogen on plastic deformation has been investigated by means of tensile tests in a commercially pure iron, Armco iron, under gaseous hydrogen. The results of the tests pointed out that the hydrogen effect on crack propagation is more important than that on uniform plastic deformation. Then, the HAFCG was investigated by means of FCG tests under various conditions of crack tip stress intensity ΔK, hydrogen gas pressure (P_{H2} = 3.5 and 35 MPa) and loading frequency (f = 0.02 – 20 Hz). It has been revealed that the FCGRs in a high ΔK regime were highly enhanced by hydrogen up to 50 times higher than the one in air. The fracture mode was a brittle intergranular fracture in a low ΔK regime, while it is a brittle transgranular quasi-cleavage one in a high ΔK regime. The value of ΔK_{tr} (value of ΔK triggering the FCGR enhancement) decreases by increasing the pressure P_{H2}. Besides, the FCGR enhancement increases by decreasing the frequency f. Once f becomes lower than a critical value, the HAFCG rate significantly decreases down to the same level as in nitrogen., The crack tip plasticity was analyzed in a multiscale approach by means of optical microscopy, out-of-plane displacement measurement, and scanning transmission electron microscopy of dislocation structure immediately beneath the fracture surface (FIB/STEM). As a result, no clear modification of monotonic crack tip plasticity by hydrogen was observed, while a drastic reduction of cyclic crack tip plasticity associated with the FCGR enhancement was identified. Based on the experimental evidences, models of the hydrogen-induced intergranular FCG mechanism involving microvoid coalescence along grain boundary and the hydrogen-induced transgranular FCG mechanism involving cyclic cleavage due to crack tip plasticity reduction have been proposed. Three characteristic criteria of HAFCG (ΔK_{tr}, hydrogen gradient $(P_{H2} \times f)^{1/2}$ and upper limit of FCGR) have been established. These criteria are expected to be useful for improving fatigue design and reliability of hydrogen-related equipment.

Keywords: Metals--Fatigue, Materials--Cracking, Hydrogen embrittlement, Iron, Plasticity, Dislocations in metals